SANDIA REPORT
SAND2024-05240
Printed April 2024

Adaptive Protection and Control for High Penetration PV and Grid Resilience Final Technical Report

Matthew J. Reno, Miguel Jimenez-Aparicio, Trupal Patel, Adam Summers, Javier Hernandez-Alvidrez, Felipe Wilches-Bernal, Armando Montoya, Andrew R. R. Dow, Daniel Kelly, Ronald Matthews, Samuel T. Ojetola, Rachid Darbali-Zamora, Felipe Palacios II, Jack D. Flicker

Sandia National Laboratories

Ali Bidram, Sajay K. Paruthiyil, Rudy Montoya, Binod Poudel, Aswathy Rajendra-Kurup, Manel Martinez-Ramon

University of New Mexico

Sukumar Brahma, Munim Bin Gani, Prabin Adhikari

Clemson University

Ashok Gopalakrishnan, Yazid Alkraimeen, Yimai Dong, Liangyi Sun, Ce Zheng

Siemens CAPE

Gary Oppedahl, Daniel Bauer

Emera Technologies

Prepared by
Sandia National Laboratories
Albuquerque, New Mexico
87185 and Livermore,
California 94550

Issued by Sandia National Laboratories, operated for the United States Department of Energy by National Technology & Engineering Solutions of Sandia, LLC.

Available to DOE and DOE contractors from

U.S. Department of Energy
Office of Scientific and Technical Information
P.O. Box 62
Oak Ridge, TN 37831

Telephone: (865) 576-8401
Facsimile: (865) 576-5728
E-Mail: reports@osti.gov
Online ordering: http://www.osti.gov/scitech

Available to the public from

U.S. Department of Commerce
National Technical Information Service
5301 Shawnee Rd
Alexandria, VA 22312

Telephone: (800) 553-6847
Facsimile: (703) 605-6900
E-Mail: orders@ntis.gov
Online order: https://classic.ntis.gov/help/order-methods/

ABSTRACT

The report summarizes the work and accomplishments of DOE SETO funded project 36533 "Adaptive Protection and Control for High Penetration PV and Grid Resilience". In order to increase the amount of distributed solar power that can be integrated into the distribution system, new methods for optimal adaptive protection, artificial intelligence or machine learning based protection, and time domain traveling wave protection are developed and demonstrated in hardware-in-the-loop and a field demonstration.

ACKNOWLEDGEMENTS

This material is based upon work supported by the U.S. Department of Energy's Office of Energy Efficiency and Renewable Energy (EERE) under the Solar Energy Technologies Office Award Number 36533.

CONTENTS

Abstract 3

Acknowledgements 4

Contents 5

List of Figures 10

List of Tables 18

Acronyms and Terms 20

1. Introduction 25
   - 1.1. Objective 1: Creating an adaptive protection platform 26
   - 1.2. Objective 2: Creating communication-free local adaptive modular protection 26
   - 1.3. Objective 3: Creating protection algorithms for equipment in low inertia power systems 26
   - 1.4. Objective 4: Creating fault location techniques suitable for unbalanced networks fed by high penetration of and inverter-based DERs 27
2. Adaptive Protection Platform 29
   - 2.1.1. Circuit Model Management Module 30
   - 2.1.2. Short Circuit Study Module 30
   - 2.1.3. Data Import Module 30
   - 2.1.4. Sensitivity Module 31
   - 2.1.5. Protection Settings Optimizer 33
   - 2.1.6. Protection Coordination Study Module 34
   - 2.1.7. APMS/Relay Interface 34
   - 2.2. Optimization Formulation 35
     - 2.2.1. Formulate Network Graph 35
     - 2.2.2. Identify Primary Backup Pairs 36
     - 2.2.3. Determine Pickup Settings 37
     - 2.2.4. Determine Device Type. 39
     - 2.2.5. Formulate Objective Function. 41
     - 2.2.6. Formulate Constraint Function. 42
     - 2.2.7. Optimize 44
   - 2.3. Interaction with PSS®CAPE 46
     - 2.3.1. The PSS®CAPE Coordination Macro – User Inputs 46
     - 2.3.2. The PSS®CAPE Coordination Macro – Studies Performed & Outputs 48
     - 2.3.3. IBR Model in CAPE [7] 49

2.4. Equipment Damage Constraints [9] 51
2.5. Coordination with Distance Relays 54
2.6. Hardware in the Loop Setup 58
    2.6.1. SEL Hardware Configuration with OPAL-RT 60
    2.6.2. Virtual Protection Device Setup in the OPAL-RT 64
    2.6.3. Communications from Virtual Relays and SEL Relays to APMS 65
    2.6.4. Overview of Adaptive Protection Code 67
    2.6.5. Collection of PMU Data in the Adaptive Protection Code 68
    2.6.6. Sensitivity Analysis Check 69
    2.6.7. Real Time Digital Twin with CAPE 71
    2.6.8. Running Optimizer in Real-Time 73
    2.6.9. Writing Settings to the Database 73
    2.6.10. Writing Settings to Relays 73
2.7. Hardware-in-the-Loop Demonstration of the Adaptive Protection System 77
    2.7.1. Power System Protection Refresher and the Need for Adaptive Protection 77
    2.7.2. Without Adaptive Protection 77
    2.7.3. With Adaptive Protection 79
    2.7.4. Partial System Re-energization. 80
    2.7.5. Adaptive Protection coordinating in a Fuse Blowing Scheme. 81
3. Communication-free Adaptive Protection Modules 83
3.1. Learning Protection Settings [18] 83
    3.1.1. Learning Protection Settings Methodology 83
    3.1.2. The Prophet Algorithm 83
    3.1.3. Parameters to Predict 84
    3.1.4. Prediction Analysis 84
    3.1.5. Results for Local Parameter Prediction 84
3.2. Zonal Setting-less Protection LAMP 87
    3.2.1. Local Adaptive Modular Protection Methodology 87
    3.2.2. Simulation Results 90
    3.2.3. HIL Verification of LAMP: 95
    3.2.4. Comparison of SVM with Other Classifiers: 97
3.3. ML-Based AC Fault Detection 97
    3.3.1. Simulation Results 100

3.3.2. HIL Verification of ML-Based Fault Detection 102

3.4. ML-Based DC Fault Detection 103

3.4.1. DC Power system model 103

3.4.2. DC Fault Detection using Linear Classification Algorithms 104

3.4.3. DC Fault Detection using Time-Series Classification Algorithms 106

4. Traveling Wave Protection 109

4.1. AC Systems 109

4.1.1. Hardware-in-the-loop Testing of the Limitations of Existing Traveling Wave Relays for Distribution Systems [26, 27] 110

4.1.2. Fault Detection 119

4.1.3. Fault Location 122

4.1.4. Implementation of a Traveling Wave Fault Detection and Location Scheme 124

4.1.5. Analysis of a Traveling Wave Protection Scheme for AC Systems 125

4.2. DC Systems 128

4.2.1. High-Frequency Fault Signatures in a DC system 128

4.2.2. Fault Classification and Location Scheme 130

4.2.3. Hardware Implementation of a TW Protection for the Emera DC Microgrid 136

5. Fault Location Techniques 145

5.1. Summary of Work Performed 145

5.2. Time-Domain Distance and Directional Relays 146

5.2.1. Formulation of the Method 146

5.2.2. Results 148

5.2.3. Performance for Faults on Distribution Feeders 149

5.2.4. Comparing the Performance with a Commercial Time Domain Relay 152

5.2.5. Conversion to Directional Relay 153

5.3. Single-Ended Fault Location and Protection of a DC Feeder in a DC Microgrid: 153

5.3.1. Theory of Fault Location in a DC Feeder 153

5.3.2. Simulation Results with Ideal DC Sources: 155

5.3.3. Extension to Feeders with Converter-Based Sources 156

5.3.4. Undervoltage Based Backup protection for 4-bus DC Ring Main System 157

5.3.5. Simulating and Testing Main and Backup Protection on RTDS 159

5.3.6. Results 160

5.3.7. Testing the Main Protection in Hardware in the Loop 161

      - 5.3.8. Calculating Fault Location using the Sampled Values 162
- 6. Demonstration....165
  - 6.1. Overview of the Microgrid....165
  - 6.2. Sensor Installation 168
    - 6.2.1. Global Positioning System pulse generator....168
  - 6.3. Fault Generator and Fault Testing....169
  - 6.4. Baseline Measurements....170
  - 6.5. Emera Model Development and Validation....176
    - 6.5.1. Description of the Energy Storage System (ESS) Boost Converter Model 176
    - 6.5.2. Description of the Nanogrid Models....177
    - 6.5.3. Description of the Grid following inverter 177
    - 6.5.4. Description of the Grounding System....178
    - 6.5.5. Fault Response Comparison....178
  - 6.6. Microgrid Model for Real-Time Testing [49, 50]....180
  - 6.7. Development of High-Frequency Fault Location Hardware....182
  - 6.8. Field Testing with Relay....186
    - 6.8.1. Installation and Implementation in the Field....186
    - 6.8.2. Fault Detection and Recording....187
    - 6.8.3. Fast Fault Type and Location Class Algorithm Results 189
    - 6.8.4. Fast Fault Distance Location Algorithm Results....190
- 7. Conclusions....193
  - 7.1. Accomplishments and Final Deliverables....193
  - 7.2. Project Publications....193
    - 7.2.1. Journal Papers....193
    - 7.2.2. Conference Proceeding Publications....195
  - 7.3. Patents 198
  - 7.4. Path Forward....198
- 8. References 199

Appendix A....205
  - Inverse-Time Overcurrent Relays....205
  - Definite-Time Overcurrent Relays 205
  - Distance Relays....206
    - Mho Characteristics....207

Current Compensation Factor....208
Distribution....209

LIST OF FIGURES

Figure 1. APP Diagram 29

Figure 2. APMS block diagram 29

Figure 3. Fault analysis output from CAPE 30

Figure 4. Example element range data imported from CAPE. 31

Figure 5. Sensitivity check 32

Figure 6. Calculated and optimized variables 33

Figure 7. Protection coordination module flow diagram 34

Figure 8. Network graph representation of the IEEE 123 system 36

Figure 9. Comparison of operating times with and without type select. 40

Figure 10. Comparison of coordination gaps with and without type select. 41

Figure 11. Histogram of primary operating times 44

Figure 12. Primary-backup CGs 45

Figure 13. Invoking the PSS®CAPE coordination macro in the GUI. 47

Figure 14. Summary output – one line per fault studied. 49

Figure 15. Incorporating momentary cessation into IBR model. 50

Figure 16. Generic voltage relay in CAPE. 51

Figure 17. Equipment damage constraint integration with adaptive protection optimization. 52

Figure 18. CAPE database editor - conductor input required for damage calculation. 53

Figure 19. Distribution Coordination Macro output for conductor time-to-damage. 53

Figure 20. Subnetwork with R1 & single-phase branch 13-16. If R1 is not subject to conductor damage constraint, the R1 ground element may infringe upon damage curves. 54

Figure 21. Small 3-bus example for demonstration of distance relay protection zones. The shape of the of the zones does not reflect the complex impedances, only the physical line length or impedance magnitude along the horizontal dimension. 55

Figure 22. Sample 10-bus system with sparse relay placement. 56

Figure 23. Computation of Zone 1 and Zone 2 impedances as introduced in [14]. The Zone 1 computation is to the left, and the Zone 2 computation is to the right. 57

Figure 24. Sample mho circles using algorithm summarized in Figure 23. The diameters of the circles are also plotted to the represent the reach of each zone. Zone 1 is the smaller blue circle; Zone 2 is the larger green circle. 58

Figure 25. Modified IEEE 123 circuit with relay and DER locations. 59

Figure 26. Hardware-in-the-Loop diagram showing communication setup between devices. 60

Figure 27. Example of point on wave data collection. 61

Figure 28. Scaling voltage and current measurements and then sending the data out via an Analog Out block. 61
Figure 29. Low-Level SEL relay interface. 62
Figure 30. Hardware-in-the-Loop Setup at Sandia. 62
Figure 31. Opal-RT input connection from hardware relays. 63
Figure 32. Mockup of Out101 contact and monitoring. 63
Figure 33. Voltage divider circuit 64
Figure 34. Dedicated Protection Subsystem. 65
Figure 35. 50/51 Overcurrent Relay Block from OPAL-RT Simulink library. 65
Figure 36. Configuration of PMUs in RT-LAB. 66
Figure 37. Connecting PMU data points within RT-LAB. 66
Figure 38. OpOutput blocks used in Simulink for PMU mappings. 67
Figure 39. Adaptive Protection Flow Diagram. 68
Figure 40. Example csv file of PMU data. 69
Figure 41. Sensitivity Analysis Loop time. 69
Figure 42. Sensitivity Analysis Flow Diagram. 70
Figure 43. Python function to update CAPE. 71
Figure 44. CAPE modeling updating system configuration and PV status timing. 72
Figure 45. Terminal displaying CAPE updating system configuration and PV rating. 72
Figure 46. Example of CAPE updating a PV unit output. 73
Figure 47. Example of optimizer output. 73
Figure 48. Example of SEL 751 set1.txt file. 74
Figure 49. Section of python code showing how to update SEL relay settings with text file. 75
Figure 50. Configuration of Modbus datapoints within RT-LAB software 76
Figure 51. OpInput blocks used to receive Modbus parameter updates. 76
Figure 52. Python script used to write Modbus settings back to the OPAL-RT simulation 77
Figure 53. Protection coordination for a radial system 78
Figure 54. Unnecessary loss of Load. 78
Figure 55. HIL results of scenario 1 79
Figure 56. Adaptive Protection limiting the number of customer outages. 79
Figure 57. Comparison with and without Adaptive Protection 80
Figure 58. HIL results for scenario 2 80
Figure 59. Partial System Restored. 81

Figure 60. Scenario 3 results....81
Figure 61. Adaptive Protection coordinating with a fuse. 82
Figure 62 Scenario 4 results....82
Figure 63. Adaptive Protection updating during Scenario 1-4. 82
Figure 64. Relay 2 Comparison Between Predicted and Actual TDS Values. 85
Figure 65. Relay 6 Comparison Between Predicted and Actual IPickup Settings. 86
Figure 66. Comparison pf CTIs for different Protection Settings. 86
Figure 67. (a) LAMP in a DS; (b) LAMP protection zones....88
Figure 68. LAMP architecture....88
Figure 69. Modified IEEE 123 node system that shows the LAMPs' locations and the boundary of their Zone 1 in the Configuration 1. 90
Figure 70. LAMPs' locations and the boundary of their Zone 1 in the Configuration 2. 92
Figure 71. LAMPs' locations and the boundary of their Zone 1 in the Configuration 3. 92
Figure 72. LAMP locations and the boundary of their Zone 1 in the Configuration 4. 93
Figure 73. Fault type classification results for LAMP R1. 94
Figure 74. Zonal setting-less machine leaning protection sequence of actions. 96
Figure 75. RTL1's Zone 1 boundary....96
Figure 76. HIL testbed block diagram for circuit topology estimation and non-supervised fault detection algorithms. 96
Figure 77. Fault and trip signals for RTL1. 97
Figure 78. Proposed structure for fault classification and detection probability estimations....99
Figure 79. Structure of the CNN used for the classification of configurations. 100
Figure 80. A fault detector is constructed and trained for each one of the possible configurations.100
Figure 81. Modified IEEE 123 bus distribution system showing the fault locations.... 100
Figure 82. Probability of failure and probability of false alarm in fault detection. The probability of false alarm is dramatically lower when the number of test samples is less than 5×10^4..... 101
Figure 83. (a) Circuit topology estimation results with CNN; (b) Fault detection results using non-supervised GP. 102
Figure 84. One-line diagram of the ETL-KAFB DC Microgrid 103
Figure 85. Confusion Matrix showing the ML classification based of fault type. 105
Figure 86. Confusion Matrix showing the ML classification based off fault type and fault resistance. 106
Figure 87. Confusion Matrix of MINIROCKET Case 1 and Case 2 respectively.... 107
Figure 88. CWT Scalogram of the central box PPG voltages for faults at the NG1 and NG9 nodes 108

Figure 89. Confusion matrix of CNN ... 108

Figure 90. Traveling Wave on the voltage signal... 109

Figure 91. Testing power network to evaluate TW transient dynamics. ... 111

Figure 92. Flowchart that describes how to upload offline simulation signals to a TW relay... 112

Figure 93. Current traces from simulation case 1. (a) Magnified segment of faulted current trace after fault inception. (b) TWs extracted by the relay, with the relay calculating a fault distance of 8.06 km. ... 113

Figure 94. Traces from simulation case 2. (a) Magnified segment of faulted current trace after fault inception. (b) TWs extracted by the relay, with the relay calculating a fault distance of 12.8 km. ... 114

Figure 95. TW-based double-ended protection scheme. ... 115

Figure 96. Simulation model used to test double ended schemes. ... 115

Figure 97. Fault current traces of phase A and TWs at bus B_L. ... 116

Figure 98. Fault current traces of phase A and TWs at bus B_R. ... 117

Figure 99. Dependability contour for a line of 8.23 km. ... 118

Figure 100. Fault current traces and TWs at bus B_L from impedance tests. ... 119

Figure 101. Fault current traces and TWs at bus B_R from impedance tests. ... 119

Figure 102. Application of DMD to a TW waveform. ... 120

Figure 103. Threshold determination and fault TW detection rates for nodes 800 and 842. ... 121

Figure 104. Absolute and average fault location error percentage compared to the distance to the substation for the method that combines both SWT and MM tools for feature creation. ... 122

Figure 105. Workflow of the Detection, Signal-Processing, and Machine-Learning stages for the microRF method. ... 123

Figure 106. The IEEE 34 node system is divided into 11 protection zones. ... 124

Figure 107. Playback testing setup using 2 DSPs. ... 124

Figure 108. IEEE 34 node system, divided into 7 protection zones, and with 3 solar farms. ... 126

Figure 109. System-wide system detection rate using both db4 and db2 wavelet filters... 127

Figure 110. Simple DC microgrid system. ... 129

Figure 111. Cable configuration of the DC system in Figure 110. ... 129

Figure 112. Parseval energy values for different fault locations on the cable of DC system with 1 MHz sampling frequency in Figure 110 (a) MRA's level 1; (b) MRA's level 2; (c) MRA's level 3. ... 130

Figure 113. Parseval energy values for different fault locations on the cable of DC system with 2 MHz sampling frequency. ... 130

Figure 114. Fault classification and location algorithm. ... 132

Figure 115. Gaussian process regression model training procedure. ... 136

Figure 116. The TW fault detection algorithm for Emera microgrid. 137

Figure 117. (a) Comparison of level 1 Parseval energy calculated in DSP versus Python for VPP; (b) Comparison of level 2 Parseval energy calculated in DSP versus Python for VPP. 138

Figure 118. Radial configuration of Emera microgrid and location of faults and sensors. 139

Figure 119. PSCAD model validation: Positive pole voltage for a positive pole to ground fault at Gathering Space with 1 Ω resistance (measurement at DETL). 139

Figure 120. PSCAD model validation: Negative pole voltage for a positive pole to ground fault at Gathering Space with 1 Ω resistance (measurement at DETL). 140

Figure 121. PSCAD model validation: Positive pole voltage for a pole to pole fault at DETL with 4.7 Ω resistance (measurement at Central Box). 140

Figure 122. PSCAD model validation: Negative pole voltage for a pole to pole fault at DETL with 4.7 Ω resistance (measurement at Central Box). 140

Figure 123. Fault prediction using DSP where TWPD is at CENT when a pole-to-pole fault occurs at DETL. 142

Figure 124. Fault prediction using DSP where TWPD is at DETL when a pole-to-ground fault occurs at GATH. 143

Figure 125. Model of an unbalanced transmission line. 146

Figure 126. Two time-instances where fault voltage is the same due to symmetry. 147

Figure 127. Siemens Logic implementation for grid following inverter. 149

Figure 128. IEEE 123-node test feeder with added IBRs. 150

Figure 129. HIL Test-setup 152

Figure 130. Simulation system with (a) synchronous generator feeding the fault (b) IBR feeding the fault 152

Figure 131. Direction asserted by (a) 321 directional element when fed by an IBR (b) 32Q1 directional element when fed by an SS and (c) proposed relay using the samples from 32Q1.. 153

Figure 132. Two-bus DC circuit with ideal DC sources (a) time-domain representation (b) s domain representation. 154

Figure 133. Simulated and calculated currents from Bus 1 to fault for faults at (a) 80 m distance, (b) 40 m distance from Bus 1. 155

Figure 134. (a) Two bus DC microgrid fed with converters. (b) Parameters for the system. 156

Figure 135. Comparison of faults current sourced by an ideal source and a converter. 157

Figure 136. Calculated distances to fault point from Bus 1 and Bus 2. 157

Figure 137. Four bus DC ring system. 158

Figure 138. Voltages of different buses due to a fault between Bus 1 and Bus 2. 158

Figure 139. Schematic of Nano Grid box 159

Figure 140. Core assignments in RTDS for demonstrating backup protection. 160

Figure 141. Backup protection demonstration in RTDS 161
Figure 142. Sampled Voltage and Current by the DSP board. 162
Figure 143. Sampled (unfiltered) and filtered voltage. 162
Figure 144. Sampled (unfiltered) and filtered current. 162
Figure 145. Comparison of calculated fault locations from simulated values (inside the RTDS by software relay) and from sampled values (by the DSP board). 163
Figure 146. KAFB DC microgrid serving housing, utility, and DETL sites. 165
Figure 147. BlockBox nanogrid architecture showing integration of DERs into residential application. 166
Figure 148. (a) High-impedance grounding scheme found at CEP and (b) protection device used to detect and disable faults 167
Figure 149. KAFB microgrid architecture in a radial feed bus configuration. 167
Figure 150. KAFB microgrid architecture in a loop feed bus configuration. 167
Figure 151. Experimental fault test setup with measurement equipment connected to sections of the microgrid. 168
Figure 152. GPS Pulse Generator assembled into polycarbonate enclosure for 3rd scope location. 169
Figure 153. Fault emulator hardware installed onto microgrid distribution bus at the DETL. 169
Figure 154. Experimental fault test results for a 4.7 Ω line-to-line fault captured at the fault location (Gathering Space). 170
Figure 155. Experimental fault test results for a 4.7 Ω line-to-line fault captured at the DETL's nanogrid box (NG9). 171
Figure 156. Experimental fault test results for a 4.7 Ω line-to-line fault captured at the CEP (Community Box). 171
Figure 157. Comparing time-synchronized voltage waveforms (Gathering Space, DETL) during fault event. 172
Figure 158. Grid-Tie Inverter Fault Setup 172
Figure 159. Grid-Tie Inverter Fault Data Socomec Islanded (Fault Contribution in Yellow). 173
Figure 160. Grid-Tie Inverter Fault Data Socomec Operating at Idle (0 kW) Power State. 173
Figure 161. Protection Device Characterization Sensor Locations. 174
Figure 162. Protection Device Response to 500 Ohm Pole-Pole Fault (Ring Bus Topology). 174
Figure 163. Protection Device Response to a 4.7 Ohm Pole to Pole Fault (Isolated Bus). 175
Figure 164 Protection Device Response to 1.1 Ohm Pole-Pole Fault (Isolated Bus) 175
Figure 165. Schematic of EMERA DC microgrid. 176
Figure 166. Model of the voltage-controlled boost converter 177
Figure 167. Nanogrid box model including the DC-DC converters, PV module, BESS, and an inverter. 177

Figure 168. The grounding system model of Emera microgrid in PSCAD. 178

Figure 169. The frequency dependent model used in PSCAD for modeling the microgrid's cables.179

Figure 170. The combined RLC modules utilized for model tunning under fault condition. 179

Figure 171. PSCAD model validation: (a) Positive pole voltage for a positive pole to ground fault at Gathering Space with 1 Ω resistance (measurement at DETL); (b) Positive pole voltage for a pole to pole fault at DETL with 4.7 Ω resistance (measurement at Central Box). 180

Figure 172. Block diagram of the Nanogrid. 181

Figure 173. Simulation results obtained for the varying DC microgrid generation/consumption (a) Power (b) Voltage... 181

Figure 174. Comparison Between Simulation Model and Field Data collected for a Nanogrid....... 182

Figure 175. Comparison Between Simulation Model and Field Data collected for a Nanogrid....... 182

Figure 176. TW detection prototype box... 183

Figure 177. Analog interface circuitry used to condition sensed voltage/current outputs to correct ADC input range.. 184

Figure 178. CPUs and clock management of the DSP. 185

Figure 179. Sampling, fault detection, and data storage process. 186

Figure 180. Installation and connection of the DSP box into the microgrid. 186

Figure 181. Data flow in the presented testing methodology, assuming that the DSP box is located at the Central Box.. 187

Figure 182. Control room monitoring setup showing fault detection and location results.............. 187

Figure 183. Positive and negative pole voltage measurements. 188

Figure 184. Absolute value of filter output.. 189

Figure 185. Positive pole current measurements. 189

Figure 186. Fault prediction using DSP where TWPD is at DETL when a pole-to-ground fault occurs at GATH... 190

Figure 187. The TWPD's monitoring screen when TWPD is at CENT and a pole-to-ground fault occurs at DETL.. 190

Figure 188. Fault location setup for KAFB Emera Microgrid.. 190

Figure 189. Circular buffer of the estimated fault distance. 191

Figure 190. Time-distance characteristic for standard three-zone distance protection scheme. The vertical axis is trip time and the horizontal axis is length down the line.............................. 206

Figure 191. Sample mho circles. The line impedances are $Z1 = 0.1 + j0.2$, $Z2 = 0.2 + j0.25$, and $Z3 = 0.1 + j0.3$. The diameters of the circles are plotted to represent the reach of each zone.. 208

Figure 192. Sample mho circles using algorithm summarized in Figure 23 utilizing zero-sequency compensation factor $k0$. The reach of each zone is the same as that shown in Figure 24.

However, the observed fault impedance marked in red shifts inward when taking the zero-sequence current into account.. 208

LIST OF TABLES

Table 1. Comparison of number of settings update wit and without sensitivity....................................32
Table 2. Primary-backup coordination pairs...37
Table 3. Directional element operating and polarizing values. 38
Table 4. TCC parameters...41
Table 5. optimized settings for IEEE 123 system wiht RTL2 open..45
Table 6. IEEE 1547a-2020 amended requirements regarding mandatory voltage tripping (the range of allowable settings)..50
Table 7. Impact of equipment damage constraint on optimizer runtime – 1500 run sample..............54
Table 8. Per-unit impedance values for example of Figure 22..57
Table 9. Relay identifications 59
Table 10. PV rating and locations 59
Table 11 Example of Protection Settings Data...83
Table 12. Accuracy of the Prophet algorithm for Predicting Settings through time............................84
Table 13. Number of CTI Values By Region..87
Table 14. List of circuit configurations...91
Table 15. IBRs' specifications...91
Table 16. Circuit topology estimation accuracy at different LAMP units. 93
Table 17. Zone classification accuracy at different LAMP units in Configuration 1.............................95
Table 18. Zone classification accuracy at different LAMP units in Configuration 2.............................95
Table 19. Zone classification accuracy at different LAMP units in Configuration 3.............................95
Table 20. Zone classification accuracy at different LAMP units in Configuration 4.............................95
Table 21. Comparison of SVM with other classifiers for fault type classification at RTL1. 97
Table 22. Comparison of SVM with other classifiers for fault zone classification at R1......................97
Table 23. Final fault classification error rates (×10−3) of the proposed combined meta-structure. 102
Table 24. Probabilities of false alarm (P_{fa}) and of no detection $1 - p_d$ (×10−3) of the proposed structure. 102
Table 25. Data Distribution by fault type.. 104
Table 26. Data Distribution by fault type and fault Resistance 105
Table 27. Accuracy score of linear classifiers.. 106
Table 28. Fault simulation details... 107
Table 29. Configuration of each CNN Layer... 108
Table 30. Simulation parameters and values... 111
Table 31. Simulation and test parameters for case 3. 116

Table 32. Relay's calculated fault distances from each test. 117
Table 33. Source impedances used in simulation case 4. 118
Table 34. Recorded TW arrival times for impedance tests. 119
Table 35. Signal-Processing and Machine-Learning stages for the microRF methodology 125
Table 36. Accuracy, true positive and negative rates. 127
Table 37. RF data labels for TWPD at CENT. 141
Table 38. RF data labels for TWPD at DETL. 141
Table 39. Calculated length using the proposed method for zero fault resistance. 148
Table 40. Calculated length using proposed method using one synchronized sample from the other end. 148
Table 41. Calculated length using the proposed method in presence of IBR for zero fault resistance. 149
Table 42. Load Data of the 123-node Test Feeder 151
Table 43. IBR Placement and Generation Capacity 151
Table 44. Calculated length for zero fault resistance in grid connected mode. 151
Table 45. Calculated length for zero fault resistance in islanded mode. 151
Table 46. Comparison between the TW relay and the proposed method for AG fault. 152
Table 47. Calculated distance from Bus 1 to fault. 156
Table 48. Tested Fault Parameters and Recorded Detection Delays. 188
Table 49. Parameters for SEL-751 relay with characteristic described by (13). 205

ACRONYMS AND TERMS

Acronym/Term	Definition
ADC	Analog-To-Digital Converter
ADCI	Analog-To-Digital Current
ADCV	Analog-To-Digital Voltage
ANN	Artificial Neural Network
APMS	Adaptive Protection Management System
APP	Adaptive Protection Platform
APS	Adaptive Protection System
ATP	Alternative Transient Program
BESS	Battery Energy Storage System
BT	Boosted Trees
CDF	Cumulative Distribution Function
CENT	Central Box
CG	Coordination Gap
CEP	Central Energy Park
CHIL	Controller Hardware In The Loop
CLA	Control-Law Accelerator
CNN	Convolutional Neural Network
CODO	Closing-Opening-Difference-Operation
COOCMG	Close-Opening Open-Closing Morphological Gradient
CPU	Central Processing Unit
CSV	Comma-Separated-Variable
CTI	Coordination Time Interval
CWT	Continuous Wavelet Transform
DAC	Digital-To-Analog Converter
Db	Daubechies
DER	Distributed Energy Resources
DETL	Distributed Energy Technologies Lab
DIST	Distance
DL	Deep Learning
DMD	Dynamic Mode Decomposition

Acronym/Term	Definition
DOE	Department Of Energy
D-SCADA	Distribution System Supervisory Control And Data Acquisition
DS	Distribution System
DSF	Differentiator-Smoother Filter
DSP	Digital Signal Processor
DT	Decision Tree
DTOC	Definite-Time Overcurrent
DUT	Device Under Test
DWT	Discrete Wavelet Transform
ECA	Element Characteristic Angle
EMI	Electro-Magnetic Interference
EMS	Energy Management System
EMT	Electro-Magnetic Transient
EMTP	Electromagnetic Transient Program
ESL	Equivalent Series Inductance
ETL	Emera Technologies
EUT	Equipment Under Test
FD	Frequency Dependent
FFT	Fast Fourier Transform
FPGA	Field Programmable Gate Array
FPU	Floating-Point Unit
FRT	Fault Ride Through
FTPS	Fast Tripping Protection Scheme
GA	Genetic Algorithm
GAM	Generalized Additive Model
GATH	Gathering Space
GCN	Graph Convolutional Network
GFM	Grid-Forming
GNN	Graph Neural Network
GP	Gaussian Process
GPS	Global Positioning System

Acronym/Term	Definition
GUI	Graphical User Interface
HIL	Hardware In The Loop
HRWT	High-Resolution Wavelet Transform
HVDC	High-Voltage Direct Current
IBR	Inverter-Based Resource
IEEE	Institute Of Electrical And Electronics Engineers
IED	Intelligent Electronic Devices
IF	Isolation Forest
IPC	Inter-Processor Communications
ITOC	Inverse-Time Overcurrent
KAFB	Kirtland Air Force Base
KVL	Kirchhoff's Voltage Law
LAMP	Local Adaptative Modular Protection
LDA	Linear Discriminant Analysis
LV	Low-Voltage
MAE	Mean Absolute Error
MAPE	Mean Absolute Percent Error
MAX ABS V	Maximum Absolute Value
MCU	Microcontroller
MDL	Minimum Description Length
MINIROCKET	Minimally Random Convolutional Kernal Transformation
MINLP	Mixed Integer Nonlinear Problem
ML	Machine Learning
MLP	Multi-Layer Perception
MM	Mathematical Morphology
MPPT	Maximum Power Point Tracking
MRA	Multi-Resolution Analysis
MTGP	Multitask Gaussian Process
NB	Naïve Bayes
NC	Nearest Centroid
NG	Nanogrid

Acronym/Term	Definition
NPG	Negative-Pole-To-Ground
OC	Overcurrent
PD	Protection Device
PE	Parseval Energy
PG	Pole-To-Ground
PMU	Phasor Measurement Unit
PP	Pole-To-Pole
PPG	Positive-Pole-To-Ground
PPS	Pulse Per Second
PSEL	Photovoltaic System Evaluation Lab
PV	Photovoltaic
PWM	Pulse Width Modulation
RF	Random Forest
RMS	Root-Mean-Square
RMSE	Root Mean Square Error
RTDS	Real Time Simulator
SEL	Schweitzer Engineering Laboratories
SETO	Solar Energy Technologies Office
SG	Synchronous Generator
SGD	Stochastic gradient descent
SLG	Single-Line-To-Ground
SNL	Sandia National Laboratories
SNR	Signal-To-Noise Ratio
SOC	State of charge
SVC	Support Vector Classifier
SVM	Support Vector Machine
SWT	Stationary Wavelet Transform
TCC	Time Current Curve
TDS	Time Dial Settings
TOA	Time Of Arrival
TOC	Time Overcurrent

Acronym/Term	Definition
TPH	Three-Phase To Ground
TW	Traveling Wave
TWPD	Traveling Wave Protection Device
UNM	University Of New Mexico
VPP	Pole-To-Pole Voltage
Vs	Voltage Source
WT	Wavelet Transform

1. INTRODUCTION

The conventional protection system lacks the intelligence required to modify the protective responses according to system conditions. Rather, it utilizes fixed settings for protective relays, which are well-tuned only for the normal operating conditions. Particularly, in a smart distribution system, the coordination of the conventional protection system is affected by the high penetration of distributed energy resources (DERs)[1,2]. The challenges stem from the specific characteristics of fault currents supplied by power-electronics-based DERs, which are limited and often only include positive sequence components. Moreover, the existence of DERs along the distribution circuits can potentially impose a reverse power flow condition which endangers the selectivity and sensitivity of the underlying protection system, and results in unwanted events like sympathetic tripping[3].

This project developed a scalable adaptive protection platform (APP) for distribution systems and microgrids (AC, DC, and hybrid) with high penetration of DERs, including photovoltaic (PV) systems. As opposed to the existing logic-based adaptive protection technologies[4], which are based on a set of pre-defined logics chosen based on a limited number of contingencies, the developed model-based APP is not contingency-specific, i.e., it can adapt in real-time given the latest power system conditions. Compared to logic-based APP, the model-based APP provides more flexibility and scalability and can be integrated into any distribution system (DS) and microgrid. Moreover, it is modular, utilizing local adaptive protection modules located on individual Intelligent Electronic Devices (IEDs) (e.g., protection relays, DERs, etc.). The adaptive protection modules on IEDs are intelligent enough to accommodate a safe, communication-free operation during communication network outages.

Fault location techniques for both transmission and distribution systems have previously been developed with an underlying assumption that the faulted system is linear. For distribution systems, due to unbalance, phase-domain methods are more suitable than sequence-domain[13]. However, the fault response of inverter-based resources (IBRs) is nonlinear. Both current-magnitude and power factor during faults are controlled. In addition to the modular adaptive protection platform, the performance of existing protection devices is improved for fast fault location using new, local time domain fault location schemes especially suited for unbalanced distribution systems in the presence of traditional and inverter-based resources.

The components of the project and results presented here are:

- *Objective 1*: creating an adaptive protection platform;

---

[1] S. Brahma, S. Ranade, M. E. Elkhatib, A. Ellis, and M. J. Reno, "Development and testing of protection scheme for renewable-rich distribution system," *Sandia National Laboratories*, SAND2017-10326R, 2017.

[2] A. Salmani, S. Flores, M. Bello, M. A. Zamani, F. Katiraei, and A. Bidram, "Impact analysis of high PV penetration on protection of distribution systems using real-time simulation and testing – A utility case study", *PV Systems Symposium*, 2019.

[3] J. Seuss, M. J. Reno, R. J. Broderick, and S. Grijalva, "Determining the impact of steady-state PV fault current injections on distribution protection," *Sandia National Laboratories*, SAND2017-4955, 2017.

[4] M. Singh, T. Vishnuvardhan, and S. G. Srivani, "Adaptive protection coordination scheme for power networks under penetration of distributed energy resources," *IET Gen. Trans. & Dist.,* vol. 10, no. 15, pp 3919-3929, Nov. 2016.

- *Objective 2*: designing communication-free adaptive protection modules on individual protection IEDs;
- *Objective 3*: creating protection algorithms for equipment in low inertia power systems.
- *Objective 4*: creating fault location techniques suitable for unbalanced networks fed by a varying combination of traditional (linear) and inverter-based (nonlinear) sources.

The results presented from this project provide improved protection system sensitivity, reliability, scalability, and resilience in highly DER penetrated distribution systems using a scalable adaptive protection platform with communication-free adaptive protection modules for IEDs.

1.1. Objective 1: Creating an adaptive protection platform

Chapter 1 of this report presents the developed APP for modern DS, hosting high penetration of PV as well as AC and DC microgrids. The APP is directed by the adaptive protection management systems (APMS) located at DS substation and AC/DC microgrids. DS APMS receive the latest circuit status and measurements through the distribution system supervisory control and data acquisition (D-SCADA) and calculates the proper settings to be sent to the relays located on its supervised region. By accommodating the possibility of different circuit topologies, APMS facilitates the reliable operation of DS subjected to preplanned load transfers through tie lines. DS APMS coordinates Local Adaptive Modular Protection (LAMP) units on individual DS protection devices, as well as AC/DC microgrid APMS units.

1.2. Objective 2: Creating communication-free local adaptive modular protection

Chapter 3 presents the communication-free LAMP units that guarantee the reliable operation of the protection system under extreme events. During normal operation of the communication system, protection IEDs rely on the settings/commands received from the proposed APMS. However, the communication network of protection systems might be endangered under different scenarios (e.g., broken communication links due to natural disasters). Under these scenarios, protection IEDs lose access to the information received from APMS or neighboring IEDs, but it is imperative for protection IEDs to still adopt proper settings and safely protect the system. A LAMP unit is technically a local setting calculation module that is added to individual protection IEDs. The role of the LAMP unit is to find the optimized settings for the protection functions for a list of fault scenarios in the protection IED's local zone of protection. The optimized relay settings will be calculated based on the fault currents gathered from a local short circuit model.

1.3. Objective 3: Creating protection algorithms for equipment in low inertia power systems

Chapter 4 presents a new device-level protection algorithm that can protect the equipment in low inertia distribution systems using signal-based fast tripping protection schemes (FTPS) for hybrid microgrids. With higher penetrations of inverter-based DER, traditional distribution system protection schemes may not be effective and fast enough. Instead of calculating statistics on the fundamental AC frequency, these methods use the time domain high-frequency measurements (>100 kHz) at the protection device to identify the signature characteristics of faults. Conventional traveling wave (TW) based schemes require communication or the first and second TW to identify both the fault direction and zone5. However, they are not applicable to microgrids with short electrical distance among terminals, which results in the high attenuation of second TW. The developed methods are based on the amount of energy in each frequency band of the traveling wave, and are tested in a field demonstration in Chapter 1.

1.4. Objective 4: Creating fault location techniques suitable for unbalanced networks fed by high penetration of and inverter-based DERs

For single-ended fault location (without communication), distance relays are popular, but it has been shown that the sequence-domain approach in distance relays gives large errors in distribution systems with IBRs[6]. Error due to fault resistance is also a known weakness of distance relays. Reactive-power based methods have been proposed for distribution systems to remove the error due to fault resistance7, but they are all in sequence-domain. Chapter 1 presents a method that uses time-domain samples and the physics underpinning the transient behavior of AC and DC systems for precise and fast fault location. The rate of change of currents and voltages, as well as their instantaneous samples that characterize the fault response of such systems, are measured as a time-series. The constants in the defining differential equations are the feeder parameters, which are solved using successive measurements in the time series. The developed fault location method is fast enough to even inform the protective relays for tripping decisions, as shown in Chapter 1.

---

[5] J. Wu, H. Li, G. Wang, and Y. Liang, “An improved traveling-wave protection scheme for LCC-HVDC transmission lines,” *IEEE Trans. Power Del.*, vol. 32, no. 1, pp. 106–116, Feb. 2017.

[6] Sukumar Brahma, “Protection of Distribution System Islands Fed by Inverter-Interfaced Sources”, *Proc. IEEE PES PowerTech* 2019, Milan, Italy.

[7] M. A. Faradonbeh and H. Bin Mokhlis, "Unbalance fault location in electrical distribution system," *16th Electrical Power Distribution Conference*, Bandar Abbas, 2011, pp. 1-8.

2. ADAPTIVE PROTECTION PLATFORM

The proposed APP is a model-based protection settings management system. The APP observes the system conditions and determines the optimal protection settings for all controllable protection devices to ensure the protection systems dependability, security and selectivity while minimizing the operating times and maintaining required coordination gaps (CGs). The APP also validates and communicates the optimized settings to the protection devices. The APP consists of a communication hub used to communicate between the various devices in the protection system and the APMS. The general from of the APP is shown in Figure 1.

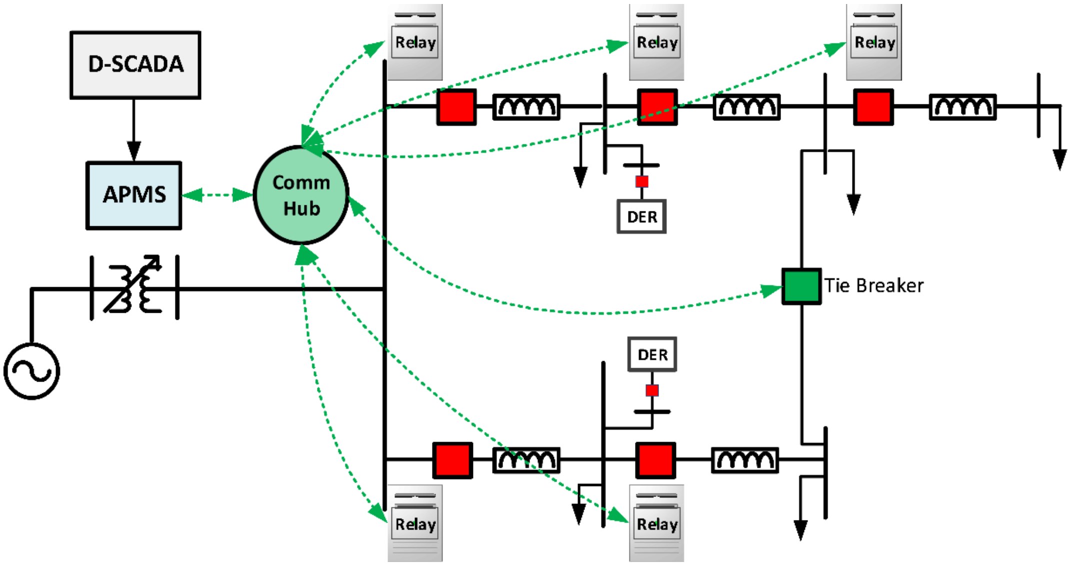

Figure 1. APP Diagram

The APMS located at the distribution system sub-station serves as the main component of the APP. The block diagram of the proposed APMS is shown in Figure 2. APMS has several different modules, including a circuit model management module, data import module, settings optimizer module, co-ordination study module, and relay interface module. APMS receives the latest circuit status and measurements from the system. From the real-time information, the APMS calculates the proper settings to be sent to the protection devices.

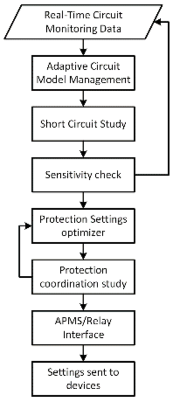

Figure 2. APMS block diagram

2.1.1. *Circuit Model Management Module*

The circuit model management module monitors the circuit status and maintains an updated power flow and short circuit model of the distribution system. It stores the current protection settings issued to the system and monitors the DERs status and outputs. This module updates the model as change occurs. The model is updated based on the most recent data acquired from the communication network for connecting APMS to protection devices creating a digital twin of the system.

2.1.2. *Short Circuit Study Module*

The short circuit study modules contain a short circuit model for the system and is used to generate the fault analysis required for the relay settings optimizer and the sensitivity analysis. The short circuit model has been developed in CAPE [1]. The module updates the short circuit model by incorporating the latest system state based on the status of the switches in the system. The model is also updated to account for the changes in the status and output of the DERs. The short circuit model in CAPE acts as a fault current solver to calculate the fault currents observed by the protection devices in the system. The short circuit study module simulates three-phase, line-line, double-line-to-ground, and single-line-to-ground (SLG) faults. The faults are simulated at two fault resistances, 0.05 **Ω**, and 1 **Ω**. To avoid simulating faults at each bus in the system, fault locations are preselected to produce the minimum and maximum fault current for each protection device in the system. For each fault, the voltage and current at each protection device are stored and output as a comma-separated-variable (CSV) file to be used by the protection settings optimizer module. A section of the output fault report is shown in Figure 3.

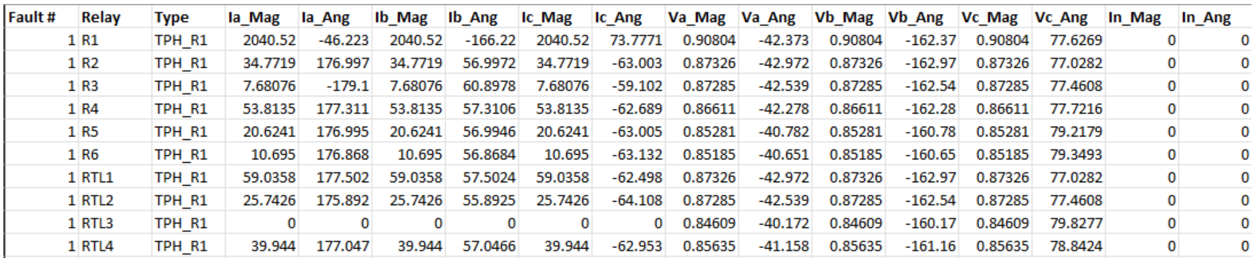

Fault #	Relay	Type	Ia_Mag	Ia_Ang	Ib_Mag	Ib_Ang	Ic_Mag	Ic_Ang	Va_Mag	Va_Ang	Vb_Mag	Vb_Ang	Vc_Mag	Vc_Ang	In_Mag	In_Ang
1	R1	TPH_R1	2040.52	-46.223	2040.52	-166.22	2040.52	73.7771	0.90804	-42.373	0.90804	-162.37	0.90804	77.6269	0	0
1	R2	TPH_R1	34.7719	176.997	34.7719	56.9972	34.7719	-63.003	0.87326	-42.972	0.87326	-162.97	0.87326	77.0282	0	0
1	R3	TPH_R1	7.68076	-179.1	7.68076	60.8978	7.68076	-59.102	0.87285	-42.539	0.87285	-162.54	0.87285	77.4608	0	0
1	R4	TPH_R1	53.8135	177.311	53.8135	57.3106	53.8135	-62.689	0.86611	-42.278	0.86611	-162.28	0.86611	77.7216	0	0
1	R5	TPH_R1	20.6241	176.995	20.6241	56.9946	20.6241	-63.005	0.85281	-40.782	0.85281	-160.78	0.85281	79.2179	0	0
1	R6	TPH_R1	10.695	176.868	10.695	56.8684	10.695	-63.132	0.85185	-40.651	0.85185	-160.65	0.85185	79.3493	0	0
1	RTL1	TPH_R1	59.0358	177.502	59.0358	57.5024	59.0358	-62.498	0.87326	-42.972	0.87326	-162.97	0.87326	77.0282	0	0
1	RTL2	TPH_R1	25.7426	175.892	25.7426	55.8925	25.7426	-64.108	0.87285	-42.539	0.87285	-162.54	0.87285	77.4608	0	0
1	RTL3	TPH_R1	0	0	0	0	0	0	0.84609	-40.172	0.84609	-160.17	0.84609	79.8277	0	0
1	RTL4	TPH_R1	39.944	177.047	39.944	57.0466	39.944	-62.953	0.85635	-41.158	0.85635	-161.16	0.85635	78.8424	0	0

Figure 3. Fault analysis output from CAPE

2.1.3. *Data Import Module*

The data import module interfaces with the utility model in CAPE. The CAPE database provides information about the network and protection devices. The data import module imports the network data to be used by the optimizer. A list of buses, lines, transformers, DERs and protection devices is obtained from the CAPE model. The imported network data contains the following information:

- Bus Data - Bus name, rated voltage, number of phases, connected phases for each bus.
- Line Data - Line name, to bus, from Bus, status, number of phases, rated voltage, line length, positive and zero sequence impedance for each line.
- Transformers Data - Transformer name, to bus, from Bus, status, number of phases, rated voltages, positive and zero sequence impedance for each transformer.
- DER Data - Name, connected bus, status, phases for each DER.

The module imports the protection device information as a separate file, which contains the protection device To Bus, From Bus, Element code, designation, and CTR/PTR. Each device typically consists of several elements which are identified by the designation. For each element with the protection device information about its settings, range and type is imported. For example, for an inverse time overcurrent (TOC) element, the data import module imports the pickup range, the time dial range, and a list of available time current curves (TCCs). For a definite time and element, the module imports the pickup range and time delay range. An example CSV file containing the protection element setting ranges is shown in Figure 4.

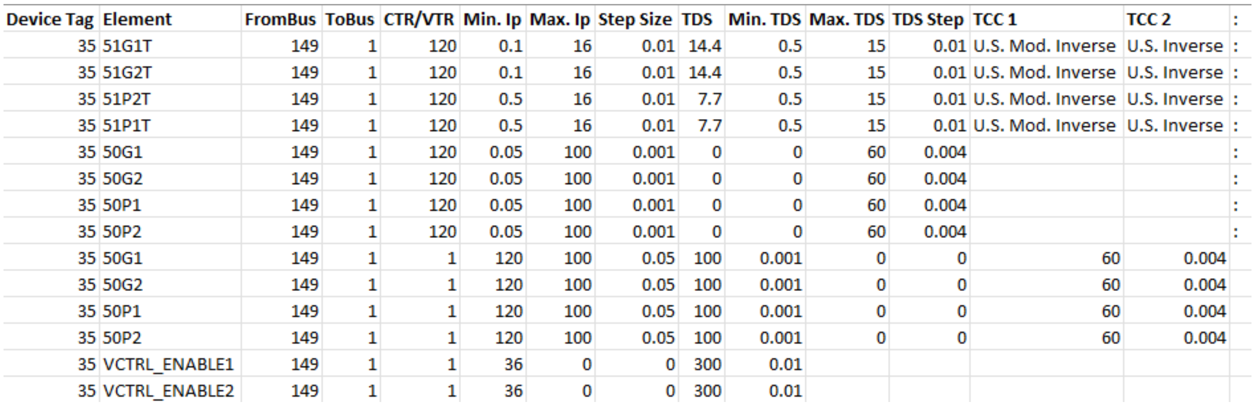

Device Tag	Element	FromBus	ToBus	CTR/VTR	Min. Ip	Max. Ip	Step Size	TDS	Min. TDS	Max. TDS	TDS Step	TCC 1	TCC 2	:
35	51G1T	149	1	120	0.1	16	0.01	14.4	0.5	15	0.01	U.S. Mod. Inverse	U.S. Inverse	:
35	51G2T	149	1	120	0.1	16	0.01	14.4	0.5	15	0.01	U.S. Mod. Inverse	U.S. Inverse	:
35	51P2T	149	1	120	0.5	16	0.01	7.7	0.5	15	0.01	U.S. Mod. Inverse	U.S. Inverse	:
35	51P1T	149	1	120	0.5	16	0.01	7.7	0.5	15	0.01	U.S. Mod. Inverse	U.S. Inverse	:
35	50G1	149	1	120	0.05	100	0.001	0	0	60	0.004			:
35	50G2	149	1	120	0.05	100	0.001	0	0	60	0.004			:
35	50P1	149	1	120	0.05	100	0.001	0	0	60	0.004			:
35	50P2	149	1	120	0.05	100	0.001	0	0	60	0.004			:
35	50G1	149	1	1	120	100	0.05	100	0.001	0	0	60	0.004	
35	50G2	149	1	1	120	100	0.05	100	0.001	0	0	60	0.004	
35	50P1	149	1	1	120	100	0.05	100	0.001	0	0	60	0.004	
35	50P2	149	1	1	120	100	0.05	100	0.001	0	0	60	0.004	
35	VCTRL_ENABLE1	149	1	1	36	0	0	300	0.01					
35	VCTRL_ENABLE2	149	1	1	36	0	0	300	0.01					

Figure 4. Example element range data imported from CAPE.

2.1.4. *Sensitivity Module*

The sensitivity module monitors the system state and effectiveness of the protection settings to determine if new settings are required. The sensitivity module continuously monitors the system switch states, DER status, and the real time voltage and currents to identify changes in the system state. The module also uses the fault analysis form the short circuit module, the real time measurements, and the last set of protection settings sent to the system to calculate the operating times and coordination gaps to determine the effectiveness of the protection system. The sensitivity module flags the optimizer to calculate new settings if any of the following conditions are met:

- Change in switch status.
- Change in DER status.
- Change in load current compared to the currents load current when the optimizer calculated the last time settings.
- Minimum calculated coordination time interval (CTI) is less than the desired CTI.
- Maximum operating time exceeds the set value.

A flow chart of the sensitivity module is shown in Figure 5.

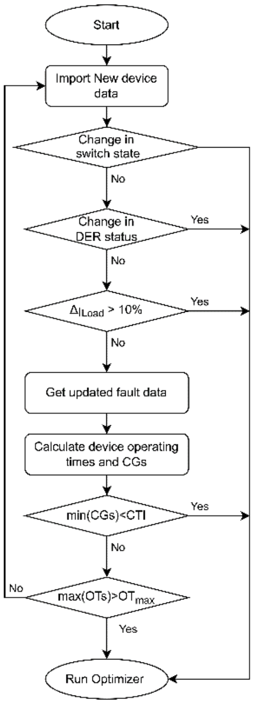

Figure 5. Sensitivity check

The sensitivity check enables the APMS to continuously monitor the protection coordination call for updated settings when the protection system coordination is compromised. This allows the APMS to update the settings only when necessary, rather than updating at a fixed interval. A comparison with and without using sensitivity analysis was performed in [2]. A modified Institute of Electrical and Electronics Engineers (IEEE) 13 bus system was used to simulate a year of settings updates. The settings optimizer was run every 5 minutes when calculating the adaptive protection settings without sensitivity analysis, resulting in 105120 settings updates. The same system. with the sensitivity analysis enabled. resulted in 7367 settings updates for the year, a 93% reduction. Table 1 shows a comparison of the number of settings issued for each month with and without sensitivity enabled. All months have a reduction of 90% or greater, dramatically reducing the number of settings issued and reducing the burden on the communication system.

Table 1. Comparison of number of settings update wit and without sensitivity

Month	% Reduced	With sensitivity	Without sensitivity
Jan	93.51%	579	8928
Feb	93.28%	542	8064
Mar	93.19%	569	8352
Apr	94.90%	455	8928
May	91.46%	738	8640
Jun	92.71%	651	8928
Jul	90.50%	821	8640
Aug	90.14%	880	8928
Sep	92.89%	635	8928

Month	% Reduced	With sensitivity	Without sensitivity
Oct	93.74%	541	8640
Nov	94.74%	470	8928
Dec	94.38%	486	8640
Average	93.12%	614	8928

2.1.5. Protection Settings Optimizer

The protection settings optimizer module calculates the optimized protection setting using the fault current information generated by the short circuit study model in CAPE and real-time measurements from the protection devices. The goal of the protection settings optimizer is to calculate settings that minimize the operating times for all protection devices in the system while maintaining the coordination between devices. The protection settings optimizer identifies the primary and backup pairs for the current system configuration, determines the pickup settings for the protection devices, and formulates the objective and constraint functions. A list of variables that are calculated during the formulation of the optimization problem are refed to a calculated variable. A list optimization variables are shown in Figure 6.

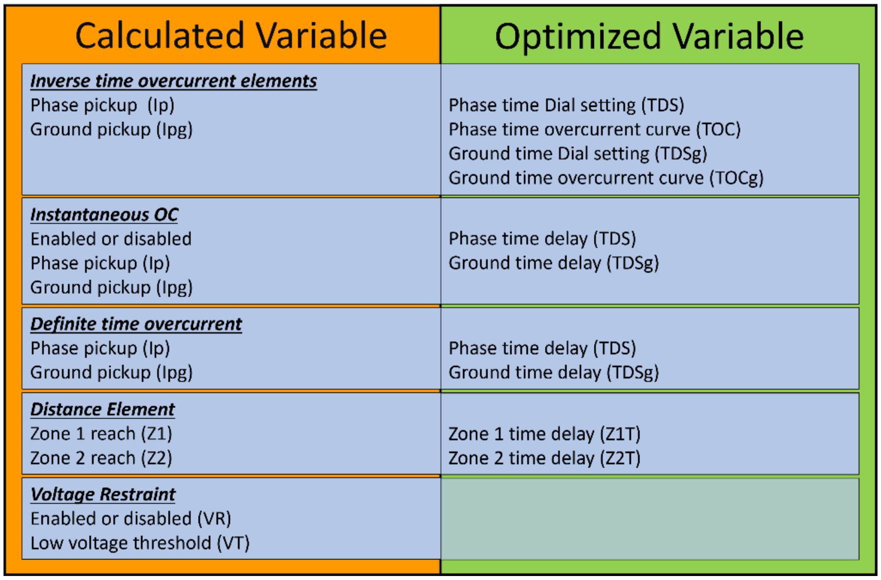

Calculated Variable	Optimized Variable
Inverse time overcurrent elements Phase pickup (Ip) Ground pickup (Ipg)	Phase time Dial setting (TDS) Phase time overcurrent curve (TOC) Ground time Dial setting (TDSg) Ground time overcurrent curve (TOCg)
Instantaneous OC Enabled or disabled Phase pickup (Ip) Ground pickup (Ipg)	Phase time delay (TDS) Ground time delay (TDSg)
Definite time overcurrent Phase pickup (Ip) Ground pickup (Ipg)	Phase time delay (TDS) Ground time delay (TDSg)
Distance Element Zone 1 reach (Z1) Zone 2 reach (Z2)	Zone 1 time delay (Z1T) Zone 2 time delay (Z2T)
Voltage Restraint Enabled or disabled (VR) Low voltage threshold (VT)	

Figure 6. Calculated and optimized variables

The protection settings optimizer formulates the relay settings problem as a mixed integer nonlinear problem (MINLP), where the objective function is the sum of operating times, and the constraints are the coordination gaps for primary and backup devices. The details of the optimization formulation and will be discussed in more detail in section 2.2.

The optimizer utilizes a genetic algorithm (GA)-based solver to solve the minimization problem. GA is a method for solving optimization problems based on a natural selection process that mimics biological evolution. GA works by modifying a population of individuals at each step, then it selects a few individuals from that population as parents to create the next generation. The population evolves toward an optimal solution over generations, and the algorithm continues to improve the solution until some predetermined criteria is satisfied or the best solution stops improving for a set number of generations [3]. A GA based approach was used due to the nonlinear, nondifferentiable, and discontinuous nature of the problem, which invalidates any derivative-based optimization methods. The GA function, provided by PYGAD, is used to solve and optimize the MINLP [4].

2.1.6. Protection Coordination Study Module

The protection coordination study module's purpose is to validate and identify any potential miscoordinations in the proposed protection settings. The Protection coordination study module tests the settings generated by the protection settings optimizer using the CAPE coordination study macro. The optimizer uses a set of predefined faults to generate settings in order reduce the time required to calculate the optimized settings, whereas the protection coordination module tests the settings thoroughly by simulating multiple faults on each line in the system. The coordination study macro can be configured to test multiple fault types with close-in, 10%, 15%, 50%, 85% and remote faults on each line. The coordination study module simulates the faults and calculates the expect operating times for all enable elements. For each fault simulation the coordination macro identifies the correct primary and backup protection device, calculates the coordination gap, and reports any issues in the protection coordination. If the protection coordination module identifies any miscoordinations or CTI violations, it reports the miscoordination or violation which is then used by the optimizer as an additional constraint to recalculate the settings. The recursive process shown in Figure 7 verifies the recommended settings to address any identified coordination issues before the settings are sent to the protection devices.

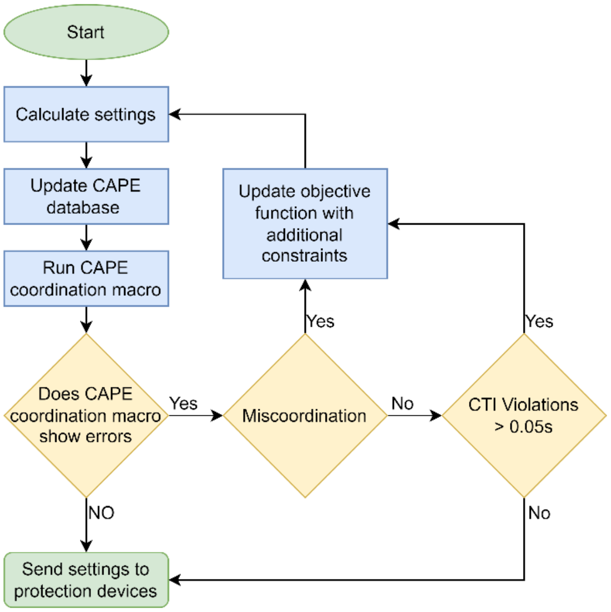

Figure 7. Protection coordination module flow diagram

2.1.7. APMS/Relay Interface

Once the settings calculated by the protection settings optimizer are validated by the protection coordination study module, the settings are sent to the protection devices through the APMS/Relay interface module. This module communicates the new settings to the protection devices by sending an updated settings file.

2.2. Optimization Formulation

The protection settings optimizer formulates the relay settings problem as MINLP to minimize relay operating times while satisfying the CTI margin between primary and backup relay pairs. The MINLP optimization problem formulation can be broken down into the following steps:

i. Formulate network graph.
ii. Identify primary backup pairs.
iii. Determine pickup settings.
iv. Determine device type.
v. Formulate objective function.
vi. Formulate constraint function.
vii. Optimize.

2.2.1. Formulate Network Graph

The network data imported by the data import module is utilized to create a node graph representation of the system. NetworkX an opensource python package is utilized to create the node graph [5]. The Lines, transformers and switches represent branches of the node graph connecting the nodes which represent the buses. Each node is assigned properties to represent the type of bus the node represents. For example, if bus that has a PV source attached to it then the node has the property “isPV” set to true. Similarly, if a branch has a relay on it, the branch has the property “isRelay” set to true. Each node is assigned properties that represent the name, status, rated voltage, phases, source type, group number, and numerical id. Each branch is assigned properties that represent name, status, from bus, to bus, type (switch, transformer etc.), protection type (relay, recloser etc.), phases, and electrical impedance. The network graph of a modified IEEE 123 system is shown in Figure 8, which will be utilized for examples and explanations through this section. The IEEE system has been modified by adding nine PV systems to the IEEE 123 system, and four lines are converted to tie lines marked as RTL1, RTL2, RTL3 and RTL4, of which one remains open to create four different configurations. In Figure 8, the tile line RTL2 is open. Ten relays are also added to the system, four of which are on the tile line. Therefore 9 relays are active for any given configurations.

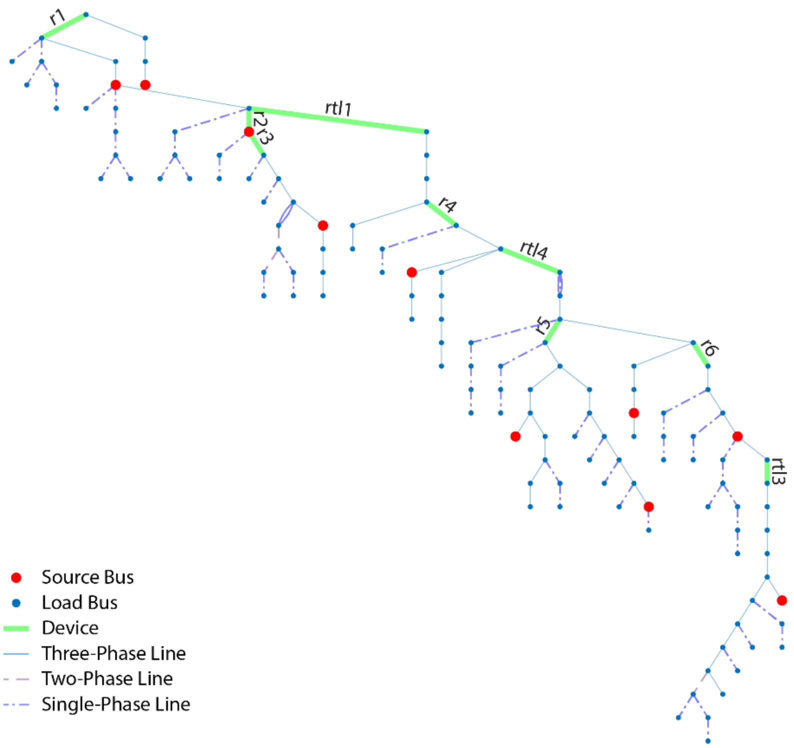

Figure 8. Network graph representation of the IEEE 123 system

Once the network graph is generated, it is then modified based on the current state of the system, if a switch is open then the branch that represents that switch is disabled, and omitted from the node graph. The network graph is further modified depending on certain system settings. If a protection device is set to use directional settings, then that device is represented as two devices: a forward and reverse device. In this case, direction settings are calculated to make the device's sensitivity react to faults only in their respective direction. For example, if relay R1 located on the branch, 149 to 1 is set to be a directional relay. Then in the formulation it is represented as 2 devices: $R1_F$ (looking from 149 to 1) the forward relay operating for fault downstream and $R1_R$ (looking from 1 to 149) the reverse relay operating for faults upstream. The network graph is updated using the most recent switch status and network conditions from real-time data each time the settings optimizer is called to generate new settings.

2.2.2. Identify Primary Backup Pairs

To formulate the constraints for the optimization problem, the primary-backup coordination pairs are identified. A path-tracing algorithm is used to identify the primary-backup pairs by identifying the protection device pairs in the path of fault currents. Using the network graph representation of the circuit, the algorithm creates a list of source buses and fault buses. The fault buses are selected to represent the start and end of a protection zone. A protection zone is a specific region within the system monitored and protected from faults by a protective device. Using the shortest path algorithm, a list of paths that start at the source buses and end at the fault buses are generated. The traced paths are then processed to identify any protection device in the path between a source and fault bus. If a path contains, more than one protection device is identified as a primary-backup pair that needs to be coordinated. The primary-backup pair is added to a list of primary-backup pairs if it is not already in the list [6]. A list of primary backup-pairs identified for the network graph shown in Figure 8 is shown in Table 2.

Table 2. Primary-backup coordination pairs

	Relay	From	To	Relay	From	To
1	$R1_R$	1	149	$RTL1_R$	152	13
2	$R1_R$	1	149	$R2_R$	18	13
3	$RTL1_F$	13	152	$R2_R$	18	13
4	$RTL1_F$	13	152	$R1_F$	149	1
5	$R2_F$	13	18	$R1_F$	149	1
6	$R2_F$	13	18	$RTL1_R$	152	13
7	$RTL1_R$	152	13	$R4_R$	57	54
8	$RTL4_R$	160	60	$R6_R$	197	97
9	$RTL4_R$	160	60	$R5_R$	72	67
10	$R2_R$	18	13	$R3_R$	21	18
11	$R3_F$	18	21	$R2_F$	13	18
12	$R6_R$	197	97	$RTL3_R$	151	300
13	$RTL3_F$	300	151	$R6_F$	97	197
14	$R4_F$	54	57	$RTL1_F$	13	152
15	$R4_R$	57	54	$RTL4_R$	160	60
16	$RTL4_F$	60	160	$R4_F$	54	57
17	$R5_F$	67	72	$R6_R$	197	97
18	$R5_F$	67	72	$RTL4_F$	60	160
19	$R6_F$	97	197	$RTL4_F$	60	160
20	$R6_F$	97	197	$R5_R$	72	67

2.2.3. Determine Pickup Settings

For each controllable protection device, such as an overcurrent relays, a pickup setting is calculated. The pickup is based on the real time load current (I_L) observed by the device and the minimum fault current (IF_{min}) for which the device needs to operate. The load currents are obtained from the real-time circuit monitoring, and the fault currents are imported from short circuit study performed in CAPE. For each fault in the fault analysis imported from CAPE, fault paths are identified from the faulted bus to all sources in the system, and the primary and backup device for that fault is identified. For each primary or backup device, a list of faults for that device is created, and the minimum fault current observed by the relay from those faults is selected as the minimum fault current for which this device must operate. Once the I_L and the IF_{min} are calculated, the pickup(I_p) for overcurrent elements is determined using the following equation:

$$I_p = \begin{cases} I_L * 1.25, & 1.5 * I_L \leq IF_{min} \\ IF_{min} * 0.5\,, & I_L * 1.1 < IF_{min} < I_L * 1.5 \\ IF_{min} * 0.1\,, & IF_{min} \leq I_L * 1.1 \end{cases}$$

This process is used to calculate the pickup for the phase and ground elements. For phase elements, the load current is the maximum phase current and IF_{min} is the minimum phase fault current. For ground elements, the load current is the ground or residual current (I_{Ln}) and the IF_{min} is the minimum ground fault current observed by the protection devices. If the minimum fault current observed by a device for which it is either the primary or backup device is less than 150% of the load current, then voltage restrain element is enabled and set. The voltage restraint blocks the device from operating under normal voltage levels. Therefore, the pickup can be set below the load current value when necessary. When the minimum fault current is less than 150% of the load current, the pickup is selected to 50% of the minimum fault current to ensure that the operating times remain reasonable by ensuring that the minimum multiple of pickup remains above 2 as the operating times of most standard TCC curves suffer below that value. Similarly, if the minimum fault current is lower than 110%, the pickup is set extremely low and supervised by the voltage to ensure that the minimum multiple of pickup remains sufficiently high. Additionally, if desired, the voltage restraint can be forced to be enabled for all devices that have the capability. The pickup is then set such that they allow for all faults to be isolated, even when the fault current is limited due to IBRs.

2.2.3.1. Instantaneous Trip

If available and justified, the instantaneous trip setting is also set. The instantaneous trip is justified if the ratio of maximum fault current (close in fault) observed are relayed and the minimum fault current observed by the relay (far end fault) is greater than 1.3. The instantaneous trip setting is set to 125% of the maximum fault current for which the relay operates as the backup ($IF_{Backup\ max}$).

2.2.3.2. Directional Settings

If the optimizer has be flagged to calculate settings for directional elements, the optimizer calculates either sequence-based directional settings or phase-based directional settings. The directional elements work based on the angle difference between operating and polarizing quantities for the phase and ground directional elements. A list of operating and polarizing values used to calculate the direction is shown in Table 3. If the angle between the operating and polarizing values is smaller than $90°$, then the phase elements declare a forward direction; otherwise, a reverse direction is assumed. For the 67N, if the angle difference between the operating value and the polarizing value is smaller than the forward direction angle limit ($FDIR_{Lim}$), then the direction is assumed to be forward; otherwise, the reverse direction is output. For both the 67P and 67N, the Element Characteristic Angle (ECA) is selected by calculating the average impedance angle observed by the relays forward direction. The ECA angle for relay is calculated by first finding all end nodes in the forward direction from the relay. Then the path impedance for each end node is calculated, and the average angle is used as the ECA angle.

Table 3. Directional element operating and polarizing values.

Element	Operating Value	Polarizing Value
67P	I_A	$V_{BC}\angle ECA$
	I_B	$V_{CA}\angle ECA$
	I_C	$V_{AB}\angle ECA$
67N	$I_0\angle ECA$	$-V_0$

2.2.3.3. Distance Relay Pickup

The distance operates based on the impedance calculated form the measured voltage and current. The distance relay calculates phase-to-ground impedance using the following equation:

$$Z_a = \frac{V_a}{I_a + \frac{Z_0 - Z_1}{Z_1} * \frac{1}{3}(I_a + I_b + I_c)}$$

Where Z0 is the zero-sequence impedance of the protection zone, Z1 is the positive sequence impedance of the protection zone. Additionally, the distance relay also calculates the Line-Line impedance using the equation:

$$Z_{ab} = \frac{V_a - V_b}{I_a - I_b}$$

The minimum of these is compared against the mho circles, which define the tripping zone of the distance relay. The Mho circles are defined as a percentage of the line the distance relay is protecting. However, this is not feasible for space placement in distribution systems where a relay protects a section consisting of several lines and branching laterals. A method has been developed to calculate the mho characteristics for such protection zones. Mho zone 1 is calculated as 90% of the impedance of the shortest path to the next protective device. This zone serves as the primary protection for most of protection zone 1. The magnitude of Mho zone 2 is calculated as the maximum of Z_{remote} and $Z_{unprotected}$. Z_{remote} is the sum of line impedance on the path to the furthest device backed up by the distance relay. $Z_{unprotected}$ is the sum of line impedances to the furthest unprotected bus. The angle of mho zone 2 is calculated as the average angle obtained for Z_{remote} and $Z_{unprotected}$. This allows the mho relay to operate as a backup when operating in mho zone 2 and as the primary when operating in mho zone 1.

2.2.4. *Determine Device Type.*

A typical modern numerical relay can use various protection functions such as inverse-time overcurrent (ITOC), definite-time overcurrent (DTOC), and distance (DIST). Based on the device and coordination requirements, the optimizer can select the element that will likely result in the lowest operating times. The type of element that will coordinate well and produce the best operating times is selected based on the minimum fault current observed by the relay and the relay coordination range. If the relay needs to back up a fuse, then an ITOC is selected as ITOC curves coordinate best with a fuse curves. If a device has a maximum fault current much greater than the minimum fault current, the optimizer will select an ITOC and set the instantaneous overcurrent trip as this would likely result in fast operating times for faults through the zone of protection. If the minimum fault current is less than 200% of the load current, then equation below is used to determine which type of element would be best.

$$Type = \begin{cases} DTOC, & IF_{min} < I_{th} \text{ and } \frac{IF_{max}}{IF_{min}} \leq IF_{th} \\ DIST, & IF_{min} < I_{th} \text{ and } \frac{IF_{max}}{IF_{min}} > IF_{th} \text{ and } |Z_2| > |Z_{th}| \\ ITOC, & Otherwise \end{cases}$$

Where I_{th} is the threshold set to 200 % of load current observed by the relay. IF_{min} is the minimum fault current for which the relay needs to operate, IF_{max} is the maximum fault current for which the relay needs to operate and IF_{th} is the coordination range threshold. Z_2 is the impedance from the relay to the furthest fault for which the relay needs to operate, and Z_{th} is the minimum threshold impedance for which the distance relay can be selected. The Z_{th} value must be significantly greater than the expected fault impedance. The IF_{th} threshold can be tweaked to favor distance, definite time, or the opposite. A low value of IF_{th} favors distance over a definite-time element, whereas a high value of IF_{th} favors a definite-time element over distance. A distance relay can offer better operating times and coordination with downstream devices because of its multiple operating times. A definite-time relay has the same operating time for all faults and therefore can have a higher operating when coordinating with downstream devices. For distribution systems where the zone is smaller, a DTOC is typically the better option.

To observe the impact of the relay type, selection settings were calculated for the modified IEEE 123 system with and without type selection enabled. A comparison of the system operating times and coordination gaps with and without type selection enabled are shown in Figure 9 and Figure 10 respectively. The settings without type selection have an average operating time of 0.67 s and a maximum operating time of 2.91 s compared to the case with type select enabled, which has an average operating time of 0.62 s and a maximum operating time of 2.12 s. The case without type select enabled has and an average coordination gap of 0.51 s, the settings with type selection enabled have an average coordination gap of 0.48 s. The case with type selection enabled has both lower operating times and coordination gaps.

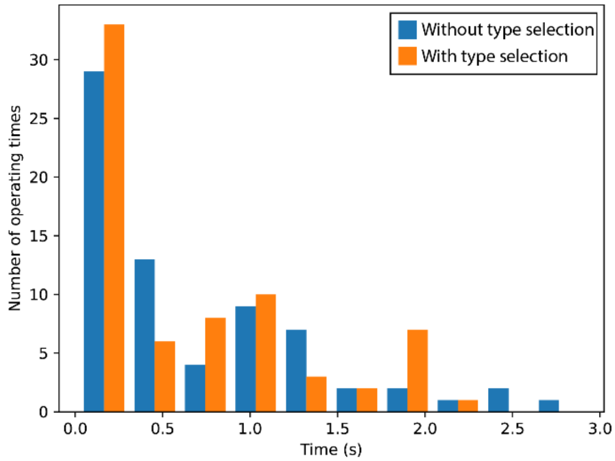

Figure 9. Comparison of operating times with and without type select.

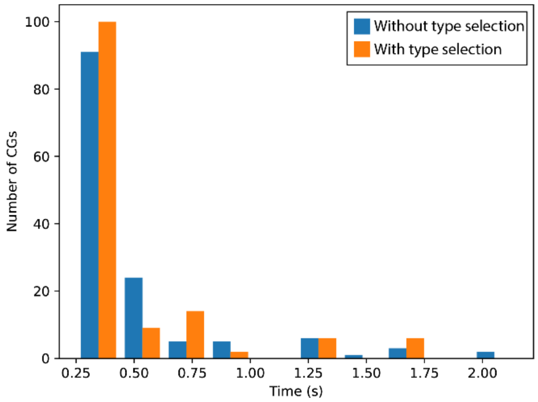

Figure 10. Comparison of coordination gaps with and without type select.

2.2.5. Formulate Objective Function.

The objective of the protection settings optimizer is to minimize operating times. Therefore, the objective function for the MINLP is the sum of operating times which are to be minimized. Once the pickup settings are calculated and the device type is selected, the operating time for the devices is calculated based on the minimum operating time for the active elements for the device. For overcurrent elements, the operating time is calculated using the following equation. The same equation can be used for both phase and ground elements.

$$Ot_{OC,ij} = TDS_i * \left(\frac{k}{\left(\frac{IF_{ij}}{I_{pi}}\right)^{\alpha} - 1} + c \right)$$

The parameters k, α, c are values that describe the time overcurrent curve (TOC). The values for a select few curves are shown in Table 4. TDS_i is the time dial setting (TDS) for element i, IF_{ij} is the fault current observed by the relay i for a fault j, and I_{pi} is the pickup setting of relay i.

Table 4. TCC parameters

TOC #	Type	k	c	α
1	U1: Moderately Inverse	0.0104	0.0226	0.02
2	U2: Inverse	5.9500	0.0180	2.00
3	U3: Very Inverse	3.8800	0.0963	2.00
4	U4: Extremely Inverse	5.6700	0.0352	2.00
5	U5: Short-Time Inverse	0.0034	0.0026	0.02
6	DT: Definite time	0.0000	1.00	1.00

For curves that cannot be defined easily using equations, such as fuse curves or recloser curves, the operating time curve data is imported from CAPE as a list of operating times and associated currents. The lists are used to create a pricewise liner fit which can used to obtain the operating time for any fault current. For instantaneous elements, the following equation is used to determine if the element will operate. If the element operates, then as the name suggests the operating time is instant; for the purpose of optimization this time is set to 0.01s.

$$Ot_{IT,ij} = \begin{cases} 0.01, & IF_{ij} < I_{pIT} \\ \infty , & IF_{ij} \geq I_{pIT} \end{cases}$$

I_{pIT} represents the instantaneous trip pickup and IF_{ij} is the fault current observed by the relay i for a fault j. For distance relays, the operating time is a function of the calculated impedance and the mho circle in which the calculated impedance to the fault is located. The operating time of the protection device is calculated as the minimum of the operating time of the elements within the device. For example, the operating time of a relay i (OT_i) with phase and ground inverse time overcurrent elements along with an instantaneous trip is calculated as follows:

$$OT_{ij} = \min(Ot_{OCP,ij}\,, Ot_{OCN,ij}\,, OT_{ITP,ij}, OT_{ITN,ij})$$

Where $Ot_{OCP,ij}$ and $Ot_{OCN,ij}$ are the operating times for the inverse time overcurrent phase, ground elements of relay i, $OT_{ITP,ij}$ and $OT_{ITN,ij}$ are the operating times for the instantaneous phase and ground elements of relay i. Each element has its own set of optimization variables shown in Figure 6. With each additional element the number of control variables, and thus problem complexity, increases. The objective function is created by parsing through each device i and summing the operating time (OT_{ij}) for fault j to the total operating time (T_{tot}). The objective function is formulated as follows:

$$T_{tot} = \sum_{i=1}^{n}\sum_{j=1}^{m} OT_{ij}$$

Where n is the number of controllable protection devices and m is the number of faults for which device i is the main protection device.

2.2.6. *Formulate Constraint Function.*

The nonlinear constraint function is formulated based on primary-backup coordination pairs, the required CTI, and the device operating times. The faults, along with the coordination pairs, are used to write protection coordination constraints. The protection coordination constraints ensure that there exist settings for the protection devices such that the primary overcurrent relay trips before its backup. For each primary-backup pair identified in the system, constraints are written for each fault for which the pair is expected to operate. Depending on the type of device, different constraints are written to ensure the primary device operates before the backup and coordination gap between the devices is greater than the desired minimum CTI.

2.2.6.1. Relay-Relay coordination constraints

Let device i and device k be a primary-backup pair where both devices are relays. Then for a fault j (for which the device i is the primary device) the following constraint is written to ensure the primary device operates before the backup:

$$OT_{kj} \geq OT_{ij} + CTI$$

2.2.6.2. Relay-Recloser coordination constraints

Let device i and device k be a primary-backup pair where device i is an overcurrent relay and device k is a recloser. Then for a fault j, for which the device i is the primary device, the following three constraints are written to ensure coordination:

$$OT_{kj,Slow} \geq OT_{kj\ Fast} + T_{reset}$$

$$OT_{kj,Slow} \geq OT_{ij} + CTI$$

$$OT_{ij} \geq OT_{kj,Fast} + CTI$$

Where $OT_{kj,Slow}$ and $OT_{kj,Fast}$ are the slow and fast curve operating times for the recloser k. T_{reset} is the minimum coordination gap required between the fast and slow operation of the recloser. These three constraints ensure that for a fault j the recloser fast curve operates before the primary relay, allowing any temporary faults to clear without the need for the primary relay operating and disconnecting a section of the system. If the fault is not removed then next the primary relay will operate and the slow curve of the recloser acts as the backup if the primary fails to operate. If the recloser is the primary device, then the following constraints are written to ensure the correct sequence of operations.

$$OT_{kj,S} \geq OT_{ij\ Fast} + T_{reset}$$

$$OT_{ij} \geq OT_{kj,Slow} + CTI$$

In this case, the recloser is the primary device and both the fast and slow curves need to operate before the relay operates as a backup.

2.2.6.3. Relay-Fuse coordination constraints

For the relay-fuse coordination, relay settings are the only variables that can be optimized and updated to ensure coordination. Therefore, in the case where a relay k is backing up a fuse i, the coordination constraints are written as follows.

$$OT_{kj} \geq OT_{ij} + CTI_f$$

Where CTI_f is the minimum CTI for the relay-fuse coordination, typically CTI_f is lower than CTI for other coordination types. For the reverse scenario where the fuse is backing up, the relay the constraints can be written. However, this should be avoided if possible as it can lead to situations where coordination is not achievable in both directions. The fuse cannot account for directional current or be adjusted and thus needs to be sized for the largest load current observed. This can lead to the fuse becoming inoperable for fault current from inverter-based resources and other fault current limited sources. This makes the coordination nearly impossible in many cases; therefore, fuses should be used mostly to protect laterals with no DERs.

2.2.6.4. Recloser-Fuse coordination constraints

The recloser-fuse coordination can be achieved either with fuse saving or without fuse saving. Without fuse saving, the coordination is like the relay fuse coordination with the recloser fast action being treated as the relay. For the fuse saving coordination, the recloser fast curve needs to operate before the fuse operates. When a recloser is backing up a fuse with fuse saving, constraint is written to ensure that the reclosers fast operation operates before the fuse blows and the slow/delayed operation of recloser operates after the fuse operates. The constraints for a recloser k backing up a fuse i with fuse saving for a fault j are as follows.

$$OT_{ij} \geq OT_{kj,Fast} + CTI_f$$

$$OT_{kj,Slow} \geq OT_{kj,Fast} + T_{reset}$$

$$OT_{kj,Slow} \geq OT_{ij} + CTI_f$$

Similar to the relay fuse coordination, the case where the fuse backs up a reclose should be avoided.

For each pair type a different set of constraints are written to ensure the proper order of operation for a given fault. These constraints are written for each pair identified by the optimizer for all relevant faults in the system. The constraints are then converted to penalty value if the constraint is not satisfied and added to the objective function. For example, if the constraint inequality $OT_{kj} \geq OT_{ij} + CTI$ is not satisfied then the value of $\left(OT_{kj} - \left(OT_{ij} + CTI\right)\right) * -w_1$ is added to the objective function to signal the optimizer that the solution does not meet the constraints. The weight assigned to the constraint is w_1.

2.2.7. Optimize

Once the objective and constraint functions are formulated, the MINLP is setup and can be solved for using the GA-based optimization discussed in section 2.1.5. Based on the type of protection devices that are present in the system, the number of optimization variables varies. For an inverse-time, overcurrent relays for the control variables are the TDSs, and the time overcurrent characteristics (TOCs) for overcurrent (OC) elements. For a definite-time overcurrent relay the control variable is the time delay setting. The GA-based optimization attempts to find the values for these variables that will result in the lowest objective value while maintaining coordination. The GA algorithm minimizes the objective function while meeting the constraints outlined in the constraint function to output a solution that contains the optimized control variables. An example set of settings output by the optimizer for the IEEE 123 system are shown in Table 1. The optimized settings have an average operating time of 0.93 s and a maximum operating time of 2 s. A histogram of the primary relay operating times is shown in Figure 11.

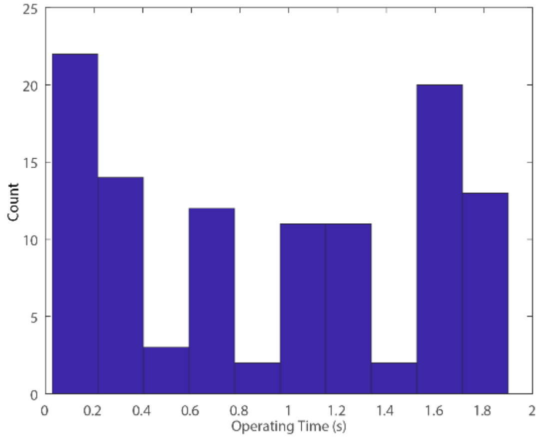

Figure 11. Histogram of primary operating times

The settings output by the optimizer ensures that all CGs remain greater than the required CTI of 0.25 s. Figure 12 shows the cumulative distribution function (CDF) of the CGs resulting from the optimized settings. From the CDF, it can be observed that all coordination gaps are above the 0.25 s threshold and a majority of the CGs are below 0.4 s with the maximum CG of 1.57 s.

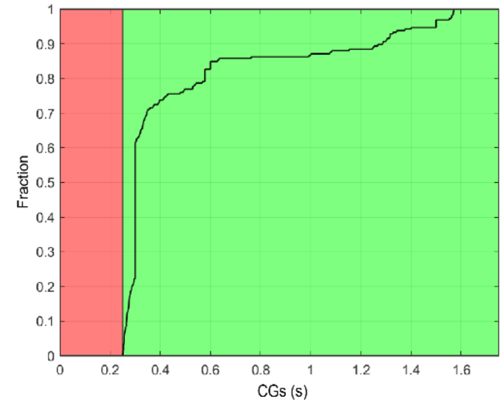

Figure 12. Primary-backup CGs

Table 5. optimized settings for IEEE 123 system wiht RTL2 open

Name	Ip (primary A)	TDS/ Time delay	TOC	Ipg (primary A)	TDSg/ Time delay	TOCg	VR
$R1_F$	137.9	7.5	U1	219.4	7.4	U1	0
$R1_R$	279.3	0.1	DT	123.2	0.1	DT	1
$RTL1_F$	112.1	6.0	U1	189.1	10.7	U3	0
$RTL1_R$	176.1	0.7	DT	106.8	0.7	DT	1
$R2_F$	176.2	5.1	U5	173.1	6.2	U4	0
$R2_R$	84.1	1.6	DT	36.3	1.6	DT	1
$R3_F$	187.0	0.5	U5	164.2	7.9	U4	0
$R3_R$	30.0	1.9	DT	10.0	1.9	DT	1
$R4_F$	108.4	14.8	U5	110.2	4.9	U1	0
$R4_R$	211.8	1.0	DT	55.5	1.0	DT	1
$RTL4_F$	117.5	9.7	U5	147.6	4.1	U1	0
$RTL4_R$	213.7	1.3	DT	81.6	1.3	DT	0
$R5_F$	161.2	0.5	U5	143.5	7.0	U4	0
$R5_R$	118.3	1.6	DT	36.5	1.6	DT	0
$R6_F$	144.9	4.7	U5	134.8	2.8	U3	0
$R6_R$	110.7	1.6	DT	51.4	1.6	DT	0
$RTL3_F$	149.9	0.5	U5	111.7	1.5	U4	0
$RTL3_R$	81.6	1.9	DT	37.7	1.9	DT	1

2.3. Interaction with PSS®CAPE

The PSS®CAPE protection engineering software package is an integral part of the adaptive protection platform. The software includes several algorithms for performing protection sensitivity and selectivity studies on distribution and transmission systems. These algorithms have been developed over the past several years and have been validated via usage in utility-scale studies.

For use with the adaptive protection platform, Siemens extended the existing algorithms in PSS®CAPE and developed a new PSS®CAPE coordination macro especially suited for radial distribution networks.

The results of the coordination study are provided to the adaptive protection settings optimizer. The optimizer reviews the results and determines new protection settings that will help mitigate the protection coordination problems found by PSS®CAPE.

The newly calculated settings are then incorporated into the short-circuit model programmatically. The PSS®CAPE coordination study is repeated to re-evaluate the performance of the protection system. The results of the most recent study are provided again to the adaptive protection setting algorithms for further adjustment (if needed)

Thus, a closed-loop connection between the PSS®CAPE algorithms and the adaptive protection settings calculations was established, giving the protection system the ability to respond continuously to changing network conditions, generation levels, etc.

2.3.1. The PSS®CAPE Coordination Macro – User Inputs

In this section, we describe the salient features of the PSS®CAPE coordination macro, its capabilities, and the types of output it provides to the adaptive protection settings optimizer. While the macro was developed to run within the PSS®CAPE Graphical User Interface (GUI), it can be called from any other external program (such as the adaptive protection optimizer) using PSS®CAPE's ability to be run from a batch file, without having to use the user interface.

If run from inside the user interface, the user will be presented with a data entry form as shown in Figure 13.

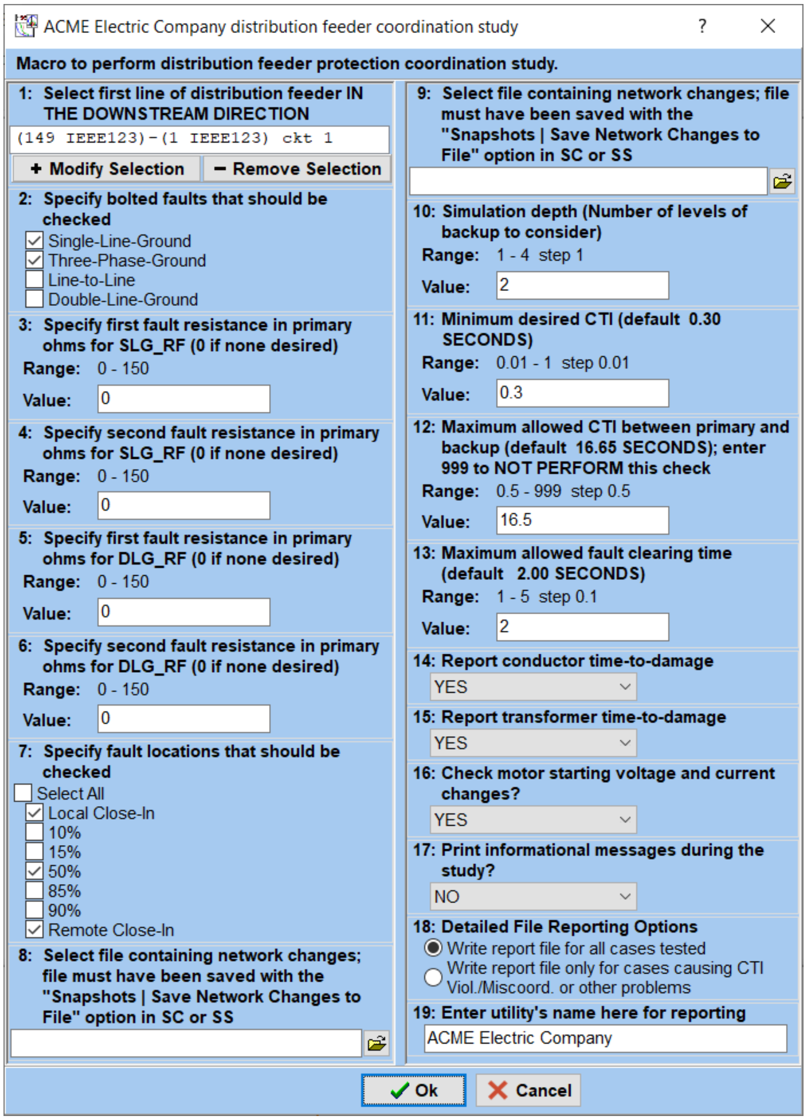

ACME Electric Company distribution feeder coordination study

Macro to perform distribution feeder protection coordination study.

1: Select first line of distribution feeder IN THE DOWNSTREAM DIRECTION
(149 IEEE123)-(1 IEEE123) ckt 1
+ Modify Selection — Remove Selection

2: Specify bolted faults that should be checked
☑ Single-Line-Ground
☑ Three-Phase-Ground
☐ Line-to-Line
☐ Double-Line-Ground

3: Specify first fault resistance in primary ohms for SLG_RF (0 if none desired)
Range: 0 - 150
Value: 0

4: Specify second fault resistance in primary ohms for SLG_RF (0 if none desired)
Range: 0 - 150
Value: 0

5: Specify first fault resistance in primary ohms for DLG_RF (0 if none desired)
Range: 0 - 150
Value: 0

6: Specify second fault resistance in primary ohms for DLG_RF (0 if none desired)
Range: 0 - 150
Value: 0

7: Specify fault locations that should be checked
☐ Select All
☑ Local Close-In
☐ 10%
☐ 15%
☑ 50%
☐ 85%
☐ 90%
☑ Remote Close-In

8: Select file containing network changes; file must have been saved with the "Snapshots | Save Network Changes to File" option in SC or SS

9: Select file containing network changes; file must have been saved with the "Snapshots | Save Network Changes to File" option in SC or SS

10: Simulation depth (Number of levels of backup to consider)
Range: 1 - 4 step 1
Value: 2

11: Minimum desired CTI (default 0.30 SECONDS)
Range: 0.01 - 1 step 0.01
Value: 0.3

12: Maximum allowed CTI between primary and backup (default 16.65 SECONDS); enter 999 to NOT PERFORM this check
Range: 0.5 - 999 step 0.5
Value: 16.5

13: Maximum allowed fault clearing time (default 2.00 SECONDS)
Range: 1 - 5 step 0.1
Value: 2

14: Report conductor time-to-damage
YES

15: Report transformer time-to-damage
YES

16: Check motor starting voltage and current changes?
YES

17: Print informational messages during the study?
NO

18: Detailed File Reporting Options
● Write report file for all cases tested
○ Write report file only for cases causing CTI Viol./Miscoord. or other problems

19: Enter utility's name here for reporting
ACME Electric Company

Figure 13. Invoking the PSS®CAPE coordination macro in the GUI.

The form requests several pieces of information from the user:

1. The starting segment (or first section) of the feeder in the downstream direction. Based on this first segment, the macro will determine the rest of the feeder paths using a topology search algorithm.
2. Types of bolted (zero Ω) faults to be applied. Four fault types are supported:
3. Fault resistance in primary Ω for first single-line-ground fault (if resistive fault is desired).
4. Fault resistance in primary Ω for second single-line-ground fault (if resistive fault is desired).
5. Fault resistance in primary Ω for first double-line-ground fault (if resistive fault is desired).
6. Fault resistance in primary Ω for second double-line-ground fault (if resistive fault is desired).
7. Fault locations (up to 7) on each segment of the feeder.
8. Scenario 1: Allows the user to repeat all fault studies with a predefined set of network contingencies.

9. Scenario 2: Allows the user to repeat all fault studies with a predefined set of network contingencies.
10. Number of levels of protection backup to include in each fault application.
11. Number of mutual coupling levels to consider (typically not applicable for distribution feeders).
12. Default CTI for detection of selectivity issues – 18 cycles is typical, but adjustable by the user.
13. Maximum allowed CTI between primary and backup protection elements.
14. Evaluate conductor damage: Check whether fault clearing is fast enough to prevent conductor damage (among all conductor types used on the feeder under study). Report time to conductor damage for each segment of the feeder.
15. Evaluate transformer damage: Check whether fault clearing is fast enough to prevent transformer damage (among all transformers modeled downstream from the substation). Report time to transformer damage for each transformer.
16. Perform induction motor starting calculations: If induction motors are present downstream in the feeder, determine the worst-case (largest current, smallest voltage) conditions seen at protective device locations on the feeder. This data will allow the adaptive protection optimizer to adjust overcurrent settings so as to not operate during motor starting conditions.
17. Items 17, 18 and 19 – for reporting purposes.

While the coordination study utilizes a form for the user to enter their inputs, it does have the ability to be invoked silently (where the user inputs are provided to the macro via a file). This allows PSS®CAPE, and consequently the coordination study macro, to be incorporated into the closed loop described earlier.

2.3.2. The PSS®CAPE Coordination Macro – Studies Performed & Outputs

Upon specifying the required parameters in Figure 13, the user clicks the “Ok” button to start the study. The user inputs can also be provided via a file, allowing the macro to be called silently. The macro then performs the following tasks:

1. Use the starting segment to perform a topology search.
2. Identify the various segments that make up the feeder tree.
3. For each segment, apply the requested faults at the requested locations.
4. Simulate sequential fault clearing.
5. Provide summary report – one line of output per fault simulated.
6. Provide several CSV files with various pieces of information for use by the adaptive protection optimizer.

The summary output is shown in Figure 14. The tabulated output will be produced for each segment in the distribution feeder. Color coding is used to indicate the severity of problems found:

- Pink – CTI violation.
- Red – Miscoordination.
- No color – Fault is cleared selectively.

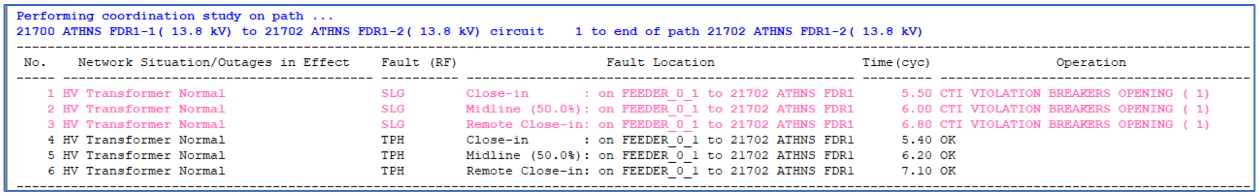

```
Performing coordination study on path ...
21700 ATHNS FDR1-1( 13.8 kV) to 21702 ATHNS FDR1-2( 13.8 kV) circuit    1 to end of path 21702 ATHNS FDR1-2( 13.8 kV)
------------------------------------------------------------------------------------------------------------------------------------------------------
 No.    Network Situation/Outages in Effect    Fault (RF)                  Fault Location                      Time(cyc)                Operation
----- ---------------------------------------- ---------- ------------------------------------------------- --------- ----------------------------------------
    1 HV Transformer Normal                    SLG        Close-in        : on FEEDER_0_1 to 21702 ATHNS FDR1      5.50 CTI VIOLATION BREAKERS OPENING ( 1)
    2 HV Transformer Normal                    SLG        Midline (50.0%): on FEEDER_0_1 to 21702 ATHNS FDR1      6.00 CTI VIOLATION BREAKERS OPENING ( 1)
    3 HV Transformer Normal                    SLG        Remote Close-in: on FEEDER_0_1 to 21702 ATHNS FDR1      6.80 CTI VIOLATION BREAKERS OPENING ( 1)
    4 HV Transformer Normal                    TPH        Close-in        : on FEEDER_0_1 to 21702 ATHNS FDR1      5.40 OK
    5 HV Transformer Normal                    TPH        Midline (50.0%): on FEEDER_0_1 to 21702 ATHNS FDR1      6.20 OK
    6 HV Transformer Normal                    TPH        Remote Close-in: on FEEDER_0_1 to 21702 ATHNS FDR1      7.10 OK
------------------------------------------------------------------------------------------------------------------------------------------------------
```

Figure 14. Summary output – one line per fault studied.

- Network situation is "HV Transformer Normal" – this reflects the condition that the station transformer at the distribution substation is in its "Normal" configuration, whatever that configuration is:
    - Normal could be two transformers feeding the bus (most common configuration for the utility).
    - Contingency situation would be when one of the transformers is outaged.
- In this example, the user requested:
    - Two fault types (SLG, three-phase to ground [TPH])
    - Three fault locations (Local Close-in, 50% and Remote Close-in)

A table similar to the one in Figure 14 will be produced for each segment in the feeder. On transformer segments, only close-in faults (local and remote) are applied.

In addition to the summary output shown in Figure 14, the coordination macro produces several CSV files, which are processed by the adaptive protection optimizer for determining new protection settings that would help mitigate the coordination issues determined by the PSS®CAPE macro. The information contained in these files include:

1. Voltage and current measured by each protection element applied on the feeder for each fault studied.
2. Operating times for each protection element applied on the feeder for each fault studied.
3. Classification of the protective elements as Primary (primary responsibility for clearing the fault) or Backup (not a primary element, and therefore, needs to be slower than any primary element).
4. Settings ranges (minimum, maximum, step-size, discrete settings values, etc.) for each protection element applied on the feeder, to serve as settings range constraints for the adaptive protection optimizer.

New settings calculated by the optimizer and then written back to the relay instances in the PSS®CAPE model. The coordination macro re-evaluates the feeder to ensure that the new settings mitigate the coordination issues found previously.

2.3.3. IBR Model in CAPE [7]

The IEEE 1547 standard's requirement regarding mandatory voltage tripping is based on three categories related to the response of IBR under abnormal conditions [8]. Among these categories, the abnormal operating performance Category III accounts for the stability and reliability requirements of both bulk power systems and distribution systems and was amended in 1547a-2020. According to this standard, the IBR response to the abnormal voltages under Category III should be based on the settings provided in Table 6.

Table 6. IEEE 1547a-2020 amended requirements regarding mandatory voltage tripping (the range of allowable settings).

Element	Voltage Threshold (pu)	Clearing Time (s)
OV2	1.2	0.16
OV1	1.1-1.2	1-13
UV1	0-0.88	2-50
UV2	0-0.5	0.16-21

In addition to the above requirements, the voltage ride-through requirements of IEEE 1547a-2020 standard for Category III requires the momentary cessation of IBR's current when the voltage at its terminal falls below 0.5 pu with a maximum response time of 5 cycles. However, the minimum ride-through time is equal to 1 s. Momentary cessation is defined as the temporary cessation of the energization of an IBR when a severe disturbance (e.g., fault) occurs and large deviations in the system voltage or frequency are observed. The momentary cessation, however, allows for the instantaneous restoration of IBR when the system voltage and frequency return to allowable ranges. If the temporary disturbance is cleared before the ride-through minimum time (the ride-through minimum time should be ≥ 1 s), the IBR can instantaneously restore supply power to the rest of the power grid.

2.3.3.1. Momentary Cessation Modeling for Short Circuit Studies

For the purpose of short circuit studies of a DS in the presence of IBRs, the short circuit software package should be able to stop IBRs from injecting currents when their terminal voltage after fault drops below 0.5 pu. For example, in PSS®CAPE model, the voltage-controlled current source (VCCS) model can be utilized to force an IBR to stop injecting current when its voltage falls below 0.5 pu. In Figure 15, the utilized values for accommodating momentary cessation in a tabular format for the voltage-controlled current source model are summarized.

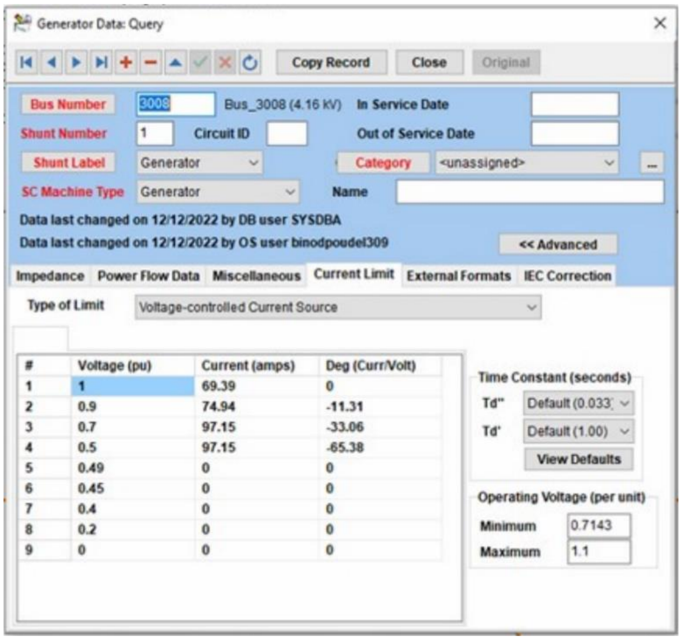

Bus Number: 3008 Bus_3008 (4.16 kV)
In Service Date:
Shunt Number: 1
Circuit ID:
Out of Service Date:
Shunt Label: Generator
Category: <unassigned>
SC Machine Type: Generator
Name:
Data last changed on 12/12/2022 by DB user SYSDBA
Data last changed on 12/12/2022 by OS user binodpoudel309
Type of Limit: Voltage-controlled Current Source

#	Voltage (pu)	Current (amps)	Deg (Curr/Volt)
1	1	69.39	0
2	0.9	74.94	-11.31
3	0.7	97.15	-33.06
4	0.5	97.15	-65.38
5	0.49	0	0
6	0.45	0	0
7	0.4	0	0
8	0.2	0	0
9	0	0	0

Time Constant (seconds)
Td'': Default (0.033
Td': Default (1.00)

Operating Voltage (per unit)
Minimum: 0.7143
Maximum: 1.1

Figure 15. Incorporating momentary cessation into IBR model.

2.3.3.2. Momentary Cessation Modeling for Coordination Studies

The coordination study is referred to as evaluating the selectivity of the protection system by applying different types of faults at different locations of the distribution system and verifying the coordinated operation of protection relays for all of the studied fault scenarios. To this end, each primary/backup protection relay pair should satisfy a minimum CTI determined by the utility standards (e.g., 0.3 s). The coordination study should account for the sequence of actions by different relays in response to a fault scenario. To accommodate the requirements of IEEE 1547 regarding IBR's response to abnormal voltages and momentary cessation, one can create a generic under-voltage relay model in PSS®CAPE and add them to the tie-breakers interconnecting IBRs to the rest of the system. The created under-voltage relay model is shown in Figure 16.

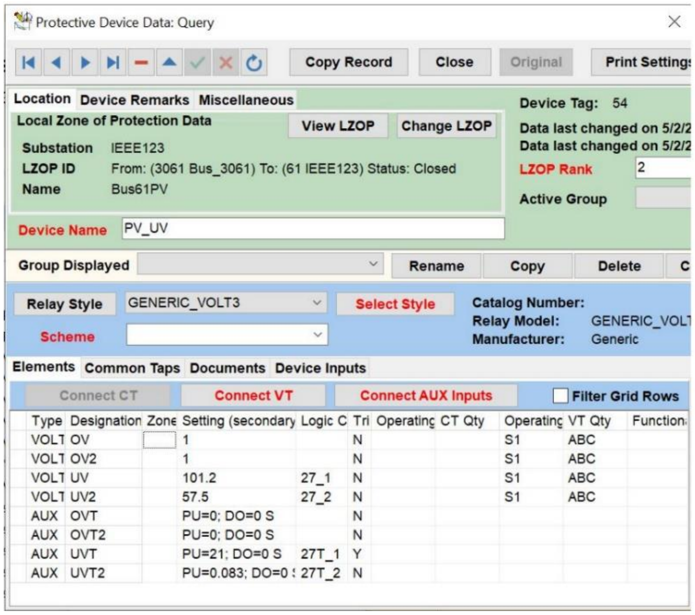

Local Zone of Protection Data

Substation IEEE123
LZOP ID From: (3061 Bus_3061) To: (61 IEEE123) Status: Closed
Name Bus61PV

Device Tag: 54
Data last changed on 5/2/2
Data last changed on 5/2/2
LZOP Rank 2
Active Group

Device Name PV_UV

Group Displayed

Relay Style GENERIC_VOLT3
Scheme

Catalog Number:
Relay Model: GENERIC_VOL
Manufacturer: Generic

Type	Designation	Zone	Setting (secondary	Logic C	Tri	Operating	CT Qty	Operating	VT Qty	Function
VOLT	OV		1		N			S1	ABC	
VOLT	OV2		1		N			S1	ABC	
VOLT	UV		101.2	27_1	N			S1	ABC	
VOLT	UV2		57.5	27_2	N			S1	ABC	
AUX	OVT		PU=0; DO=0 S		N					
AUX	OVT2		PU=0; DO=0 S		N					
AUX	UVT		PU=21; DO=0 S	27T_1	Y					
AUX	UVT2		PU=0.083; DO=0	27T_2	N					

Figure 16. Generic voltage relay in CAPE.

2.4. Equipment Damage Constraints [9]

Equipment time-to-damage based on maximum available fault current for conductors and transformers should be considered as an upper bound on the relay operating time. For long chains of protection devices, the slower operating devices may be allowed by the optimizer to infringe upon equipment damage curves if time-to-damage is not considered as a constraint. A flow diagram showing how the equipment damage constraint integrates with the remainder of the adaptive protection optimization is shown in Figure 17.

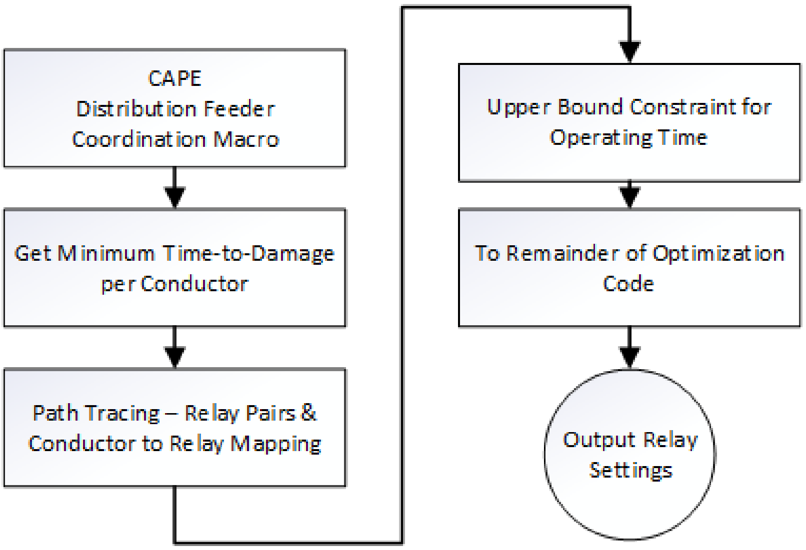

Figure 17. Equipment damage constraint integration with adaptive protection optimization.

The CAPE equipment database is queried during the Distribution Coordination Macro and calculates equipment time-to-damage for each fault scenario. An example of the required input for conductor damage information is shown in Figure 18, and the output of the coordination macro displaying time-to-damage is shown in Figure 19. The results of each fault scenario are aggregated to determine the worst-case time-to-damage for each conductor and transformer in the system.

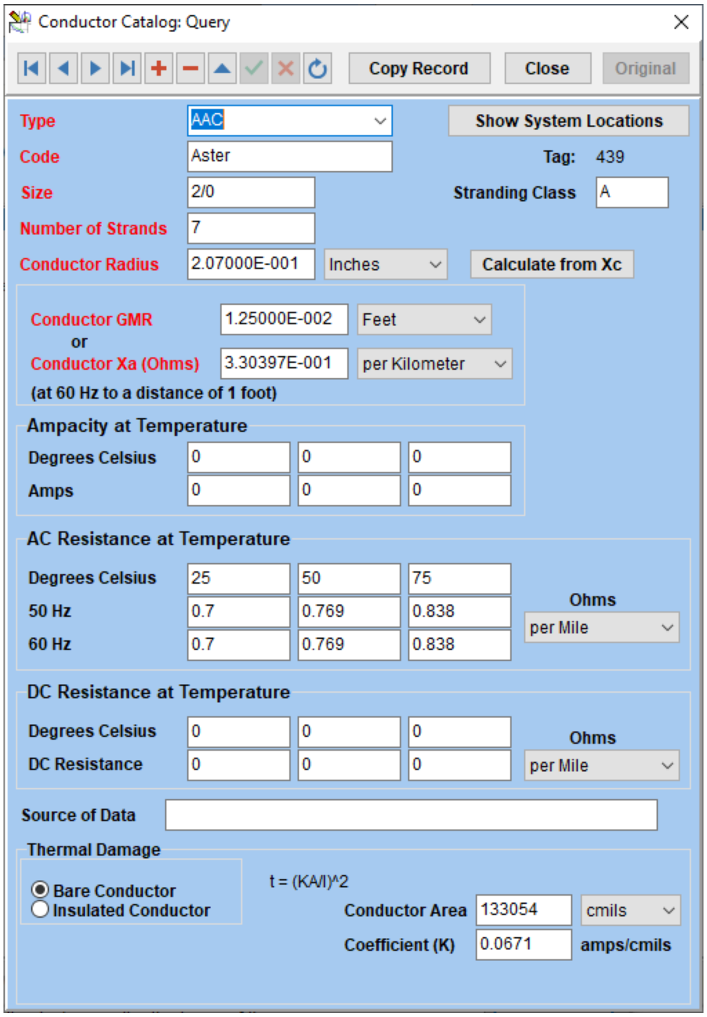

Type: AAC
Code: Aster
Size: 2/0
Number of Strands: 7
Conductor Radius: 2.07000E-001 Inches
Tag: 439
Stranding Class: A

Conductor GMR: 1.25000E-002 Feet
or
Conductor Xa (Ohms): 3.30397E-001 per Kilometer
(at 60 Hz to a distance of 1 foot)

Ampacity at Temperature

Degrees Celsius	0	0	0
Amps	0	0	0

AC Resistance at Temperature

Degrees Celsius	25	50	75
50 Hz	0.7	0.769	0.838
60 Hz	0.7	0.769	0.838

Ohms per Mile

DC Resistance at Temperature

Degrees Celsius	0	0	0
DC Resistance	0	0	0

Ohms per Mile

Source of Data:

Thermal Damage
● Bare Conductor
○ Insulated Conductor
t = (KA/I)^2
Conductor Area: 133054 cmils
Coefficient (K): 0.0671 amps/cmils

Figure 18. CAPE database editor - conductor input required for damage calculation.

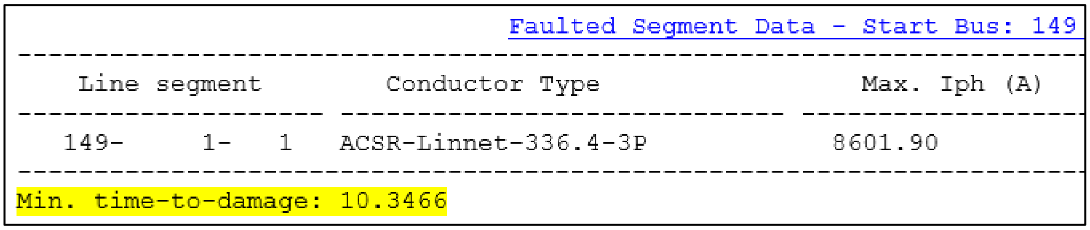

```
                                   Faulted Segment Data - Start Bus: 149
---------------------------------------------------------------------------
    Line segment          Conductor Type                  Max. Iph (A)
-------------------- ---------------------------- -----------------------
  149-      1-    1   ACSR-Linnet-336.4-3P             8601.90
---------------------------------------------------------------------------
Min. time-to-damage: 10.3466
```

Figure 19. Distribution Coordination Macro output for conductor time-to-damage.

During the path tracing step in the optimization process (when primary-backup relay pairs are determined) all conductors and transformers in the system are mapped to their appropriate relay. This facilitates calculation of the worst-case equipment time-to-damage in each relay's zone of protection, which sets a constraint on the maximum operating time of the relay. This constraint is applied separately to phase and ground elements in order to avoid over-constraining the optimization problem. Specifically, the constraint is relaxed on the relay's phase element by not requiring it to coordinate with single-phase circuit damage requirements. These circuits typically have stricter (lower) time-to-damage and are protected by the relay's ground elements.

$$OT_{phase} \leq T_{damage_{3ph}} - CTI$$

$$OT_{ground} \leq min\left\{T_{damage_{3ph}}, T_{damage_{1ph}}\right\} - CTI$$

OT is the relay's operating time for phase and ground elements, T_{damage} is the worst-case time-to-damage in the relay's zone of protection, and CTI is a constant CTI required between devices (e.g., 0.25 s).

The main substation relay as the furthest upstream device in the network is the most susceptible to equipment damage violations, as shown in Figure 20. The single-phase circuit from bus 13 to 16 is protected by R1, which may have a relatively long operating time due to coordination with a series of downstream protective devices.

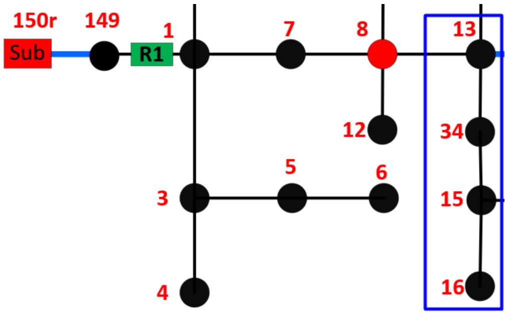

Figure 20. Subnetwork with R1 & single-phase branch 13-16. If R1 is not subject to conductor damage constraint, the R1 ground element may infringe upon damage curves.

The impact of adding the additional damage constraint to the optimization process is summarized in Table 7. A sample of 1500 runs of the optimizer was performed. The average runtime is increased by 6 seconds on the test PC for the separated constraints case with no damage violations. With a single constraint applied to both phase and ground elements, there were 2 damage violations. Both of these violations were due to the optimizer trying to coordinate the phase element of main substation relay R1 with the single-phase circuit shown in Figure 20.

Table 7. Impact of equipment damage constraint on optimizer runtime – 1500 run sample.

Case	Average Runtime (s)	Damage Violations
Base	32	N/A
Single Constraint	41	2
Separated Constraints	38	0

2.5. Coordination with Distance Relays

For the distance relay, the operating time is a function of both current and voltage. For the work undertaking during this project, mho characteristics have been utilized. However, the same logic may be applied to quad or custom characteristics. Consider the example of Figure 21. The impedance of line 1-2 is Z_{12} and the impedance of line 2-3 is Z_{23}. In literature, it is relatively consistent for overhead lines that Zone 1 covers 80-85% of the line 1-2 [10, 11]; Zone 2 covers all of line 1-2 plus about 50% of line 2-3 ; and Zone 3 covers 25% of line 3-4 [12, 13]. This may be summarized as follows:

$$Z_{zone\ 1} = (0.80\ to\ 0.85)Z_{12}. \tag{1}$$

$$Z_{zone\ 2} = Z_{12} + 0.5Z_{23}. \tag{2}$$

$$Z_{zone\ 3} = Z_{12} + Z_{23} + 0.25Z_{34}. \tag{3}$$

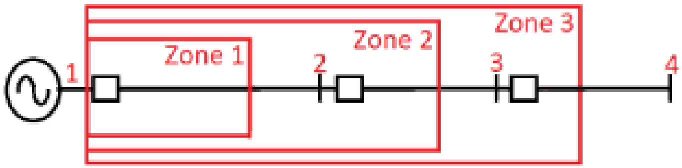

Figure 21. Small 3-bus example for demonstration of distance relay protection zones. The shape of the of the zones does not reflect the complex impedances, only the physical line length or impedance magnitude along the horizontal dimension.

The distance relay does not directly measure line impedance. The line impedance is estimated using (4). In conventional application, Zone 1 is an instantaneous trip ($d_1 = 0$), and the two remaining zones are time graded ($0 \leq d_1 < d_2 < d_3$). The standard trip time is therefore defined as:

$$T_{ij} = \begin{cases} d_1, & \text{if } Z_f^{est} \leq Z_{zone\ 1} \\ d_2, & \text{if } Z_f^{est} \leq Z_{zone\ 2} \\ d_3, & \text{if } Z_f^{est} \leq Z_{zone\ 3} \\ \infty, & \text{otherwise} \end{cases}. \tag{4}$$

where, d_2 and d_3 are the time delays for the Zone 2 and Zone 3 trips respectively. All zones are definite time trip. It must hold that $0 \leq d_1 < d_2 < d_3$ for the zones to trip in the correct order. An example of the zones of protection is shown in Figure 21 for the radial line.

In [14], we introduced an alternative method for defining zones of protection for distance relays. The reason for this was to account for branching paths where relays are sparsely placed. Consider the system shown in Figure 22. The line lengths are approximately representative of the line impedances in magnitude only. The zones only represent the fraction of the line covered and not the complex impedances of the zones of protection. For Zone 1, the following is applied:

1. Locate the source end of the line where the distance relay is placed (bus 1)
2. Trace a path from the source end relay (bus 1) to the next closest relay (bus 4)
3. Set the Zone 1 reach as 80 to 90 % of the sum of the line impedances along this path. For the example of Figure 22, the path is $Z_{z1} = Z_{12} + Z_{24}$, so that:

$$Z_{zone\ 1} = (0.80\ to\ 0.90)Z_{z1} \tag{5}$$

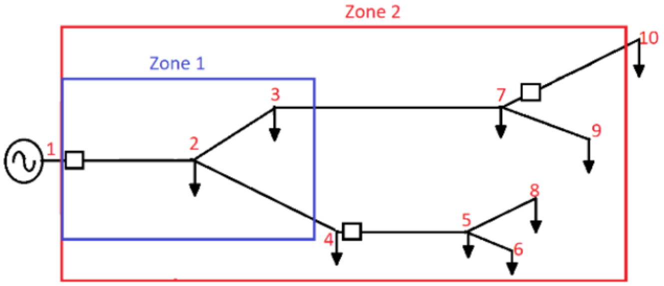

Figure 22. Sample 10-bus system with sparse relay placement.

As for Zone 2, the following algorithm is applied:

1. Locate the sending source end (bus 1) of the distance relay.
2. Trace a path from the source end relay (bus 1) to:
   a. The farthest backup relay (bus 7)
   b. The farthest unprotected line (bus 9)
3. For the paths in Step 2, determine the path with the maximum impedance Z_{max}.
   a. $Z_{max} = \max(Z_{12} + Z_{23} + Z_{37}, Z_{12} + Z_{23} + Z_{37} + Z_{79})$
4. Set the Zone 2 reach to 110 to 120% of Z_{max} so that:
   a. $Z_{zone\ 2} = (1.1\ to\ 1.2)Z_{max}$.

This process is summarized in Figure 23. For this algorithm, there are two underlying assumptions:

1. Fault impedances are much smaller than line impedances.
2. Line impedances are much smaller than load impedances.

As an example, again consider the example of Figure 22. The line impedances are given in Table 8. Applying the algorithm shown in Figure 23, the sparse placement, Zone 1 reach is:

$$\tilde{Z}_{zone\ 1} = 0.85\left(\tilde{Z}_{12} + \tilde{Z}_{24}\right) = 0.0911 + j0.0774. \tag{6}$$

Also,

$$\tilde{Z}_{remote} = \tilde{Z}_{12} + \tilde{Z}_{23} + \tilde{Z}_{37} = 0.2040 + j0.0862 \tag{7}$$

and

$$\tilde{Z}_{unprotected} = \tilde{Z}_{12} + \tilde{Z}_{23} + \tilde{Z}_{37} + \tilde{Z}_{79} = 0.2241 + j0.0916 \tag{8}$$

so that

$$\tilde{Z}_{mag} = \max(|\tilde{Z}_{remote}|, |\tilde{Z}_{unprotected}|)\ . \tag{9}$$

and

$$\tilde{Z}_{ang} = arg\left(\tilde{Z}_{remote} + \tilde{Z}_{unprotected}\right) = 22.554°. \tag{10}$$

The Zone 2 reach is then:

$$\tilde{Z}_{zone\ 2} = 1.3\tilde{Z}_{mag}\angle\tilde{Z}_{ang} = 0.3147\angle 22.554°. \tag{11}$$

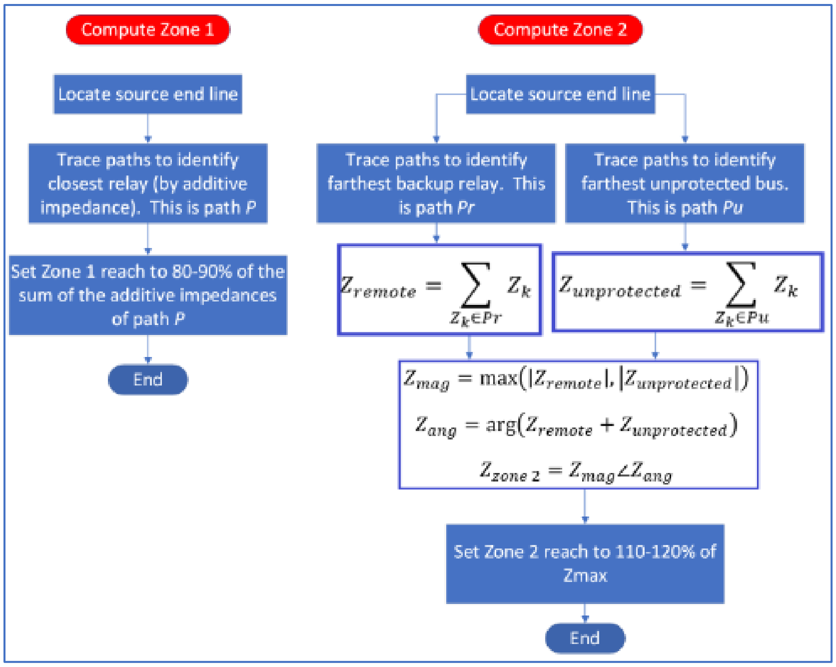

Figure 23. Computation of Zone 1 and Zone 2 impedances as introduced in [14]. The Zone 1 computation is to the left, and the Zone 2 computation is to the right.

Table 8. Per-unit impedance values for example of Figure 22.

From	To	R	X
1	2	0.09138	0.05917
2	3	0.06203	0.00543
3	7	0.12263	0.02162
7	10	0.0622	0.00217
7	9	0.02005	0.00537
2	9	0.08776	0.03194
4	5	0.06192	0.00651
5	8	0.02487	-0.00130
5	6	0.01241	-0.00109

Based on these values, the mho characteristics for a distance relay in a system with sparse relay placement are shown in Figure 24. d_1^{ij} and d_2^{ij} are the Zone 1 and Zone 2 trip delays for relay ij respectively.

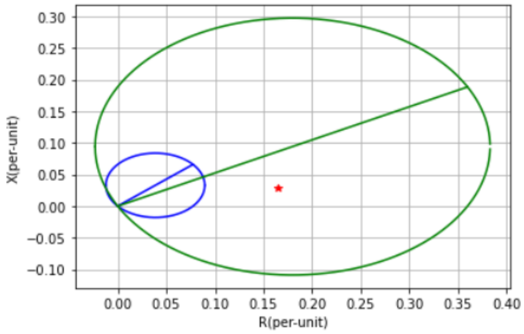

Figure 24. Sample mho circles using algorithm summarized in Figure 23. The diameters of the circles are also plotted to the represent the reach of each zone. Zone 1 is the smaller blue circle; Zone 2 is the larger green circle.

2.6. Hardware in the Loop Setup

Protection engineers aim to provide validated systems that operate with reliability, security, speed and selectivity. Testing is necessary to ensure that systems meet performance criteria, but the increasing complexity of interconnected equipment makes comprehensive testing more challenging. The need for increased power grid resilience requires systems capable of delivering realistic and high-fidelity test conditions for a broad range of system configurations.

To test the adaptive protection system, we configure the IEEE 123 bus system with 5 Schweitzer Engineering Laboratories (SEL) relays (3 – SEL 751s and 2- SEL 351s), and five virtual relays in the simulation. The modified system layout is shown in Figure 25. The relay location and related device information are listed in Table 9. The system also had nine virtual PV devices in the system, the location and ratings are shown Table 10.

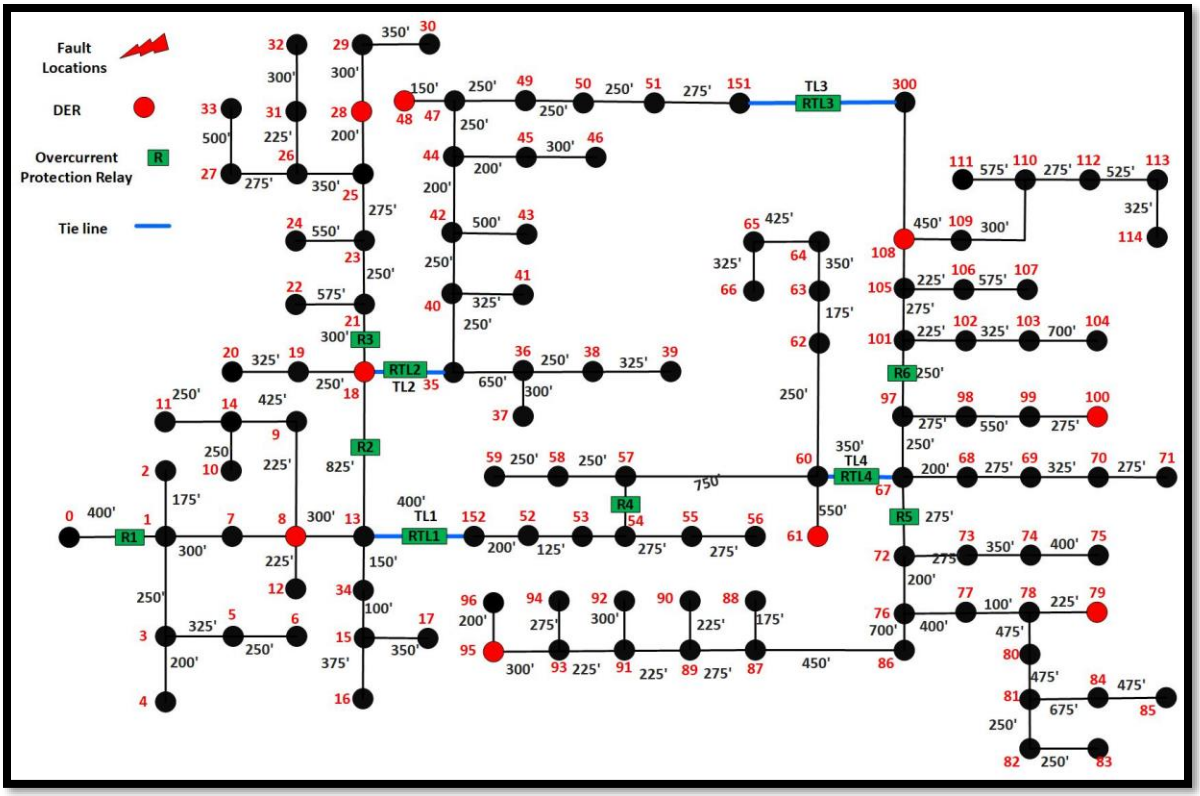

Figure 25. Modified IEEE 123 circuit with relay and DER locations.

Table 9. Relay identifications

Location	Device	IP	TCP Port
Relay 1	SEL 751-1	10.1.6.5	9506
Relay TL1	SEL 751-2	10.1.6.71	9507
Relay 4	SEL 751-3	10.1.6.72	9508
Relay 2	SEL 351-0	10.1.6.80	9580
Relay TL2	SEL 351-1	10.1.6.81	9581
Relay 3	PMU-3	10.1.6.3	7503
Relays TL3	PMU-RTL3	10.1.6.3	8503
Relay 5	PMU-5	10.1.6.3	7505
Relay 6	PMU-6	10.1.6.3	7506
Relay TL4	PMU-RTL4	10.1.6.3	8504

Table 10. PV rating and locations

PV Name	Bus Location	Rating in MW
PV1	Bus 8	1.0
PV2	Bus 18	0.7
PV3	Bus 28	0.5
PV4	Bus 48	1.0
PV5	Bus 61	0.5
PV6	Bus 79	0.5
PV7	Bus 95	1.0
PV8	Bus 100	0.5
PV 9	Bus 108	0.5

The diagram in Figure 26 shows how the relays, adaptive protection system, and the OPAL-RT simulator were connected. The total adaptive protection process takes 1 minute.

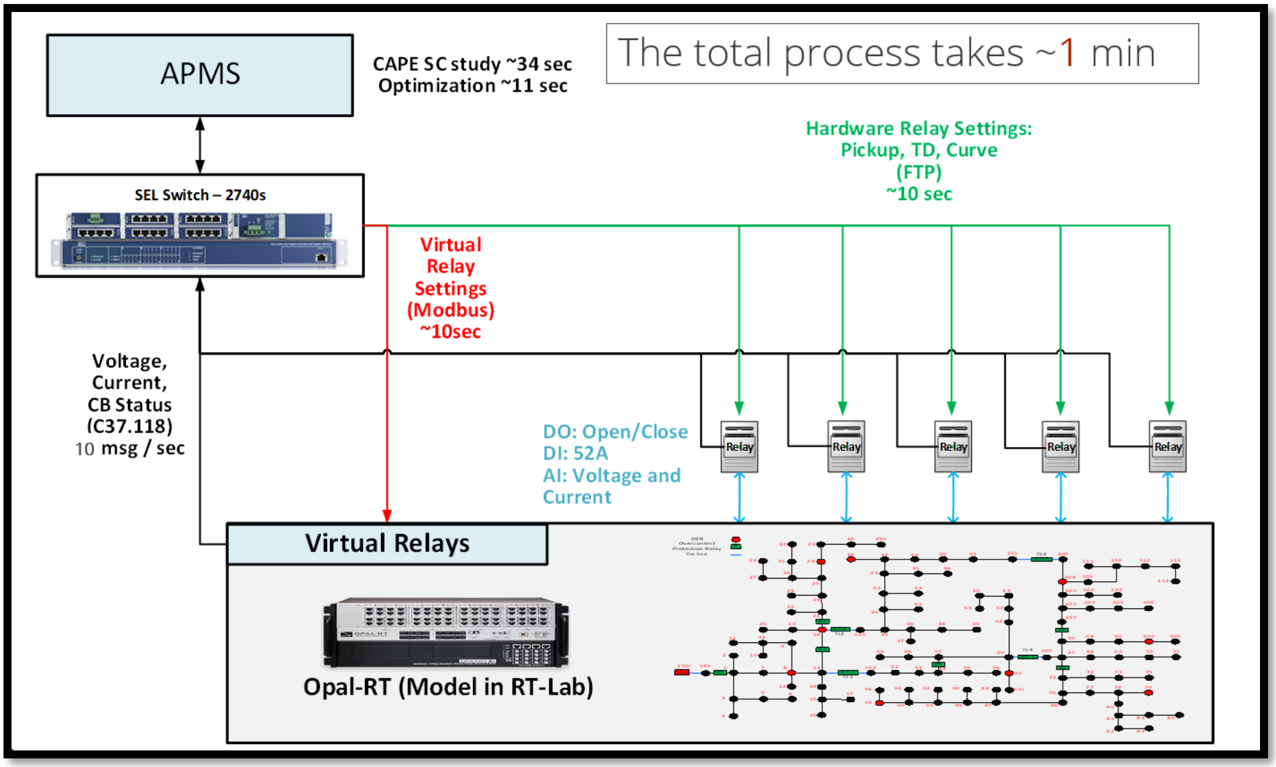

Figure 26. Hardware-in-the-Loop diagram showing communication setup between devices.

2.6.1. SEL Hardware Configuration with OPAL-RT

The SEL relays were configured in a hardware-in-the-loop (HIL) setup with the OPAL-RT. The voltage and current point on wave data for each of the SEL relays was measured in Figure 27. These measurements where then scaled down as shown in Figure 28. The 'CurrentCT' and 'VoltagePT' flags in Figure 28 contained a divisor that would scale down the measurement value. This scaled-down value would then be sent out of the OPAL-RT analog out card to the SEL relay.

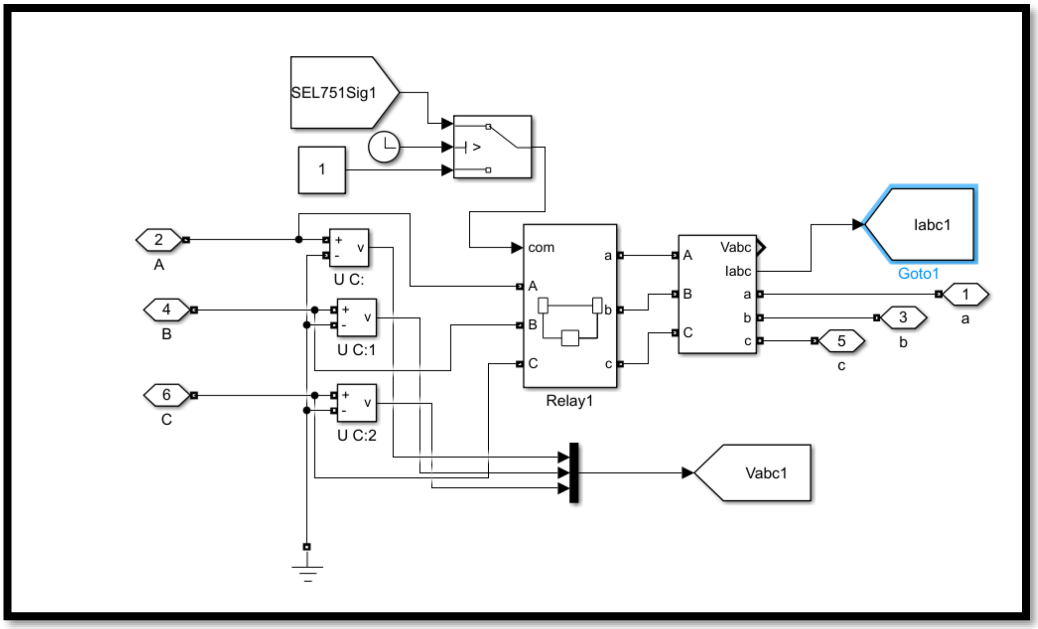

Figure 27. Example of point on wave data collection.

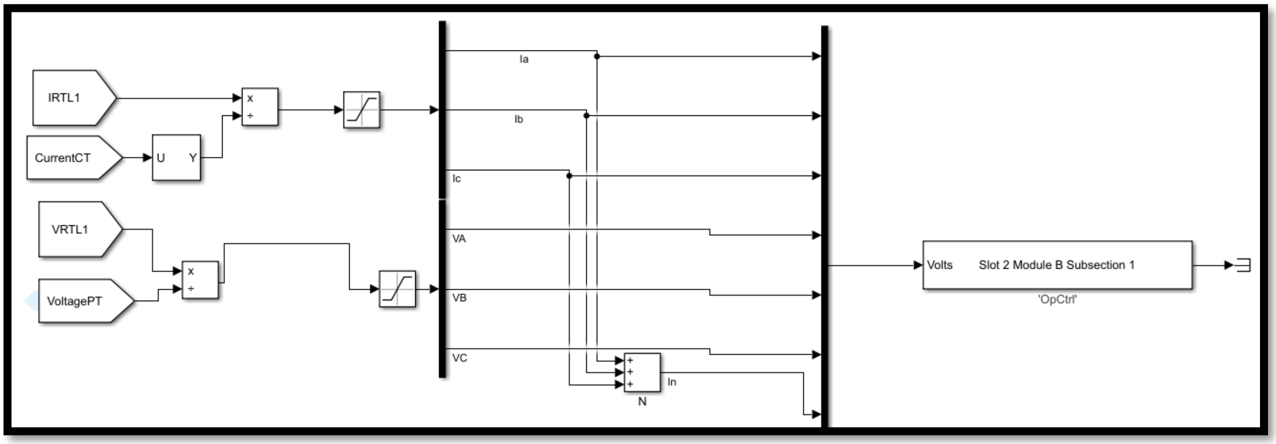

Figure 28. Scaling voltage and current measurements and then sending the data out via an Analog Out block.

The measurement value was scaled down for two reasons.

1. The OPAL-RT analog cards only support voltages in the range of +/-16V.
2. Each of the SEL relays low-level inputs support a range smaller voltage signal. Figure 29 displays the low-level interface for the SEL relays.

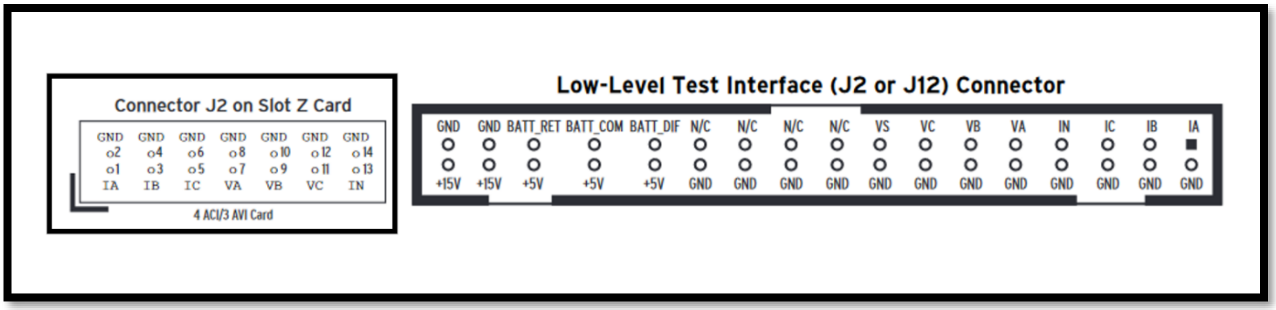

Figure 29. Low-Level SEL relay interface.

The scaled measurement values from the OPAL-RT simulation were sent to the SEL relays via ribbon cable. Figure 30 displays the SEL relays and the OPAL-RT setup at Sandia.

Figure 30. Hardware-in-the-Loop Setup at Sandia.

When a relay detected a fault or was issued an open command, the HIL loop was closed by connecting the Out101 contacts of the relays to the OPAL-RT. The Out101 contact of each relay can take a DC voltage of 24-48VDC. However, the OPAL-RT analog input card was rated for +/-

16V. Therefore, a voltage divider circuit was constructed (shown in Figure 31) that would monitor the OUT101 contact. A simple example of monitoring the OUT101 contact is shown in Figure 32. The voltage divider circuit is shown in Figure 33.

Figure 31. Opal-RT input connection from hardware relays.

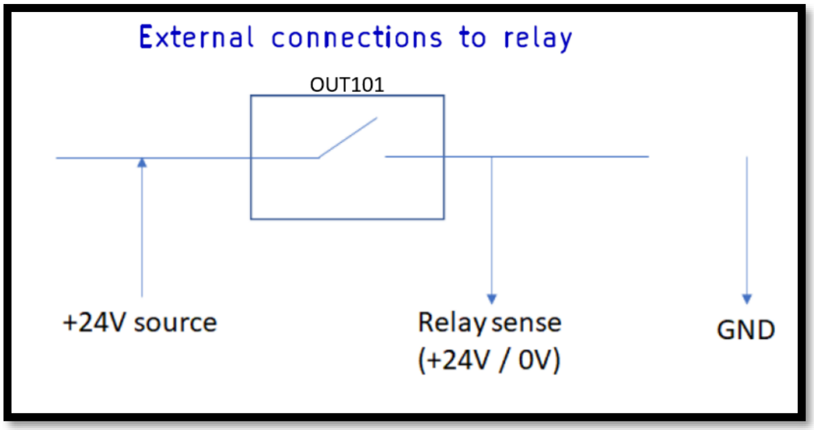

Figure 32. Mockup of Out101 contact and monitoring.

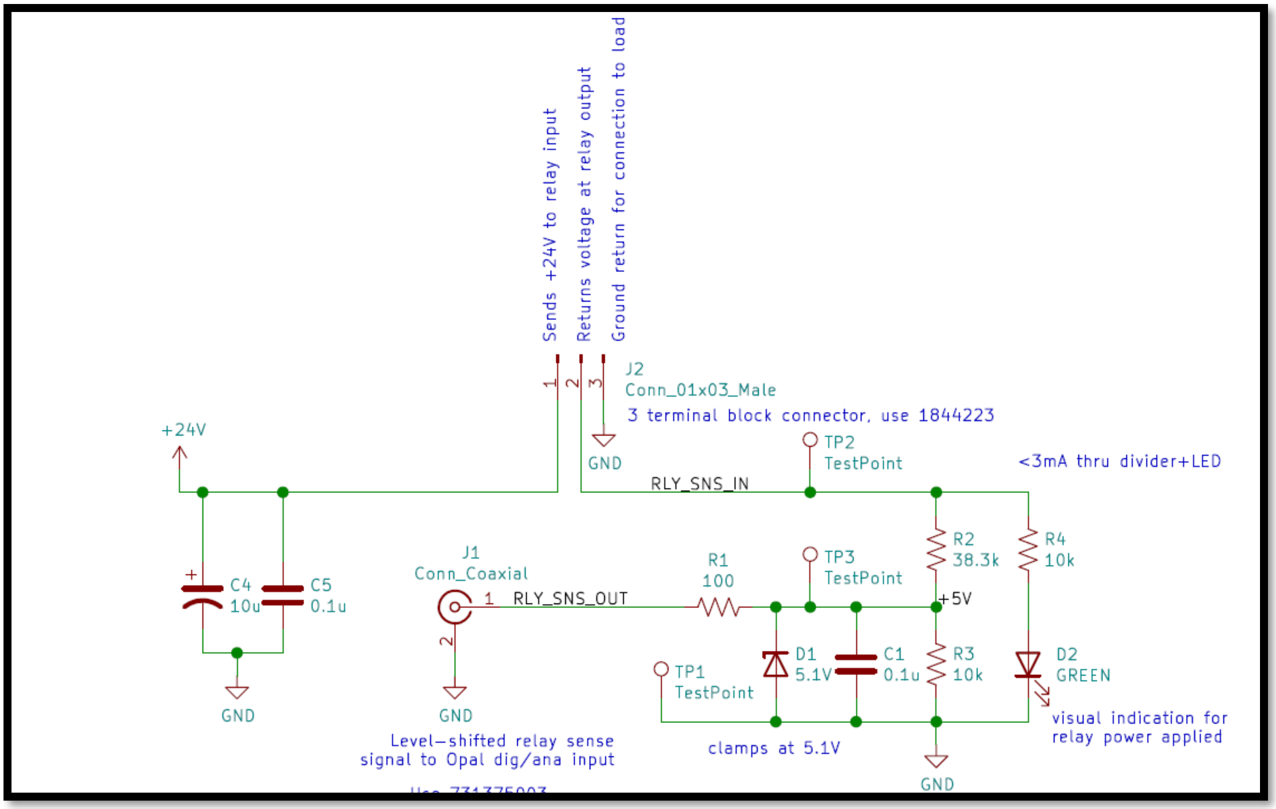

Figure 33. Voltage divider circuit.

If the relay was in a closed state, the OUT101 contact would have 24Vdc across, it and a 5Vdc signal would be sent into the simulation. If the OUT101 contact was in an open state, the signal into the simulation would be 0 Vdc. This signal would be sent to its associated virtual breaker in the simulation. The flag 'SEL751Sig1' would be connected to Relay 1.

2.6.2. Virtual Protection Device Setup in the OPAL-RT

As stated previously, five of the relays in the simulation were virtual protective devices. These devices received voltage and current measurements as in Figure 27. However, the measurements for the virtual protective relays were sent to a dedicated protection subsystem within the OPAL-RT simulation shown in Figure 34.

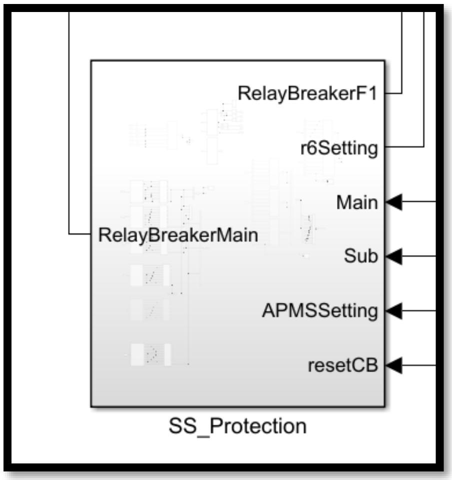

Figure 34. Dedicated Protection Subsystem.

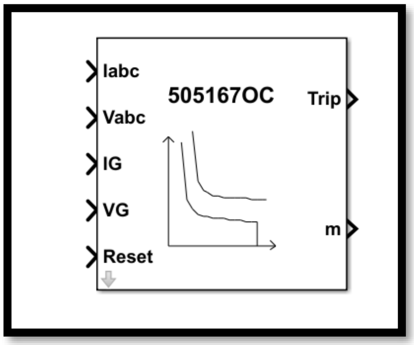

Figure 35. 50/51 Overcurrent Relay Block from OPAL-RT Simulink library.

The signals for voltage and current were streamed to the overcurrent relay block in Figure 35. The 'Trip' signal from this block was calculated based on the programmed time-overcurrent settings, before being sent to open the associated virtual relays' circuit breaker.

2.6.3. Communications from Virtual Relays and SEL Relays to APMS

The communication from the virtual relays and SEL relays to the APMS computer is shown in Figure 26. The communication protocol used was IEEE C37.118. The virtual and SEL relays were configured to stream phasor measurement unit (PMU) data at a rate of 10 messages per second to the APMS.

The virtual PMUs were configured in the RT-LAB software as shown in Figure 36 and Figure 37.

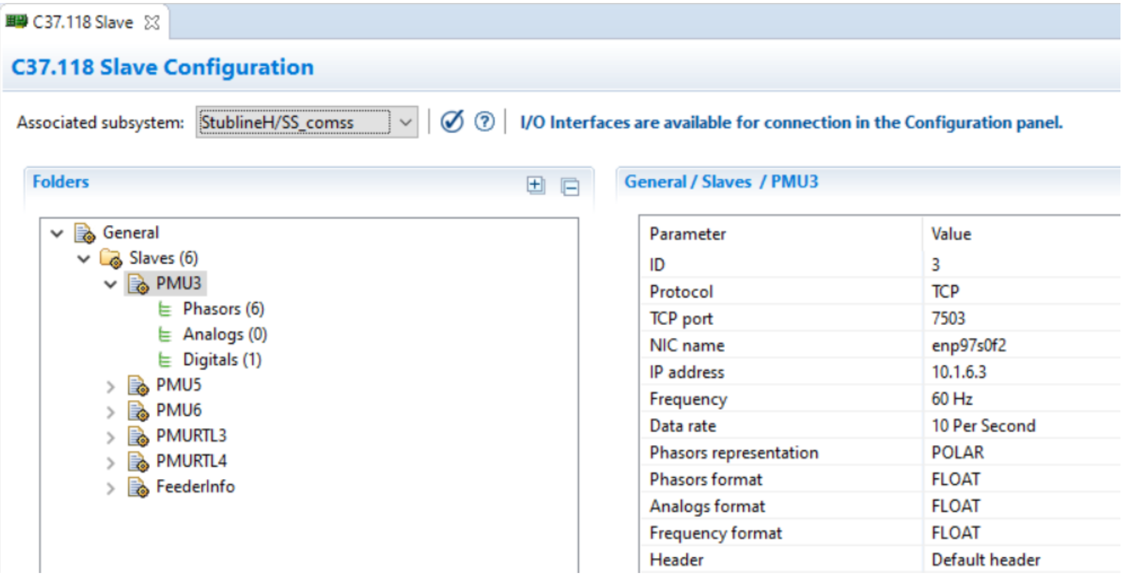

C37.118 Slave Configuration

Associated subsystem: StublineH/SS_comss

I/O Interfaces are available for connection in the Configuration panel.

Folders

- General
  - Slaves (6)
    - PMU3
      - Phasors (6)
      - Analogs (0)
      - Digitals (1)
    - PMU5
    - PMU6
    - PMURTL3
    - PMURTL4
    - FeederInfo

General / Slaves / PMU3

Parameter	Value
ID	3
Protocol	TCP
TCP port	7503
NIC name	enp97s0f2
IP address	10.1.6.3
Frequency	60 Hz
Data rate	10 Per Second
Phasors representation	POLAR
Phasors format	FLOAT
Analogs format	FLOAT
Frequency format	FLOAT
Header	Default header

Figure 36. Configuration of PMUs in RT-LAB.

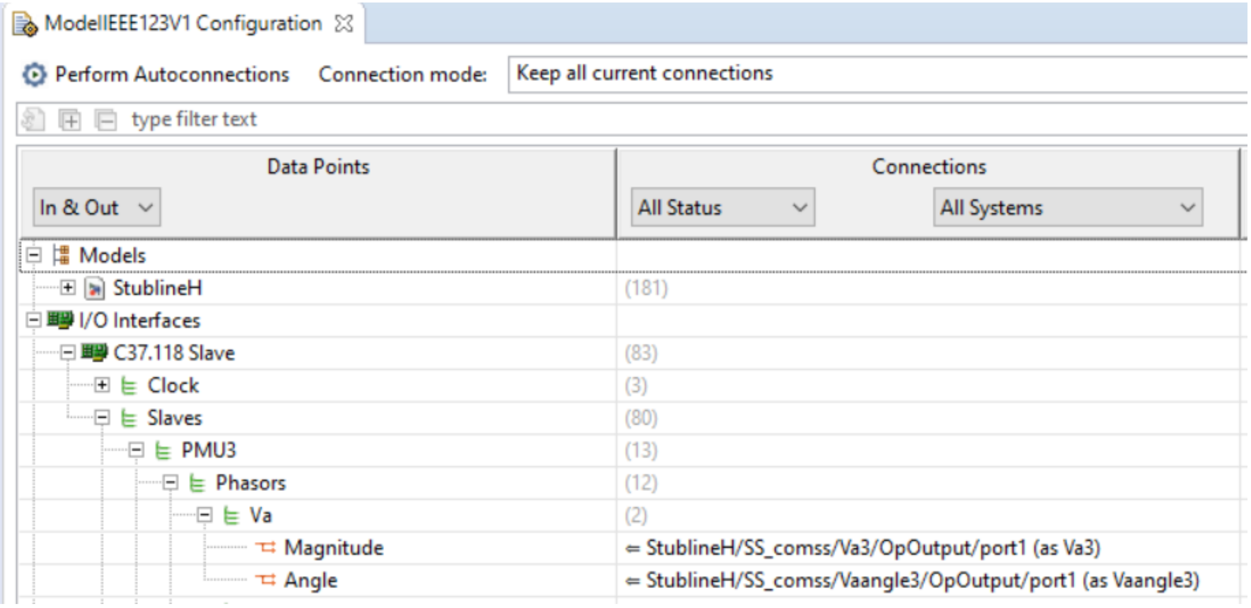

Connection mode: Keep all current connections

Data Points	Connections
Models	
StublineH	(181)
I/O Interfaces	
C37.118 Slave	(83)
Clock	(3)
Slaves	(80)
PMU3	(13)
Phasors	(12)
Va	(2)
Magnitude	⇐ StublineH/SS_comss/Va3/OpOutput/port1 (as Va3)
Angle	⇐ StublineH/SS_comss/Vaangle3/OpOutput/port1 (as Vaangle3)

Figure 37. Connecting PMU data points within RT-LAB.

The mapping from Figure 37 corresponded to Figure 38 below within the simulation. Three-phase voltage and current data, as well as circuit breaker status are split into individual OpOutput blocks for each signal.

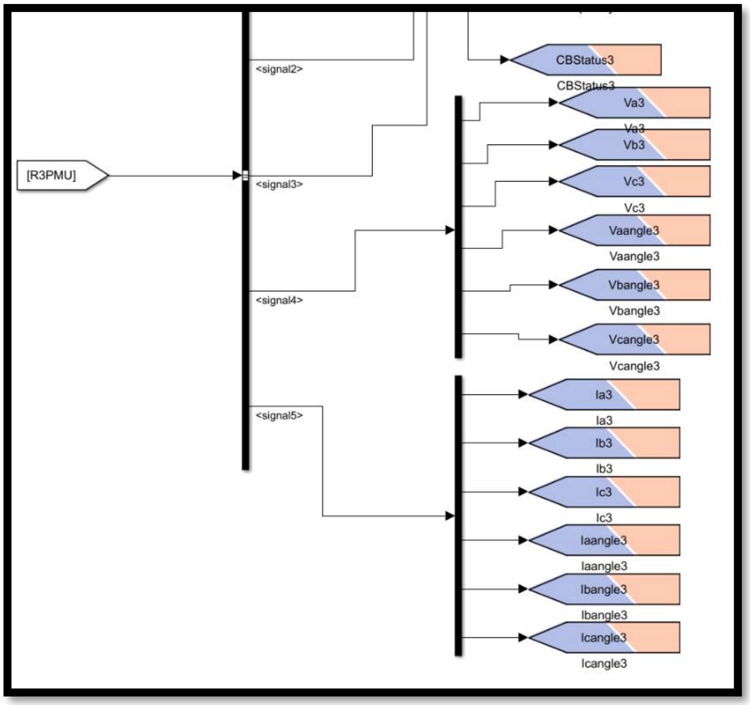

Figure 38. OpOutput blocks used in Simulink for PMU mappings.

2.6.4. Overview of Adaptive Protection Code

The APMS code was written in the python programming language for opensource development [15]. The code follows the flow diagram shown in Figure 39.

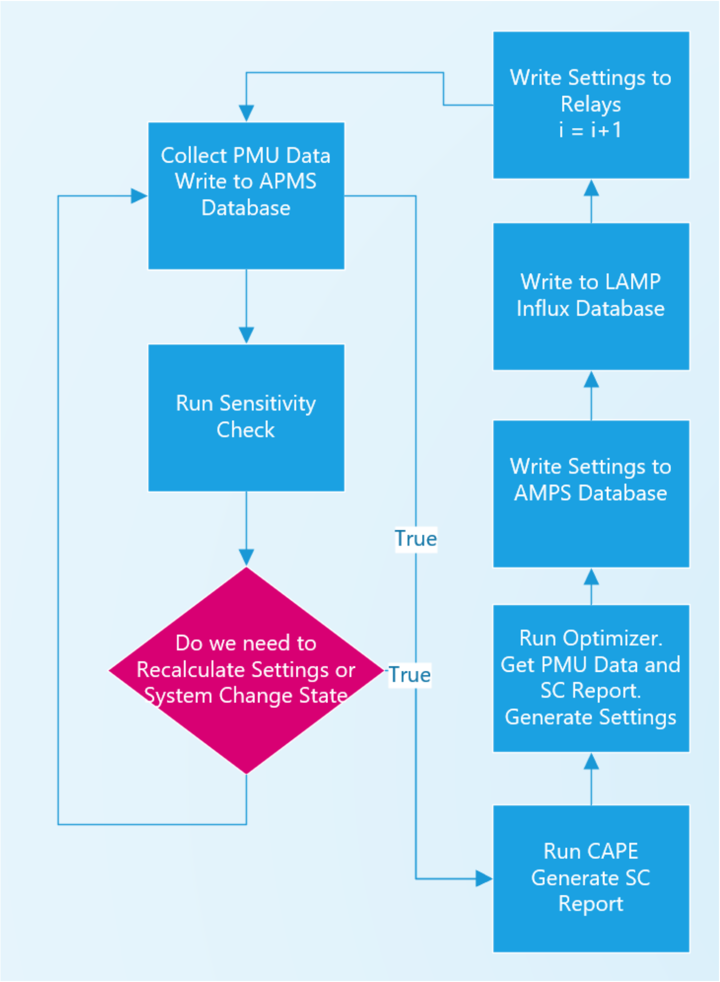

Figure 39. Adaptive Protection Flow Diagram.

2.6.5. Collection of PMU Data in the Adaptive Protection Code

The first step, as shown in the flow diagram in Figure 39, was to collect the PMU data that is streaming from the OPAL-RT simulation and the SEL relays, and send it back to the APMS machine, as in Figure 26. The Python package pyPMU [16, 17] was used to collect the PMU relay measurements, the PV status, and real power output. These measurements where then compiled into a csv file as show in Figure 40.

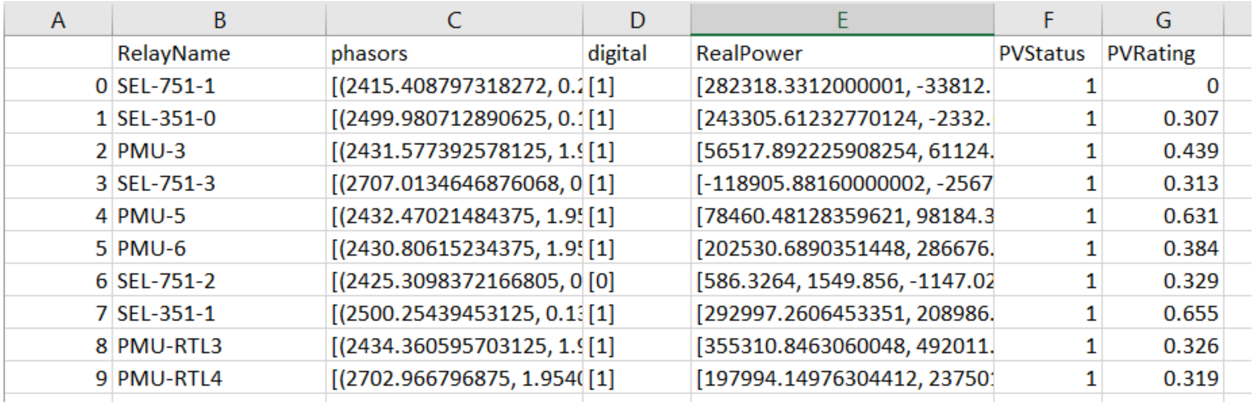

A	B	C	D	E	F	G
	RelayName	phasors	digital	RealPower	PVStatus	PVRating
0	SEL-751-1	[(2415.408797318272, 0.	[1]	[282318.3312000001, -33812.	1	0
1	SEL-351-0	[(2499.980712890625, 0.	[1]	[243305.61232770124, -2332.	1	0.307
2	PMU-3	[(2431.577392578125, 1.	[1]	[56517.892225908254, 61124.	1	0.439
3	SEL-751-3	[(2707.0134646876068, 0	[1]	[-118905.88160000002, -2567	1	0.313
4	PMU-5	[(2432.47021484375, 1.9	[1]	[78460.48128359621, 98184.3	1	0.631
5	PMU-6	[(2430.80615234375, 1.9	[1]	[202530.6890351448, 286676.	1	0.384
6	SEL-751-2	[(2425.3098372166805, 0	[0]	[586.3264, 1549.856, -1147.0	1	0.329
7	SEL-351-1	[(2500.25439453125, 0.1	[1]	[292997.2606453351, 208986.	1	0.655
8	PMU-RTL3	[(2434.360595703125, 1.	[1]	[355310.8463060048, 492011.	1	0.326
9	PMU-RTL4	[(2702.966796875, 1.954	[1]	[197994.14976304412, 23750	1	0.319

Figure 40. Example csv file of PMU data.

2.6.6. *Sensitivity Analysis Check*

A sensitivity analysis was used to check if new settings should be calculated based on if the system configuration had changed, the load current had changed, and if the PV output had changed. The Sensitivity Analysis function took 0.2 seconds to run as shown in Figure 41. The flow diagram for this method is shown in Figure 42. [2] documents the effectiveness of this solution.

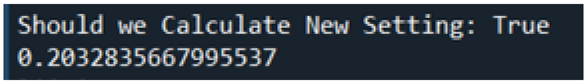

```
Should we Calculate New Setting: True
0.2032835667995537
```

Figure 41. Sensitivity Analysis Loop time.

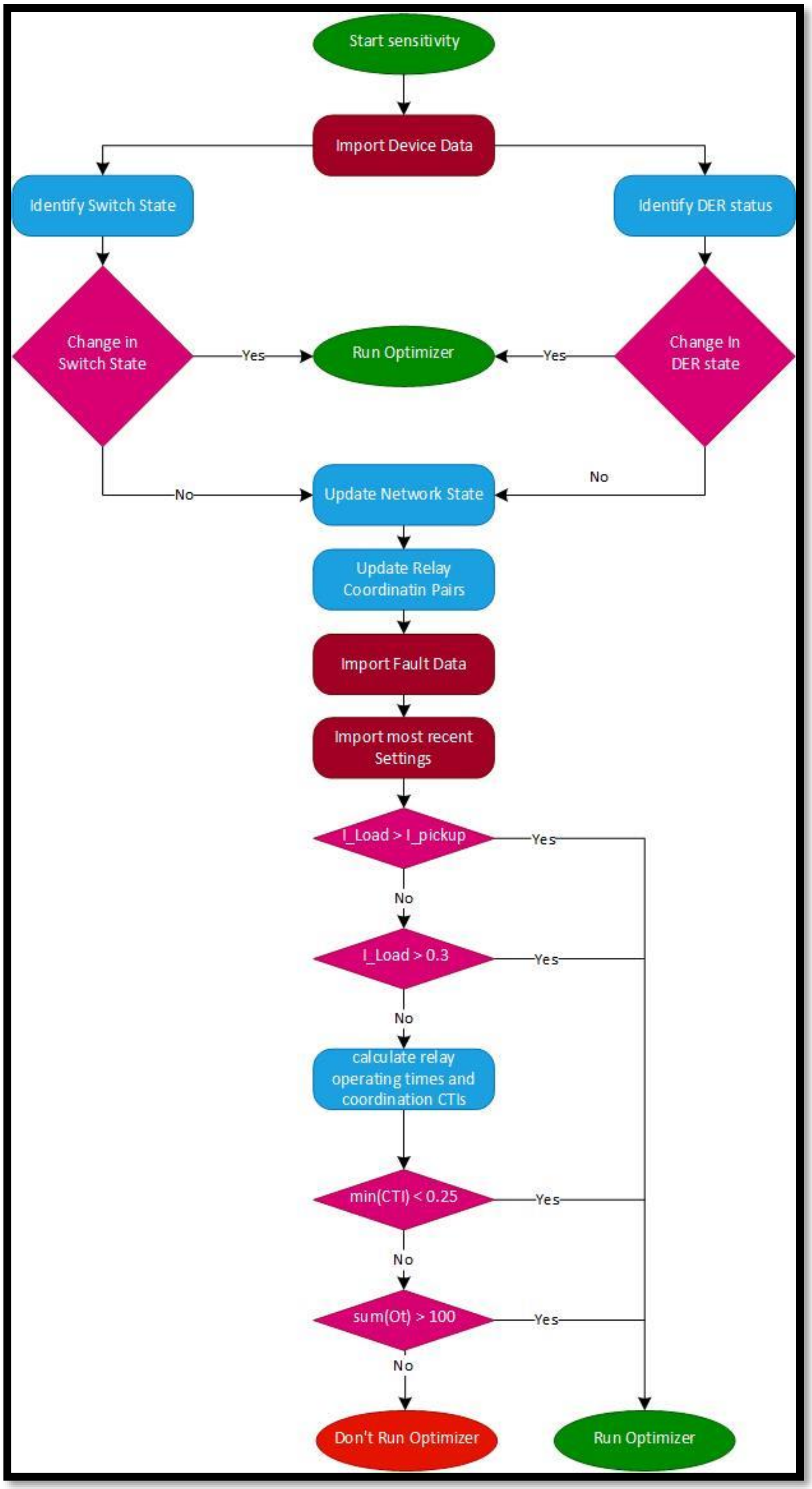

Figure 42. Sensitivity Analysis Flow Diagram.

2.6.7. Real Time Digital Twin with CAPE

PSS®CAPE is a short circuit software that is widely used by protection engineers to analyze electric grid systems. The IEEE 123 model was created in this software. A python script, shown in Figure 43, was created to run the CAPE model using the PMU CSV file to:

1. Update the system configuration by opening or closing tie line breakers.
2. Update the PV rating from the PMU CSV file.
3. Run a short circuit analysis and return the results as a CSV file.

This allowed the latest prevailing system conditions to be updated from the short circuit report. Running this section of the code takes about 7.1 seconds.

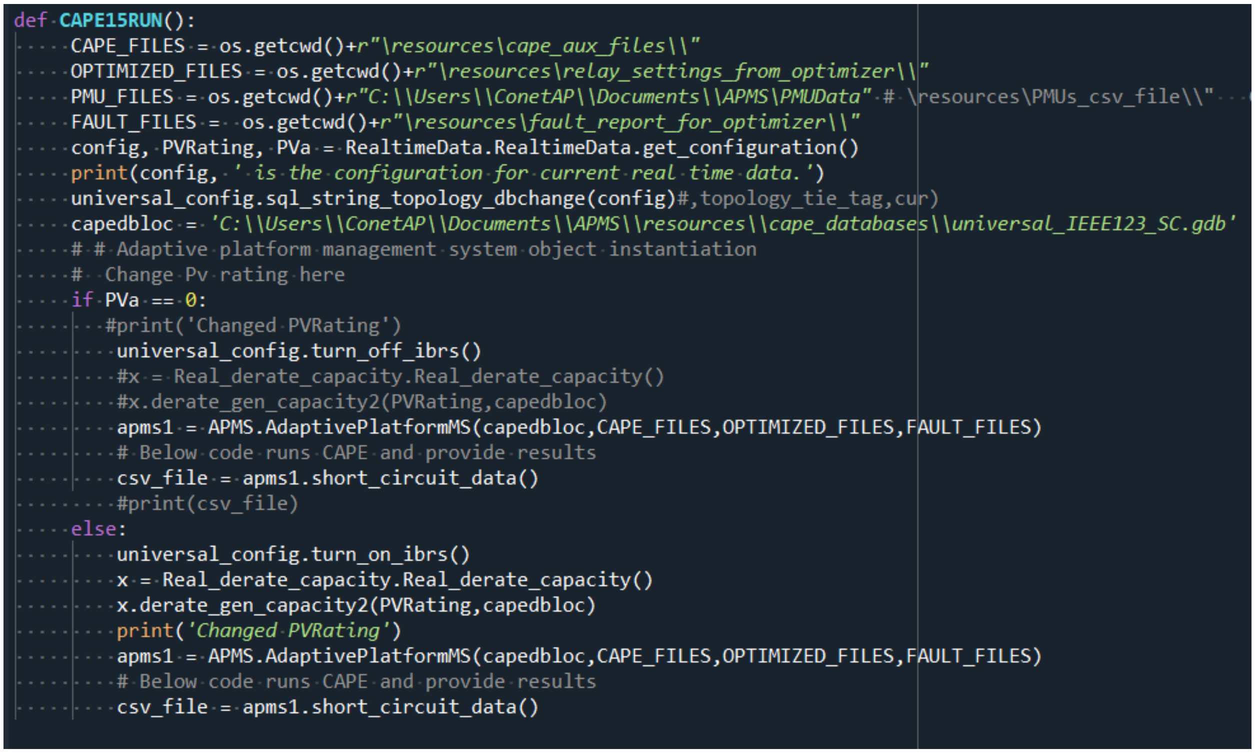

```
def CAPE15RUN():
    CAPE_FILES = os.getcwd()+r"\resources\cape_aux_files\\"
    OPTIMIZED_FILES = os.getcwd()+r"\resources\relay_settings_from_optimizer\\"
    PMU_FILES = os.getcwd()+r"C:\\Users\\ConetAP\\Documents\\APMS\PMUData" # \resources\PMUs_csv_file\\"
    FAULT_FILES =  os.getcwd()+r"\resources\fault_report_for_optimizer\\"
    config, PVRating, PVa = RealtimeData.RealtimeData.get_configuration()
    print(config, ' is the configuration for current real time data.')
    universal_config.sql_string_topology_dbchange(config)#,topology_tie_tag,cur)
    capedbloc = 'C:\\Users\\ConetAP\\Documents\\APMS\\resources\\cape_databases\\universal_IEEE123_SC.gdb'
    # # Adaptive platform management system object instantiation
    #  Change Pv rating here
    if PVa == 0:
       #print('Changed PVRating')
        universal_config.turn_off_ibrs()
        #x = Real_derate_capacity.Real_derate_capacity()
        #x.derate_gen_capacity2(PVRating,capedbloc)
        apms1 = APMS.AdaptivePlatformMS(capedbloc,CAPE_FILES,OPTIMIZED_FILES,FAULT_FILES)
        # Below code runs CAPE and provide results
        csv_file = apms1.short_circuit_data()
        #print(csv_file)
    else:
        universal_config.turn_on_ibrs()
        x = Real_derate_capacity.Real_derate_capacity()
        x.derate_gen_capacity2(PVRating,capedbloc)
        print('Changed PVRating')
        apms1 = APMS.AdaptivePlatformMS(capedbloc,CAPE_FILES,OPTIMIZED_FILES,FAULT_FILES)
        # Below code runs CAPE and provide results
        csv_file = apms1.short_circuit_data()
```

Figure 43. Python function to update CAPE.

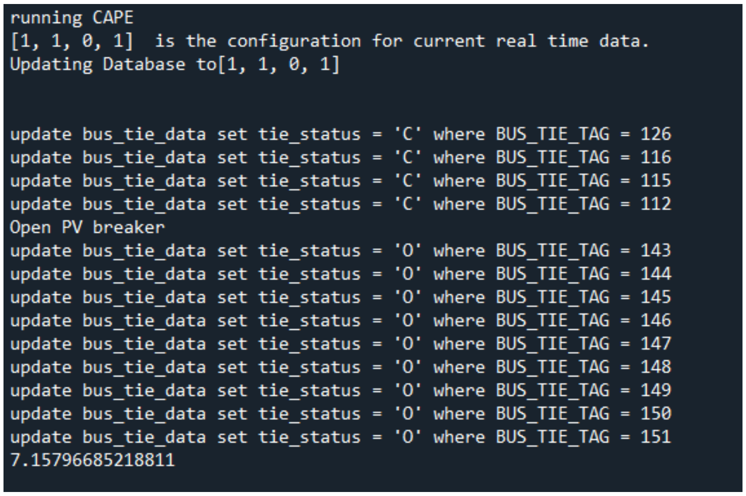

```
running CAPE
[1, 1, 0, 1]  is the configuration for current real time data.
Updating Database to[1, 1, 0, 1]


update bus_tie_data set tie_status = 'C' where BUS_TIE_TAG = 126
update bus_tie_data set tie_status = 'C' where BUS_TIE_TAG = 116
update bus_tie_data set tie_status = 'C' where BUS_TIE_TAG = 115
update bus_tie_data set tie_status = 'C' where BUS_TIE_TAG = 112
Open PV breaker
update bus_tie_data set tie_status = 'O' where BUS_TIE_TAG = 143
update bus_tie_data set tie_status = 'O' where BUS_TIE_TAG = 144
update bus_tie_data set tie_status = 'O' where BUS_TIE_TAG = 145
update bus_tie_data set tie_status = 'O' where BUS_TIE_TAG = 146
update bus_tie_data set tie_status = 'O' where BUS_TIE_TAG = 147
update bus_tie_data set tie_status = 'O' where BUS_TIE_TAG = 148
update bus_tie_data set tie_status = 'O' where BUS_TIE_TAG = 149
update bus_tie_data set tie_status = 'O' where BUS_TIE_TAG = 150
update bus_tie_data set tie_status = 'O' where BUS_TIE_TAG = 151
7.15796685218811
```

Figure 44. CAPE modeling updating system configuration and PV status timing.

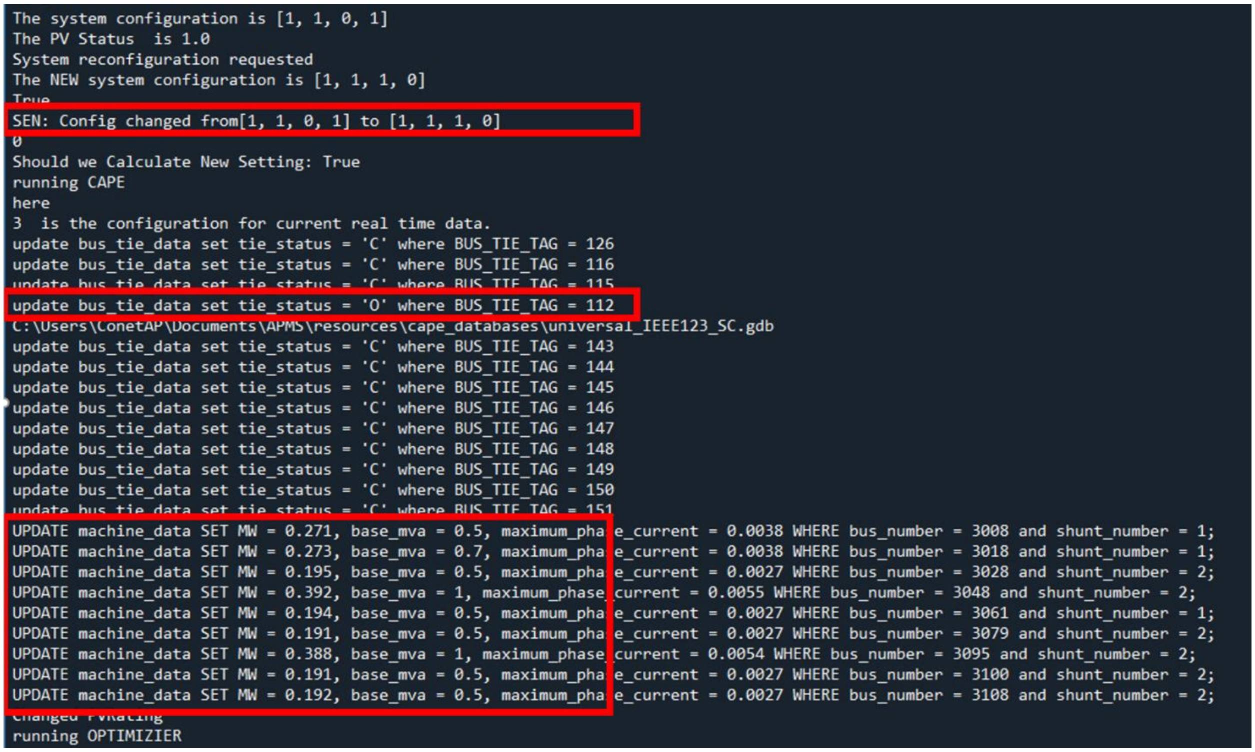

```
The system configuration is [1, 1, 0, 1]
The PV Status  is 1.0
System reconfiguration requested
The NEW system configuration is [1, 1, 1, 0]
True
SEN: Config changed from[1, 1, 0, 1] to [1, 1, 1, 0]
0
Should we Calculate New Setting: True
running CAPE
here
3  is the configuration for current real time data.
update bus_tie_data set tie_status = 'C' where BUS_TIE_TAG = 126
update bus_tie_data set tie_status = 'C' where BUS_TIE_TAG = 116
update bus_tie_data set tie_status = 'C' where BUS_TIE_TAG = 115
update bus_tie_data set tie_status = 'O' where BUS_TIE_TAG = 112
C:\Users\ConetAP\Documents\APMS\resources\cape_databases\universal_IEEE123_SC.gdb
update bus_tie_data set tie_status = 'C' where BUS_TIE_TAG = 143
update bus_tie_data set tie_status = 'C' where BUS_TIE_TAG = 144
update bus_tie_data set tie_status = 'C' where BUS_TIE_TAG = 145
update bus_tie_data set tie_status = 'C' where BUS_TIE_TAG = 146
update bus_tie_data set tie_status = 'C' where BUS_TIE_TAG = 147
update bus_tie_data set tie_status = 'C' where BUS_TIE_TAG = 148
update bus_tie_data set tie_status = 'C' where BUS_TIE_TAG = 149
update bus_tie_data set tie_status = 'C' where BUS_TIE_TAG = 150
update bus_tie_data set tie_status = 'C' where BUS_TIE_TAG = 151
UPDATE machine_data SET MW = 0.271, base_mva = 0.5, maximum_pha e_current = 0.0038 WHERE bus_number = 3008 and shunt_number = 1;
UPDATE machine_data SET MW = 0.273, base_mva = 0.7, maximum_pha e_current = 0.0038 WHERE bus_number = 3018 and shunt_number = 1;
UPDATE machine_data SET MW = 0.195, base_mva = 0.5, maximum_pha e_current = 0.0027 WHERE bus_number = 3028 and shunt_number = 2;
UPDATE machine_data SET MW = 0.392, base_mva = 1, maximum_phase current = 0.0055 WHERE bus_number = 3048 and shunt_number = 2;
UPDATE machine_data SET MW = 0.194, base_mva = 0.5, maximum_pha e_current = 0.0027 WHERE bus_number = 3061 and shunt_number = 1;
UPDATE machine_data SET MW = 0.191, base_mva = 0.5, maximum_pha e_current = 0.0027 WHERE bus_number = 3079 and shunt_number = 2;
UPDATE machine_data SET MW = 0.388, base_mva = 1, maximum_phase current = 0.0054 WHERE bus_number = 3095 and shunt_number = 2;
UPDATE machine_data SET MW = 0.191, base_mva = 0.5, maximum_pha e_current = 0.0027 WHERE bus_number = 3100 and shunt_number = 2;
UPDATE machine_data SET MW = 0.192, base_mva = 0.5, maximum_pha e_current = 0.0027 WHERE bus_number = 3108 and shunt_number = 2;
changed PVRating
running OPTIMIZIER
```

Figure 45. Terminal displaying CAPE updating system configuration and PV rating.

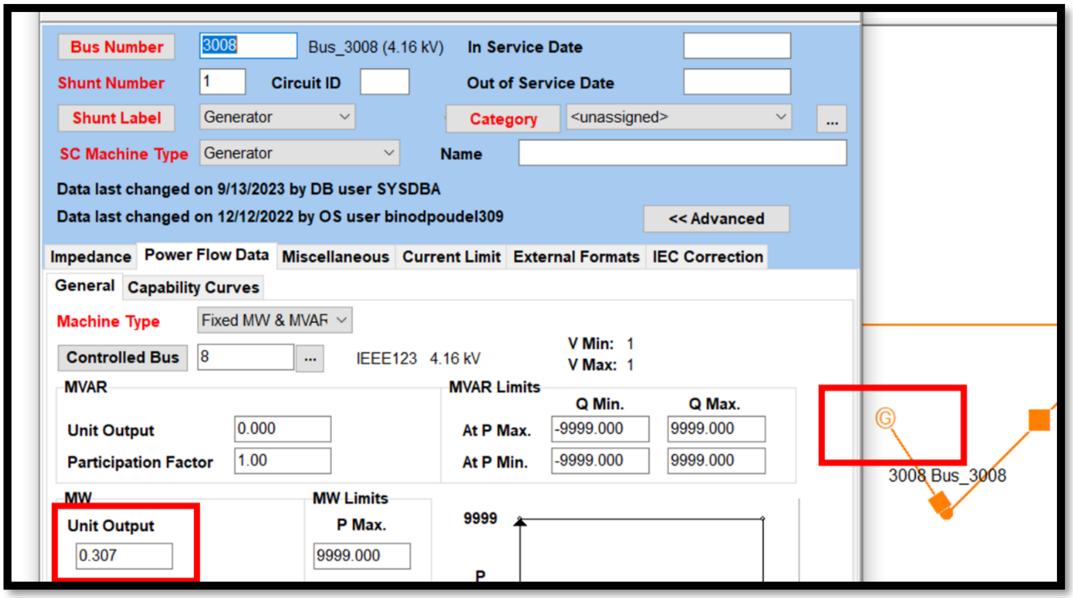
Bus Number 3008 Bus_3008 (4.16 kV) **In Service Date**

Shunt Number 1 **Circuit ID** **Out of Service Date**

Shunt Label Generator **Category** <unassigned>

SC Machine Type Generator **Name**

Data last changed on 9/13/2023 by DB user SYSDBA

Data last changed on 12/12/2022 by OS user binodpoudel309

Machine Type Fixed MW & MVAR

Controlled Bus 8 IEEE123 4.16 kV V Min: 1 V Max: 1

MVAR

Unit Output 0.000

Participation Factor 1.00

MVAR Limits

	Q Min.	Q Max.
At P Max.	-9999.000	9999.000
At P Min.	-9999.000	9999.000

MW

Unit Output 0.307

MW Limits

P Max. 9999.000

Figure 46. Example of CAPE updating a PV unit output.

2.6.8. *Running Optimizer in Real-Time*

The next step from the flow diagram would be to run the protection setting optimizer. The protection setting optimizer section of the python code would use the PMU and short circuit csv files to calculate new settings for each protective relay. The output of the optimizer was a protection settings csv file. An example is shown in Figure 47.

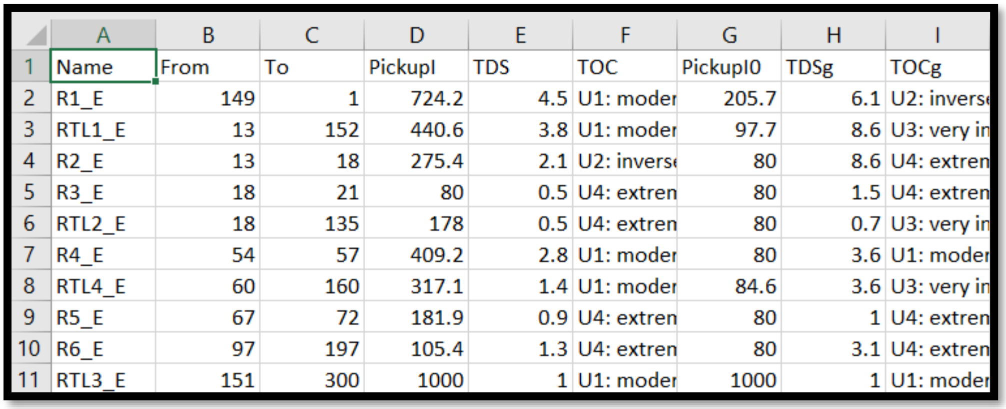

	A	B	C	D	E	F	G	H	I
1	Name	From	To	PickupI	TDS	TOC	PickupI0	TDSg	TOCg
2	R1_E	149	1	724.2	4.5	U1: moder	205.7	6.1	U2: invers
3	RTL1_E	13	152	440.6	3.8	U1: moder	97.7	8.6	U3: very in
4	R2_E	13	18	275.4	2.1	U2: invers	80	8.6	U4: extren
5	R3_E	18	21	80	0.5	U4: extren	80	1.5	U4: extren
6	RTL2_E	18	135	178	0.5	U4: extren	80	0.7	U3: very in
7	R4_E	54	57	409.2	2.8	U1: moder	80	3.6	U1: moder
8	RTL4_E	60	160	317.1	1.4	U1: moder	84.6	3.6	U3: very in
9	R5_E	67	72	181.9	0.9	U4: extren	80	1	U4: extren
10	R6_E	97	197	105.4	1.3	U4: extren	80	3.1	U4: extren
11	RTL3_E	151	300	1000	1	U1: moder	1000	1	U1: moder

Figure 47. Example of optimizer output.

2.6.9. *Writing Settings to the Database*

The Influx database was used to store the results of the optimizer output 1) To have a historical record of settings 2) To display these settings in an interface.

2.6.10. *Writing Settings to Relays*

The relay settings were communicated back to the SEL relays and the virtual relays in two different ways detailed below.

2.6.10.1. Writing Settings to SEL Relays

The next step in the flow diagram was to send the protection settings to the relays. Generally, SEL relay settings are updated using their AcSELerator® software. However, this software cannot currently be called from python to update the settings. The SEL 751 and 351S relays are configured using text files, as shown in Figure 48, that can be edited and then sent back to the relays. A python function was created to take advantage of this feature as shown in Figure 49.

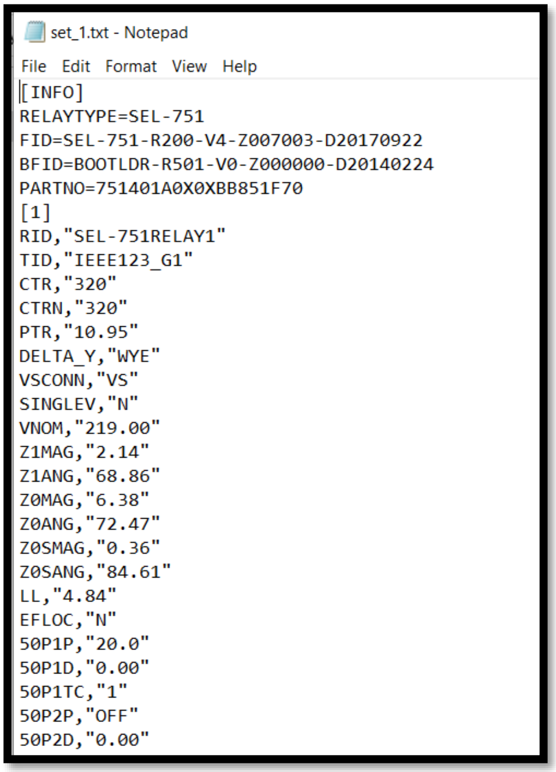

```
[INFO]
RELAYTYPE=SEL-751
FID=SEL-751-R200-V4-Z007003-D20170922
BFID=BOOTLDR-R501-V0-Z000000-D20140224
PARTNO=751401A0X0XBB851F70
[1]
RID,"SEL-751RELAY1"
TID,"IEEE123_G1"
CTR,"320"
CTRN,"320"
PTR,"10.95"
DELTA_Y,"WYE"
VSCONN,"VS"
SINGLEV,"N"
VNOM,"219.00"
Z1MAG,"2.14"
Z1ANG,"68.86"
Z0MAG,"6.38"
Z0ANG,"72.47"
Z0SMAG,"0.36"
Z0SANG,"84.61"
LL,"4.84"
EFLOC,"N"
50P1P,"20.0"
50P1D,"0.00"
50P1TC,"1"
50P2P,"OFF"
50P2D,"0.00"
```

Figure 48. Example of SEL 751 set1.txt file.

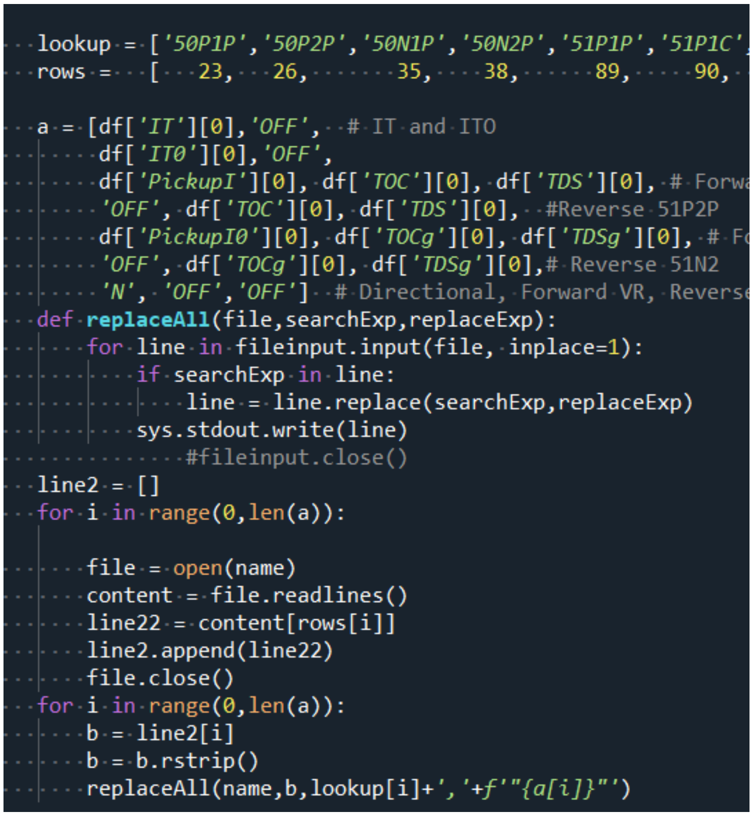

```
   lookup = ['50P1P','50P2P','50N1P','50N2P','51P1P','51P1C'
   rows =   [  23,  26,      35,   38,      89,     90,
   
   a = [df['IT'][0],'OFF',  # IT and ITO
        df['IT0'][0],'OFF',
        df['PickupI'][0], df['TOC'][0], df['TDS'][0], # Forwa
        'OFF', df['TOC'][0], df['TDS'][0],  #Reverse 51P2P
        df['PickupI0'][0], df['TOCg'][0], df['TDSg'][0], # Fo
        'OFF', df['TOCg'][0], df['TDSg'][0],# Reverse 51N2
        'N', 'OFF','OFF']  # Directional, Forward VR, Reverse
   def replaceAll(file,searchExp,replaceExp):
       for line in fileinput.input(file, inplace=1):
           if searchExp in line:
               line = line.replace(searchExp,replaceExp)
           sys.stdout.write(line)
               #fileinput.close()
   line2 = []
   for i in range(0,len(a)):
   
       file = open(name)
       content = file.readlines()
       line22 = content[rows[i]]
       line2.append(line22)
       file.close()
   for i in range(0,len(a)):
       b = line2[i]
       b = b.rstrip()
       replaceAll(name,b,lookup[i]+','+f'"{a[i]}"')
```

Figure 49. Section of python code showing how to update SEL relay settings with text file.

The function would use the protection settings csv file to determine which relay settings needed to be updated. For example, if the '51P1P' setting in Figure 49 needed to be updated, it corresponds to row 89 in the set1.txt file in Figure 48. The script would then search for the '51P1P' setting text, remove the value, and replace it with the value from the updated protection settings file.

2.6.10.2. Writing Settings to Virtual Relays.

The virtual relays were configured to use a Modbus connection between the APMS and the OPAL-RT as shown in Figure 26. Figure 50 shows the configuration for the Modbus points in the RT-LAB software, and Figure 51 shows the configuration of the OpInput blocks within MATLAB/Simulink. The python library pyModbus was used to write the protection parameters of the virtual relays back into the OPAL-RT simulation as shown in Figure 52.

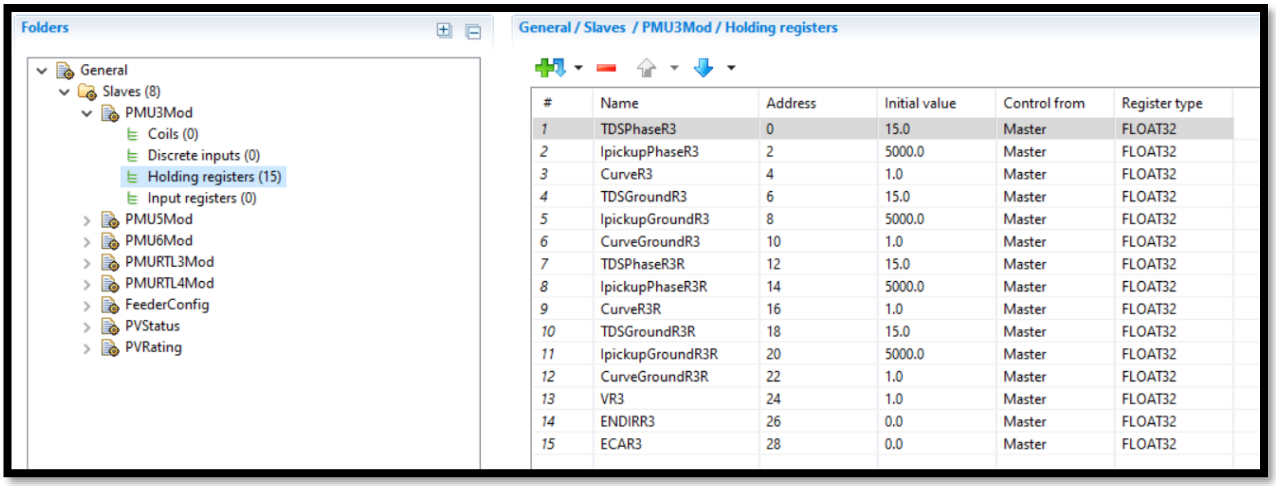

#	Name	Address	Initial value	Control from	Register type
1	TDSPhaseR3	0	15.0	Master	FLOAT32
2	IpickupPhaseR3	2	5000.0	Master	FLOAT32
3	CurveR3	4	1.0	Master	FLOAT32
4	TDSGroundR3	6	15.0	Master	FLOAT32
5	IpickupGroundR3	8	5000.0	Master	FLOAT32
6	CurveGroundR3	10	1.0	Master	FLOAT32
7	TDSPhaseR3R	12	15.0	Master	FLOAT32
8	IpickupPhaseR3R	14	5000.0	Master	FLOAT32
9	CurveR3R	16	1.0	Master	FLOAT32
10	TDSGroundR3R	18	15.0	Master	FLOAT32
11	IpickupGroundR3R	20	5000.0	Master	FLOAT32
12	CurveGroundR3R	22	1.0	Master	FLOAT32
13	VR3	24	1.0	Master	FLOAT32
14	ENDIRR3	26	0.0	Master	FLOAT32
15	ECAR3	28	0.0	Master	FLOAT32

Figure 50. Configuration of Modbus datapoints within RT-LAB software.

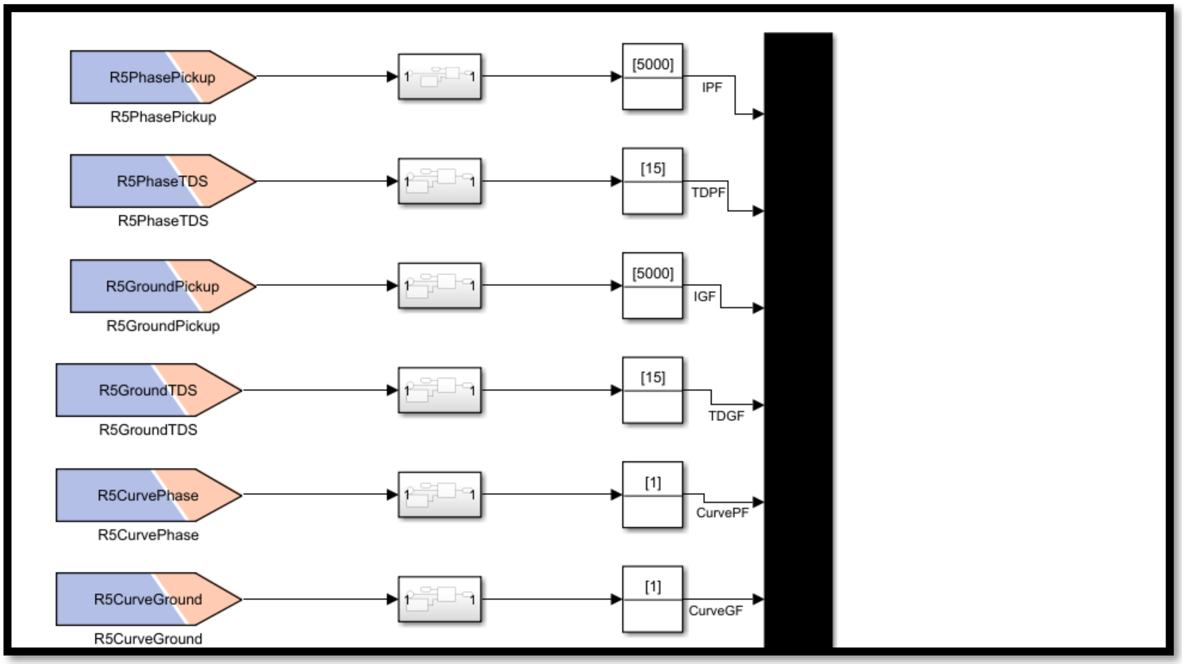

Figure 51. OpInput blocks used to receive Modbus parameter updates.

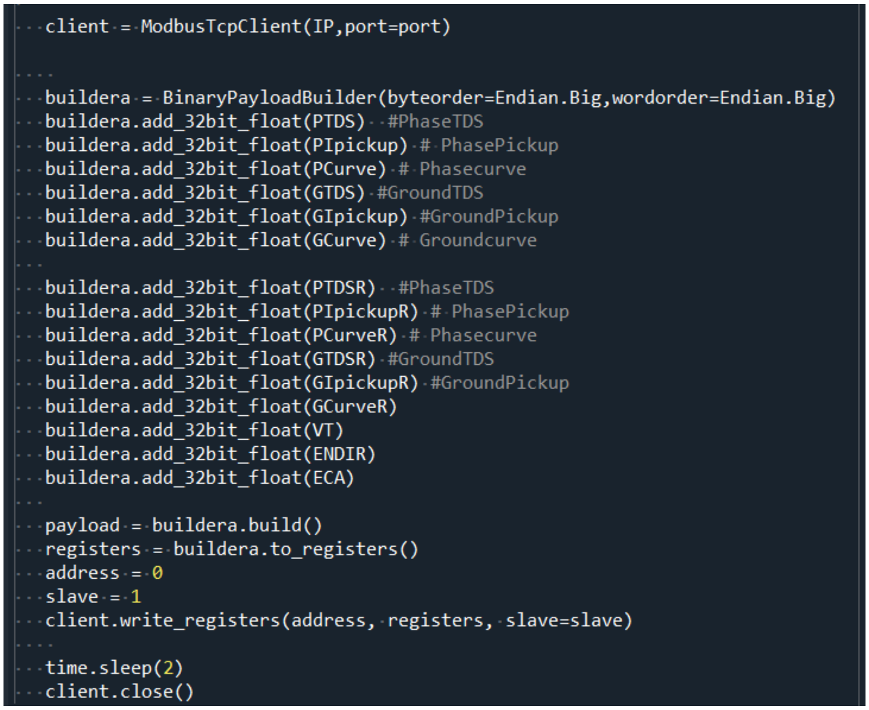

```
    client = ModbusTcpClient(IP,port=port)

    buildera = BinaryPayloadBuilder(byteorder=Endian.Big,wordorder=Endian.Big)
    buildera.add_32bit_float(PTDS)  #PhaseTDS
    buildera.add_32bit_float(PIpickup) # PhasePickup
    buildera.add_32bit_float(PCurve) # Phasecurve
    buildera.add_32bit_float(GTDS) #GroundTDS
    buildera.add_32bit_float(GIpickup) #GroundPickup
    buildera.add_32bit_float(GCurve) # Groundcurve

    buildera.add_32bit_float(PTDSR)  #PhaseTDS
    buildera.add_32bit_float(PIpickupR) # PhasePickup
    buildera.add_32bit_float(PCurveR) # Phasecurve
    buildera.add_32bit_float(GTDSR) #GroundTDS
    buildera.add_32bit_float(GIpickupR) #GroundPickup
    buildera.add_32bit_float(GCurveR)
    buildera.add_32bit_float(VT)
    buildera.add_32bit_float(ENDIR)
    buildera.add_32bit_float(ECA)

    payload = buildera.build()
    registers = buildera.to_registers()
    address = 0
    slave = 1
    client.write_registers(address, registers, slave=slave)

    time.sleep(2)
    client.close()
```

Figure 52. Python script used to write Modbus settings back to the OPAL-RT simulation.

2.7. Hardware-in-the-Loop Demonstration of the Adaptive Protection System

This section details the benefit of using adaptive protection with a use case detailed below.

4. Section 2.7.2 is a use case without adaptive protection, and the need for adaptive protection.
5. Section 2.7.3 is a use case with adaptive protection.
6. Section 2.7.4 is a use case of partial system restoration.
7. Section 2.7.5 is a use case with adaptive protection coordinating with a fuse.

2.7.1. Power System Protection Refresher and the Need for Adaptive Protection

The grid is getting more complicated, with an increasing number of possible states. The conventional protection system lacks the intelligence required to modify the protective responses according to the system conditions. APP is utilized in modern distribution systems with a high penetration of PV, as well as AC and DC microgrids to determine appropriate relay settings in real-time for all devices in the network based on the current system state (switching, grid-connected, generator dispatch, etc.)

2.7.2. Without Adaptive Protection

Radial distribution systems are generally coordinated with inverse time overcurrent curves shifted with delays, as shown in Figure 53.

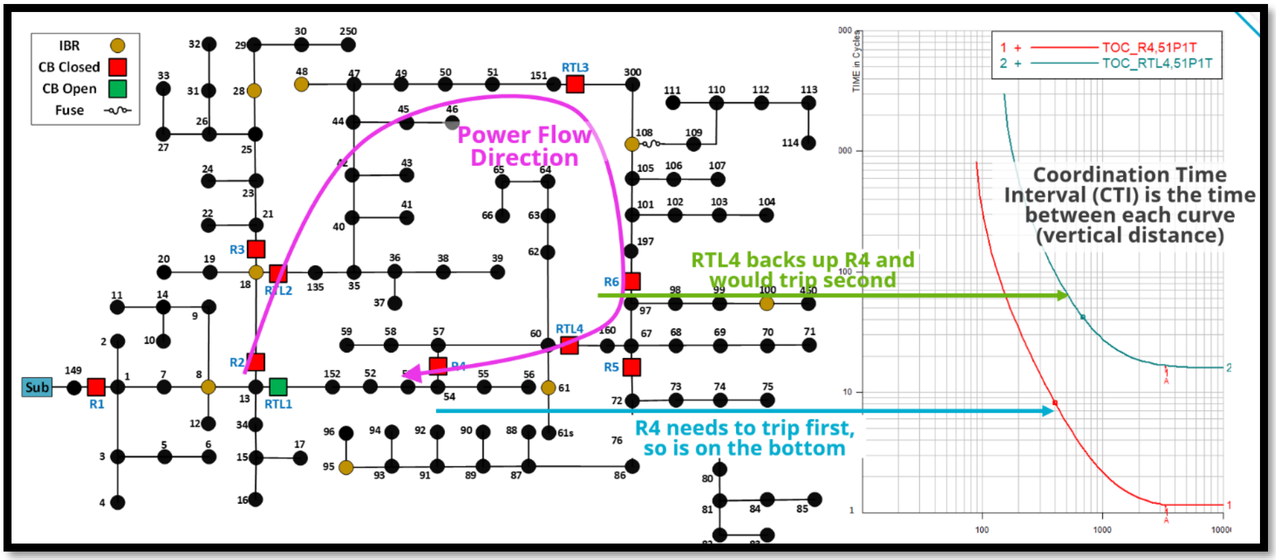

Figure 53. Protection coordination for a radial system

However, without adaptive protection and a system configuration change as shown in Figure 54 below, this results in a change in the power flow direction and the system is now uncoordinated. If a fault is applied to Bus 67, we would expect RTL4 to clear the fault. However R4 operates first, resulting in an unnecessary loss of service as indicated by the greyed-out sections in Figure 54. Figure 55 displays the Grafana dashboard for this scenario and result.

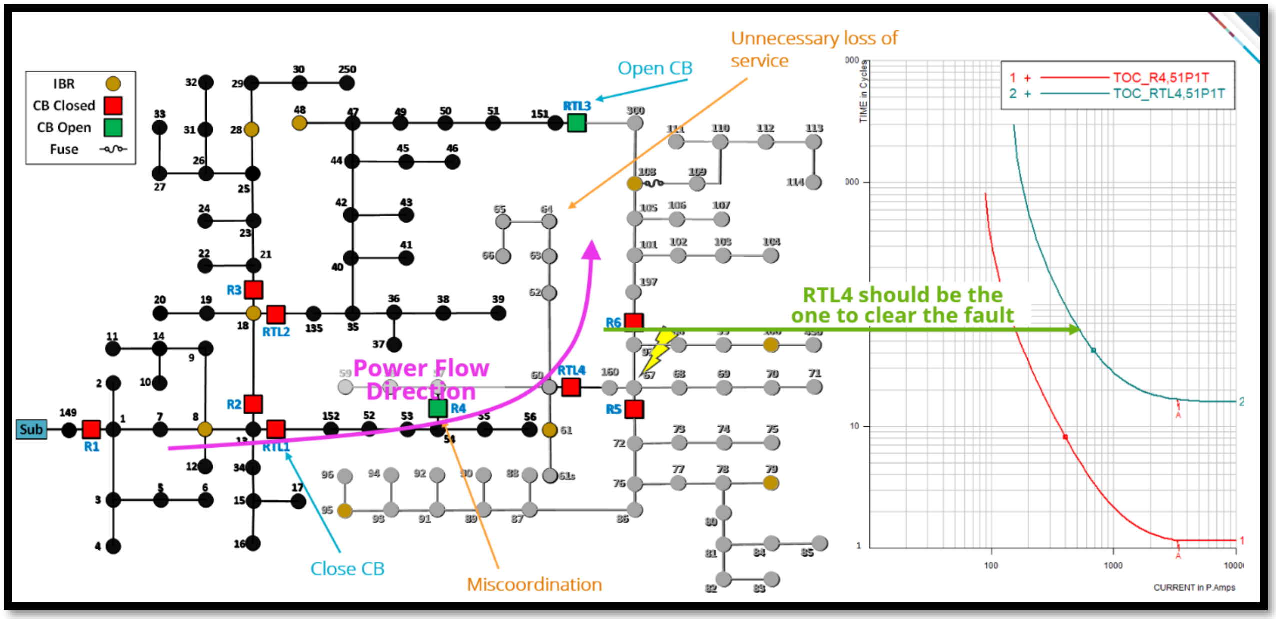

Figure 54. Unnecessary loss of Load.

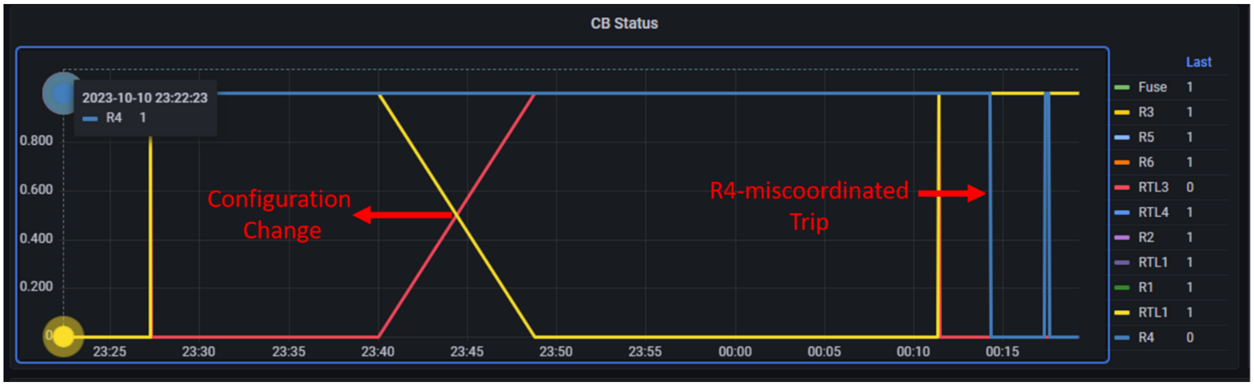

Figure 55. HIL results of scenario 1

2.7.3. *With Adaptive Protection*

The same scenario is rerun with adaptive protection enabled. By using communication to detect system changes (breaker status, DER dispatch), the digital twin model in CAPE is updated in real-time. A fault study is performed for all possible faults in the system. The optimizer determines new optimal protection settings, and sends them to the relays. Relay settings (curve type, time dial, and pickup current) are optimized by minimizing the sum of the relay operating times for all possible faults. Figure 56 and Figure 57 show the resulting feeder configuration with the customers that are now kept in service due to adaptive protection. Figure 58 shows the Grafana dashboards results for scenario 2.

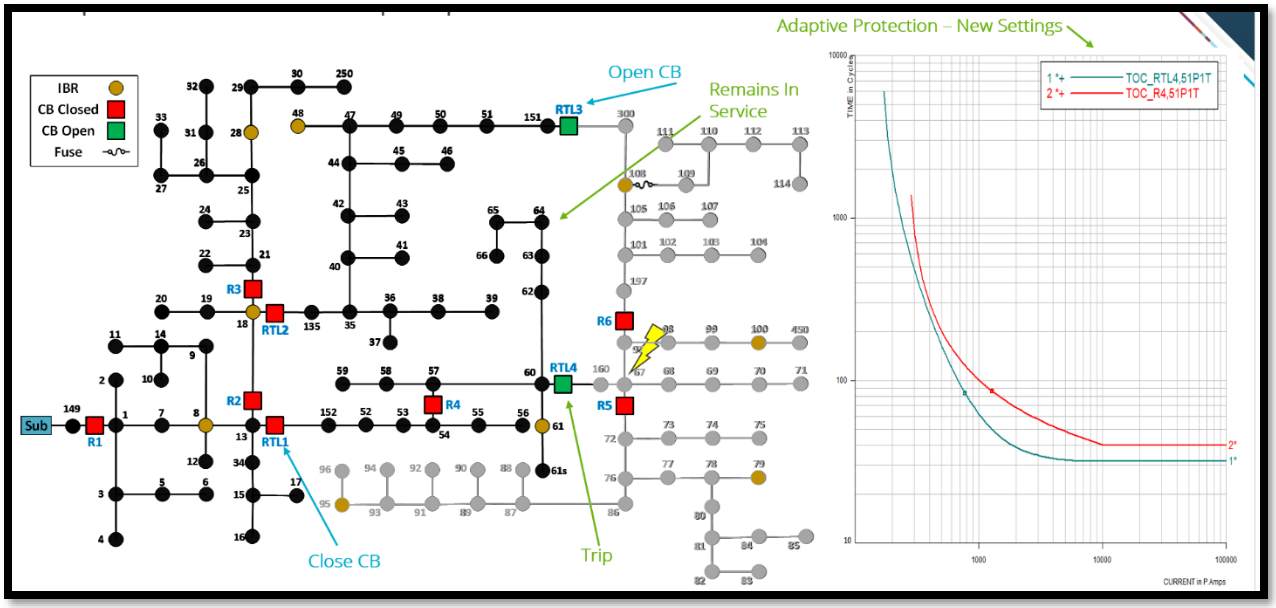

Figure 56. Adaptive Protection limiting the number of customer outages.

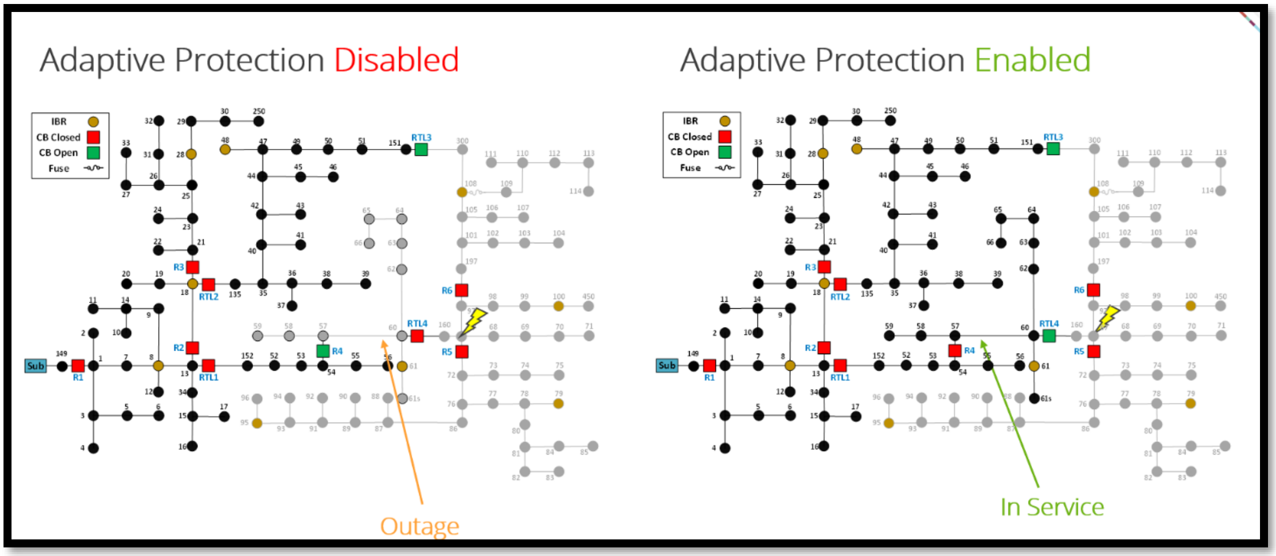

Figure 57. Comparison with and without Adaptive Protection

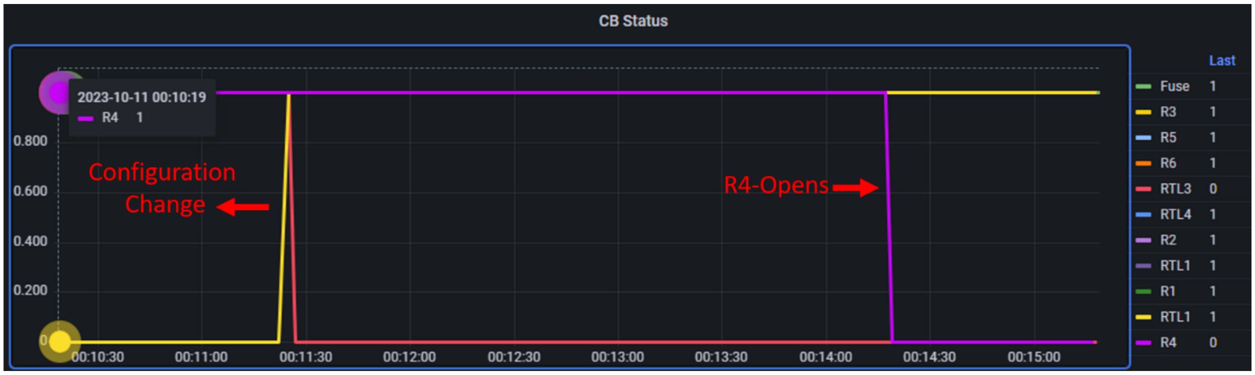

Figure 58. HIL results for scenario 2

2.7.4. Partial System Re-energization.

This use case follows Section 2.7.3, in that a system operator decides to close RTL3 to restore customers between RTL3 and R6. The adaptive protection code detects the system configuration change and generates new optimal systems as shown in Figure 59. Figure 60 displays the Grafana dashboard with RTL4 and R4 settings updated by adaptive protection and the correct coordination result.

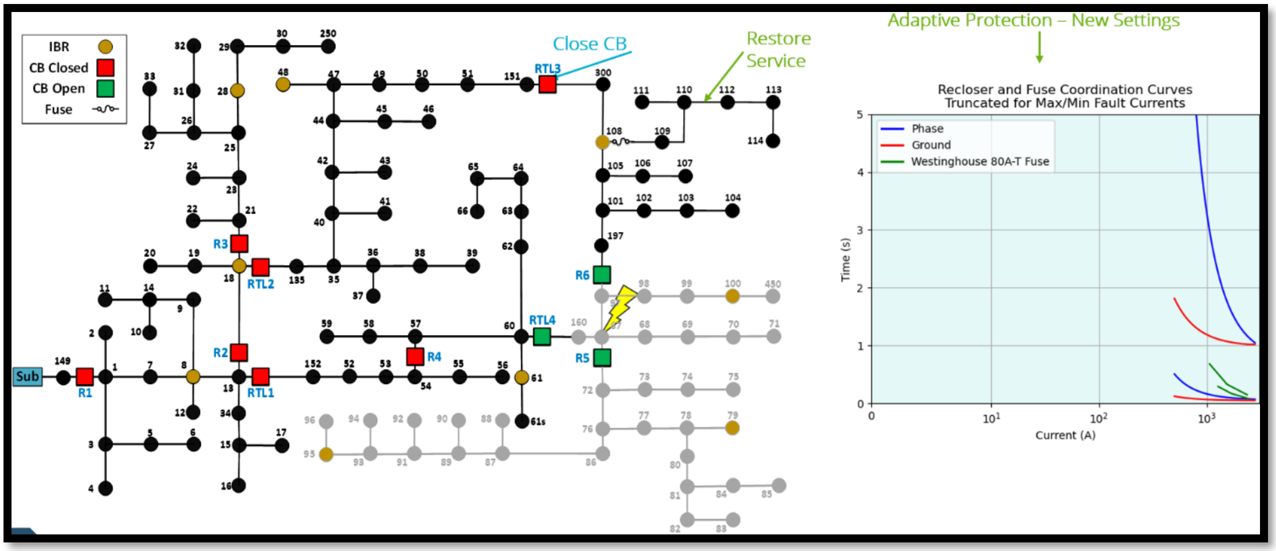

Figure 59. Partial System Restored.

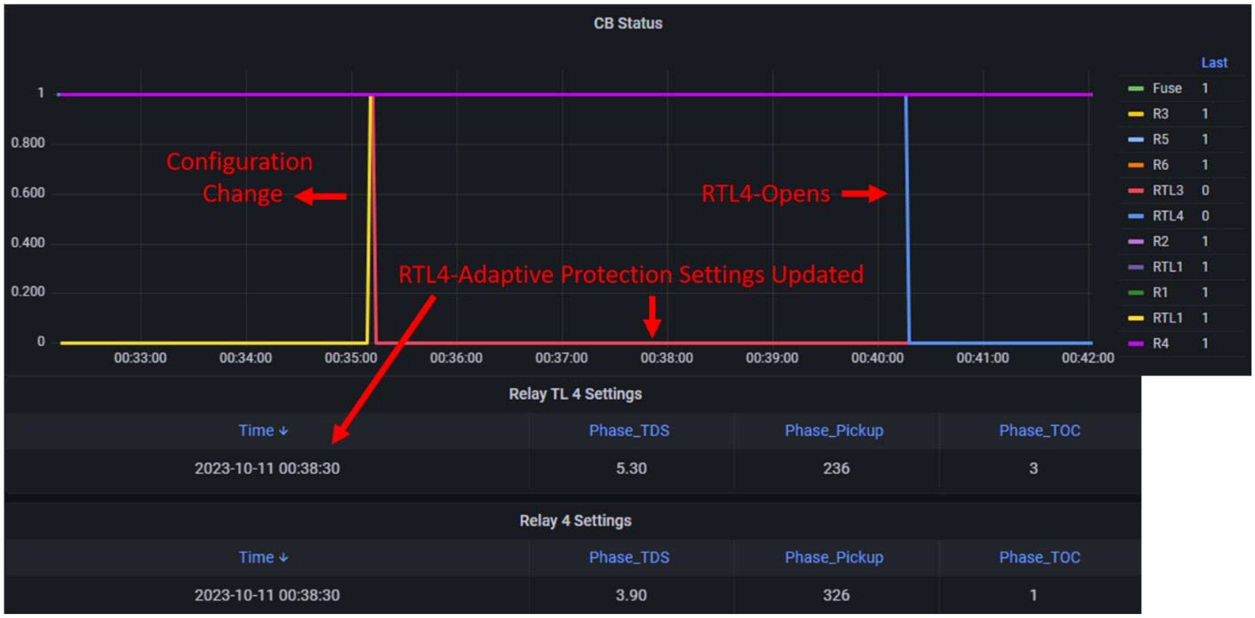

Relay TL 4 Settings

Time ↓	Phase_TDS	Phase_Pickup	Phase_TOC
2023-10-11 00:38:30	5.30	236	3

Relay 4 Settings

Time ↓	Phase_TDS	Phase_Pickup	Phase_TOC
2023-10-11 00:38:30	3.90	326	1

Figure 60. Scenario 3 results

2.7.5. Adaptive Protection coordinating in a Fuse Blowing Scheme.

This use case follows the events of Section 2.7.4. A fault is applied to Bus 114 as shown in Figure 61. RTL3 is a recloser that has fast and slow reclose curves. When the fault is applied to Bus 114, the fast curve of RTL3 operates first to try and clear the fault. However, the fault is still at Bus 114. RTL3 recloses resulting in the fuse at Bus 108 operating to clear the fault from the system. Figure 62 displays the sequence of operations for the result of scenario 4. Figure 63 displays the adaptive protection updates for scenarios two through four.

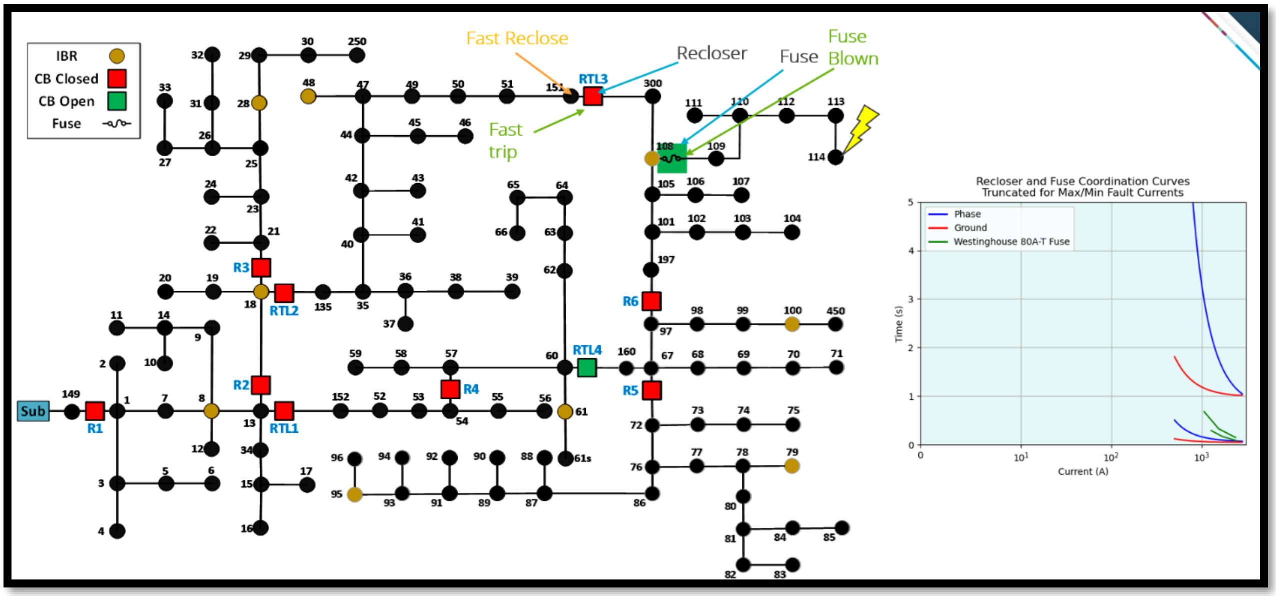

Figure 61. Adaptive Protection coordinating with a fuse.

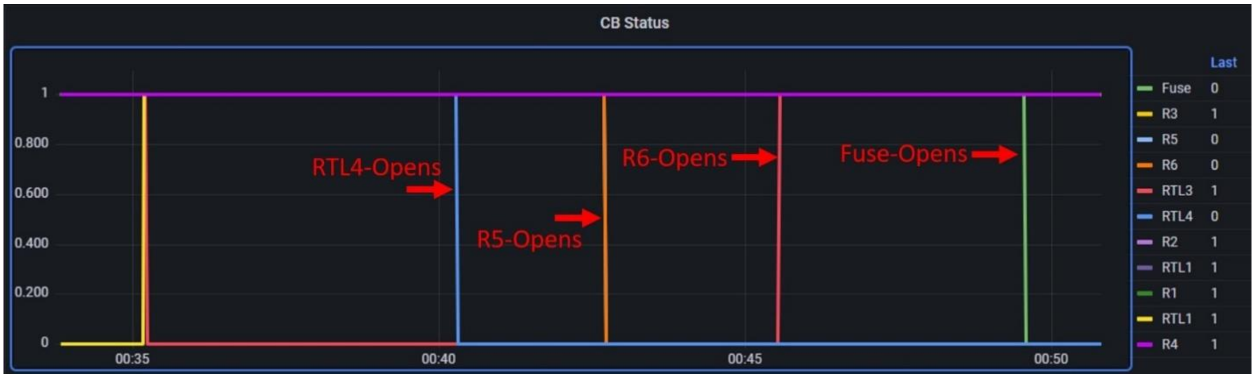

Figure 62 Scenario 4 results

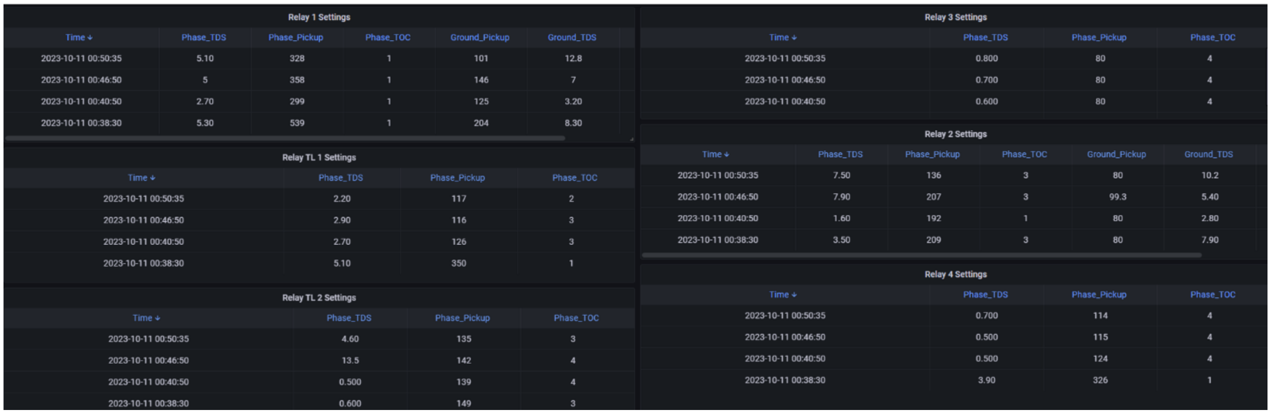

Relay 1 Settings

Time ↓	Phase_TDS	Phase_Pickup	Phase_TOC	Ground_Pickup	Ground_TDS
2023-10-11 00:50:35	5.10	328	1	101	12.8
2023-10-11 00:46:50	5	358	1	146	7
2023-10-11 00:40:50	2.70	299	1	125	3.20
2023-10-11 00:38:30	5.30	539	1	204	8.30

Relay TL 1 Settings

Time ↓	Phase_TDS	Phase_Pickup	Phase_TOC
2023-10-11 00:50:35	2.20	117	2
2023-10-11 00:46:50	2.90	116	3
2023-10-11 00:40:50	2.70	126	3
2023-10-11 00:38:30	5.10	350	1

Relay TL 2 Settings

Time ↓	Phase_TDS	Phase_Pickup	Phase_TOC
2023-10-11 00:50:35	4.60	135	3
2023-10-11 00:46:50	13.5	142	4
2023-10-11 00:40:50	0.500	139	4
2023-10-11 00:38:30	0.600	149	3

Relay 3 Settings

Time ↓	Phase_TDS	Phase_Pickup	Phase_TOC
2023-10-11 00:50:35	0.800	80	4
2023-10-11 00:46:50	0.700	80	4
2023-10-11 00:40:50	0.600	80	4

Relay 2 Settings

Time ↓	Phase_TDS	Phase_Pickup	Phase_TOC	Ground_Pickup	Ground_TDS
2023-10-11 00:50:35	7.50	136	3	80	10.2
2023-10-11 00:46:50	7.90	207	3	99.3	5.40
2023-10-11 00:40:50	1.60	192	1	80	2.80
2023-10-11 00:38:30	3.50	209	3	80	7.90

Relay 4 Settings

Time ↓	Phase_TDS	Phase_Pickup	Phase_TOC
2023-10-11 00:50:35	0.700	114	4
2023-10-11 00:46:50	0.500	115	4
2023-10-11 00:40:50	0.500	124	4
2023-10-11 00:38:30	3.90	326	1

Figure 63. Adaptive Protection updating during Scenario 1-4.

3. COMMUNICATION-FREE ADAPTIVE PROTECTION MODULES

3.1. Learning Protection Settings [18]

While forecasting loads and IBR generation are well presented in the literature, predicting protection settings could not be identified. This section adds to the previous work that used machine learning (ML) algorithms for power system forecasting by providing an analysis focused on the following items:

- Predicting a relay's local TDS settings using the Prophet algorithm.
- Predicting a relay's local I_{PICKUP} settings using the Prophet algorithm.
- A review of the individual relay's predicted protection setting overall coordination.

3.1.1. Learning Protection Settings Methodology

The IEEE 123 feeder was modeled in OpenDSS. A year-long, hourly simulation with varying residential and commercial loads and varying PV profiles was used.

The SNL optimal protection coordination algorithm generates relay settings by formulating the relay coordination problem as an MINLP problem that is solved and optimized using a genetic algorithm (GA) based solver. The protection coordination constraints ensure that there are existing settings for the protection devices such that the primary device trips before its backup. The sum of the primary relay operating times is used as the objective function being minimized by the genetic algorithm. The final output of the optimizer is defined in Table 11 for each relay.

Table 11 Example of Protection Settings Data

Date	TDS	I_{PICKUP}	OT
1/1/17 0:00	0.84	23.82	0.15
1/1/17 1:00	0.68	21.21	0.12

3.1.2. The Prophet Algorithm

The Prophet algorithm, created by Taylor and Letham, models time series as a generalized additive model (GAM) represented by Equation 1.

$$y(t) = g(t) + s(t) + h(t) + e(t) \qquad (1)$$

g(t) represents the trend function that models the non-periodic changes in the value of the times; s(t) represents periodic changes, such as daily, weekly, and year seasonality; h(t) represents the effects of holidays which occur potentially at irregular schedules; ε(t), is an error term for any changes not accommodated by the model. Note that this model is inherently different from time series forecasting models, such as autoregressive forecasting, that predict the value at time t using measurements from t-1. Instead, this formulation is essentially a curve-fitting exercise that provides advantages of not needing regularly spaced data, ability to handle missing data and outliers, and the ability to capture long seasonality trends. Each training point is a separate sample, where time is used as one of the regressors. The Prophet algorithm has several tunable hyperparameters.

3.1.3. Parameters to Predict

Equation 2 is the time overcurrent equation that the relays in this experiment will use. For this paper, we are interested in predicting the TDS and IPICKUP from equation 2 for each relay. The variables A, B, and p relate to the curve type, which for each relay is set to an inverse (U2) type, and the variable I is the measured rms current on the secondary side of the relay. The variable OT is the final operating time of the relay. The TDS value can range from 0.25 to 15, while the IPICKUP values range in the hundreds of amperes. In Table 11, the columns in green indicate settings and operating time that the SNL Optimizer calculated from the local rms current and voltage relay measurements.

$$OT = TDS * \frac{A}{\left(\frac{I}{I_{PICKUP}}\right)^{P} - 1} + \mathrm{B} \qquad (2)$$

3.1.4. Prediction Analysis

The prediction of protection setting TDS and IPICKUP focused on the potential of the Prophet algorithm's accuracy and precision. This prediction method considered the time-series dependencies of the data. Since the adaptive protection settings are dependent on the load in the feeder and the PV power output, the prediction method must incorporate the diurnal PV power shape as well as the seasonal and weekly load variations. The simulation generated 8,360 data points for each relay. The first step involved splitting the dataset into a training set that contained 7,824 data points and a testing set that contained 936 data points. The final analysis shows the results for the testing data.

3.1.5. Results for Local Parameter Prediction

Two different prediction models were made for each relay. The model that was designed to predict the TDS setting of each relay used the regressors OT and the rms phase voltages, and the model that was designed to predict the IPICKUP setting of each relay used the regressors rms phase currents. The added regressors were used to predict the same timestep for the TDS and IPICKUP settings. The training set included the first 7,824 points of data indicated by values to the left of the purple vertical line in Figure 64. For the last part of the year, it is assumed that communication is lost, and the settings are predicted for each time point using the trained Prophet algorithm with the time and other regressors (e.g., rms phase voltages) as inputs. In this scenario, it is assumed that each relay still has access to its local measurements (such as voltage and current) to use as inputs to estimate the correct settings locally for that relay. Each model was evaluated on predicting the remaining 936 data points, the test set length, and compared to the actual values of that set. Table 12 presents the final models' mean absolute percent error (MAPE) and root mean squared error (RMSE) metric results for predicting and comparing to the testing data. The results only considered the prediction metrics for the test data set.

Table 12. Accuracy of the Prophet algorithm for Predicting Settings through time

	MAPE %		RMSE	
	TDS	I_{PICKUP}	TDS	I_{PICKUP}
R1	3.216	0.041	0.320	0.127
R2	8.038	0.004	0.721	0.013
R3	0.427	0.040	0.007	0.019
R4	0.469	0.021	0.005	0.005
R5	16.810	0.033	0.150	0.049

R6	12.459	0.034	0.505	0.064
RTL2	3.647	0.049	0.347	0.141
RTL3	5.290	0.031	0.410	0.057
RTL4	0.702	0.094	0.026	0.052

The MAPE metric for all but three relays were less than 5%. Relays 2, 5, and 6 had the least good predictions for the TDS setting in Table 12. For example, relay 6 has a MAPE metric of 12.46% that signifies the average deviation from the actual TDS value that the optimizer calculated over the testing period, from 2017-11-22 00:00:00 to 2017-12-31 23:00:00, that included 936-time points, was 84.54% accurate. However, the best prediction when using the MAPE metric was relay 3, which was 99.57 % accurate over the same period. Note that the MAPE for the TDS predictions was higher than the MAPE for the I_{PICKUP}. This is partially due to the fact that the TDS are generally smaller numbers (less than 15), so the percent error metrics are higher than for I_{PICKUP}.

The RMSE metric provides a different evaluation of the TDS prediction. Relays 2, 6, and tie line 3 had the highest RMSE values. For example, relay 2 with the highest RMSE value of 0.721, means that on average the prediction values were 0.721 values away from the actual value. Figure 64 shows the predicted values plotted against the actual TDS setting for relay 2. The implication in the TDS predicted settings will be explored in the next section.

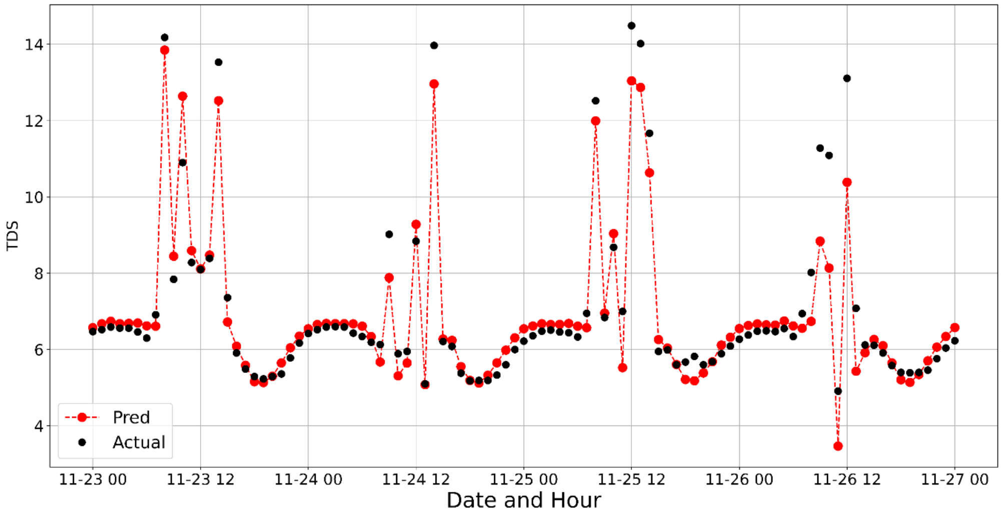

Figure 64. Relay 2 Comparison Between Predicted and Actual TDS Values.

The MAPE metric for predicting the I_{PICKUP} is significantly better than the prediction for TDS as shown in Table 12. For example, all relays have a MAPE metric well below 1%. This means that the prediction of I_{PICKUP} for each relay was ~99.9% accurate with this metric. Figure 65 shows the prediction results for the I_{PICKUP} setting for relay 6. The RMSE metric provides a similar positive evaluation of the I_{PICKUP} prediction. The I_{PICKUP} setting for each relay is generally in the hundreds of amperes and the RMSE values for each prediction is in the tenths of amperes. This would not affect the response of the relay for the I_{PICKUP} setting in a relay.

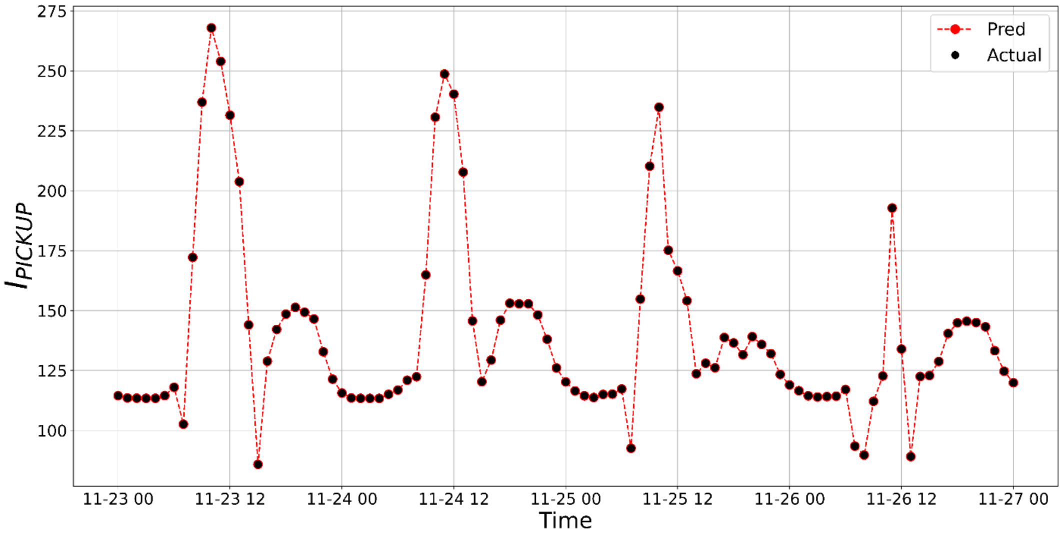

Figure 65. Relay 6 Comparison Between Predicted and Actual IPickup Settings.

If one or more relays' communication to the centralized adaptive protection algorithm is interrupted either unintentionally (weather-related or equipment failure) or maliciously (cyber-attacks) for an extended period, the protection scheme may not operate with the speed and selectivity intended during that period. It is assumed that communication has been lost and the CTI for relays 1, 2, 3, and tie line 2 are plotted for the predicted, optimizer, and static protection settings.

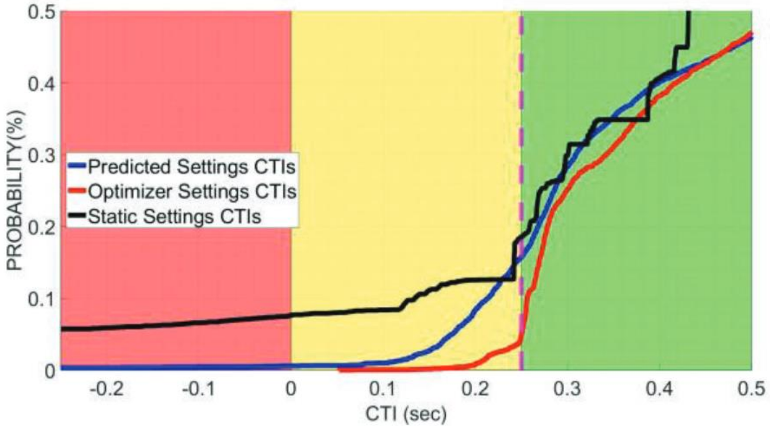

Figure 66. Comparison pf CTIs for different Protection Settings.

The vertical dashed purple line represents a CTI value of 0.25 seconds. The green zone in Figure 66 to the right of the CTI value 0.25 indicated that the protection is coordinated for relays 1, 2, 3, and tie line 3. The yellow zone, between a CTI of 0 and 0.25, indicates that there is a CTI violation, but the system is still coordinated. The red zone indicates that the protection is mis-coordinated. The static settings CTI curve is utilized if the protection does not have the ability to change settings.

Table 13 presents a summarization of the CTI by method and region from Figure 66. Using the Prophet algorithm reduced the number of miscoordinations by 92.5% to 19%, rather than defaulting to a static protection setting.

Table 13. Number of CTI Values By Region

Region	Predicted	Optimizer	Static
Red	19	0	254
Yellow	504	157	365
Green	2,817	3,183	2,721

3.2. Zonal Setting-less Protection LAMP

Adaptive protection is defined as a real-time system that can modify the protective actions according to the changes in the system condition. An adaptive protection system (APS) is conventionally coordinated through a central management system located at the distribution system substation. An APS depends significantly on the communication infrastructure to monitor the latest status of the electric power grid and send appropriate settings to all of the protection relays existing in the grid. This makes an APS highly vulnerable to communication system failures (e.g., broken communication links due to natural disasters as well as wide-range cyber-attacks). To this end, this section presents the addition of LAMP units to the protection system to guarantee its reliable operation under extreme events when the operation of the APS is compromised. LAMP units operate in parallel with the conventional APS. As a backup, if APS fails to operate because of an issue in the communication system, LAMP units can accommodate reliable fault detection and location on behalf of the protection relay. The performance of the proposed APS is verified using IEEE 123 node test system [19].

3.2.1. Local Adaptive Modular Protection Methodology

Each LAMP unit is installed in parallel with the conventional protection relay used in APS. LAMP will operate all of the time and provide redundancy for the adaptive protection of distribution systems (DS). In particular, if the communication system is outaged, the conventional APS will be ineffective, and LAMP can effectively detect and isolate faults. Figure 67(a) shows the location of each LAMP unit in the system. As shown, LAMP will utilize the local current and voltage transformers and can send a trip command to the local circuit breaker.

To show the proposed LAMP functionality, a portion of IEEE 123 bus system shown in Figure 67(b) is considered. Also, we have utilized PSS®CAPE software to simulate fault scenarios. As mentioned earlier, LAMP units can accommodate setting-less protection for the system. Each LAMP unit is associated with an operating region. For example, in Figure 67(b), LAMP R1 region includes all the lines/cables and buses between Bus 149 (as the start bus) and Bus 13 (as the end bus), at which the forward LAMP R2 is located. Each LAMP is expected to provide (i) primary protection for its own region and (ii) backup protection for the LAMP units in front of it. To accommodate a well-coordinated LAMP operation, this approach proposes to utilize two protection zones for each LAMP unit. For the protection Zone 1, the LAMP unit operates instantaneously while, for Zone 2, the LAMP unit operates with some delay to guarantee an acceptable CTI margin with the LAMP units in front of it. This delay depends on the utility practice. In this approach, we have assumed a delay of 0.2 sec for the backup protection. As an example, the protection zones for R1 and R2 are shown in Figure 67.b. To avoid the mis-operation of LAMP units for the faults occurring in the neighboring LAMPs' regions, this approach proposes to include the branches connected to the remote bus of the LAMP region in the protection Zone 2. By doing so, one can ensure that LAMP units are well-coordinated and they avoid instantaneous operation for faults on neighboring lines/cables. The LAMP architecture is shown in Figure 68. As illustrated in Figure 68, LAMPs are expected to (i) detect circuit topology, (ii) identify the fault type (e.g., 3-phase to ground, phase-to-phase, and bolted and resistive single phase and double phase to ground faults), and (iii) identify if the fault is within their primary or backup zones. The circuit topology estimation is performed using pre-fault data. In fact, LAMPs keep monitoring the circuit topology during system normal conditions. So, once a fault occurs, a LAMP is already aware of the circuit topology. To perform the classification of fault types and fault zones, a support vector machine (SVM) classifier is utilized. SVM is a memory efficient classification approach that can classify the inputs with a very high accuracy. Once the fault type is identified, the zone classification is performed for that specific fault type.

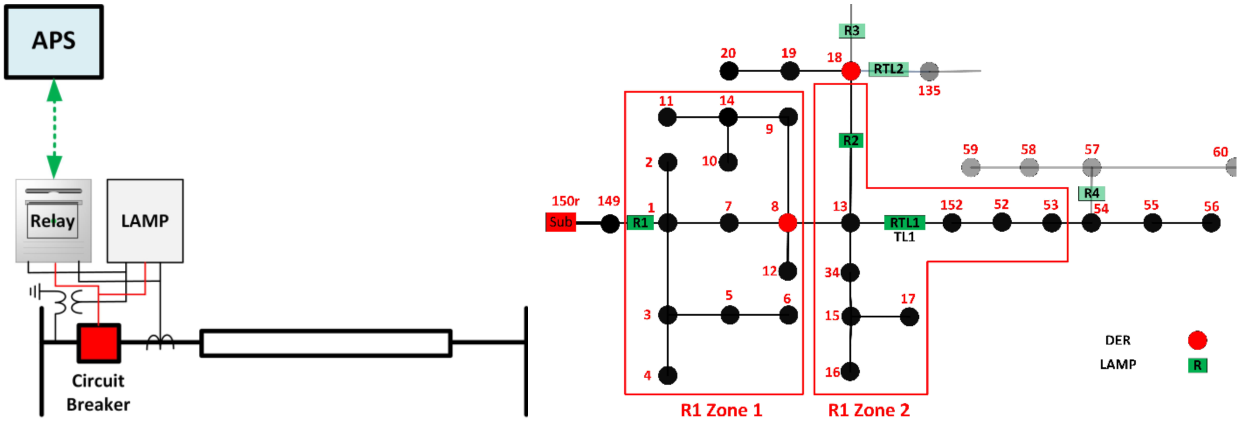

(a) (b)

Figure 67. (a) LAMP in a DS; (b) LAMP protection zones.

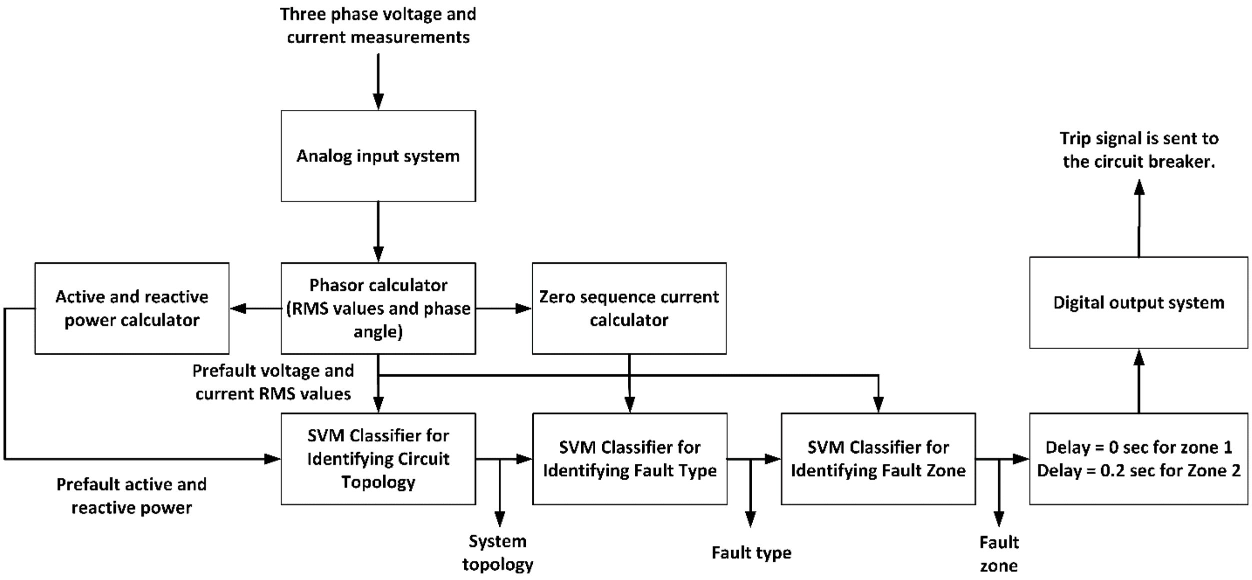

Figure 68. LAMP architecture.

3.2.1.1. Training Procedure

The proposed local adaptive protection approach includes three main classifiers: circuit topology estimator, fault type classifier, and fault zone classifier. The training procedure for each of these classifiers is provided as follows:

3.2.1.2. Circuit Topology Estimator

The circuit topology estimation is performed during the normal operating condition of system using SVM. The input to the SVM classifier includes the prefault three phase voltage and current root-mean-square (RMS) values and active and reactive power measured at the LAMP location. The topology of DS refers to the arrangement of physical devices like lines, cables, tie breakers. However, the change of circuit topology can significantly change the DS measurements (e.g., active and reactive power flow or current and voltage measured at different locations of the system). In fact, the changes observed in these measurements can be used as a local way of detecting the circuit topology. The training and testing data for the circuit topology estimator are gathered by simulating the IEEE 123 node test system in OpenDSS. In order to train the SVM classifier, different circuit topologies of DS are simulated using variable load and IBR profiles for a period of one year assuming a system normal condition. The training dataset is selected out of this simulated data. By doing so, one can ensure that the impact of seasons on the load and generation profiles are accounted for.

3.2.1.3. Fault Type Classifier

The fault type classifier utilizes another SVM to identify fault type (i.e., three-phase to ground, single line to ground, etc.) based on the locally measured three phase voltage and current RMS values, as well as the zero-sequence current. The RMS values of postfault current and voltages and zero sequence current measurement are the ones used in conventional digital relays for fault detection. This approach aims to utilize similar quantities in our algorithms to make it more practical and easier to implement. To train the SVM classifier, different types of faults are required to be simulated at different locations along each line segment within the operating zones of each LAMP unit. A line segment denotes a branch connecting two nodes of the system. The simulated faults include bolted and resistive ground faults. Faults are applied at every 5% of the line segments' length. Out of the simulated fault scenarios, 60% of them are randomly selected for training and the rest are used for testing the SVM classifier.

3.2.1.4. Fault Zone Classifier

The fault zone classification is performed after the fault type is detected. For each fault type, the simulated fault scenarios at different locations along each line segment are used to train the machine learning classifier. The data is labeled as Zone 1 and Zone 2 based on the location of fault. Similar to the fault type classifier, the locally measured three phase voltage and current RMS values, as well as the zero-sequence current are used as the inputs to the fault zone SVM classifier. As with the fault type classifier, this approach simulates faults at every 5% of the line segments in PSS®CAPE and randomly selects 60% of simulated data for training.

3.2.1.5. LAMP's Response Time and Cost

The major portion of LAMP unit response time will include the time to calculate the RMS value of the measurements (three-phase voltage and current). This usually requires around half a cycle (8 ms in a 60 Hz system). The response time of the machine learning algorithms depends on the microprocessor used for LAMP implementation. In our proposed approach, the topology estimation is performed during system normal condition. After the fault occurs, the SVM classifier for fault type identification first runs, and then the SVM for fault zone detection is deployed. It should be noted that each LAMP unit can be implemented on a microprocessor. The implementation cost of the proposed approach will be only limited to the cost microprocessors hosting LAMP units. Each LAMP unit can utilize the existing current and voltage transformers for current and voltage measurements.

3.2.2. Simulation Results

To verify the effectiveness of LAMP modules, the IEEE 123 node test system (Figure 69) is slightly modified by adding tie lines, IBRs, and LAMP units. The modifications on the original test system are as follows:

Four tie lines are included in the test system to accommodate four different circuit topologies; We assume that in each configuration, at least one of the tie lines is open to avoid a loop in the circuit. The four circuit configurations are listed in Table 14. Nine IBRs are added to the original test system to simulate a distribution system with high penetration of IBRs. The specifications and ratings of these IBRs are provided in Table 15. This table includes the inverters' DC and AC ratings, types, and maximum fault current contribution. It is assumed that the inverter's maximum fault current contribution is equal to 140% of the inverter's current rating. Ten LAMP units are located on the different cables of the circuit. Out of the ten LAMP units, four of them are located on the tie lines. In all configurations, only nine LAMP units are operational as one tile line is always out of service.

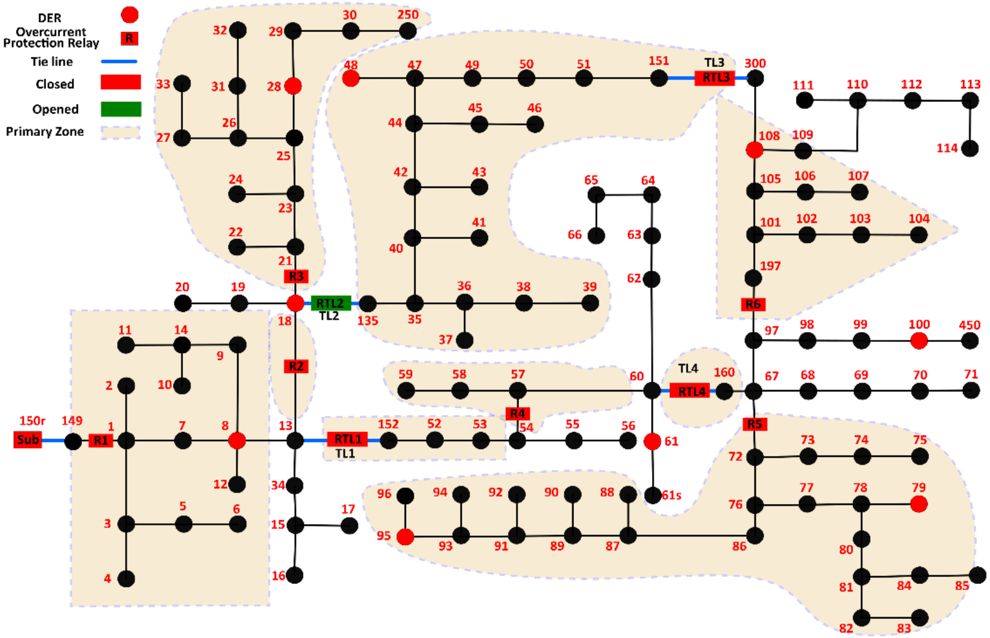

Figure 69. Modified IEEE 123 node system that shows the LAMPs' locations and the boundary of their Zone 1 in the Configuration 1.

Table 14. List of circuit configurations.

Configuration	TL1	TL2	TL3	TL4
Configuration 1	Close	Open	Close	Close
Configuration 2	Close	Close	Open	Close
Configuration 3	Close	Close	Close	Open
Configuration 4	Open	Close	Close	Close

Table 15. IBRs' specifications.

Bus Number	8	18	28	48	61	79	95	100	108
IBR's AC Rating (kVA)	500	700	500	1000	500	500	1000	500	500
IBR's DC Rating (kW)	600	840	600	1200	600	600	1200	600	600
Maximum Fault Current (A) at 4.16 kV	97.15	136	97.15	194.3	97.15	97.15	194.3	97.15	97.15

3.2.2.1. LAMP Zones for all Four Configurations:

We have performed the proposed zonal machine learning protection on IEEE 123 node system. The simulation results consider four different circuit topologies which are shown in Figure 69 to Figure 72. In these figures, the Zone 1 of all LAMPs is only highlighted. It should be noted that Zone 2 of each LAMP unit includes the branches and nodes of its region that are not included in Zone 1, and the whole Zone 1 of the LAMPs is in front of it. As seen in these figures, the change of circuit configuration only has an impact on the zone definition of LAMPs R4, R6, RTL3, and RTL4. For other LAMP units, the change of circuit topology does not have any impact on their Zone 1 boundaries. Moreover, for the LAMP units that are located at the end of the feeder and don't see any other LAMPs in front of them, only one zone is defined (e.g., R3, R5, and RTL3 in Configuration 1).

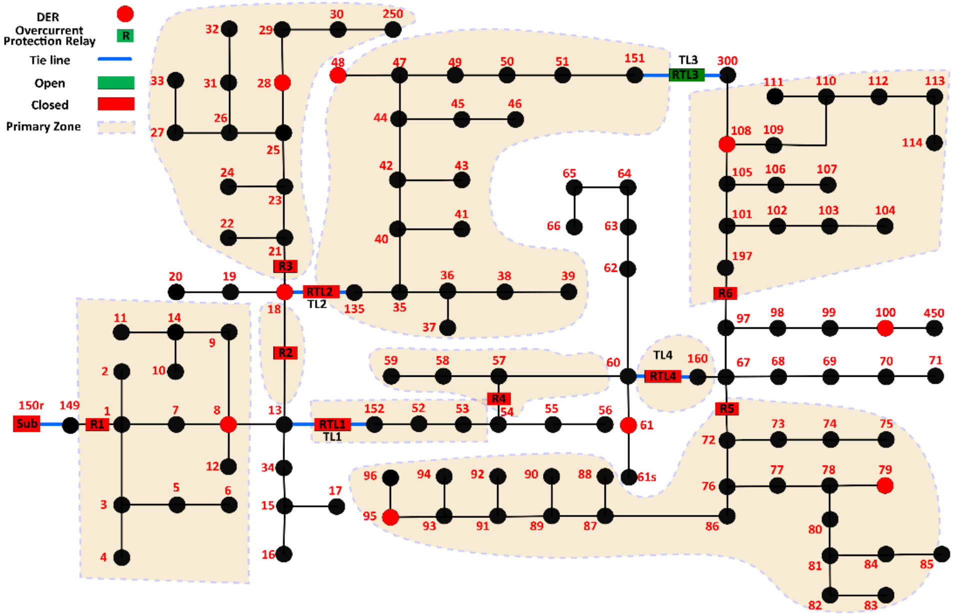

Figure 70. LAMPs' locations and the boundary of their Zone 1 in the Configuration 2.

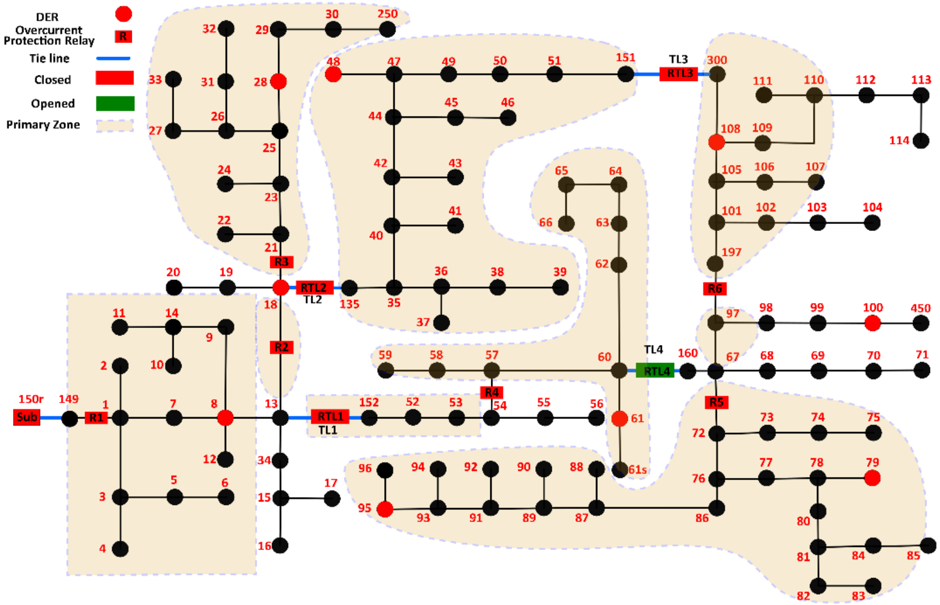

Figure 71. LAMPs' locations and the boundary of their Zone 1 in the Configuration 3.

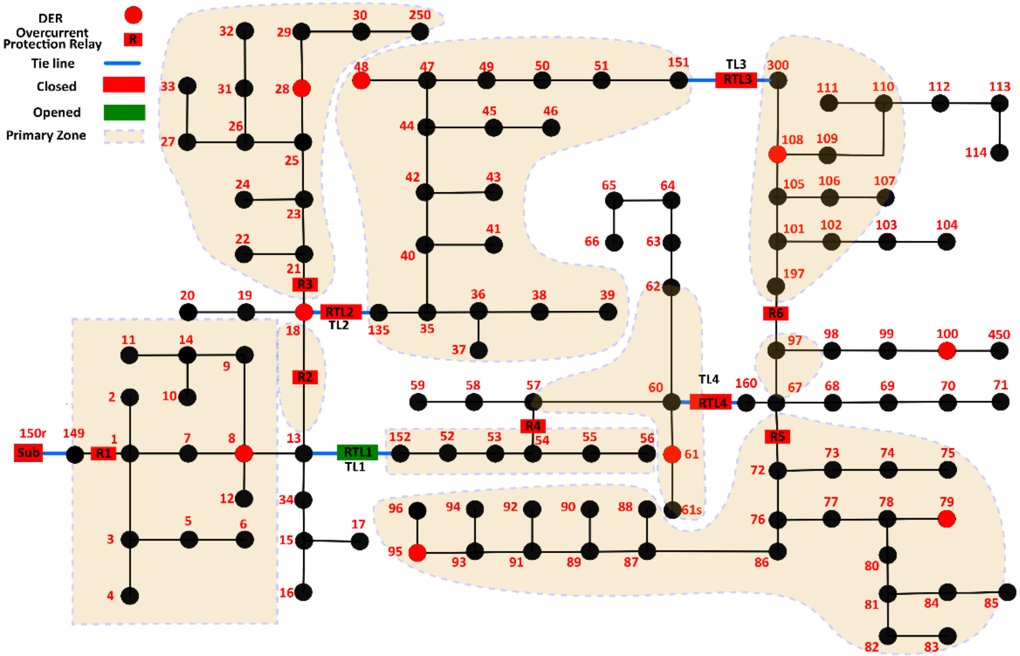

Figure 72. LAMP locations and the boundary of their Zone 1 in the Configuration 4.

3.2.2.2. Circuit Topology Estimation Results:

Each LAMP unit utilizes the normal operating condition (prefault) data to estimate the prevailing circuit topology of the system. In this report, the prefault voltage, current, active power, and reactive power measurements at the LAMP location are utilized as the inputs to the SVM to estimate the corresponding circuit topology. The data includes measurements for all four configurations. Data collected on even weeks is used for training, and data collected on odd weeks is used for testing. The training data are further downsampled to have only hourly data, i.e., only 19% of data is utilized for training using a function in *sklearn*. For four configurations, four different class labels are generated by SVM. The SVM classifier uses a linear Kernel function and parameter *C* that is equal to 0.12. It should be noted that the circuit topology estimation is only performed for LAMPs R4, R6, RTL3, and RTL4. The reason is that the change of circuit topology only has an impact on the zone definition of these LAMP units. This means that other LAMP units are not required to alter their zones definition if the circuit topology changes. The accuracy of the circuit topology estimation results is provided in Table 16.

Table 16. Circuit topology estimation accuracy at different LAMP units.

LAMP	Accuracy(%)
R4	99.9947
R6	99.9981
RTL3	99.9876
RTL4	100.0

3.2.2.3. Fault Type Classification Results:

Based on the prevailing circuit topology, the LAMP will identify fault type once a fault occurs. In PSS®CAPE software, seven different types of faults including three-phase to ground (TPH), single line to ground (SLG_A, SLG_B, SLG_C), and double line to ground (DLG_AB, DLG_AC, DLG_BC) are simulated at different locations (every 5% of each line segment) within the operating regions of LAMP units. A line segment denotes a branch connecting two nodes of the system. For example, in , the line segments for LAMP R1's Zone 1 include (1,2), (1,3), (3,4), (3,5), (3,6), (1,7), (7,8), (8,12), (8,9), (9,14), (14,10), (14,11) branches. On each line segment, faults are applied on its two terminal nodes as well as at 5%, 10%, ..., 90%, and 95% of the line segment length. Out of the simulated fault scenarios, 60% of them are used for training and the rest are used for testing. The simulated faults also include bolted and resistive ground faults. The fault resistance is equal to 1 Ω. The inputs to the fault type classifier are the three phase voltage and current RMS values, as well as the zero sequence current measured at the location of LAMP unit. The SVM classifier uses a linear Kernel function and parameter *C* is equal to 0.12. The fault type classification results render 100% accuracy for all LAMP units. The fault type classification results for LAMP R1 are provided in Figure 73. The high accuracy of SVM algorithm using the testing dataset shows that the algorithm is not overfitting.

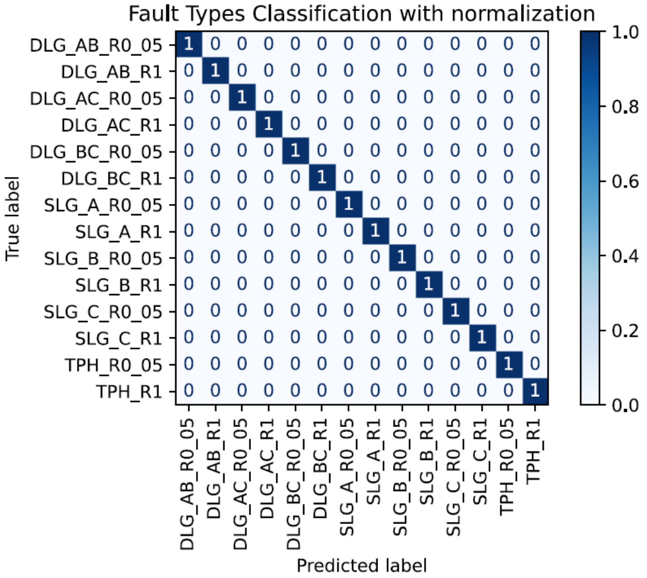

	DLG_AB_R0_05	DLG_AB_R1	DLG_AC_R0_05	DLG_AC_R1	DLG_BC_R0_05	DLG_BC_R1	SLG_A_R0_05	SLG_A_R1	SLG_B_R0_05	SLG_B_R1	SLG_C_R0_05	SLG_C_R1	TPH_R0_05	TPH_R1
DLG_AB_R0_05	1	0	0	0	0	0	0	0	0	0	0	0	0	0
DLG_AB_R1	0	1	0	0	0	0	0	0	0	0	0	0	0	0
DLG_AC_R0_05	0	0	1	0	0	0	0	0	0	0	0	0	0	0
DLG_AC_R1	0	0	0	1	0	0	0	0	0	0	0	0	0	0
DLG_BC_R0_05	0	0	0	0	1	0	0	0	0	0	0	0	0	0
DLG_BC_R1	0	0	0	0	0	1	0	0	0	0	0	0	0	0
SLG_A_R0_05	0	0	0	0	0	0	1	0	0	0	0	0	0	0
SLG_A_R1	0	0	0	0	0	0	0	1	0	0	0	0	0	0
SLG_B_R0_05	0	0	0	0	0	0	0	0	1	0	0	0	0	0
SLG_B_R1	0	0	0	0	0	0	0	0	0	1	0	0	0	0
SLG_C_R0_05	0	0	0	0	0	0	0	0	0	0	1	0	0	0
SLG_C_R1	0	0	0	0	0	0	0	0	0	0	0	1	0	0
TPH_R0_05	0	0	0	0	0	0	0	0	0	0	0	0	1	0
TPH_R1	0	0	0	0	0	0	0	0	0	0	0	0	0	1

Figure 73. Fault type classification results for LAMP R1.

3.2.2.4. Zone Classification Results:

Once the fault type is identified at the LAMP unit, zone classification is performed. The inputs to the zone classifier are the three phase voltage and current RMS values, as well as the zero sequence current measured at the location of LAMP unit. For each of the fault types, the data used to train a machine learning classifier are labeled as Zone 1 and Zone 2. The simulation results utilized for training and testing of the classifier include the faults applied at every 5% of each line segment within Zone 1 and Zone 2 of each LAMP unit. Out of the simulated fault scenarios, 60% of them are used for training and the rest are used for testing. These fault studies are performed on the modified IEEE 123 node system simulated in PSS®CAPE. The SVM classifier uses a linear Kernel function and parameter *C* is equal to 0.12. The zone classification results for all four configurations are provided in Table 17 to Table 20. The zone classification results are only provided for the LAMPs that accommodate both Zone 1 and Zone 2.

Table 17. Zone classification accuracy at different LAMP units in Configuration 1.

LAMP	Average Accuracy(%)
R1	99.7354
R2	100
R4	100
R6	99.3752
RTL1	100
RTL4	96.1039

Table 18. Zone classification accuracy at different LAMP units in Configuration 2.

LAMP	Average Accuracy(%)
R1	100
R2	100
R4	100
RTL1	100
RTL4	96.10

Table 19. Zone classification accuracy at different LAMP units in Configuration 3.

LAMP	Average Accuracy(%)
R1	99.9107
R2	100
R6	95.7741
RTL1	95.3202
RTL2	100
RTL3	98.9766

Table 20. Zone classification accuracy at different LAMP units in Configuration 4.

LAMP	Average Accuracy(%)
R1	99.9107
R2	100
R6	96.1277
RTL2	100
RTL3	99.0316
RTL4	100

3.2.3. HIL Verification of LAMP:

We implemented the zonal machine learning protection technique into a Raspberry Pi microprocessor. In this approach, LAMPs are expected to (i) identify the fault type (e.g., 3-phase to ground, phase-to-phase, and bolted and resistive single phase and double phase to ground faults) and (ii) identify if the fault is within their primary and backup zones.

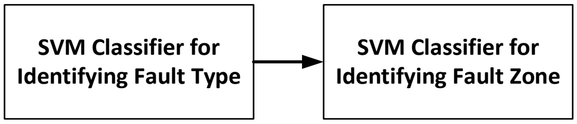

Figure 74. Zonal setting-less machine leaning protection sequence of actions.

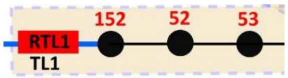

Figure 75. RTL1's Zone 1 boundary.

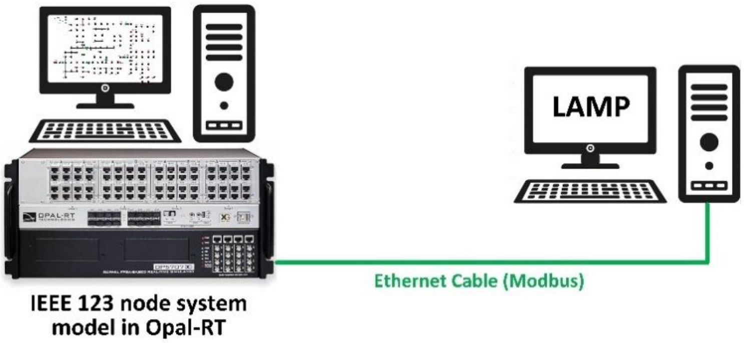

Figure 76. HIL testbed block diagram for circuit topology estimation and non-supervised fault detection algorithms.

To perform the classification of fault types and fault zones, SVM classifier is utilized. Once the fault type is identified, the zone classification is performed for that specific fault type. We have gathered the training and testing datasets for different types of faults at different locations of branches of the IEEE 123 node system. For RTL1 in the IEEE 123 node system, we implemented the SVM classifiers for fault type and fault zone identification on a Raspberry Pi microprocessor. The utilized Raspberry Pi has a BCM2835 central processing unit (CPU) with Raspbian GNU/Linux 10 operating system. On this Raspberry Pi, each of the SVM classifiers for fault type and zone detection takes around 1 to 1.5 ms to return the results, respectively. This means that after the fault happens and RMS values of measurements are calculated, it will take around 2 to 3 ms to detect fault type and fault zone in the LAMP unit. We have modeled the IEEE 123 node system with nine IBRs in Matlab/Simulink. RT-Lab is utilized to run the Matlab/Simulink model in real time on our existing Opal-RT 5707xg simulator at the University of New Mexico (UNM). The simulation is performed for the IEEE 123 node system when RTL2 is open, and all the other tie switches are closed. As discussed earlier, our zonal machine learning protection algorithms for RTL1 are implemented on a Raspberry Pi. LAMP at RTL1 receives voltage and current information from Opal-RT using MODBUS communication protocol. Opal-RT is made MODBUS slave (or server) and LAMP will be master (or client). Data refreshing time is put at 2 ms in both master and slave devices. These RTL1's classifiers are trained using V_a, V_b, V_c, I_a, I_b, I_c, I_0 generated from CAPE. During CAPE data generation, along with voltage and current values, fault type and zone information is also collected. The classifiers had 100% accuracy of classification for both fault type and zone. LAMP RTL1's Zone 1 and 2 boundaries are shown in Figure 75. We have simulated a SLG fault on Bus 53 that is applied at 25.007 s. As seen in Figure 77, LAMP RTL1 is able to detect this fault and the trip signal is received in Opal-RT after around 28 ms.

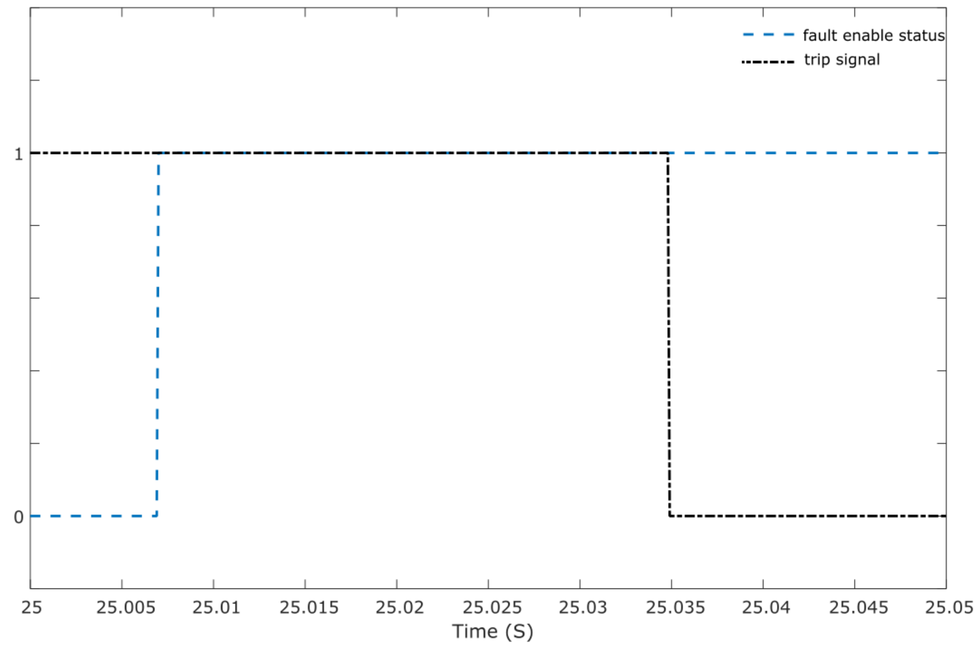

Figure 77. Fault and trip signals for RTL1.

3.2.4. Comparison of SVM with Other Classifiers:

Herein, SVM accuracy is compared against other classification algorithms like Nearest Neighbors, Decision Tree, Random Forest (RF), and Naive Bayes. For the fault type classification at RTL1, the accuracy of these techniques is summarized in Table 21. For zone identification at R1, the accuracy of classification algorithms is compared in Table 22. As seen, SVM renders a very good accuracy compared to other classifiers.

Table 21. Comparison of SVM with other classifiers for fault type classification at RTL1.

Classifier	SVM	Nearest Neighbors	Decision Tree	Random Forest	Naive Bayes
Accuracy(%)	100	100	84.21	100	100

Table 22. Comparison of SVM with other classifiers for fault zone classification at R1.

Classifier	SVM	Nearest Neighbors	Decision Tree	Random Forest	Naive Bayes
Accuracy(%)	99.82	98.25	99.46	99.7	96.52

3.3. ML-Based AC Fault Detection

This section presents a methodology for simultaneous fault detection, classification, and topology estimation for APS. The methodology estimates the probability of the occurrence of each one of these events by using a hybrid structure that combines three sub-systems, a Convolutional Neural Network (CNN) for topology estimation, a fault detection based on predictive residual analysis, and a standard multiclass SVM with probabilistic output for fault classification. The input to all these sub-systems is the local voltage and current measurements. The CNN uses these local measurements in the form of sequential data to extract features and estimate the topology conditions. The fault detector is constructed with a Bayesian stage consisting of a Multitask Gaussian Process (MTGP). The MTGP estimates a predictive posterior probability of the prediction based on the marginalization of the conditional predictive distribution, along with the posterior distribution of the parameters. This distribution is modeled as a Gaussian [20].

The estimated covariance of the predictive posterior for each one of the predictions is used to transform the error into a Standard distribution, whose values are then introduced into a One-Class SVM. The design assumes that a bias in the error may be present due to imperfect predictions, which leads to a machine that needs to be optimized with quadratic programming. There is only one parameter to be cross validated, but this cross validation needs to be done just once, as all input data will be Standard. Assuming that the error is unbiased would have led to a simpler linear programming fault detector. Since in normal operation the SVM does not need parameter validation, and all parameters of the MTGP are obtained by Maximum Likelihood over the input (test) data, the fault detector is fully unsupervised. Finally, a Multiclass SVM uses the input to perform the classification of the fault types. The multiclass option is the compact Weston-Watkins k-class formulation. All three sub-systems can work in a parallel setup for both performance and computation efficiency. We test all three sub-systems included in the structure on a modified IEEE 123 bus system, and we compare and evaluate the results with standard approaches.

The ensemble model for the joint circuit topology estimation and fault detection classifiers consists of two main blocks that operate in parallel (Figure 78) and whose outputs are combined later. The first block is a CNN trained with a sliding window of 100 voltage and current samples obtained from one of the relays. The CNN structure is shown in Figure 79. The network is trained to detect the configuration, and its output is an estimation of the probability of each configuration. Thus, at an instant t, the CNN output can be written as the probability $p\left(C_j \vee x\right)$ where $C_j$represents configuration j and x is a stack of 6 vectors containing 100 consecutive samples from instants t-99 to instant t. The six vectors contain the three voltages and currents measured at these time instants Four fault detectors are trained to detect faults from observations x of each one of the configurations. The input of the fault detectors is a vector with the three voltages and currents sampled at instant t. The corresponding structure can be seen in Figure 80. During the test phase, all fault detectors are given all data. Therefore, each data is tested for fault detection assuming all possible hypotheses over the possible configurations. These detectors provide an estimation of the fault probability given the sample under each one of the possible hypotheses over configurations C_j. These probabilities are denoted as $p\left(F \vee C_j, x\right)$, where F represents the event of a fault. Finally, a set of blocks are trained to classify over faults. These blocks are trained with faulty data only, and a different classifier is trained for each one of the possible configurations. Again, during the test phase, the data is introduced into the classifiers regardless of the configuration and the fault event. Therefore, the outputs are the fault classification under the hypothesis that a fault has happened and under the hypothesis of each one of the possible configurations. Each classifier outputs probabilities $p\left(F_{c_i} \vee C_j, x\right)$, where F_{c_i} represents fault class i. These probabilities are read as the probability that the fault is class i given the topology configuration of class j, given a fault has happened and given observation x. In Figure 78, three possible fault classes are considered, so, $1 \leq i \leq 3$.

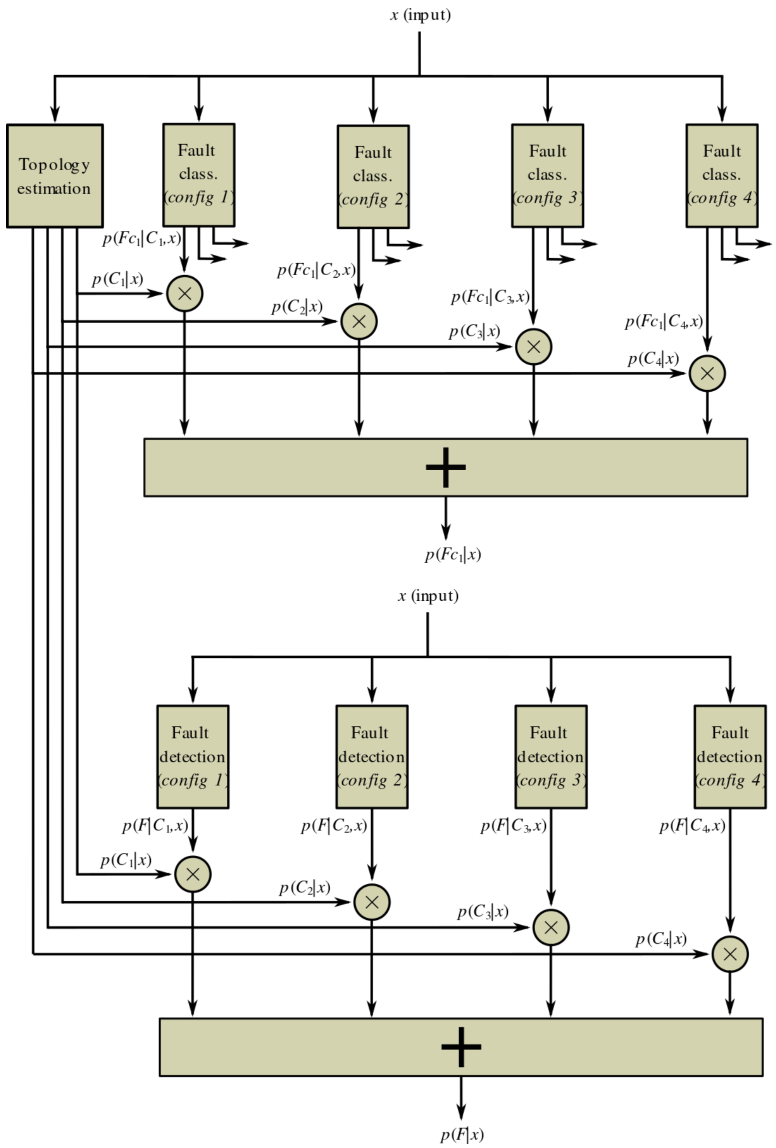

Figure 78. Proposed structure for fault classification and detection probability estimations.

Once the estimations of probabilities $p(C_j \vee x)$, $p(F|C_j, x)$and $p(F_{c_i} \vee C_j, x)$ are computed in parallel for a given input x, the estimations of the fault probabilities and the fault classes $p(C_j \vee x)$, $p(F|x)$and $p(F_{c_i} \vee x)$ can be computed. The CNN and the fault classifiers are supervised; thus, they are trained with simulated data which has been previously labeled. The fault classifiers are trained to detect the three faults, but not a normal operation. This makes the structure less structurally complex and hence less prone to overfit. Obviously, when the input does not correspond to a fault, the classifiers provide a wrong response, but this is attenuated by the output of the fault detector, which will be close to zero. The training of the fault classifiers would not be possible if the data was real, because usually, faults have a low likelihood, hence collecting enough faulty data and labeling it is an impossible task. Nevertheless, we choose a non-supervised fault detector, which is designed by taking into account the characteristics of a real fault. In other words, the fault detector simply estimates the likelihood of the observed events, and it classifies a sample as a fault when its likelihood is low. A supervised method would also be possible in this context, but a non-supervised one is better as it can distinguish novelties that are not present in the simulation which may otherwise be unnoticed. Also, the non-supervised structure will be more robust to the different levels of noise that may appear in real data, which are not present in the simulated one.

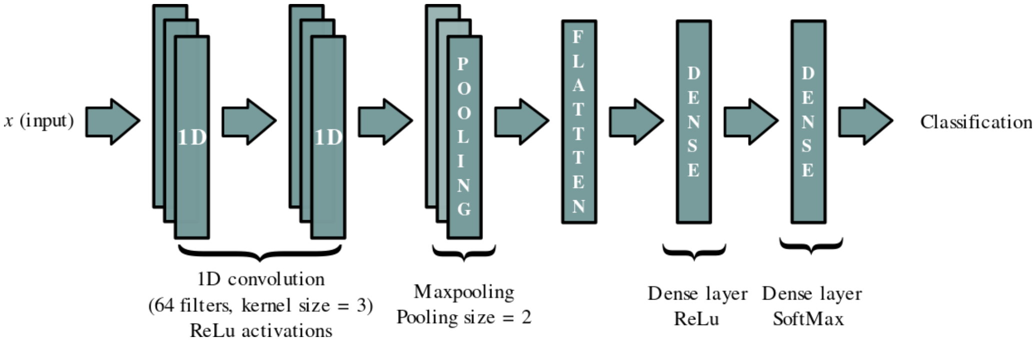

Figure 79. Structure of the CNN used for the classification of configurations.

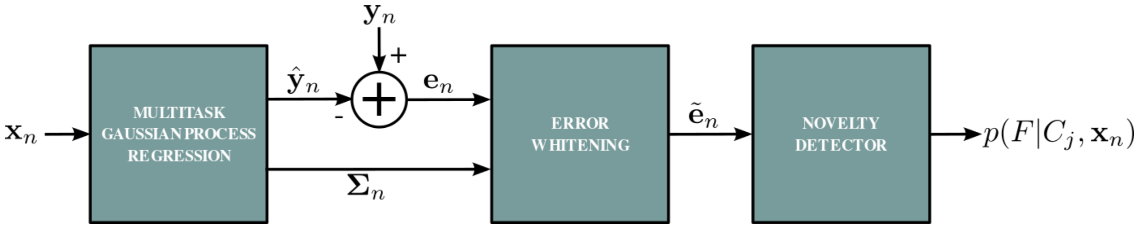

Figure 80. A fault detector is constructed and trained for each one of the possible configurations.

3.3.1. *Simulation Results*

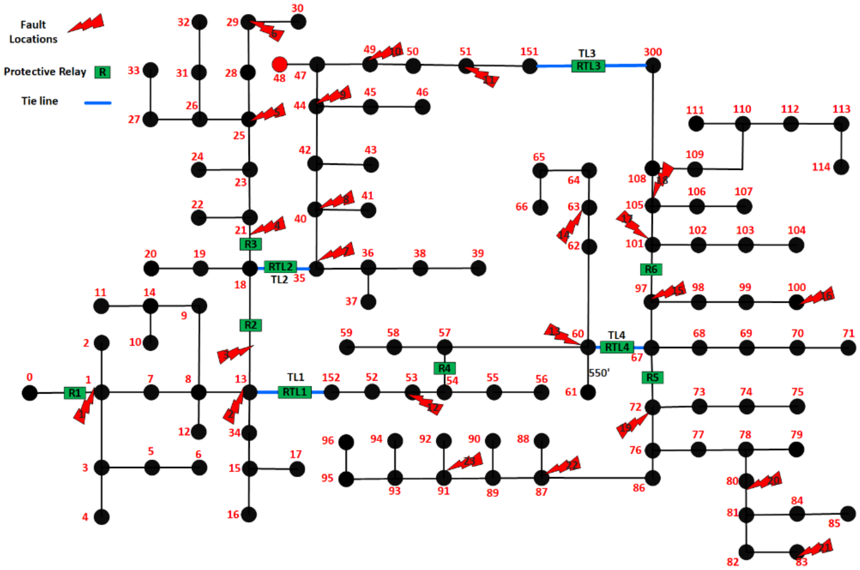

Figure 81. Modified IEEE 123 bus distribution system showing the fault locations.

Figure 81 shows the modified IEEE 123 test note feeder bus system. It is known for its convergence stability and capability to model unbalanced lines. It has a nominal voltage of 4.16 kV. The test circuit can be operated in four different configurations, changed by the status of tie-lines RTL1 to RTL4. Only one of the four tie-lines is in the open position for each circuit configuration.

The circuit contains 10 protection devices, including the four tie-lines. Three types of faults were simulated that were applied to the different locations indicated in Figure 81. These are the CG fault (Phase C to a ground fault), AB fault (A phase connected to B phase creates a short circuit), and ABCG fault (Three phases A, B, and C are connected together as well as to the ground). The data was generated from 5.6M samples at a sample rate of 12 samples per minute for each configuration at each one of the 10 relay locations. 26% of the data contained one of the different faults introduced in the 23 locations specified in Figure 81. 80% of the faults were of type CG, 15% were AB and 5% of the faults were ABCG. The fault impedances randomly ranged from 0.1 to 5 **Ω**. The data collected at each relay consisted of the three-phase RMS voltages and currents.

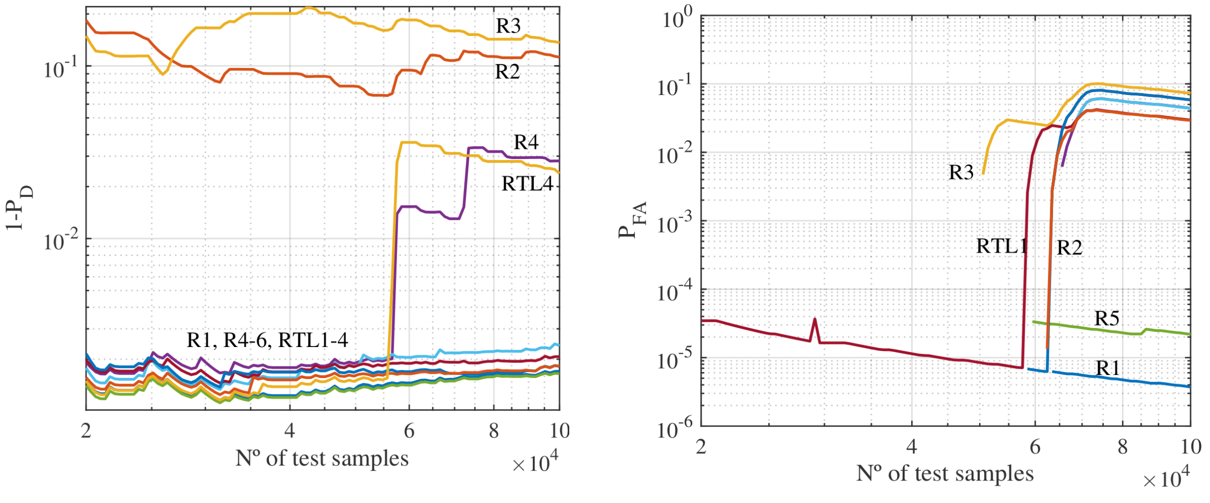

(a)

(b)

Figure 82. Probability of failure and probability of false alarm in fault detection. The probability of false alarm is dramatically lower when the number of test samples is less than 5×10^4.

The configuration classification performance of the CNN is over 95% for all relays and configurations. The impact of the classification error (about 5%) is low in fault classification and detection. Indeed, Table 23 shows the fault classification error for all configurations and relays, which ranges between 6 and 84 × 10−3. Table 24 shows the probabilities of false alarm and loss (no detection of a fault) of the structure. For all relays except for R3 and RTL1, the probability of false alarm is less than 2 × 10−6. For R3 and RTL1, the probability is still less than 10−3. Regarding the probability of loss for relays R2 and R3, the probability is high, of the order of 10−1, but for the rest, the probability is less than 2 × 10−3. Finally, Figure 82 shows the probabilities as a function of the delay between the last training sample and the test sample. The performance of the fault detection is good if the delay is less than 60.000 samples. Beyond this limit, the performance decreases due to the cyclostationarity of the data. This cyclostationarity, due to the seasonal temperatures, makes the training and the test data different, thus increasing the errors. An alternative proposal that solves the problem of the retraining would be the use of adaptive sparse Gaussian Processes (GPs) able to track the cyclostationarities and whose formulation was published after the project finished.

Table 23. Final fault classification error rates (×10−3) of the proposed combined meta-structure.

	R1	R2	R3	R4	R5	R6	RTL1	RTL2	RTL3	RTL4
p_e	6.2	65.5	84.1	39.9	10.6	36.0	25.9	45.5	26.1	24.5

Table 24. Probabilities of false alarm (P_{fa}) and of no detection $1 - p_d$ (×10−3) of the proposed structure.

	R1	R2	R3	R4	R5	R6
p_{fa}	> 0.002	> 0.002	0.32	> 0.002	> 0.002	> 0.002
$1 - p_d$	1.3	76.4	176.5	1.9	1.3	1.8
	RTL1	**RTL2**	**RTL3**	**RTL4**		
p_{fa}	0.01	> 0.002	> 0.002	> 0.002		
$1 - p_d$	1.8	1.7	1.6	1.5		

3.3.2. HIL Verification of ML-Based Fault Detection

We tested this approach in an HIL testbed. The IEEE 123 node system model is run in 5707 Opal-RT simulator in real-time. The topology estimation and fault detection algorithms are implemented on a desktop computer with the Linux operating system. The simulation time step in Opal-RT is 0.5 msec. At every 1 msec the real-time data from simulation model in Opal-RT is sampled by the Modbus module and transmitted to LAMP computer through an ethernet cable. The transmitted data includes the sequence components of voltage and currents measured at RTL1. The performance of LAMP for circuit topology estimation with CNN in HIL testbed is shown in Figure 83(a). The fault detection results using the non-supervised GP is shown in Figure 83(b). The simulation scenario in Opal-RT includes change of configuration of IEEE 123 node system and applying different types of faults in front of RTL1.

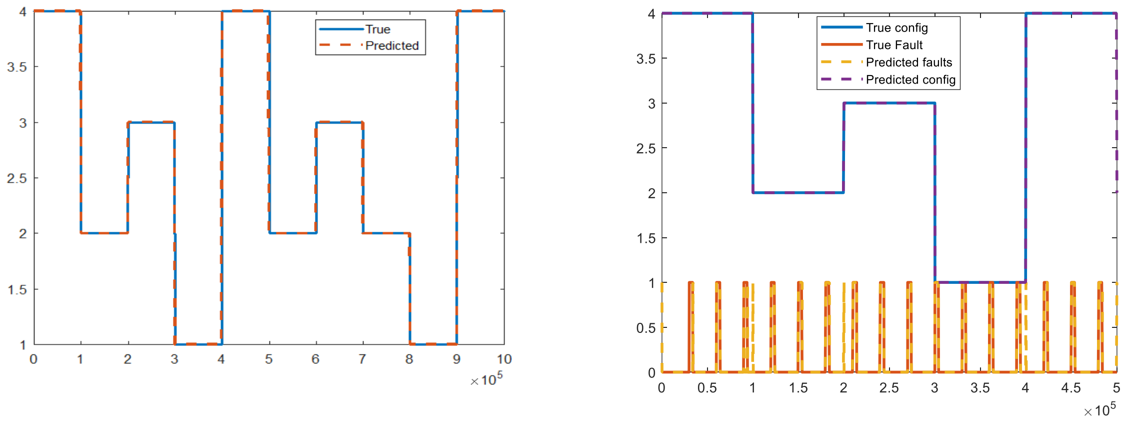

(a) (b)

Figure 83. (a) Circuit topology estimation results with CNN; (b) Fault detection results using non-supervised GP.

3.4. ML-Based DC Fault Detection

This section explores the potential for ML algorithms embedded in a protective relay to identify and classify faults in DC systems [21, 22].

3.4.1. *DC Power system model*

This research effort uses the Emera Technologies Kirtland Air Force Base (ETL-KAFB) DC Microgrid located in the southeastern part of Albuquerque, New Mexico. The ETL-KAFB DC Microgrid consists of a hierarchical, modular power electronics-based interface at each node that contains power conversion, control, protection, and storage. The DC Microgrid serves nine nanogrids (NG) which includes a residential area of six duplex buildings, a community center, a gathering space, and laboratory facility as shown in Figure 84. Each of the NGs include a load, a PV system, a Battery Energy Storage System (BESS), and a DC-to-DC converter to integrate the NG into the rest of the Microgrid. The size of the PV system in each NG varies from 5 kW to 13 kW, while the size of each BESSs is 9 kWhr. The Microgrid is operated at a bipolar voltage of ±375 VDC.

A fault emulator is installed at the gathering space of the Microgrid. The fault emulator can introduce fault of various impedance values between poles or a pole and ground on the Microgrid bus. The fault is actuated via a contactor. Fault data is collected at two locations on the Microgrid. The first batch of data is collected from a scope connected at node A, and the second batch from a scope connected to node B.

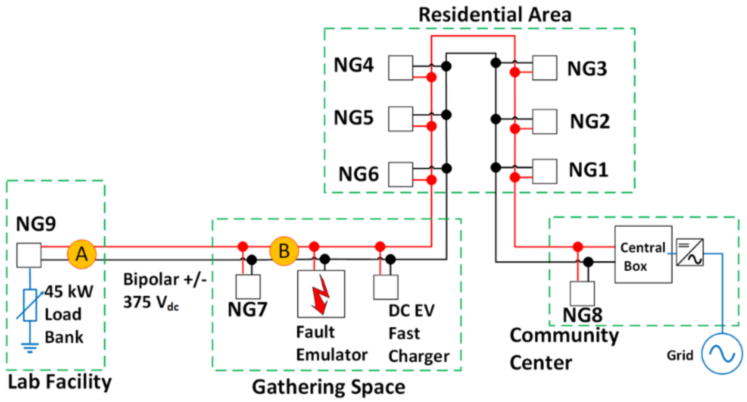

Figure 84. One-line diagram of the ETL-KAFB DC Microgrid

Additionally, the Emera DC Microgrid is modeled in PSCAD/EMTDC software package. Several faults are simulated and the fault data from node A and node B are recorded. The simulation data gathered from PSCAD is used as training data, while the real data gathered from the field is used as the testing data for the ML classification algorithms. To classify DC faults, two different categories of ML algorithms were explored:

- Linear Classification Algorithms
- Time-Series Classification learning algorithms

3.4.2. DC Fault Detection using Linear Classification Algorithms

Linear ML algorithms is a potential tool for intelligent fault detection because of its effective pattern recognition capability and its adaptability in systems with versatile operating conditions. The following supervised classification algorithms were considered for detecting DC faults.

- Support Vector Classifier (SVC)
- Naïve Bayes (NB)
- Decision Tree (DT)
- Nearest Centroid (NC)
- Multi-Layer Perception

Using these algorithms, faults were classified based on fault type and fault resistance. Fault is applied at the location of the fault emulator shown in Figure 84. Voltage measurements are recorded from node A and node B for each fault scenario. Using the PSCAD model of the DC microgrid, six different fault conditions are simulated.

- Fault 1: Positive Pole to Ground (PPG) fault with a fault resistance of 1.0 ohms
- Fault 2: Negative Pole to Ground (NPG) fault with a fault resistance of 1.0 ohms
- Fault 3: PPG fault with a fault resistance of 500 ohms
- Fault 4: NPG fault with a fault resistance of 500ohms
- Fault 5: PPG fault with a fault resistance of 1000 ohms
- Fault 6: NPG fault with a fault resistance of 1000 ohms

The measured data from the PSCAD simulation is used as training data on the five linear classification algorithms. The simulation data generated 2.4 million data points for each measurement node, which includes 400,000 points for each of the 6 fault-scenarios listed above. To test the algorithms, real data gathered from the operational DC Microgrid is used as testing data. From the field, the real data gathered has a total number of 4 million data points for each measurement node. The distribution of the data by fault type is shown in Table 25, while the distribution of the data by their fault type and fault resistance (i.e., fault 1 through 6) is shown in Table 26. The measured voltage from the PSCAD simulation data and the captured voltage measurement from the real data can be reduced to three components: the PPG, NPG, and pole to pole (PP) voltages. Each of the three components were provided as individual features to the ML classification algorithms to classify the data based on fault type and fault resistance. Each feature is then transformed such that the absolute values are mapped in the range of [0,1], i.e., the maximal absolute value is 1.0.

Table 25. Data Distribution by fault type

Data Type	**Fault Type**		
	No fault	**PPG**	**NPG**
D1: Training data (Node A)	50 %	25 %	25 %
D2: Training data (Node B)	50 %	25 %	25 %
D3: Testing data (Node A)	20 %	35 %	45%
D4: Testing data (Node B)	50 %	25 %	25 %

The performance of each of the ML classification algorithms is evaluated with a confusion matrix by comparing the predicted and actual outcomes. This format allows for the review of true positive, false positive, true negative, and false negative. In addition, an accuracy score is also computed as the ratio of the number of correct predictions to the total number of predictions. The accuracy score ranges from 0 to 1. The higher the score, the more accurate the classification.

Table 26. Data Distribution by fault type and fault Resistance

Data Type	Fault Type and Fault Resistance						
	No Fault	Fault 1	Fault 2	Fault 3	Fault 4	Fault 5	Fault 6
D1	50 %	8.3 %	8.3 %	8.3 %	8.3 %	8.3 %	8.3 %
D2	50 %	8.3 %	8.3 %	8.3 %	8.3 %	8.3 %	8.3 %
D3	20 %	22.5 %	22.5 %	0 %	22.5 %	12.5 %	0%
D4	50 %	12.5 %	12.5 %	12.5 %	12.5 %	0 %	0 %

The ML models are used to classify the fault data into three categories: No fault (NF), PPG fault and NPG fault. Figure 85 shows the performance of all five ML algorithms in classifying node A's data based on their fault type. Out of the five classifiers, the SVC, NC, and the Multi-Layer Perception (MLP) accurately classified the data based on fault type. The NB and DT classifiers had a low accuracy score. NB algorithm assumes that every feature is independent and DT algorithm has the problem of overfitting. These properties make the NB and DT algorithms unstable for this application.

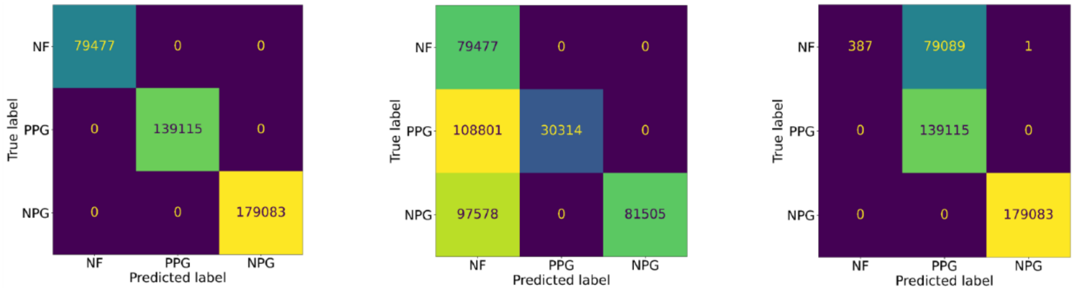

(a) Support Vector Classifier (b) Bernoulli NB (c) Decision Trees

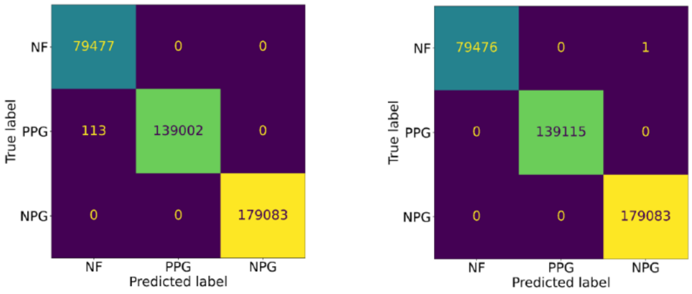

(d) Nearest Centroid (e) Multi-layer Perception

Figure 85. Confusion Matrix showing the ML classification based of fault type.

Since the SVC, NC, and the MLP algorithms accurately classified the data based on the fault type, these three classifiers are used to classify the data based on both the fault type and fault resistance. The data is classified into 5 labels: No fault, 1 ohm PPG fault, 1 ohm NPG fault, 500 ohms PPG fault and 500 ohms NPG fault. Figure 86 shows the performance of the classifiers in classifying node B's data based on the fault type and fault resistance. Table 27 shows the accuracy score for each ML classifier. In classifying by fault type, the SVC, NC, and MLP classifiers had a score of at least 0.99. When classifying by fault resistance, only the MLP classifier performed accurately with a perfect score of 1.0.

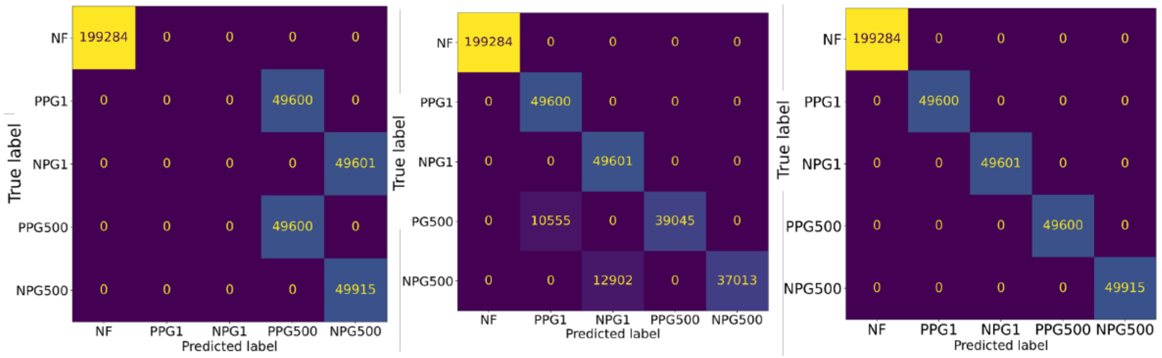

(a) Support Vector Classifier (b) Nearest Centroid (c) Multi-layer Perception

Figure 86. Confusion Matrix showing the ML classification based off fault type and fault resistance.

Table 27. Accuracy score of linear classifiers

ML Classifier	Node A Accuracy Score		Node B Accuracy Score	
	Fault Type	Fault Resistance	Fault Type	Fault Resistance
SVC	1.00	0.75	1.00	0.75
NB	0.48	0.48	0.75	0.74
DT	0.80	0.77	0.49	0.25
NC	0.99	0.94	1.00	0.94

3.4.3. DC Fault Detection using Time-Series Classification Algorithms

The linear learning algorithms discussed above treats each data point as an independent point. They ignore the information contained in the time order of the data, i.e., if the data order were scrambled, the predictions wouldn't change. Hence, linear classifiers perform poorly when used for fault location classification. To accurately classify faults based on their location, it is necessary that the algorithm consider the time-ordered sequence of the fault data. Time Series Classification (TSC) uses supervised machine learning to analyze multiple labelled classes of time series data and predict or classify the class that a new data set belongs to. Two algorithms are considered. The first is based on a Minimally Random Convolutional Kernel Transformation (MINIROCKET) and a regularized linear classifier. The second is based on a CNN. A continuous wavelet transform (CWT) is applied on the fault data and the CNN is trained to learn the characteristic patterns in the coefficients of the transformed data.

Three types of faults are simulated in the PSCAD model of the ETL-KAFB DC Microgrid; PPG fault, NPG fault and PP fault. The faults are simulated for several fault resistances at three different locations on the DC Microgrid as shown in Table 28. A total of 31 faults scenarios are simulated. 25 of them are used for training while the remaining 6 are used for testing the classification algorithms.

The measured voltages and currents from the PSCAD simulations are used as the input data. The voltage measured consists of three components: the PPG, NPG, and PP Voltages, and the measured current consists of two components: the positive and negative current, I+ and I-. Therefore, at each measurement node, there are five signals. There are ten measurement nodes in the system. This includes a node at each of the nine NG terminal and a node at the central box terminal. These measured signals are for a total simulation time of 10 ms, 4000 data points with a time step of 2.5 μs. The fault in each sample is applied at the 5 ms point. The labels used for training are the fault locations (NG1, NG4 and NG9).

Table 28. Fault simulation details

Parameter	Value
Type of fault	PPG, NPG, PP
Resistance (Ohms)	1.0, 1.1, 5, 9, 500
Fault Locations	NG1, NG4, NG9

For the MINIROCKET time series classification, two different cases are studied. In the first case, it is assumed that the voltage and current measurement at all nine NG box terminals and central box terminal are readily available, i.e., all 50 signals are used as the features for both training and testing models. In the second case, it is assumed that only the voltage and current measurements from the central box are readily available, i.e., only 5 signals measured from one location are used as the feature in the model. Figure 87 shows the performance of the trained model on the test data for both cases. The model for case 1 had an accuracy score of 0.99, while the model for case 2 had an accuracy score of 0.855. The MINIROCKET and stochastic gradient descent (SGD) Classifiers accurately detected the fault locations using all measurements from all nine nodes and the central box. However, in large power systems, it may be expensive to install multiple measurement nodes and challenging to access measurements from all nodes in real-time. Using the signals from the central box or from one measurement node significantly reduces the accuracy of the MINIROCKET time series classification algorithm.

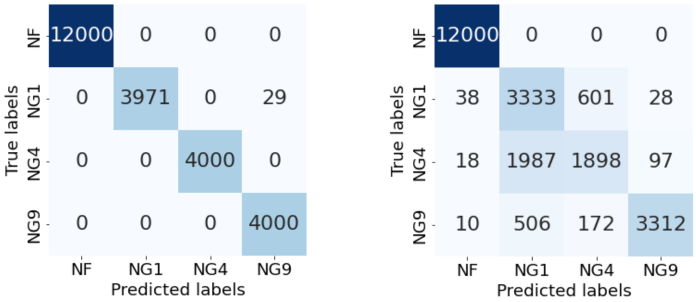

Figure 87. Confusion Matrix of MINIROCKET Case 1 and Case 2 respectively

Building a CNN to classify the time series data used in MINIROCKET Case 2 above. A CWT is applied on the signals to generate coefficient matrices. These matrices can be represented as images and used to train the CNN models. A CWT is a signal processing tool that is used to analyze the frequency components of a signal for a period. A CWT decomposes a signal into components that appear at different scale or resolution. CWT is based on the convolution of the signal with a dilated impulse response, mapping the signal onto a two-dimensional function of time and frequency. In this work, Gaussian wavelet is selected as the mother wavelet because they provide the best resolution in time and frequency. The different wavelets in scales and time are shifted along the entire signal and multiplied by its sampling interval to obtain physical significance, resulting in coefficients that are a function of wavelets scales and positions.

For example, if we apply CWT with a scale range of 100 to the measured PPG Central box voltage signals for faults at NG1 and NG9, and then visualize the ensuing coefficients in a 2D scalogram, we obtain the following result shown in Figure 88. Such visualization can be used as images into the CNN to distinguish different signals.

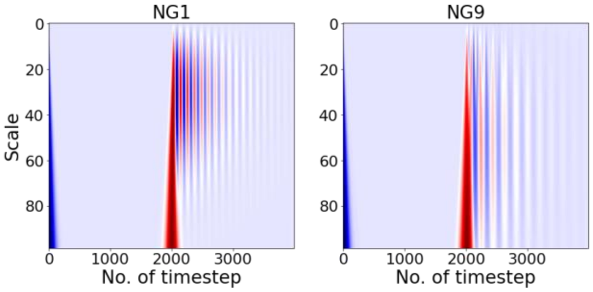

Figure 88. CWT Scalogram of the central box PPG voltages for faults at the NG1 and NG9 nodes

A detailed description of the CNN layer structure used can be found in Table 29. The CNN model accurately detected the location of the faults in the system. It had an accuracy score of 1. Figure 89 shows the multi-labeled confusion matrix in which the predicted locations are plotted against the true location.

Table 29. Configuration of each CNN Layer

Layer	Kernel Size	Output size	Activation
Convolution	32 x 5	100 x 4000 x 32	ReLU
Max pooling	-	50 x 200 x 32	-
Convolution	64 x 5	100 x 4000 x 64	ReLU
Max Pooling	-	25 x 1000 x 64	-
Flatten	-	1600000	-
Fully Connected	-	128	ReLU
Fully Connected	-	54	ReLu
Fully Connected	-	3	Softmax

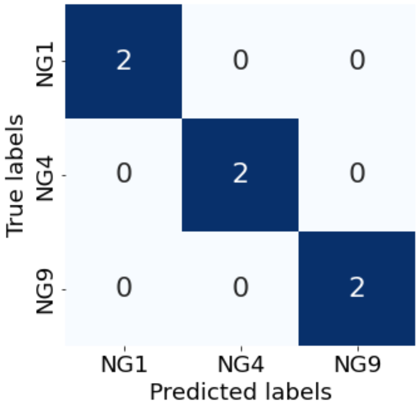

Figure 89. Confusion matrix of CNN

4. TRAVELING WAVE PROTECTION

Faster protection schemes for AC and DC systems can be designed by exploiting the TW signatures that occur in the first microseconds after the fault inception. TWs are originated by electrical charges suddenly moving through conductive elements, and they propagate through the system at almost the speed of light. TWs do not depend much on the pre-fault steady-state conditions. Instead, the magnitude of the generated TW depends more on the fault type and fault resistance. TWs are wide-band signals, as their frequency spectrum ranges from kHz up to the level of MHz. They are characterized by steep wavefronts followed by numerous reflections, which originate from line discontinuities, such as junctions or the fault point, and shunt elements. TWs suffer from distortion and attenuation due to line distance and discontinuities. Figure 90 shows an example of a TW.

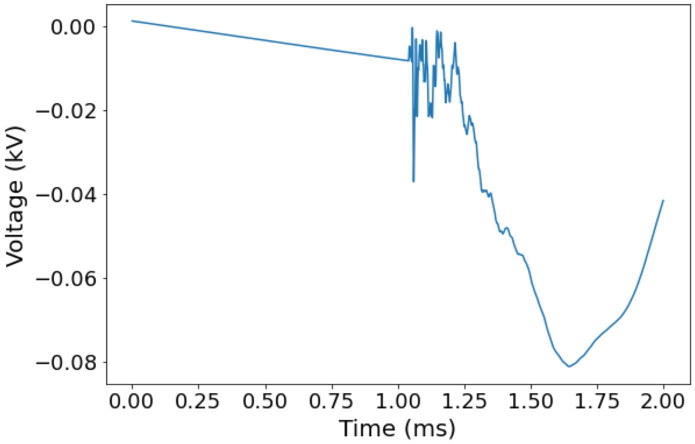

Figure 90. Traveling Wave on the voltage signal.

4.1. AC Systems

AC distribution networks still rely on over-current protection, which is effective and secure, but often requires several cycles to act. The development of faster distribution systems protection could help avoid equipment damage risks during violent failures on highly loaded networks. On the other hand, fast protection on transmission systems, based on TWs, has been widely applied for years. TW relays can clear a fault in just a millisecond, while traditional impedance protection can take more than a cycle. Until now, there have been no commercial TW fault location approaches for distribution systems. The reasons are not trivial: first, distribution lines are shorter than transmission lines which poses a challenge to existing signal-processing algorithms found in TW relays for transmission systems; and second, such fault location algorithms depend on the clear identification of TW reflections in a single-line setting. Unfortunately, this is not the case in distribution systems: junctions, laterals, and shunt devices create a populated sequence of reflections that make fault location very challenging.

In addition, the high-frequency effect of certain elements, such as capacitor banks or voltage regulators, cannot be neglected when working with TWs. Simulation models must be updated to take into account such effects. Regarding capacitor banks, the consideration of the Equivalent Series Inductance (ESL) is of great importance. Even a parasitic impedance can become significant at higher frequencies and it has to be measured and taken into account. Secondly, a fixed inductor is typically placed in series with capacitor banks to limit inrush currents, and it has to be modeled as well. Regarding voltage regulators and transformers, their behavior is mainly capacitive due to the parasitic stray capacitance, while the action of the core is not significant at high frequencies over the level of 100 kHz. Therefore, the effect on the TW propagation is determined by the stray capacitance, which leads to TW distortion and attenuation and produces a significant wave energy loss. The effect of such elements has been studied in [23, 24].

The TW waveforms can be analyzed using a variety of transforms and signal-processing tools that can be applied to extract relevant information. For example, it is well known that both Clarke and Karrenbauer Transforms can be used to compute the ground mode, which provides insightful information about the TW propagation path as this mode is more prone to attenuation. The signal-processing tools can be either time or frequency-domain-focused. Regarding the first group, techniques such as Mathematical Morphology (MM), Dynamic Mode Decomposition (DMD), or the Teager Energy Operator have been used to analyze TWs. In particular, MM and DMD study the waveform structure in multiple time frames. In frequency-domain techniques, several types of Wavelet Transforms (WTs) have a leading role, such as the CWT, Discrete Wavelet Transform (DWT), and Stationary Wavelet Transform (SWT), among others [25]. The WTs provide a detailed time-frequency decomposition that allows us to study the TW frequency bands independently.

4.1.1. Hardware-in-the-loop Testing of the Limitations of Existing Traveling Wave Relays for Distribution Systems [26, 27]

HIL testing allows users to anticipate and mitigate for limitations related to the dependability and security of the devices under test by incorporating real equipment into a simulation with distribution or transmission power lines. The real-time simulation platform used for this project was the one provided by Opal-RT Technologies. The hardware device model used was the OP5707-XG, which is a high-end performance, real-time simulator that relies on 8 CPU processor cores for co-simulation purposes, and a state of the art field programmable gate array (FPGA) for ultra-fast simulation time-steps (less than 1 μs) capable of capturing the transient dynamics of events involving TWs. The real-time simulation platform relies on Simulink and the corresponding power systems libraries for building the desired power network. Once the design and capturing of the desired network is completed, it is uploaded into the cores or into FPGA of the simulator for real-time simulation processing.

4.1.1.1. HIL testing setup with SEL TW relays.

The simulation of systems involving the transient dynamics of TWs require the use of proper frequency dependent (FD) transmission lines models, which are based upon the numerical solution of the D'Alambert formulas that solve the telegraph's partial differential equations for transmission lines. Before performing real-time simulations, the transmission line models provided by Simulink were validated against two other simulator programs: ATP and PSCAD. Both are electromagnetic-transient-based simulators that provide frequency-dependent transmission line models.

The diagram of the simulated power network is shown in Figure 91. Notice that the transmission line labeled TL 3 is split into two FD transmission line models, and a fault is applied 8 km away from bus B5, which is the measurement point of the 3-phase currents and voltages that are sent to the TW relay.

The simulation parameters and values of the different elements used in the simulation model are summarized in Table 30. For traveling wave comparison purposes, a SLG fault was applied using a fault impedance of 10 mΩ.

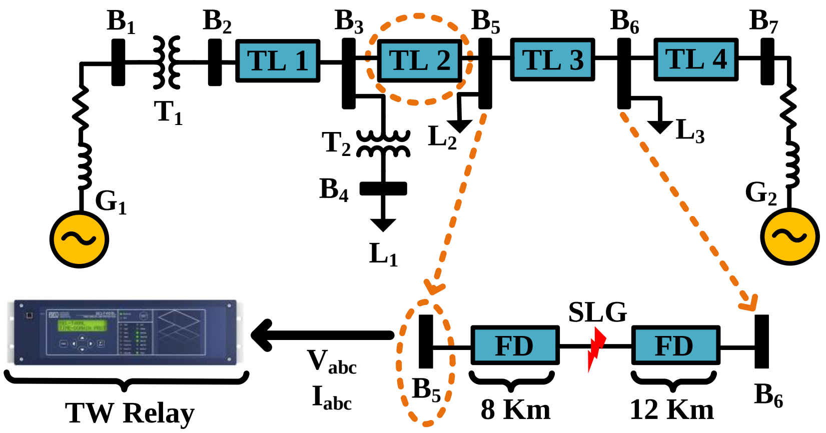

Figure 91. Testing power network to evaluate TW transient dynamics.

Table 30. Simulation parameters and values.

Generators’ Parameters				
Label	**Voltage**	**Source resistance**	**Source inductance**	
G_1	161 kV	6 Ω	50 mH	
G_2	138 kV	6 Ω	50 mH	
Transformers’ Parameters				
Label	**Configuration**	**Rating**	**Cooper Losses**	**Leakage inductance**
T_1	Yg-Yg	55 MVA	0.0008 p.u.	0.015 p.u.
T_2	Yg-Delta	10 MVA	0.0008 p.u.	0.015 p.u.
Loads’ Values				
Label	**Real Power**	**Reactive Power**		
L_1	4 MW	1 MVar		
L_2	2 MW	0 MVar		
L_3	2 MW	0 MVar		
Transmission Lines’ Parameters				
Label	**Length**	**Type**		
TL1	0.8 km	Frequency Dependent		
TL2	20 km	Frequency Dependent or PI		
TL3	20 km	Frequency Dependent		
TL4	5.6 km	PI		

The Simulink model was simulated using the real-time simulator, and the fault was controlled manually from the user’s console. The simulations in ATP and PSCAD were performed offline, capturing the high-resolution voltage and current signals measured at bus B5. Then, these signals were converted into the proper COMTRADE format and loaded into the TW relay for its use with the event playback feature of the relay, which allows the testing and analysis of sets of signals originated from simulation studies. The event playback feature of the relay comes up extremely handy for situations where the user does not have a real-time simulator but still needs to test the relay prior to commissioning it. The flowchart that describes the process of loading offline-generated signals into the TW relay is depicted in Figure 92.

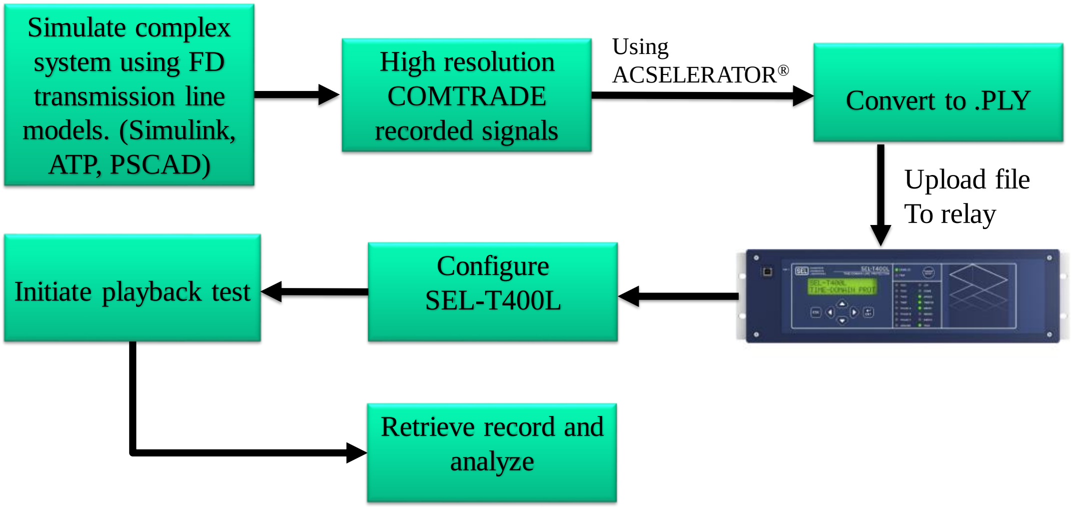

Figure 92. Flowchart that describes how to upload offline simulation signals to a TW relay.

4.1.1.2. Simulation case 1 (single-ended protection scheme)

For this case, TL2 was modeled using a PI model, and L_2 was maintained at 2 MW. The rest of the system values were the same as the ones listed in Table 30. For each simulation, either from real-time or using the playback feature, the corresponding COMTRADE file was retrieved from the relay and the data from the faulted current and the extracted TWs were used for comparison of the transient dynamics.

A magnified portion of the faulted current trace right after fault inception, and the corresponding TW extracted by the relay, are shown in Figure 93.

For all the simulation cases, the inception time was set at t_0 = 0.11 s. The TWs' first and second arrival times are given by t_1 and t_2, respectively. Based upon the single-ended TW fault location, the relay uses the following expression to calculate the distance to the fault:

$$d = \frac{(t_2 - t_1)}{2} v \tag{2}$$

From Figure 93(a), notice that the current traces generated with the Simulink HIL setup and the ATP offline simulation overlap on each other. However, the PSCAD current trace presents slight transient differences in the form of smoother transitions. Due to the overlap between the controller hardware-in-the-loop (CHIL) Simulink traces and the ATP traces, their extracted TWs will be the same. Thus, for the sake of better clarity in the TW comparisons, Figure 93(b) only shows the extracted TWs from the Simulink and PSCAD simulations, which are the ones with more significant differences in transient dynamics. Even though both TWs traces in Figure 93(b) have slightly different shapes in their amplitudes, both traces exhibit the same arrival times, with t1 = 0.1100906 s and t2 = 0.1100363 s. Using the arrival times in (2), it gives an estimated fault distance of d = 8.06 km, which is the correct distance as depicted in Figure 91, and the fault distance displayed in the TW relay's screen. This was an expected result, since both: the PI model of TL2, and the load L_2 present an impedance discontinuity at Bus B5 for the TW to be reflected properly. For this simulation case, the value of the reflection coefficient at bus B5 provides a clear TW reflection for the relay to identify the correct fault location.

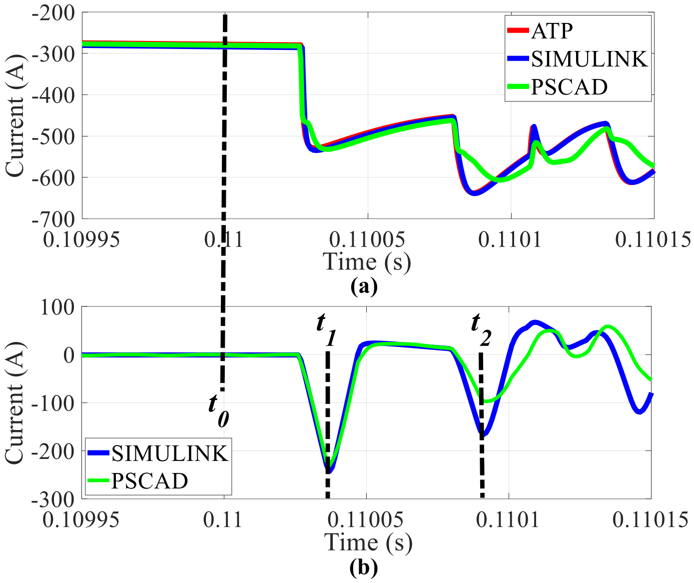

Figure 93. Current traces from simulation case 1. (a) Magnified segment of faulted current trace after fault inception. (b) TWs extracted by the relay, with the relay calculating a fault distance of 8.06 km.

4.1.1.3. Simulation case 2 (single-ended protection scheme)

This particular simulation case shows that, under certain simulation assumptions and conditions, the TW relay is not able to return an accurate fault location due to the lack of sharp and clear TW reflections at the point of measurement, B_5.

This simulation case is almost the same as case 1, except for the transmission line model of TL_2, which is now a frequency-dependent model with the same intrinsic electrical parameters as the ones of TL_3. The same result in terms of fault location was expected due to load L_2 presenting an impedance discontinuity at Bus B_5, but results depicted in Figure 94 proved this hypothesis wrong. Notice again from Figure 94(a) that the current traces between simulations right after fault inception maintained similar dynamics with some slight variations in the PSCAD trace. For this reason, the extracted TWs shown in Figure 94(b) have similar dynamics. However, it is important to point out that while the first TW arrival (t_1 = 0.1100365 s) coincides with the one from simulation case 1, the second TW arrival time (t_2 = 0.110123 s) does not correspond with the fault distance. In fact, the calculated fault distance using (2), gives d = 12.8 km, which corresponds to the distance displayed on the relay's screen. The black arrow in Figure 94(a) points out a barely noticeable bulge in the current trace that corresponds to the reflection that gives the correct fault distance. Nevertheless, such bulge is negligible for the relay's TW extraction algorithm.

This quite unnoticeable TW reflection is a consequence of two circumstances: i) the frequency-dependent model of TL_2 does not present a significant impedance discontinuity since now it is modeled using the same intrinsic parameters as TL_3. For this reason, the reflection coefficient at the boundary conditions in bus B_5, is almost zero; or the refraction coefficient is close to unity. And ii) the load L_2 is not large enough to present a significant impedance discontinuity at bus B_5. Therefore, most of the arriving TW's energy goes through TL_2, and the reflected energy is very low, as pointed out by the black arrow in Figure 94(a).

A simulation case like this emphasizes the fact that a more sensitive approach is required in terms of signal processing to capture low-energy TW events. Also, cases like this invite the use of double ended protection schemes, on which only the first arrival of TW are used at the expense of having two TW relays with a communication channel open between the two devices.

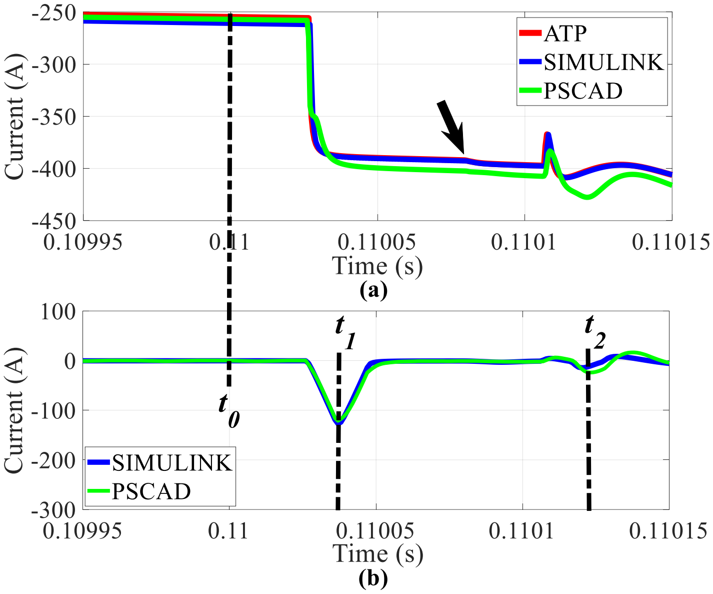

Figure 94. Traces from simulation case 2. (a) Magnified segment of faulted current trace after fault inception. (b) TWs extracted by the relay, with the relay calculating a fault distance of 12.8 km.

4.1.1.4. Playback tests with the SEL TW relays using double ended TW protection

To derive the equations that calculate the fault distance using double ended protection, the transmission line depicted in Figure 95 was used. For this scheme, each end of the line has a TW relay on which both the length of the line and the TW line propagation time, are specified. The line propagation time can be used to calculate the TW speed v, which is normally close to the speed of light for overhead lines. Also, a fiber optics connection between the two ends is needed. This way, the relays can communicate to each other the arrival times of the corresponding TWs. The fault shown in Figure 95 occurs at a distance d_1 from bus B_L, and at a distance d_2 from bus B_R. Upon fault detection, each relay will record the arrival time of the corresponding TW and communicate it to the other relay using the fiber optics link. The difference between the arrival times t_1 and t_2, gives:

$$t_2 - t_1 = \frac{d_2 - d_1}{v} \qquad (1)$$

The use of (1), along with the fact that the total length of the transmission line L is the sum of d_1 and d_2, allows to calculate the distances to the fault, giving:

$$d_1 = \frac{L - v(t_2 - t_1)}{2} \qquad (2)$$

$$d_2 = \frac{L + v(t_2 - t_1)}{2} \qquad (3)$$

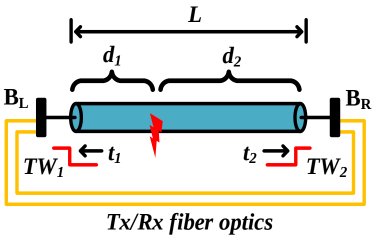

Figure 95. TW-based double-ended protection scheme.

The system depicted in Figure 96 was simulated using the ATP. To capture the TWs dynamics, the power lines were modeled using the J. Marti frequency-dependent model. The load L_U represents an unbalanced three-phase load.

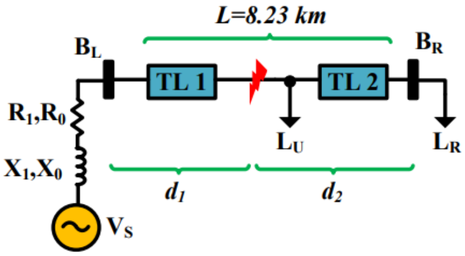

Figure 96. Simulation model used to test double ended schemes.

ATP simulations were carried out by modifying parameters that can affect the TW transient dynamics and shapes. For this study, such parameters were: the distance d1, as the fault got closer to bus BL; and the voltage source's (Vs) positive and zero sequence impedances.

4.1.1.5. Simulation case 3 (double-ended protection scheme)

For this set of tests, the system in Figure 96 was simulated using three different values of d_1 under a single line-to-ground fault (phase A) with a fault impedance of 10 mΩ. The idea behind the tests was to investigate the minimum fault distance that can be accurately calculated by the relays based on their TW detection algorithm. Furthermore, the tests were also used to visualize the detected TWs provided by the relays.

Table 31 summarizes the main parameters of each test. The signals obtained from the ATP simulations were uploaded into the corresponding relays, and the playback recording tests were executed for each case. Afterwards, the generated COMTRADE files were retrieved from each relay to plot the traces of the fault currents and the TWs. Figure 97(a) depicts a zoomed portion of the fault currents viewed from bus B_L, whereas Figure 97(b) shows the extracted TWs of such current traces along with the corresponding arrival times recorded by the relays (solid black arrows labeled t_{L1}, t_{L2}, and t_{L3}), and whose exact values are shown in Table 31 under the t_L column. Figure 98 presents the very same particulars about the traces viewed from bus B_R. The time scale is the same for all the traces in both figures and concurs with the microseconds time window that follows the fault inception marked by the dashed vertical lines at $t = 500$ μs.

Table 31. Simulation and test parameters for case 3.

Simulation model parameters			
Parameter	**Value**	**Parameter**	**Value**
V_1	34.5 kV	R_0	4.5 Ω
R_1	1.5 Ω	X_0	1.131 Ω
X_1	0.377 Ω	L	8.23 km
Test parameters and results (TWs arrival times)			
Test #	**d_1 (km)**	**t_L (μs)**	**t_R (μs)**
Test 1	3.66	523.389	525.859
Test 2	2.74	520.300	528.897
Test 3	0.914	528.000	534.935

For ease of visual reference, each test's traces, and their related relevant information tabulated in Table 30 and Table 31 are depicted in the same color. Test 1 (row and traces in red) is the baseline case, since d_1 is within a detectable distance from both relays. Notice that the TWs' traces have a relative sharp and quick rise with a low dispersion front end. Also, such current traces have a staircase shape due to the subsequent reflections that follow the fault. For TW detection and arrival time estimation, the relay uses a Differentiator-Smoother Filter (DSF) with a full-window length of 20 μs. This window can be observed in all the traces in Figure 98(b), where the lengths of the bases of all the triangular-shaped TWs are around 20 μs. The main purpose of the DSF is to detect the sharp current transitions originated by the TWs. The DSF is a reliable mechanism to detect and estimate the arrival times of TWs, but the window length restricts the minimum fault distance that the relay can locate, which can be a limitation when locating faults in short distribution lines.

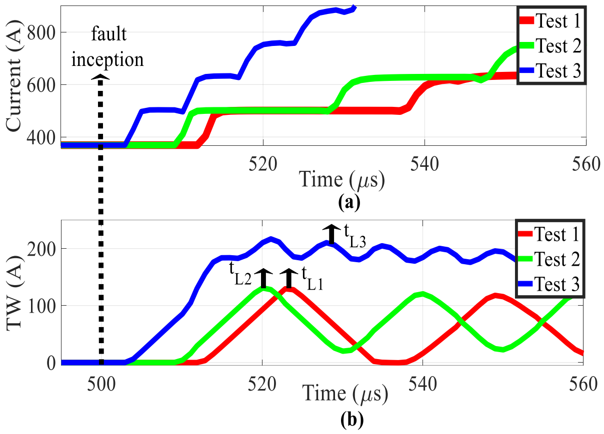

Figure 97. Fault current traces of phase A and TWs at bus B_L.

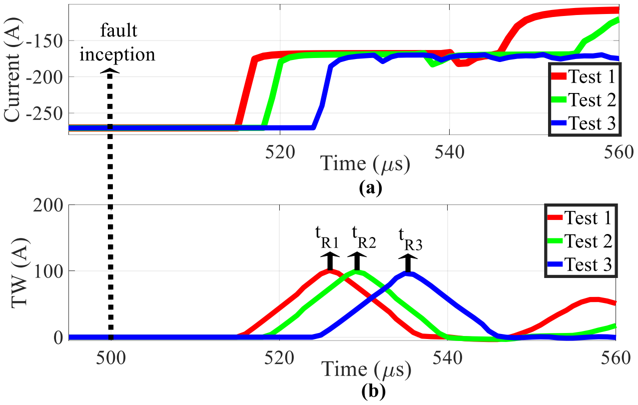

Figure 98. Fault current traces of phase A and TWs at bus B_R.

Table 32. Relay's calculated fault distances from each test.

Test #	Calculated Distance	Actual Distance	% Of Error
Test 1	3.7 Km	3.66 Km	1.1 %
Test 2	2.8 Km	2.74 Km	2.1 %
Test 3	2.42 Km	0.914 Km	164 %

Table 32 shows the relay's calculated distances to the fault for all three tests, which are the results of using (2) with the arrival times shown in Table 31. Also, the percentage of errors with respect to the real fault distance is shown.

From Table 32, notice that in tests 1 and 2, the calculated fault location was very precise. This accuracy can be corroborated by the corresponding arrival times in the red and green traces in Figure 97(b) and Figure 98(b), where the shapes are triangular with their peaks coinciding with the correct TW arrival times. However, in test 3, the calculated fault location was incorrect. Test 3 highlights the distance limits that the 20 μs window imposes over the fault location. From the blue trace in Figure 97(b), notice the lack of a triangular shape which misleads the TW qualification criteria of the relay; and thus, delays the recorded TW arrival time as shown by the solid black arrow labeled t_{L3}. The main causes of this delay are the subsequent overlapping of the fault reflections after the first TW arrival, which are depicted by the stair-shaped blue trace in Figure 97(a). The time elapsed between each reflection (stair) is less than 20 μs. Consequently, this causes the DSF's output to not roll off monotonically, which in turn obscures the TW qualification criteria.

Another way to visualize the performance of the previous tests is with the aid of a fault locating dependability contour, as the one shown in Figure 99, which depicts the contour for the transmission line's length used in the simulations. The y-axis is the fault distance (m) in per unit; whereas the x-axis is the parameter δ, which is the ratio between half the DSF's window length (10 μs) and the TW's line propagation time (27.7 μs) for a line of 8.23 km. Thus, δ=0.36 for the transmission line used in the ATP simulations. The portion of the red vertical line within the area delimited by the green triangle is the dependability region for the simulation case. Furthermore, the colored dots correspond to the different values of d_f used in the tests. Notice that tests 2 and 3 (green and blue dots, respectively) are outside the dependability region.

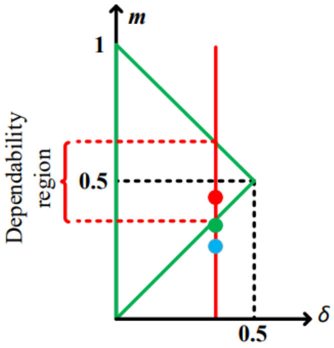

Figure 99. Dependability contour for a line of 8.23 km.

4.1.1.6. Simulation case 4 (double-ended protection scheme)

This case analyzes the effects that the current TWs experience when changing the value of the positive and zero sequence source impedances. Three fresh tests were simulated and executed in the relays. Table 33 outlines the impedances used for each test. The fault distance d_f was kept constant at 3.66 km during all tests.

Table 33. Source impedances used in simulation case 4.

Test #	R_1 (Ω)	R_0 (Ω)	X_1 (Ω)	X_0 (Ω)
Test 1	1.5	4.5	0.377	1.131
Test 2	2.5	7.5	1.885	5.655
Test 3	6	18	5.7	17.0

The corresponding current and TWs traces for each bus are depicted in Figure 100 and Figure 101. The reported TW arrival times are marked by the solid black arrows. Test 1 can be considered the baseline case where the correct distance to the fault was calculated by the relays. However, in tests 2 and 3, an incorrect fault distance was calculated. Table 34 shows the TW arrival times. Since the fault location did not change for all tests, all the arrival times should be the same. This happens in bus B_R, as depicted in Figure 101. However, the arrival times in bus B_L are different, as depicted in Figure 100, with their actual values tabulated in Table 34 under the t_L column. Notice that as the source impedance increases, so does the delay in the arrival times of tests 2 and 3. A visual illustration of the main cause of such delays is shown in Figure 100(a), where the rising times of the currents in the green and blue traces tend to be more disperse as the source impedance is increased. In summary, higher source impedance values on a radial feeder can alter the shape of the TWs' initial wavefront, which in turn, delays the detection of the corresponding arrival time.

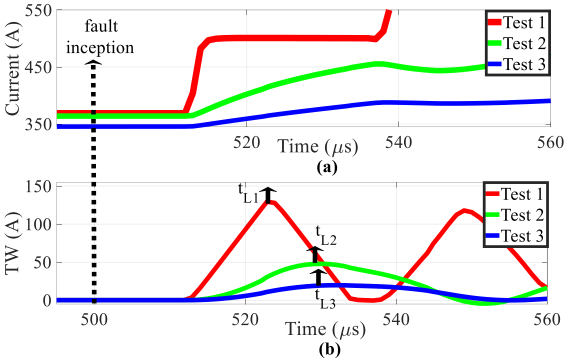

Figure 100. Fault current traces and TWs at bus B_L from impedance tests.

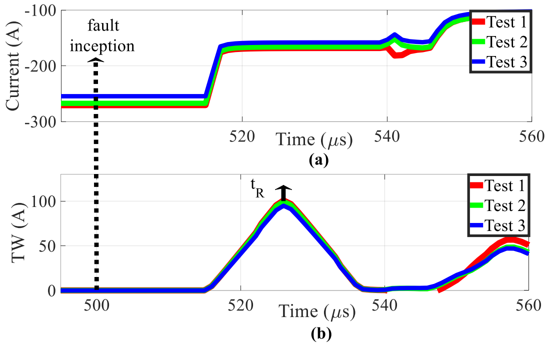

Figure 101. Fault current traces and TWs at bus B_R from impedance tests.

Table 34. Recorded TW arrival times for impedance tests.

Test #	t_L (μs)	t_R (μs)
Test 1	523.389	525.859
Test 2	529.711	525.859
Test 3	532.455	525.859

As TW protection schemes have proven their reliability (security) in protecting lines in transmission systems, attempting to use such schemes in distribution systems for fault location requires more sophisticated signal processing techniques. The simulations and experiments carried out in this paper showed that the actual TW-based fault location algorithms of commercially available relays tend to compromise (reduce) the dependability of the scheme as the lengths of the protected lines decrease. Based upon the simulations performed, qualitative analyses showed that short fault distances and variability in source impedances can also disperse the shapes of the TWs. Such dispersions interfere with the detection of the arrival times of consecutive TWs, which in return obscures the accuracy of the fault location algorithms.

4.1.2. Fault Detection

TW detection can be performed using a variety of techniques that exploit the abrupt voltage and current changes induced by the incipient fault, or the high-frequency oscillations associated with such sudden variations.

Regarding time-domain methods, DMD can be applied at every timestamp (for example, every microsecond). The magnitude of the second real eigenvalue, α2, can be employed as a fault indicator [28]. The indicator is compared to a pre-defined threshold in every execution. The numerical value for this threshold is just above the obtained values for normal-operation disturbances. DMD has been proven to be a very sensitive fault detection method, and at least in the developed use case in the IEEE 34 node system, guarantees a 100% detection accuracy from the substation. However, one of the main shortcomings is that it may be computationally expensive.

In order to provide visual explanations of the introduced signal-processing methods, the application of DMD is depicted in the following Figure 102. Only current measurements are used for detection. DMD returns two complex eigenvalues, and it is applied using a sliding window. Note the abrupt increase of α2 at the TW arrival time.

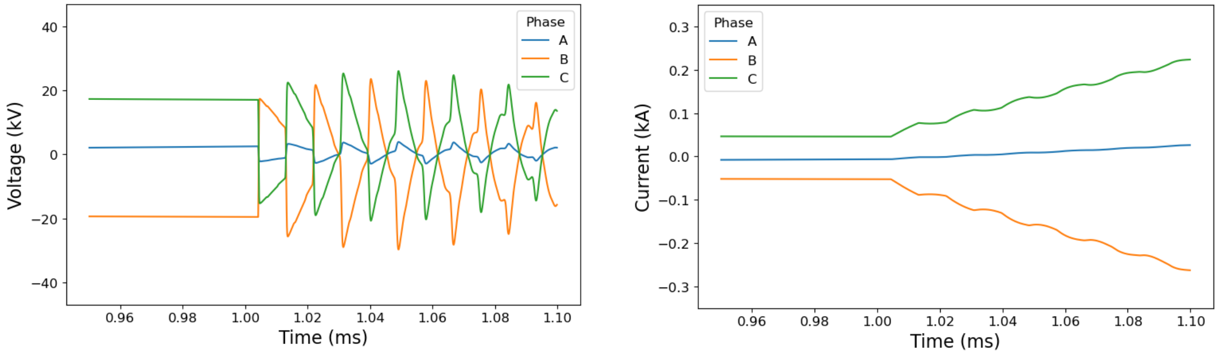

Voltage measurements

Current mesurements

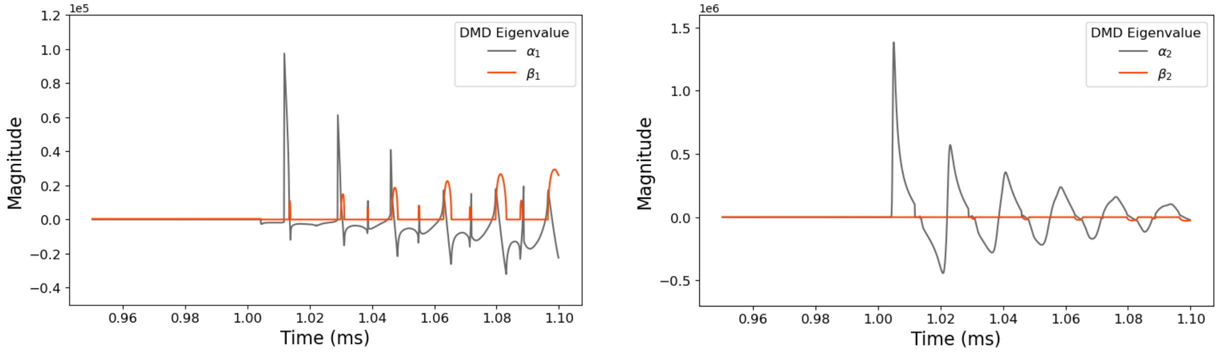

Eigenvalue 1

Eigenvalue 2

Figure 102. Application of DMD to a TW waveform.

On the other hand, the DWT is a frequency-domain tool that can be used for TW detection purposes [29]. The proposed fault detection algorithm is designed to be executed in small batches of input data (128 samples) at a sampling frequency of 1 MHz. It is run on a per-phase basis, which makes it suitable for either 3-phase (3P) or 1-phase (1P) nodes. The high-frequency information in the data is retained using a half-band high-pass filter provided by the first DWT decomposition level. This filter is calculated as a convolution between the input signal and the high-pass filter coefficients given by the mother wavelet, Daubechies 4 (db4). The output of this high-pass filtering is called “detail” wavelet coefficients, which in this case summarize the frequency components from 250 to 500 kHz. Once the first decomposition level detail coefficients are calculated, the indicator that measures the magnitude of the voltage signal's high-frequency components is the maximum absolute value of such an array of coefficients. Hereafter, it is referred to as the “MAX ABS V” indicator.

In this work, the threshold for event detection is determined by applying a safety factor to the MAX ABS V values obtained during normal operation. An event is detected if MAX ABS V is above the defined threshold. The threshold is set using the 99th percentile of the MAX ABS V values during normal operation and multiplying by a safety factor of 4. Then, DWT coefficients are revisited in chronological order to find the first coefficient that is above the node's threshold and determine the exact detection timestamp. In the Figure 103, the MAX ABS V indicator for normal operation and fault events is depicted. Note that the MAX ABS V indicator for nearby faults is clearly above the threshold, while it is indistinguishable from normal operation for distant fault events.

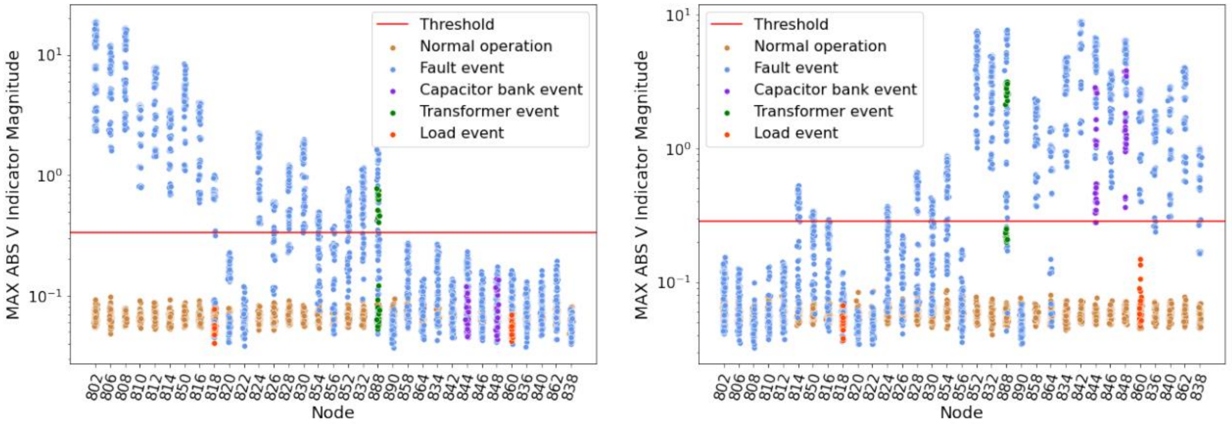

(a) MAX ABS V values for measurements in node 800

(b) MAX ABS V values for measurements in node 842

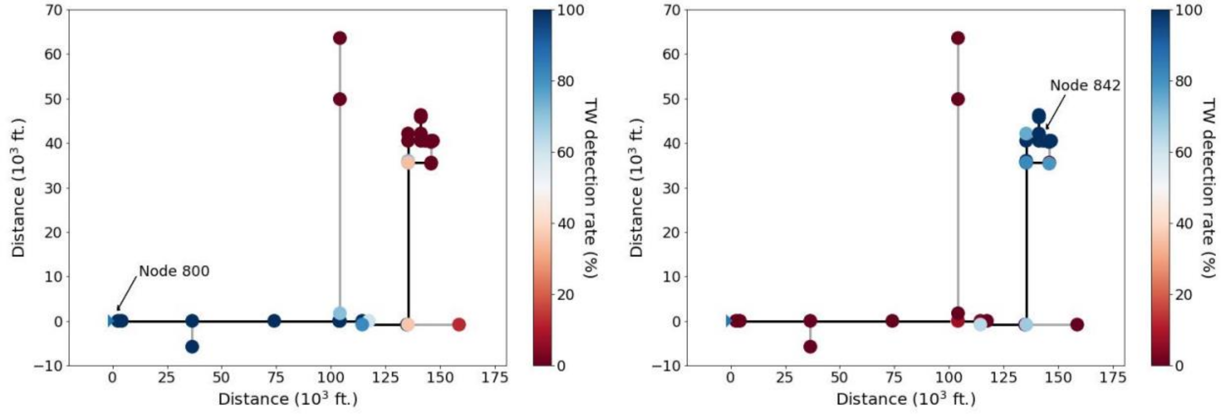

(c) Fault TW correct detection rate from node 800

(d) Fault TW correct detection rate from node 842

Figure 103. Threshold determination and fault TW detection rates for nodes 800 and 842.

The substation has the highest detection range (more than 130 thousand feet). Effective detection range means the distance to the closest fault location with a detection rate lower than 100%. In general, a sensor would have a certain effective range, including adjacent nodes and lines, and this TW detection rate will decrease as the distance to the fault increases (if the fault location is too far or there are too many discontinuities in the propagation path, the TW is significantly attenuated and therefore it cannot be distinguished from normal operation noise).

4.1.3. Fault Location

The complexity of fault location using TWs requires the usage of data-driven methods to match measurements with the location. The application of ML for fault location requires the extraction of relevant features. Some of the previously introduced signal-processing techniques have been used for feature extraction. Afterward these features are fed into an ML model that retrieves either the distance to the fault, or the protection zone in which the fault occurred.

Fault location can be achieved in an offline fashion, using just local measurements. For example, the works in [23, 30] employ the CWT to extract frequency features and then use CNNs to perform the fault location in the IEEE 34 node system. The fault node classification accuracy is up to 83%.

The works in [31-33] use RF as the fault location estimator after features are extracted using the DWT, MM, and DMD. This proof-of-concept is tested on a simplified one-line system, and the average error is about 1 to 2% of the line length.

Assuming communication, an approach using Graph Neural Networks (GNNs) is described in [34, 35]. Using the SWT for analyzing the TW signatures, it can achieve accuracy for faulty protection zone classification up to 94.38% with a signal-to-noise-ratio (SNR) = 45 dB, and 99.51% without measurement noise.

In general, there is a trade-off between accuracy and simplicity. The most complex model that has been developed combines both the SWT for frequency-domain tools and MM for time-domain tools and leverages up to 216 numerical features [36]. The number of RF estimators is limited to 400, while the maximum depth is limited to 100 levels. Fault node classification accuracy is 96.38% with SNR = 45 dB, and 99.43% without measurement noise. For the estimation of the distance to the fault, this model has an average error of 185.51 ft without measurement noise, and 1154.61 ft with SNR = 45 dB. Compared to the total system length, the average error is just 0.6%. This is closer to phasor-based fault location methods (average error of about 0.3%) than other TW-based methods (which may present up to 2.5% error for distant faults).

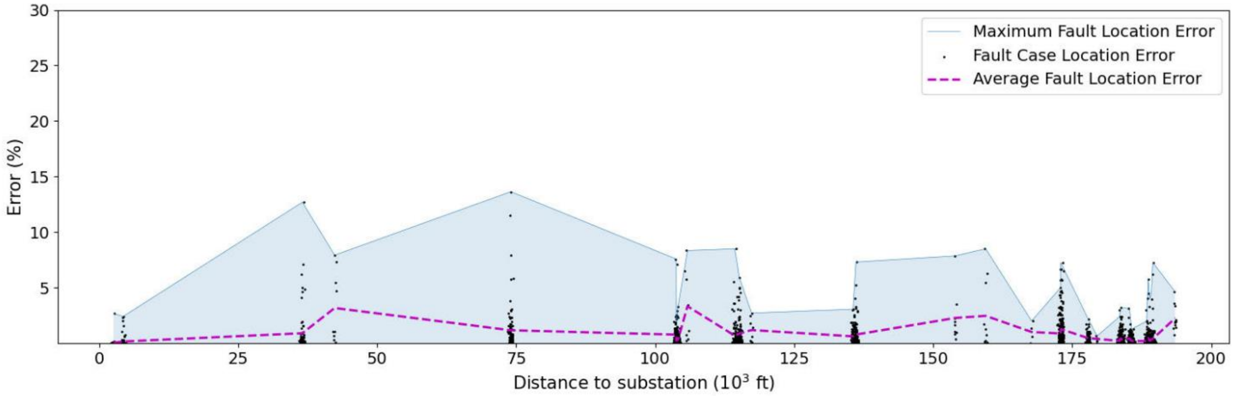

Figure 104. Absolute and average fault location error percentage compared to the distance to the substation for the method that combines both SWT and MM tools for feature creation.

The development of simpler methodologies makes implementation into a digital relay easier and faster. The lower time-consuming method relies on these basic steps [37]:

1. Karrenbauer Transform (KT), to decompose the 3-phase voltages into decoupled modes.
2. Time-frequency decomposition using the DWT, to decompose the ground mode into three frequency bands: 250-500 kHz, 125-250 kHz, and 62.5-125 kHz. The DWT is implemented using Multi-Resolution Analysis (MRA), in which an input signal is successively filtered by half-band high-pass and low-pass filters. The output of the high-pass filters is the "detail" coefficients, which summarize the signal in a certain frequency band. The filter coefficients are obtained from the mother wavelet, which in this case is db4. This step is achieved by a 3-level DWT decomposition, and further reconstruction of the three sets of detail coefficients, following the inverse process, to return signals in voltage magnitude.
3. Reconstruct signals' energy calculation using Parseval's Theorem. One benefit of Parseval Energy (PE) is the augmentation of the waves' reflections. The signals' polarity is eliminated, which implies that the fault location algorithm is just based on the PE values. The 3 arrays of PE values, corresponding to the signals that represent each frequency band, have a length of 128 values. The arrays are cropped again to remove the first and last 32 values, leaving each array with 64 samples, starting right on the TW Time Of Arrival (TOA). Finally, these arrays are concatenated to form a unique 192-values PE array that identifies the fault signature. A visual summary of the method can be observed in the Figure 105. Note that the method is designed for 3P nodes. An adaptation for 1P nodes could be made by removing the KT step. A relatively simple RF ("microRF") model has been trained for fault location on the IEEE 34 node system (divided into 11 protection zones), assuming that the sensor is placed on Node 828. With as little as 10 levels for maximum depth and 10 estimators, the fault location accuracy (as faulty protection zone identification) is 96.3%.

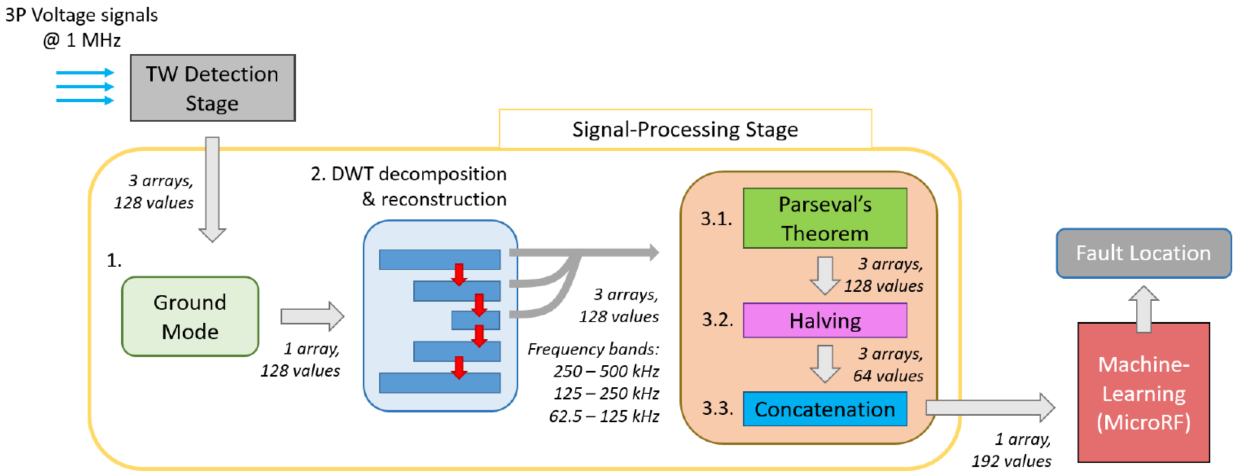

Figure 105. Workflow of the Detection, Signal-Processing, and Machine-Learning stages for the microRF method.

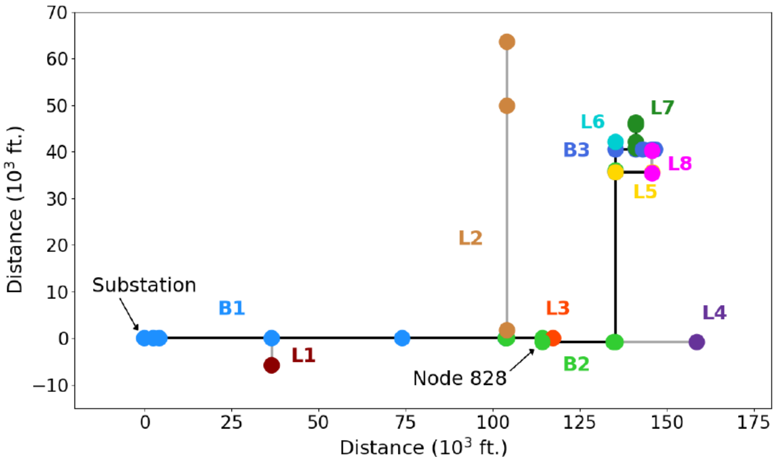

Figure 106. The IEEE 34 node system is divided into 11 protection zones.

4.1.4. *Implementation of a Traveling Wave Fault Detection and Location Scheme*

The Texas Instruments F28379D Delfino Experimenter Kit (TMDSDOCK28379D) is the selected Digital Signal-Processing (DSP) board to implement the last fault location algorithm. It has two 32-bit CPUs, with a clock frequency of 200 MHz. The RAM memory capacity is 204 kB, and the Analog-to-Digital Converter (ADC) resolution is 12-bits. This DSP counts with a co-processor, the Control-Law Accelerator (CLA), which is employed to sample at 1 MHz.

For AC systems, no testbed was available, so the validation has been done in a rudimentary laboratory setting featuring a TW playback setup.

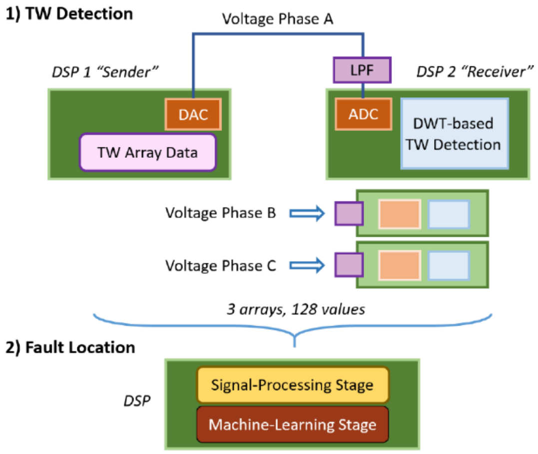

Figure 107. Playback testing setup using 2 DSPs.

The simulation of a large power system with frequency-dependent lines in Hardware-In-the-Loop is not trivial. Instead, another DSP is used to playback a pre-loaded fault TW (previously obtained in simulation) using its Digital-to-Analog Converter (DAC). This DSP, the "sender", reproduces a 3P waveform that contains a TW within the length of the signal, while the "receiver" DSP continuously samples and eventually detects the incoming TW. Due to computation limitations in the detection method, presented below, the TW detection is done in a single-phase fashion, repeating the process for each phase.

The employed TW detection method, implemented in a DSP, has already been presented in [38]. The method is based on a single-level DWT decomposition using batches of 128 samples, in which the resulting detail coefficients in the frequency band of 250-500 kHz are compared to a pre-defined threshold to determine if a TW has been measured or not. The method has been validated experimentally, and it was determined that the estimated execution time of the detection stage is between 136 to 150 microseconds (µs). Only one array (either phase A, B, or C) can be processed in this tight time window. A fully synchronized detection would require 3 DSPs. The output of this stage is 3 arrays of 128 samples that are cropped in -32/+96 samples since the TW TOA. Signals are saved, and then the 3P, 128-value arrays are fed into the device for the fault location testing.

In Table 35, the execution time for each of the signal-processing steps, and the execution of the RF model is shown. The most computationally expensive step is the level-wise DWT detail coefficients reconstruction. In total, the signal-processing stage takes around 970 µs to run [37]. The execution time of the RF model is significantly lower, taking around 10 µs. As explained in [38], the employed detection stage is executed in 150 µs. Therefore, the estimated execution time for the full detection and location process is expected to be around 1.13 ms.

Table 35. Signal-Processing and Machine-Learning stages for the microRF methodology

Stage	Process	Time (1,000 CPU cycles)	Time (microseconds)
Signal-Processing	Ground Mode & De-scaling	34.6	173
	3-level DWT Decomposition	56.2	281
	3-level DWT Reconstruction	91.3	457
	PE Level Calculation	11.2	56
Machine-Learning	MicroRF Execution	1.9	10

4.1.5. Analysis of a Traveling Wave Protection Scheme for AC Systems

So far, concepts such as TW detection rate, fault location accuracy, and execution speed have been discussed. However, a comprehensive protection analysis considering sensitivity and selectivity must be developed to really understand the potential applications of TW protection on distribution systems. The IEEE 34 nodes system was used again for this analysis, including PV farms in 3 locations. This way, IBR penetration up to 50% and bi-directional power flows can be simulated.

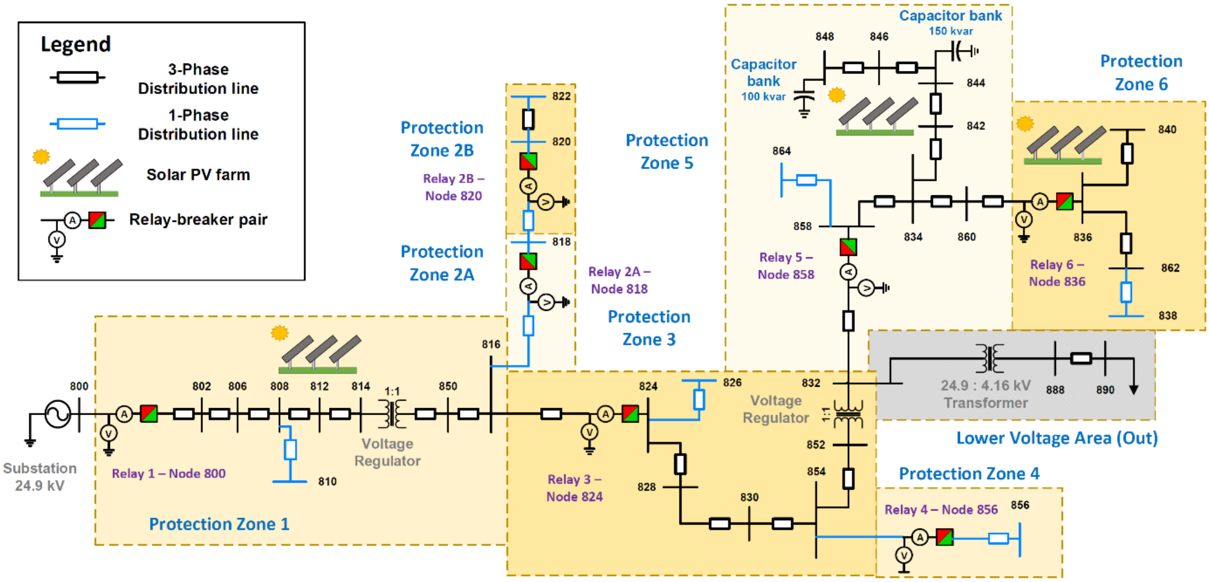

Figure 108. IEEE 34 node system, divided into 7 protection zones, and with 3 solar farms.

The system is divided into a total of 7 protection zones, excluding nodes 888 and 890 as they are in a lower voltage area. One TW relay is placed at the upstream side of each zone. The criteria for TW relay placing is heuristic: the location has been manually chosen to ensure good TW detection coverage across the system. Some relays have been placed prior to bifurcations to cover both laterals whenever possible to minimize the number of devices. When good coverage is not feasible due to low sensitivity, the relay has been placed on the lateral. Low sensitivity is directly related to high TW attenuation (long lines) or low TW magnitude (lightly loaded lines).

Regarding fault detection, the previously explained DWT has been employed with the modification that two decompositions would take place in parallel. The same decomposition using db4 is still employed, although it is aided by a second one using db2. This way, TW detection is still supported even in the case of quite attenuated TWs (in which db4 may not be very reliable). Still, most of the fault detections are achieved with db4, which is the primary decision method. The overall system-wide TW detection rate is 99.75%. The coverage is not reliable on two nodes: 822 and 864, which have a TW detection rate of 94.4% and 95.8%, respectively. This can be observed in the figure below. The reason for this is because when the voltage on these single-phase nodes is very close to the zero crossing, the magnitude of the resulting TW is too small to be detected.

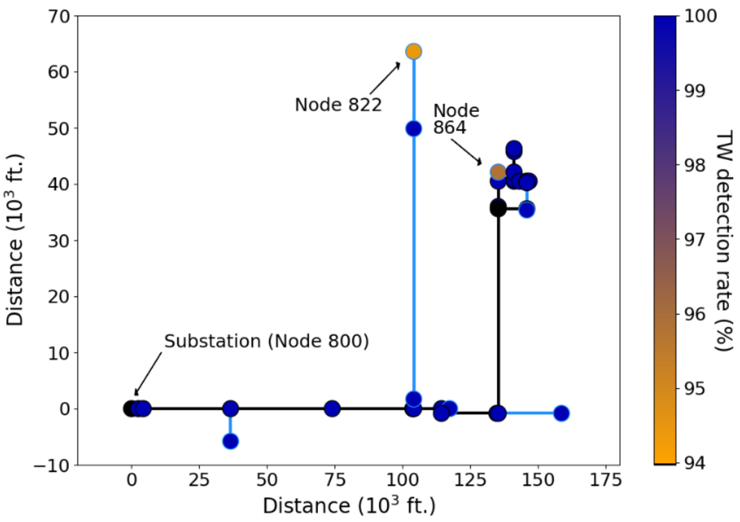

Figure 109. System-wide system detection rate using both db4 and db2 wavelet filters.

The fact that a 100% TW detection cannot be achieved throughout the system under all fault scenarios has important implications: a TW protection scheme cannot be a standalone methodology, and it must be collocated with other schemes. However, this technology would allow for a faster trip compared to traditional over-current protection in most cases. Note that, in this work, a TW relay would only activate a trip signal if the fault is located in its corresponding protection zone. If this condition is not met, then the TW delegates to slower overcurrent protection. No time delays or coordination have been studied at this time, but they will be considered in the future.

The fault location accuracy, true positive, true negative rates per relay are gathered in Table 36.

Table 36. Accuracy, true positive and negative rates.

Relay (Node)	Accuracy	True Neg. Rate	True Pos. Rate
800	98.5%	98.0%	99.3%
818	99.9%	100.0%	96.4%
820	100.0%	100.0%	100.0%
824	98.9%	99.1%	98.5%
856	99.9%	100.0%	96.3%
858	98.6%	98.4%	99.0%
836	99.9%	100.0%	99.3%

The relays fault location accuracies are between 98.5% and 100% on the detected faults. It has been determined that the level of IBR penetration does not have an impact on fault location accuracy, which is motivated by the fact that TWs don't depend on pre-fault power flow.

Regarding metrics, selectivity is achieved if these two conditions are satisfied:

- Corresponding TW relay in faulted zone detects as in its protection zone.
- No other relay says the fault is in its zone.

However, the effect of lack of selectivity can be very different:

- False trip, if another relay locates the fault in its protection zone.
- Unnecessary load loss, if the false trip occurs upstream of the fault protection zone. Therefore, some load that should be energized is disconnected due to the false trip.

Sensitivity is calculated still assuming a radial system. Sensitivity for a certain fault case is achieved if at least one of the following two conditions is satisfied:

- Corresponding TW relay in faulted zone detects as in its protection zone.
- Any other upstream TW relay detects the fault in the correct zone.

The proposed TW approach has a selectivity of 87.5%, although the percentage of cases that present a false trip is just 7.5%. Only 4.5% of the cases led to unnecessary load loss, which is estimated to be around 3.02% per fault case.

Regarding speed, it has been mentioned before that a TW detection using DWT and db4, in conjunction with a 3-level DWT decomposition and reconstruction, the calculation of PE values, and the execution of a micro RF can be performed in about 1.2 ms. As a comparison, a non-directional over-current scheme was developed for the same system with the same relay location. The average tripping time was 457 ms in order to achieve 100% selectivity and sensitivity. In conclusion, there is a trade-off between much faster but slightly less accurate TW protection schemes, and slower but more reliable over-current schemes (although there are a number of cases in which protection blinding due to elevated IBR penetration and bi-directional power flows can occur).

The path forward for this technology to be applied on other systems besides the IEEE 34 node case suggests that suitable distribution systems that can be easily modeled in a digital twin must be identified, and then high-resolution Electro-Magnetic Transient (EMT) fault simulation data must be gathered, processed, and finally used to train the models. This technology is system-dependent, and the corresponding study must be performed. Even though it may take some time to set up, the proposed technology can have significant benefits for wildfire protection, grid reliability, and fault troubleshooting.

4.2. DC Systems

In this report, a TW protection scheme utilizing ML for DC microgrids is proposed. The proposed scheme utilizes DWT to calculate the high-frequency components of DC fault currents. MRA is used along with DWT to calculate TW components for multiple high frequency ranges. The Parseval energy of MRA coefficients are then calculated to demonstrate a quantitative relationship between the fault current signal energy and coefficients' energy. The calculated Parseval energies are used to train ML engines to (i) identify the fault type and (ii) estimate the fault location on the DC cables [39].

4.2.1. High-Frequency Fault Signatures in a DC system

In order to study the high-frequency fault signatures of DC systems, a simple DC system (shown in Figure 110) is modeled in PSCAD/EMTDC. This circuit includes a controllable DC voltage source, one cable with the length of 3000 m, and a DC load with the resistance of 10 **Ω**. The nominal voltage of this system is ±375 V. The cable is modeled using the frequency-dependent distributed parameter model available in PSCAD/EMTDC. The cable specifications are provided in Figure 111.

It is assumed that each pole is buried 1 m deep. The core conductor resistivity is 2×10^{-8} Ωm while sheath resistivity is 30×10^{-8} Ωm.

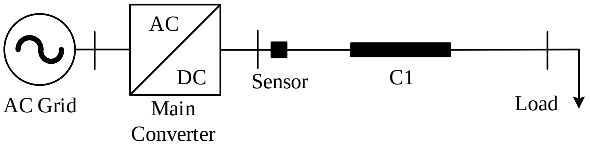

Figure 110. Simple DC microgrid system.

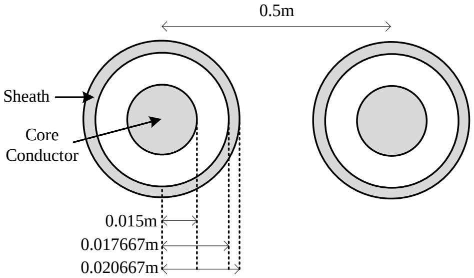

Figure 111. Cable configuration of the DC system in Figure 110.

MRA is an effective tool to demonstrate the high-frequency fault signatures in different frequency ranges. In order to show how the Parseval energy of wavelet coefficients of each MRA's level is impacted for different fault locations, PP faults are applied at every 75 m of Cable C1 in Figure 110. First, it is assumed that DWT's sampling frequency is 1 MHz. The Parseval energy values for three levels of MRA applied to the current measured at the sensor in Figure 110 are shown in Figure 112. Herein, levels 1, 2, and 3 are associated with [250 kHz, 500 kHz], [125 kHz, 250 kHz], and [67.5 kHz, 125 kHz] frequency ranges. As seen in Figure 112(a), the Parseval energy value is generally decreasing as the fault location gets closer to the end of the cable. However, some local peaks are observed that happen at every 375 m. A similar pattern is observed in Figure 112(b); however, the local peaks occur at every 750-800 m. Finally, Figure 112(c) shows that the local peaks occur at every 1500 m. As a rule of thumb, the number of local peaks approximately doubles from level 3 to level 2 and as well as from level 2 to level 1. In Figure 113, it is assumed that the DWT's sampling frequency is 2 MHz. Doing so, levels 1 and 2 are associated with [500 kHz, 1 MHz] and [250 kHz, 500 kHz] frequency ranges, respectively. As seen in Figure 113, a similar pattern to Figure 112 can be observed. In general, with a higher DWT's sampling frequency, (i) more oscillations on the Parseval energy profile of fault currents are observed, and (ii) the first incident of TW can be detected faster. The latter is based on an inherent feature of TWs in which the higher frequency TWs travel faster with a lower magnitude.

The spectrum of energy of the fault signals corresponds to the Parseval energy of wavelet coefficients. The Parseval energy patterns for different fault locations in Figure 112 and Figure 113 are based on the inherent behavior of TW currents and voltages. Since the MRA coefficients correspond to the magnitude of TW at a specific frequency range and Parseval energy sums up the square of MRA coefficients over time, the Parseval energy as a function of fault location results in the waveshapes seen in Figure 112 and Figure 113. Moreover, the local peaks of incident TW current at the sensor location as a function of fault location occur periodically and are a function of TW angular frequency. As the angular frequency increases, more local peaks with a higher frequency can occur as seen in Figure 112 and Figure 113. More information about this behavior can be found in [40].

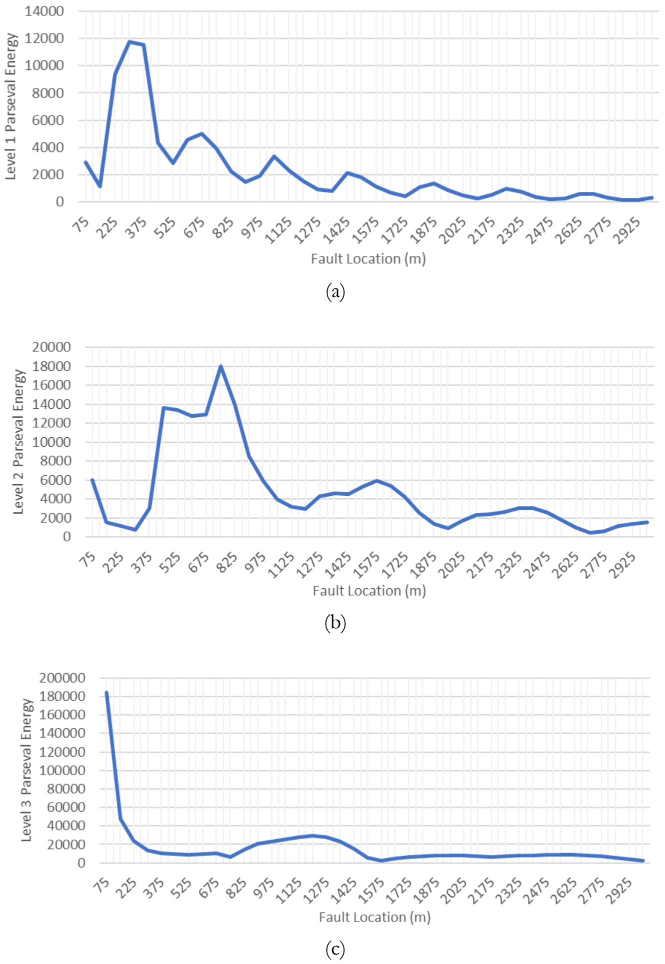

Figure 112. Parseval energy values for different fault locations on the cable of DC system with 1 MHz sampling frequency in Figure 110 (a) MRA's level 1; (b) MRA's level 2; (c) MRA's level 3.

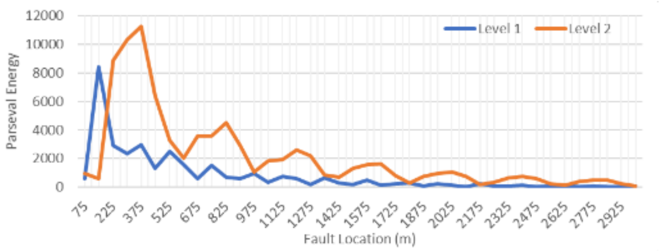

Figure 113. Parseval energy values for different fault locations on the cable of DC system with 2 MHz sampling frequency.

4.2.2. Fault Classification and Location Scheme

The proposed fault classification and location algorithm is shown in Figure 114. In this section, first, the fault direction algorithm is described. Then, the fault classification and fault location algorithms are elaborated in detail.

4.2.2.1. Fault Detection Algorithm [39]

The goal of the fault detection algorithm is to distinguish a fault scenario from a regular transient in the microgrid system. The fault detection algorithm is based on comparing the calculated Parseval energy value of the current flowing through the protection relay sensor, $E_{PRS,I}$, and a threshold η which is calculated as follows:

$$\eta = \gamma \min(E_{PRS,I,PP}, E_{PRS,I,PG}), \tag{1}$$

where EPRS,I,PP and EPRS,I,PG are the summation of the first N levels of Parseval energy of the current flowing through the protection relay sensor for remote end bolted PP and pole-to-ground (PG) faults, respectively. γ is a parameter to account for measurement noises. In general, regular microgrid transients (e.g., load outage, converter outage, etc.) create TWs with lower Parseval energy values compared to a bolted fault scenario. Therefore, (1) can be used to distinguish between a bolted fault scenario and other transients in the system. For highly resistive faults, (1) may fail to distinguish a transient condition from the fault condition since resistive faults have lower current Parseval energy values. To tackle this challenge, the summation of the first N levels of Parseval energy of the PP, PPG, and NPG voltages are utilized. For a regular transient in the system, the Parseval energy values of PP, PPG, and NPG voltages remain very small. However, for a resistive PP fault, the summation of the first N levels of Parseval energy of PP voltage is much higher than a regular transient. For a resistive PG fault, the summation of the first N levels of Parseval energy of PPG and NPG voltages are much higher than the regular transients. Therefore, by calculating the Parseval energy values of PP, PPG, and NPG voltage values, one can distinguish between a regular transient and highly resistive fault condition.

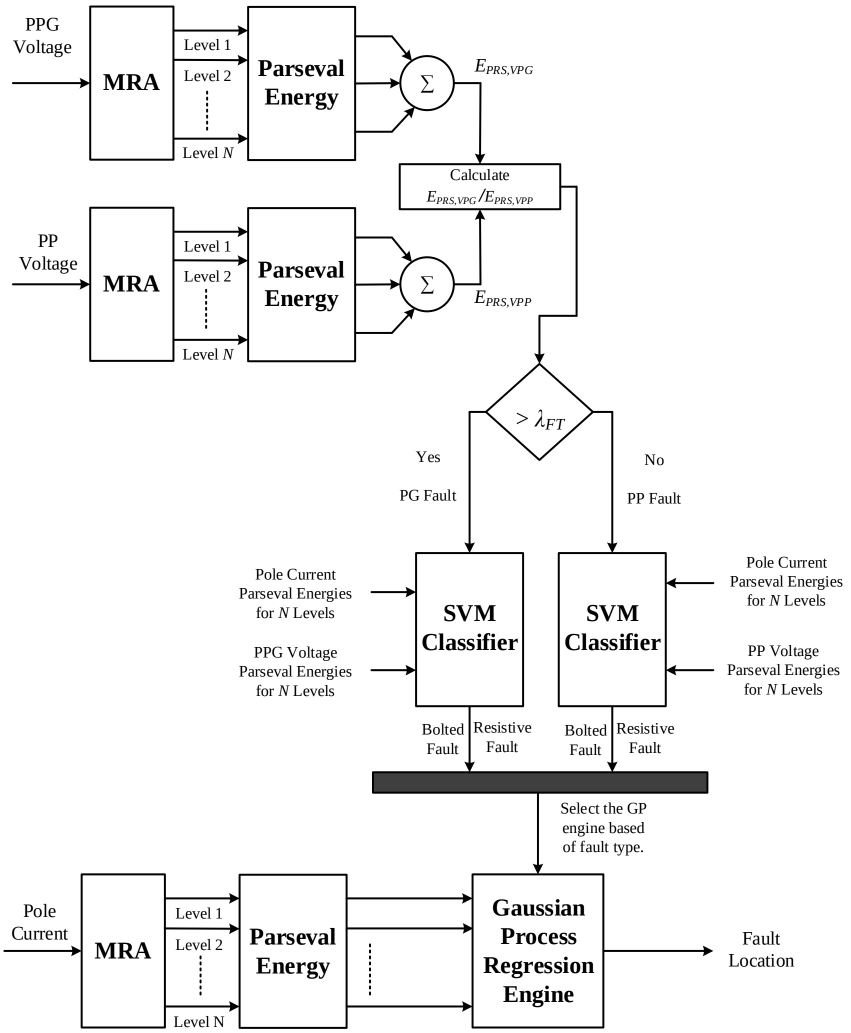

Figure 114. Fault classification and location algorithm.

4.2.2.2. Fault Classification Algorithm [39]

To distinguish between PP and PG faults, the Parseval energy of PP voltage at the sensor location is compared against the Parseval energies of the positive or negative pole to ground voltage. This procedure is shown in Figure 114. For PG faults, the Parseval energies of positive or negative pole to ground voltage are significantly higher than the Parseval energy of PP voltage. To this end, the algorithm first calculates the summation of the first N levels of Parseval energy values related to PP voltage and PPG voltage (i.e., $E_{PRS,VPP}$ and $E_{PRS,VPG}$ respectively). Then, $E_{PRS,VPP}$ and $E_{PRS,VPG}$ are compared against each other to determine the fault type. Herein, the ratio of $E_{PRS,VPG}/E_{PRS,VPP}$ is calculated and compared against λ_{FT} threshold. This threshold can be found by trial and error on the microgrid system. Since $E_{PRS,VPG}$ is significantly higher than $E_{PRS,VPP}$ for PG faults, λ_{FT} is always greater than 1. As a rule of thumb, the threshold is selected at around 10% of the $E_{PRS,VPG}/E_{PRS,VPP}$ ratio for the remote end PP and PG faults.

Once the fault type (i.e., PP versus PG) is identified, an SVM classifier is used to find if the fault is resistive or bolted. SVM has been proposed as a strong classification tool. For this purpose, multiple bolted and resistive faults are simulated at different locations of cable (e.g., every 25 m) in a simulation software package (e.g., PSCAD/EMTDC). It should be noted that the fault resistance values adopted in the simulations depend on the DC microgrid conditions like voltage level or geographical location. After the simulation results are gathered, the SVM classifier is trained using the labeled Parseval energy values. For PP faults, the inputs to the SVM classifier are the N level Parseval energy values of pole current and PP voltage at the sensor location. For PG faults, the inputs to the SVM classifier are the N level Parseval energy values of pole current and PPG voltage at the sensor location. The output of the classifier is the fault resistance value.

4.2.2.3. Fault Location Algorithm

Once the fault type is classified, first, the proposed approach ensures that the fault is located on the primary cable. To this end, the Parseval energy value of the current flowing through the protection relay sensor, $E_{PRS,I}$, is calculated. Depending on the fault type, $E_{PRS,I}$ is compared against the precalculated Parseval energy value related to the remote end bolted PP, resistive PP, bolted PG, or resistive PG fault. The proposed fault location algorithm relies on the Parseval energy values gathered from MRA. The algorithm utilizes the first N levels of MRA, calculates the Parseval energy of the first TW incidents, and then utilizes GP regression engines to find the fault location.

The fault location algorithm utilizes different GP regression engines corresponding to bolted and resistive PP and PG faults. In order to effectively train the GP regression engine, the number of MRA levels, N, requires to be greater than or equal to three. Although the higher value of N increases the accuracy of the GP regression engine, increasing the levels of MRA decreases the speed of the fault location algorithm as MRA has a slower response for lower frequency ranges. The value of Parseval energy selected for each decomposition level is the value that is observed after the first traveling wave corresponding to that decomposition level reaches the sensor location. In this report, to effectively train the GP regression engine, the Parseval energy of MRA's six levels at multiple fault locations (e.g., every 25 m of the cable) are utilized. Once trained, the GP regression tool can identify the fault location using the Parseval energy of MRA's six levels for any new fault scenario on the cable.

Herein, six MRA's levels are used as the inputs to the GP regression engine. Generally, it is preferred to utilize more MRA's levels in order to cover more signatures of the fault current at a wider frequency range. However, with a higher MRA level, the computational time of the algorithm becomes significantly higher, which in turn slows down the protection scheme. Therefore, six levels of MRA are selected to provide a tradeoff between the comprehensiveness of fault current signatures and the computational efficiency of the algorithm. It should be noted the proposed protection scheme can effectively work with different DWT sampling frequencies. The DWT sampling frequency only impacts the speed of the fault location algorithm. With a higher sampling frequency, MRA is able to calculate the first N levels of wavelet coefficients faster. For example, with 8 MHz sampling frequency and six MRA levels, the proposed algorithm will be able to find the fault location in 200 μs. With the recent advancements in signal processing and measurement technologies, high-frequency data sampling and measurement can be easily accommodated for the implementation of the proposed scheme. In fact, existing commercial TW relays are able to perform very high frequency (in the order of MHz) measurements.

4.2.2.3.1. Physics-informed ML-based Fault Location Algorithm [41]

Even though the regular GP algorithm results in an accurate fault location, it requires an extensive number of simulations in order to extract high fidelity Parseval energy curves to train GP engine. To tackle this challenge, we also created a physics-informed machine learning approach to accommodate the training of the machine learning engine with a limited number of measurements and labeled datasets. If one can extract the Parseval energy curves of a specific cable type and configuration in a simple DC system, then those Parseval energy curves can be used for fault location on the cables in another DC system with similar cable types and configurations. In fact, the Parseval energy curves for cables act as physics-based constraints that facilitate the generalization of data points required for the training of machine learning algorithms. For a specific cable type and configuration, regardless of the cable's length, the Parseval energy curves will have a similar pattern in any DC system. Only the Parseval energy curve magnitudes will change based on the change of DC system specifications (e.g., architecture, loads, converter's ratings, etc.). So, once the Parseval energy curve patterns for a specific cable type and configuration are extracted, those Parseval energy patterns can be used to identify the Parseval energy curves in any DC system regardless of its size, number of integrated converters, number of cables, etc. This approach will significantly decrease the time required to run an extensive number of simulations required for extracting high fidelity Parseval energy curves which in turn increases the scalability of MRA-based TW fault location in DC systems. After the Parseval energy curves are extracted, they are utilized to train the GP estimator. The GP estimator only needs the Parseval energy values of the current measured at the protection device (PD) location to estimate fault location. The proposed algorithm resembles a physics-informed ML approach where the GP estimator relies on the Physics laws that describe the Parseval energy curve patterns of DC cables. Our proposed fault location algorithm is summarized as follows:

Step 1: On a simple DC system, the Parseval energy values for the current at the protection device location are captured for multiple fault locations (e.g., at every 25m of the line/cable length) using PSCAD/EMTDC. This report uses at least six MRA frequency levels to incorporate an adequate portion of the frequency spectrum for extracting fault current features as the fault location changes.

Step 2: We use the patterns of the extracted Parseval energy curves from the simple DC system to identify the Parseval energy curves for a specific protection device in the DC microgrid under study. To this end, we need Parseval energy values for faults at some sample locations (l_k) along the cable protected by the protection device in the DC microgrid under study. The Parseval energy values of faults at these sample locations will be used to tune the magnitude of the Parseval energy curves. Our goal here is to construct Parseval energy curves with 25m fault location resolution. To this end, the Parseval energy values of fault locations at every 25m (l_n) are constructed by the Parseval energy values of the closest sample location using:

$$E_{PRS,i,l_n} = \frac{E_{PRS,i,l_k} E'_{PRS,i,l_n}}{E'_{PRS,i,l_k}}, \tag{1}$$

where E'_{PRS,i,l_n} and E'_{PRS,i,l_k} are the *i*th MRA level's Parseval energy values captured from simple DC system at faults at locations l_n and l_k. E_{PRS,i,l_n} and E_{PRS,i,l_k} are the i^{th} MRA level's Parseval energy values captured from DC microgrid under test for faults at locations l_n and l_k. It should be noted that the Parseval energy values of the sample locations can be either gathered from field measurements or from the simulation model of DC microgrid under study in PSCAD.

Step 3. Once the Parseval energy curves with 25 m fault location resolution are constructed for the protection device in the DC microgrid under study, the Parseval energy values will be used to train a GP regression engine (see Figure 115). Once the GP engine is trained, one can use it to find fault location for any new fault scenarios by feeding the measured Parseval energy values at the protection device location to the GP engine.

Remark 1: Mother wavelet can significantly impact the accuracy and speed of the MRA. It is of particular importance to select a suitable mother wavelet for the proposed fault location algorithm. The criteria for selecting a mother wavelet are: (i) incorporating enough number of vanishing points for accounting for the salient features of waveforms, (ii) sharp cutoff frequencies to minimize the amount of energy leakage to the next decomposition level, and (iii) being orthonormal, (iv) minimum description length (MDL). Daubechies (db) mother wavelets are promising candidates that comply with the aforementioned criteria and facilitate fast and accurate MRA.

Remark 2: The proposed protection approach can also provide backup protection for forward cables that are located in front of the protection relay. This is achieved by calculating the Parseval energy value related to faults applied at the remote end of the shortest forward cable. If the Parseval energy of the current flowing through the protection relay sensor is lower than the precalculated Parseval energy value of a fault applied at the remote end of the primary cable and greater than the Parseval energy value related to a fault applied at the remote end of the shortest forward cable, then the protection relay can provide backup protection. In order to coordinate backup and primary protection relays, the backup protection should operate with a delay named the CTI. The CTI (i) should be greater than the operating time of primary protection relay, (ii) should be greater than the operating time of solid-state DC circuit breaker, which is assumed to be around 200 μs, and (iii) must include a 20% security margin. For example, if the operating time of the primary relay is 200 μs, then the CTI is equal to (200+200)×1.2=480 μs.

The verification results for the performance of discussed fault location techniques are provided in [40].

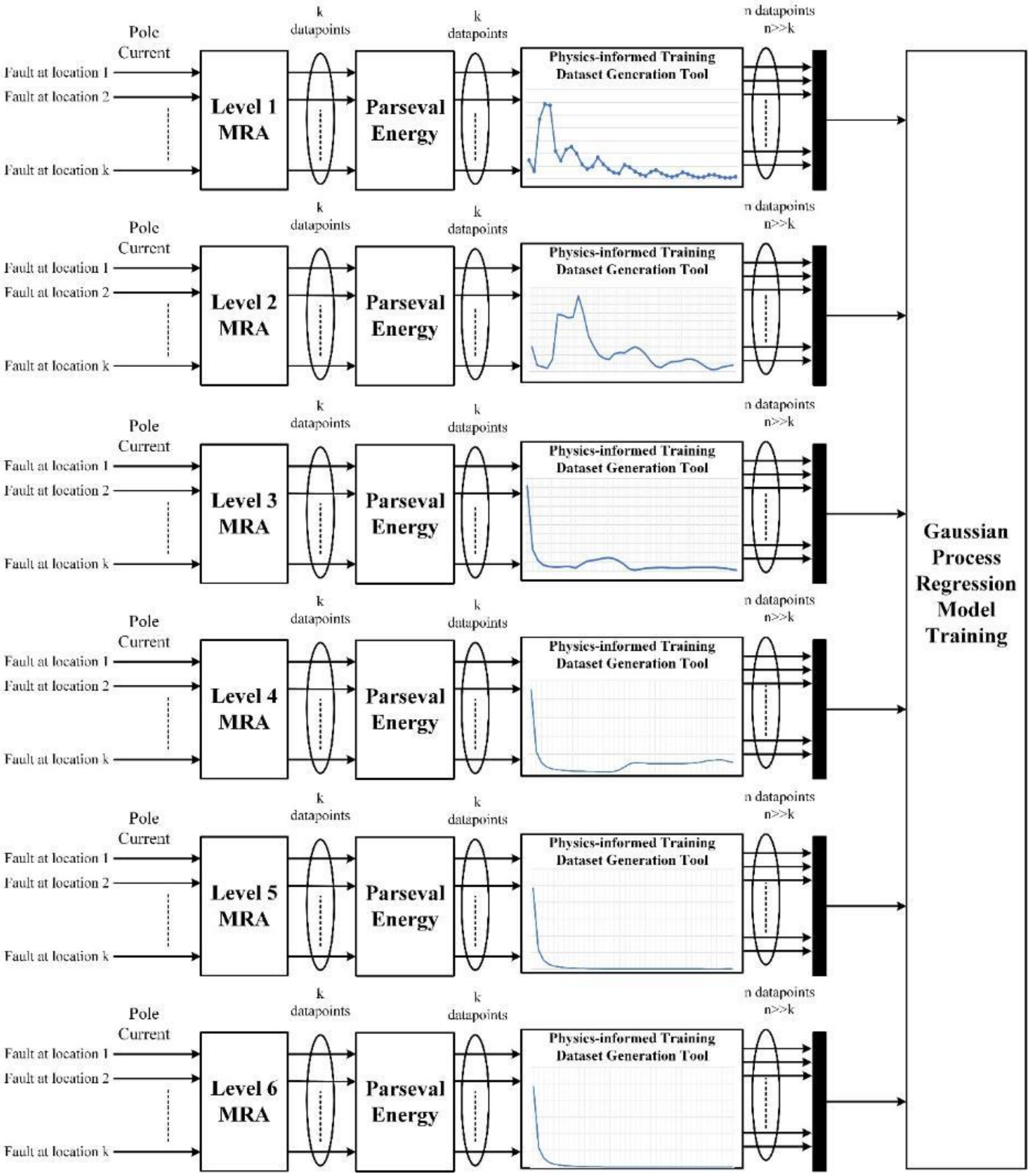

Figure 115. Gaussian process regression model training procedure.

4.2.3. Hardware Implementation of a TW Protection for the Emera DC Microgrid

We implemented a traveling wave protection device (TWPD) for Emera DC microgrid on a Texas Instrument's DSP board called TMS320F28379D. TMS320F28379D is a device member of the C2000™ microcontroller (MCU) product family. These devices are mostly used within embedded control applications. The F28379D dual-core MCU design is based on the TI 32-bit C28x CPU architecture. Each core is identical with access to its own local RAM and flash memory, as well as globally shared RAM memory. Sharing information between the two CPU cores is accomplished with an Inter-Processor Communications (IPC) module. Additionally, each core shares access to a common set of highly integrated analog and control peripherals, providing a complete solution for demanding real-time high-performance signal processing applications, such as digital power, industrial drives, inverters, and motor control [42].

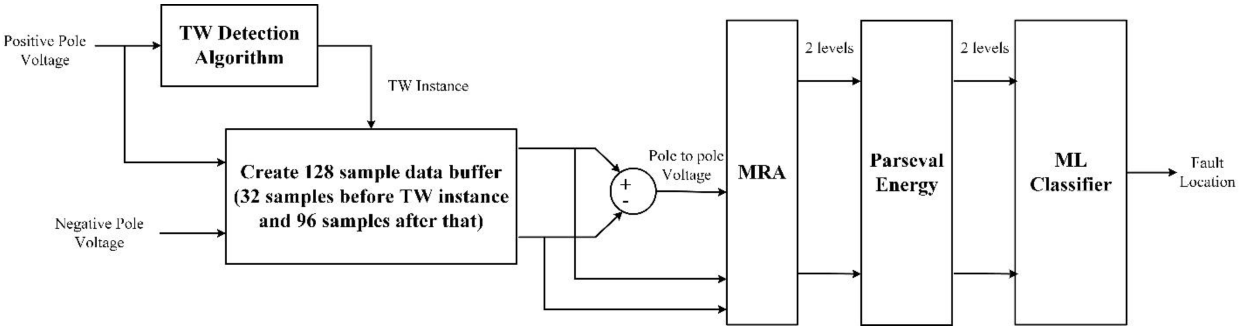

Figure 116. The TW fault detection algorithm for Emera microgrid.

The proposed algorithm is shown in Figure 116. The initial step is to perform high-fidelity sampling on the measured signals. We have implemented this step by considering a 1 MHz sampling rate on the positive and negative pole voltages that are fed to the Analog Input (AI) card of DSP. The utilized DSP has two cores. Each core is associated with a co-processor, namely the Control Law Accelerator (CLA). This enables DSP to perform parallel Floating-Point Unit (FPU) processing. The CLA can enhance DSP's bandwidth for computing purposes by allowing CPU to focus on other tasks rather than reading results from the ADC. The ADC peripheral has two sampling resolutions of 12 or 16 bits. It can also have 16 or 8 different ADC channels, respectively. This depends on the sampling resolution. The CLA then reads 128 samples from ADC samples and raises a flag to inform CPU when 128 samples are collected. These 128 samples are stored in a moving buffer as a new sample is read. DSP has an FPU library that is capable of the execution of optimized complex mathematical operations.

The TW detection algorithm (discussed in the following sections) is applied on the positive pole voltage to detect the fault incident. The algorithm requires knowing the fault instance in order to create an appropriate data buffer for the MRA stage. The fault location algorithm uses positive, negative, and pole-to-pole voltage signals. The DSP board only reads positive and negative pole voltages and calculates the pole-to-pole voltage from these two measurements. Once the TW incident is detected, a data buffer is created for each of the three signals as inputs to the MRA stage to calculate MRA coefficients. Each signal has a length of 128 samples and is given as an input to calculate its wavelet decomposition and reconstruction. In our approach, the data buffer includes 32 data samples before the TW detection instance, and 96 samples after the TW detection instance. If the TW instance ID is less than 32, samples from the previous data buffer are required in addition to the samples from the current buffer. If the TW ID is greater than 32, one requires to use data from the next data buffer, which creates a delay. If the TW ID is exactly 32, the current 128-sample buffer is used. We propose to perform two levels of MRA and calculate the Parseval energy values for these two levels.

The DWT in MRA uses Daubechies4 as the mother wavelet, which has a filter length of 8 and performs two levels of decomposition and reconstruction. For the sampling frequency of 1 MHz, the first level of DWT decomposition results in detailed coefficients that correspond to the frequency range from 250 to 500 kHz. Since the convolution library in DSP applies zero padding, one needs to account for the effect of zero padding to avoid the edge effect on the processed data.

To this end, in every data buffer, the algorithm adds the last 7 samples from the previous buffer to the current buffer. This results in 142 coefficients after performing convolution. The algorithm then discards the first and last 7 samples. However, for the first data buffer that DSP reads, since no previous buffer is available, the algorithm removes the first and last 7 samples from the results of the convolution stage and then zero pads the beginning of the signal with 7 zeros. This process is followed by performing the second level of decomposition and two levels of reconstruction which eventually creates MRA coefficients with a length of 128 samples. For these coefficients, we calculate the corresponding Parseval energy values. The calculated Parseval energy values will be used as inputs to a RF Classifier to identify the faulted node. The comparison of calculated Parseval energy values for a pole-to-pole voltage (VPP) captured from the Emera microgrid at the Central box for a pole-to-pole fault with 4.7 Ω resistance at Sandia's Distributed Energy Technologies Laboratory (DETL) is shown in Figure 117.

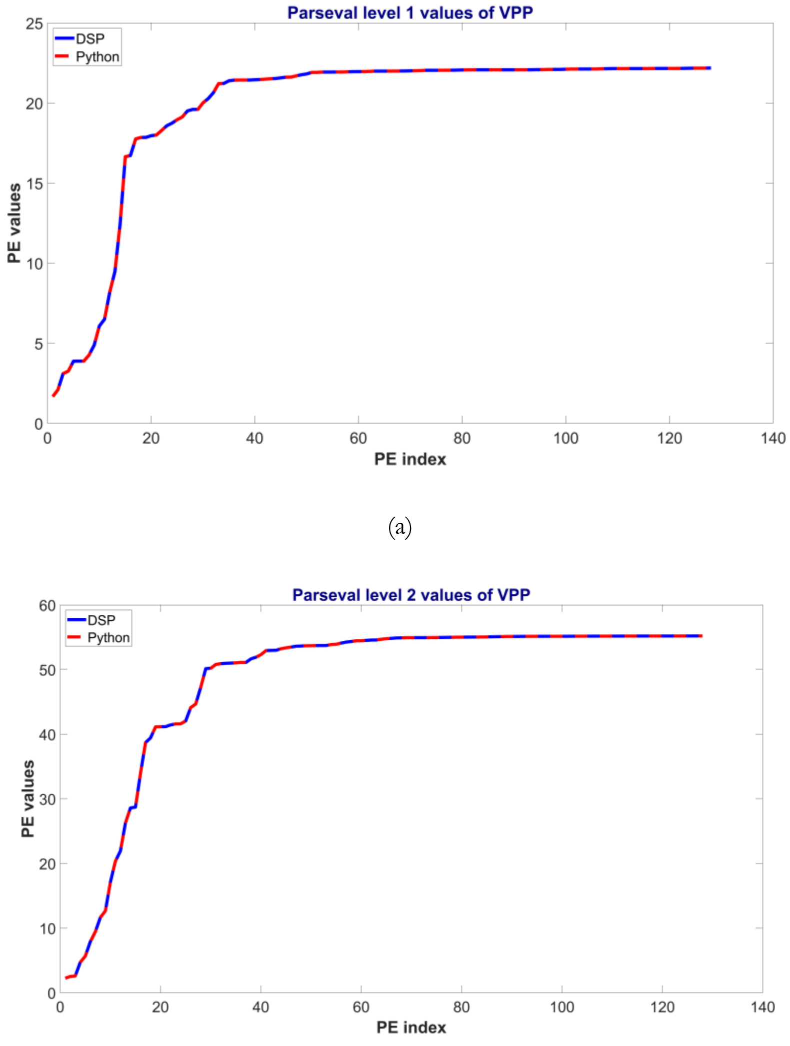

(a)

(b)

Figure 117. (a) Comparison of level 1 Parseval energy calculated in DSP versus Python for VPP; (b) Comparison of level 2 Parseval energy calculated in DSP versus Python for VPP.

In order to train the RF classifier, we performed a large number of fault simulations in the PSCAD model of the Emera microgrid. The fault simulations are performed on the circuit configuration shown in Figure 118. The sensor locations are also highlighted in this figure. The faults are applied at three nodes (Central box [CENT], DETL, and Gathering Space [GATH]). We apply different types of faults including PP, PPG, and NPG. The fault resistance values vary from 0 to 10 **Ω**. The PSCAD model is a replica of the Emera microgrid and has frequency-dependent cable models to capture TWs at different frequency ranges. A comparison between the real measurements from Emera microgrid and simulated fault current in PSCAD is provided in Figure 119 to Figure 122. The data used for training RF classifier should first be normalized to maximize the accuracy of the classifier. To this end, we utilize the Z-Score normalization method and apply it to the data extracted from PSCAD simulations. The Z-Score normalization should also be applied on positive, negative, and pole-to-pole voltage signals in DSP before feeding them to MRA stage.

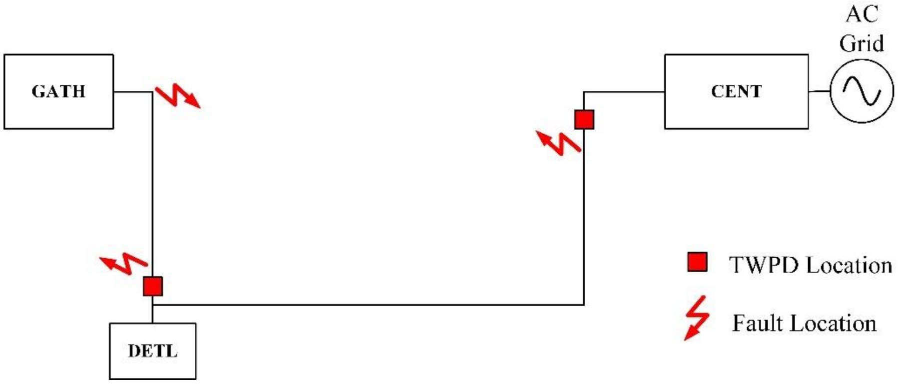

Figure 118. Radial configuration of Emera microgrid and location of faults and sensors.

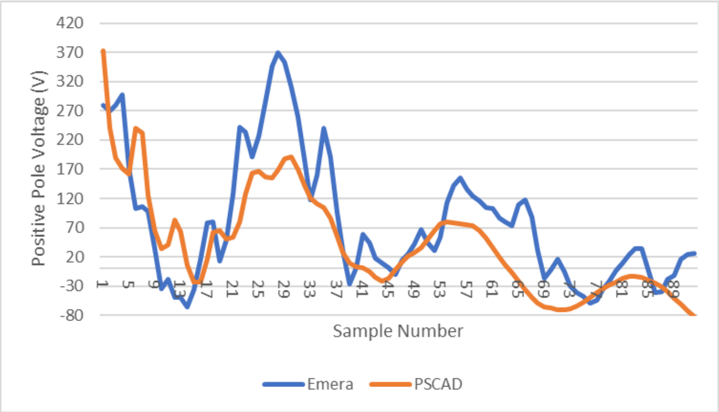

Figure 119. PSCAD model validation: Positive pole voltage for a positive pole to ground fault at Gathering Space with 1 Ω resistance (measurement at DETL).

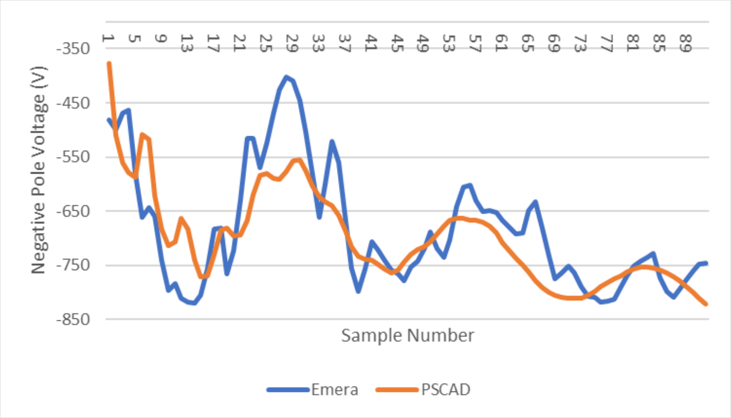

Figure 120. PSCAD model validation: Negative pole voltage for a positive pole to ground fault at Gathering Space with 1 Ω resistance (measurement at DETL).

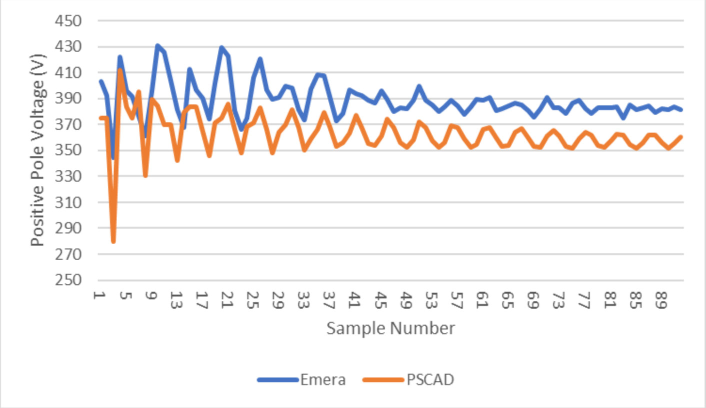

Figure 121. PSCAD model validation: Positive pole voltage for a pole to pole fault at DETL with 4.7 Ω resistance (measurement at Central Box).

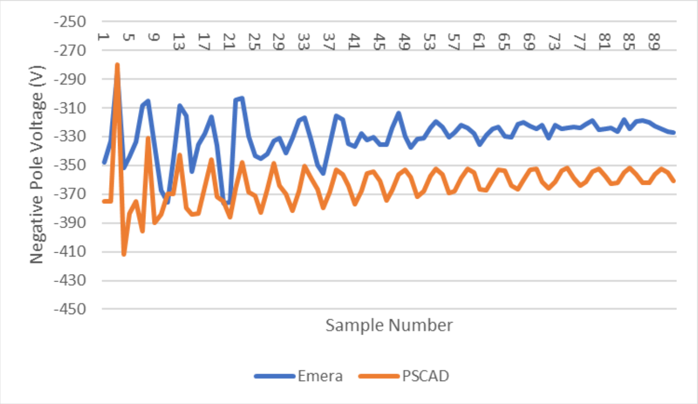

Figure 122. PSCAD model validation: Negative pole voltage for a pole to pole fault at DETL with 4.7 Ω resistance (measurement at Central Box).

The TWPD at DETL is designated to detect and identify faults in front of it (i.e. DETL and GATH), serving as primary protection. The TWPD at CENT is responsible for locating faults at CENT, DETL, and GATH. It should be noted that for the faults occurring in front of the TWPD at DETL, this protection device acts as the primary protection and the TWPD at CENT acts as a backup protection, i.e., it should operate with some delay for faults occurring at DETL and GATH.

This delay depends on the operating time of the DC circuit breaker located at DETL on the cable going to GATH. We have developed two distinct RF models: One is for situations where the TWPD is located at CENT, and another is for cases where the TWPD is situated at DETL. These models are designed to accurately locate and identify various fault types. We have optimized the performance of the RF algorithm by fine-tuning its hyperparameters. Specifically, we set the number of estimators to 120 and chose the 'gini' criterion, which offers computational efficiency over 'entropy'. The random state was determined to be 3 as optimum through Python analysis during RF model training. We performed cross-validation, achieving an accuracy of 85% for a value of fold 12. However, due to the enabled bootstrap (set as True), cross-validation isn't necessary. In random forests, cross-validation or a separate test set isn't required to estimate test set error, as each tree is constructed from a different bootstrap sample. A maximum depth of 12 was selected to optimize accuracy, based on hyperparameter tuning during RF model training. Consequently, the RF model demonstrated an accuracy of 95.45% for TWPD at CENT location and 95% for TWPD at the DETL location.

The training data for RF is labeled as shown in Table 37 (TWPD at CENT) and Table 38 (TWPD at DETL). We put the trained RF classifier to work on the DSP board by utilizing the 'emlearn' function of Python. To validate its performance, we conducted offline testing using actual data from the microgrid when TWPD is at CENT location for a pole-to-pole fault with 4.7 Ω resistance at DETL. This real-world experiment helps us assess how well our algorithm works in a genuine environment. The response of the DSP board to this fault is shown in Figure 123. As seen, the predicated class by DSP is 3, which, based on Table 37, denotes a pole-to-pole fault at DETL.

Table 37. RF data labels for TWPD at CENT.

Fault Location and Type	Label
Pole to ground fault at CENT	0
Pole to pole fault at CENT	1
Pole to ground fault at DETL	2
Pole to pole fault at DETL	3
Pole to ground fault at GATH	4
Pole to pole fault at GATH	5

Table 38. RF data labels for TWPD at DETL.

Fault Location and Type	Label
Pole to ground fault at DETL	0
Pole to pole fault at DETL	1
Pole to ground fault at GATH	2
Pole to pole fault at GATH	3

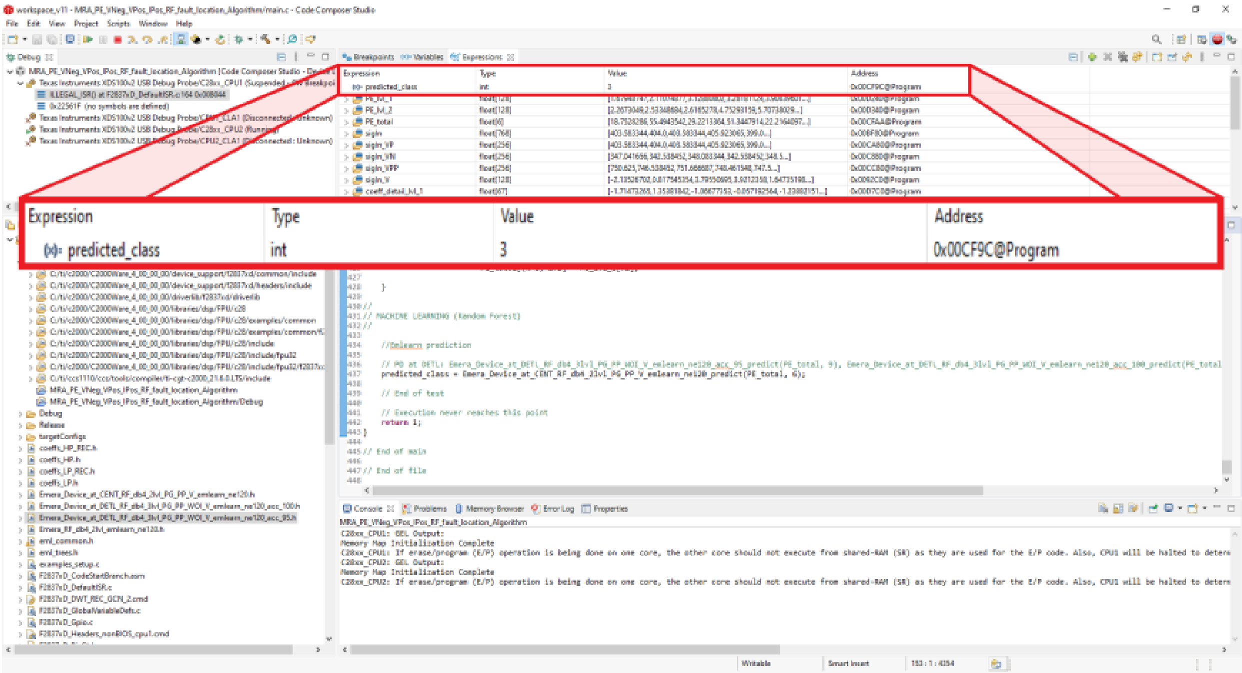

Expression	Type	Value	Address
predicted_class	int	3	0x00CF9C@Program
PE_lvl_2	float[128]	[2.2673049,2.53348684,2.6165278,4.75293159,5.70738029...]	0x00D340@Program
PE_total	float[6]	[18.7528286,55.4943542,29.2213364,51.3447914,22.2164097...]	0x00CFAA@Program
sigIn	float[768]	[403.583344,404.0,403.583344,405.923065,399.0...]	0x00BF80@Program
sigIn_VP	float[256]	[403.583344,404.0,403.583344,405.923065,399.0...]	0x00CA80@Program
sigIn_VN	float[256]	[347.041656,342.538452,348.083344,342.538452,348.5...]	0x00C880@Program
sigIn_VPP	float[256]	[750.625,746.538452,751.666687,748.461548,747.5...]	0x00CC80@Program
sigIn_V	float[128]	[-2.13526702,0.817545354,3.79550695,3.9212358,1.64735198...]	0x0092C0@Program
coeff_detail_lvl_1	float[67]	[-1.71473265,1.35381842,-1.06677153,-0.057192564,-1.23882151...]	0x00D7C0@Program

```
    }

//
// MACHINE LEARNING (Random Forest)
//

    //Emlearn prediction

    // PD at DETL: Emera_Device_at_DETL_RF_db4_3lvl_PG_PP_WOI_V_emlearn_ne120_acc_95_predict(PE_total, 9), Emera_Device_at_DETL_RF_db4_3lvl_PG_PP_WOI_V_emlearn_ne120_acc_100_predict(PE_total
    predicted_class = Emera_Device_at_CENT_RF_db4_2lvl_PG_PP_V_emlearn_ne120_predict(PE_total, 6);

    // End of test

    // Execution never reaches this point
    return 1;
}

// End of main

// End of file
```

MRA_PE_VNeg_VPos_IPos_RF_fault_location_Algorithm

```
C28xx_CPU1: GEL Output:
Memory Map Initialization Complete
C28xx_CPU1: If erase/program (E/P) operation is being done on one core, the other core should not execute from shared-RAM (SR) as they are used for the E/P code. Also, CPU1 will be halted to determ
C28xx_CPU2: GEL Output:
Memory Map Initialization Complete
C28xx_CPU2: If erase/program (E/P) operation is being done on one core, the other core should not execute from shared-RAM (SR) as they are used for the E/P code. Also, CPU1 will be halted to determ
```

Figure 123. Fault prediction using DSP where TWPD is at CENT when a pole-to-pole fault occurs at DETL.

During offline testing of TWPD at the DETL location, we used the faults positive pole to ground and negative pole to ground at GATH. Both the Python algorithm and the DSP accurately predicted the fault type as 2, indicating a pole-to-ground fault at GATH from the Table 38. The fault labels for the TWPD at DETL are provided in the Table 38, and the prediction outcomes from both Python and DSP are shown in the below figure.

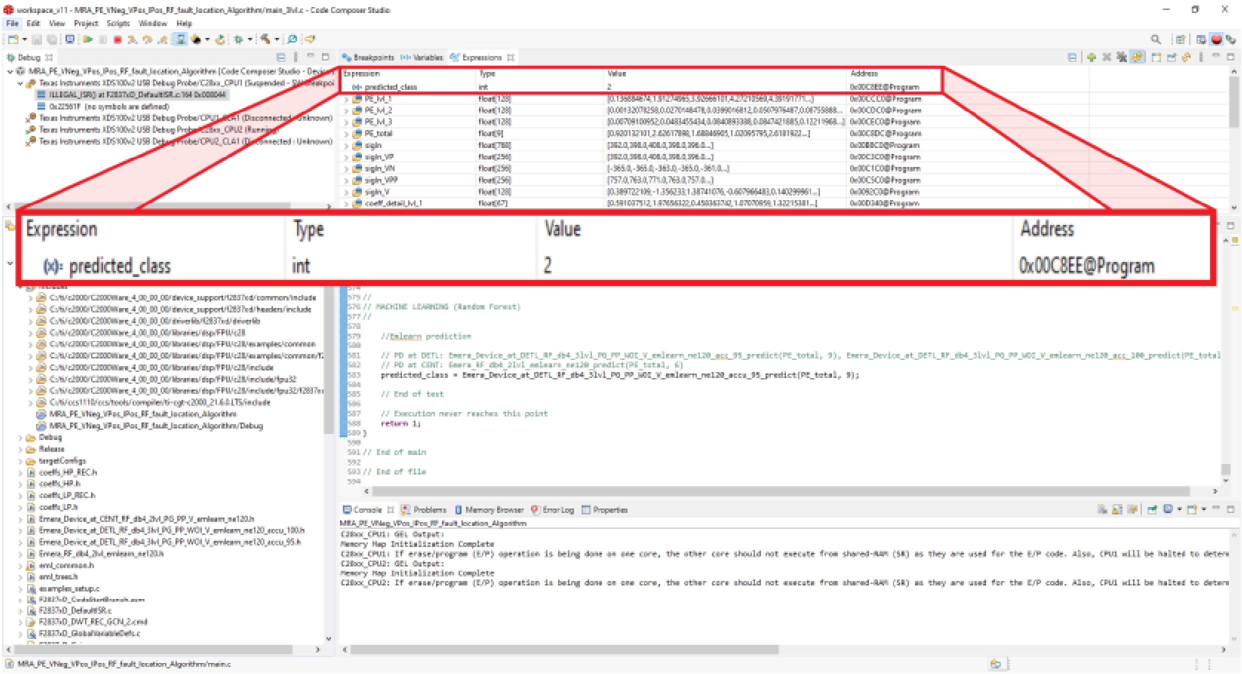

Expression	Type	Value	Address
(x)= predicted_class	int	2	0x00C8EE@Program
PE_lvl_1	float[128]	[0.136884674,1.91274965,3.92666101,4.27210569,4.38191771...]	0x00CCC0@Program
PE_lvl_2	float[128]	[0.00132078258,0.0270148478,0.0399016812,0.0507976487,0.08755888...	0x00CDC0@Program
PE_lvl_3	float[128]	[0.00709100952,0.0483455434,0.0840893388,0.0847421885,0.13211968...]	0x00CEC0@Program
PE_total	float[9]	[0.920132101,2.62617898,1.68846905,1.02095795,2.6181922...]	0x00C8DC@Program
sigIn	float[780]	[382.0,398.0,408.0,398.0,396.0...]	0x00B8C0@Program
sigIn_VP	float[256]	[382.0,398.0,408.0,398.0,396.0...]	0x00C3C0@Program
sigIn_VN	float[256]	[-365.0,-365.0,-363.0,-365.0,-361.0...]	0x00C1C0@Program
sigIn_VPP	float[256]	[757.0,763.0,771.0,763.0,757.0...]	0x00C5C0@Program
sigIn_V	float[128]	[0.389722109,-1.356233,1.38741076,-0.607966483,0.140299961...]	0x0092C0@Program
coeff_detail_lvl_1	float[67]	[0.591037512,1.97656322,0.458363742,1.07070959,1.32215381...]	0x00D340@Program

```
//
// MACHINE LEARNING (Random Forest)
//

    //Emlearn prediction

    // PD at DETL: Emera_Device_at_DETL_RF_db4_3lvl_PG_PP_WOI_V_emlearn_ne120_acc_95_predict(PE_total, 9), Emera_Device_at_DETL_RF_db4_3lvl_PG_PP_WOI_V_emlearn_ne120_acc_100_predict(PE_total
    // PD at CENT: Emera_RF_db4_2lvl_emlearn_ne120_predict(PE_total, 6)
    predicted_class = Emera_Device_at_DETL_RF_db4_3lvl_PG_PP_WOI_V_emlearn_ne120_accu_95_predict(PE_total, 9);

    // End of test

    // Execution never reaches this point
    return 1;
}

// End of main

// End of file
```

MRA_PE_VNeg_VPos_IPos_RF_fault_location_Algorithm

```
C28xx_CPU1: GEL Output:
Memory Map Initialization Complete
C28xx_CPU1: If erase/program (E/P) operation is being done on one core, the other core should not execute from shared-RAM (SR) as they are used for the E/P code. Also, CPU1 will be halted to deterr
C28xx_CPU2: GEL Output:
Memory Map Initialization Complete
C28xx_CPU2: If erase/program (E/P) operation is being done on one core, the other core should not execute from shared-RAM (SR) as they are used for the E/P code. Also, CPU1 will be halted to deterr
```

Figure 124. Fault prediction using DSP where TWPD is at DETL when a pole-to-ground fault occurs at GATH.

5. FAULT LOCATION TECHNIQUES

5.1. Summary of Work Performed

To add to the approaches covered by this project that use high frequency sampling for fault location in AC and DC microgrids, this work focused on physics-based solutions in time-domain. The idea was to utilize the Kirchhoff's Voltage Law (KVL) equations in time domain and calculate the terms in the equations using the rapidly sampled data points corresponding to the measured voltages and currents. We employed 1 MHz sampling rate in our formulation as there are commercial relays already deployed in field that sample ac waveforms at this rate. Our objective was to develop single-ended fault location methods for both AC and DC microgrids. We wanted to achieve closed form solutions for single-ended fault locations that were immune to fault resistance – a task that has always eluded researchers as fault resistance introduces an unknown that prevents phasor domain solutions to obtain enough independent equations to solve this single-ended problem. However, each new dataset in time domain yields a different equation. The idea was to use this advantage to obtain enough equations to get solutions immune to fault resistance. Time domain equations will obviously involve time derivatives of voltages and currents, which we planned to obtain accurately by using successively sampled values at high sampling rate.

For AC feeders, this ambitious task could not be fully realized, as it turned out that the symmetry of the AC waveforms yielded redundant equations, even for samples taken at different time stamps. However, the work produced a time domain distance relay that does not need polarization. In view of the extensively reported problem of failing negative sequence polarization in legacy numerical relays in presence of IBRs, this was an extremely significant result. The relay works accurately even with short, highly unbalanced distribution lines as the formulation included mutual coupling of unbalanced circuits. Additionally, with only one time-sample from the opposite end, the relay becomes immune to fault resistance, providing accurate fault location. This work has been submitted as a provisional patent. We also extended this concept to create a directional element that does not need a high sampling rate and does not need any polarization. This element can be easily integrated into any legacy numerical relay. We plan to either augment the patent with this work or start a new patent.

Our distance relay was shown to outperform the traveling wave based legacy relay that has one critical weakness (among others) of failing when the fault occurs at an instant when the voltage waveform is passing through zero crossing, as no traveling wave results in this case. This was demonstrated by connecting the SEL 401L relay as hardware in the loop with Clemson's real-time simulator (RTDS) setup, and using the same samples created within this relay to test our method. Our directional relay was also similarly tested and shown to outperform the SEL 421 relay that needs polarization, as it is formulated in phasor domain. Formulation and testing of time domain distance relay is described in detail in [43], and the directional element and its testing is described in [44].

For DC feeders, due to the exponential nature of the rise in fault current, the proposed approach yielded a closed form solution for single ended fault location that is immune to fault resistance. Only three fault samples are needed to detect and locate a fault on a DC feeder fed from both ends by dc-dc converters. The solution is agnostic to the topology of the DC microgrid that contains the feeder. This work has been submitted for a patent and is reported in detail in [45]. The solution was then repurposed for main and backup protection in a DC microgrid. The models used for different components of the microgrid (i.e., load, converter, line parameters) are closely based on components of Emera's field-installed microgrid. A DC circuit breaker model is also incorporated to realistically model the operation of main and backup protection. The system was simulated in real time on the RTDS platform and successfully tested. It took some effort to run this system in real time at a 1 MHz sampling rate, even with 6 cores enabled on the new NovaCor platform. This work is documented in [46].

Finally, the primary protection scheme was implemented on a microcontroller and connected and tested in real time on RTDS. Since the current and voltage output from RTDS was converted to analog waveforms by the DAC card, noise was introduced in the signal. Therefore, a filter had to be implemented. Since all classical filters are conceived for periodic waveforms, choosing a filter to filter out noise from an exponent was an issue and had to be resolved using a second order low pass Butterworth filter, with its cutoff frequency selected by trial and error. This introduced a delay, but more importantly, slightly reshaped the exponent (the main signal) during the inception of fault, which adversely affected the accuracy of fault location. However, the primary protection still worked correctly, as the fault distance was within the line length. The work on DC systems in its entirety is documented in [47].

5.2. Time-Domain Distance and Directional Relays

5.2.1. Formulation of the Method

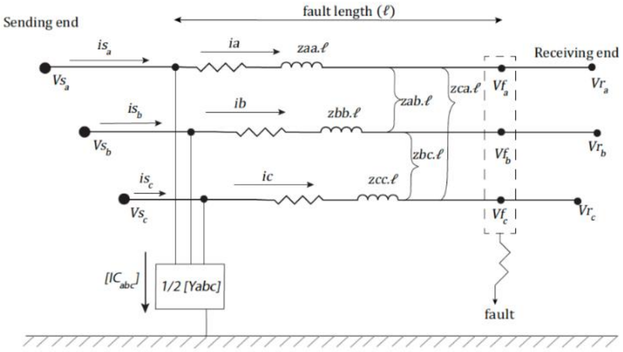

Figure 125. Model of an unbalanced transmission line.

Consider the line model shown in Figure 125. No transposition is assumed. This would require the equations to be formed in phase-domain as opposed to sequence domain. It is assumed that time-domain samples of voltages v_{sa}, v_{sb}, v_{sc}, and currents i_{sa}, i_{sb}, i_{sc}, are measured at a 1 MHz sampling rate, hence their derivatives can be calculated accurately using successive samples. Equations can be written as:

$$\mathrm{i_a = is_a - \left[C_{aa}\frac{dvs_a}{dt} + C_{ab}\frac{dvs_b}{dt} + C_{ac}\frac{dvs_c}{dt}\right]} \qquad \text{(B1)}$$

$$\mathrm{i_b = is_b - \left[C_{ab}\frac{dvs_a}{dt} + C_{bb}\frac{dvs_b}{dt} + C_{bc}\frac{dvs_c}{dt}\right]} \qquad \text{(B2)}$$

$$\mathrm{i_c = is_c - \left[C_{ac}\frac{dvs_a}{dt} + C_{bc}\frac{dvs_b}{dt} + C_{cc}\frac{dvs_c}{dt}\right]} \qquad \text{(B3)}$$

Here self and mutual capacitances are the total for the entire line, and therefore known. Following equations (B4 – B6) can further be written using the self and mutual resistance and inductances per unit length. *l* is the length to the fault, and vf_a, vf_b, vf_c are the fault voltages between each phase to ground, which are not known.

$$vs_a = vf_a + \left[iaR_{aa} + L_{aa}\frac{dia}{dt} + ibR_{ab} + L_{ab}\frac{dib}{dt} + icR_{ac} + L_{ac}\frac{dic}{dt}\right] l \tag{B4}$$

$$vs_b = vf_b + \left[ibR_{bb} + L_{bb}\frac{dib}{dt} + iaR_{ab} + L_{ab}\frac{dia}{dt} + icR_{bc} + L_{bc}\frac{dic}{dt}\right] l \tag{B5}$$

$$vs_c = vf_c + \left[icR_{cc} + L_{cc}\frac{dic}{dt} + iaR_{ac} + L_{ac}\frac{dia}{dt} + ibR_{bc} + L_{bc}\frac{dib}{dt}\right] l$$

(B4) can be re-written as:

$$\mathrm{vs_a = vf_a + Aal} \qquad \text{(B7)}$$

Here,

$$A_a = \left[iaR_{aa} + L_{aa}\tfrac{dia}{dt} + ibR_{ab} + L_{ab}\tfrac{dib}{dt} + icR_{ac} + L_{ac}\tfrac{dic}{dt}\right]$$

The logic is that if vf_a remains constant for two measurements, the following two equations (B8) can be formed and solved, yielding the length *l* as one of the solutions. Subscripts 1 and 2 denote the measurements taken at two different time instants.

$$\begin{aligned} vs_{a_1} &= vf_a + Aa_1 l \\ vs_{a_2} &= vf_a + A_{a_2} l \end{aligned} \qquad \text{(B8)}$$

Similar equations can be written for faulted phases b and c. Only one equation (of faulted phase) is needed for the calculation.

Assuming phase *a* to be a faulted phase, it was first assumed that vf_a will not change significantly over consecutive samples, which are separated by only 1 µs. This proved to be correct when the vf_a waveform was passing through peak and was "flatter" in nature, but there was no way to determine when that would happen. For other time instances the errors were high. The other approach was to locate the two points shown in Figure 126.

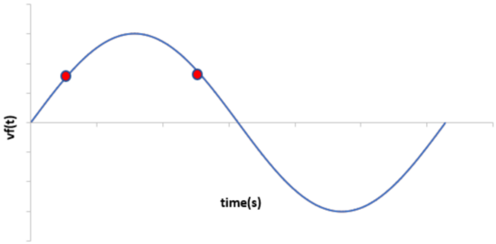

Figure 126. Two time-instances where fault voltage is the same due to symmetry.

Although one of the points can be obtained by solving (B7) when *Aa* equals zero, the second point could not be found, despite using several methods based on trigonometry, geometry, and iterations. This took a long time to explore. It should be noted here that allowing different values of Vf_a in (B8) and (B9) (say, Vf_{a1} and Vf_{a2}) will always yield one more unknown than the number of equations, no matter how many measurements are considered. Also, the equations were successfully solved while using the measured values of Vf_a from the simulations, so the formulation is correct. The problem now lies in obtaining the second instant on the waveform shown in Figure 126.

At this point, we conclude that we need one synchronized sample from the other end to obtain accurate fault location in presence of fault resistance. For zero fault resistance, the method works very well, as Vf_a is zero. Therefore, the single-ended method still has excellent value, as it will work regardless of the type of source behind the measurements, which solves a major industry problem of failure of the traditional distance relay with an IBR behind it. Even with traditional sources, the method outperforms the distance relay as it is unaffected by unbalanced lines, pre-fault currents, and immune to the decaying DC offset that affects distance relay calculations. Finally, the method does not require polarization, which is a huge advantage over distance relays, as the lack of negative sequence currents from IBRs is creating a serious issue with polarization of modern distance relays. Since it gives no errors due to unbalance, it can be ported to distribution feeders.

5.2.2. Results

The test system consists of a 230-kV overhead transmission line of length 150 km, unbalanced, and modeled using distributed line parameters. The live voltage and frequency are 230 kV and 60 Hz respectively. The tower configuration is a 3-conductor flat tower with 6 m of horizontal spacing between the conductors 20 m above the ground, and untransposed. Each phase has a stranded ACSR Chukar conductor.

Results for faults at 100 km without fault resistance are given in Table 39, showing the method is immune to known weaknesses of traditional distance relays. Table 40 shows the faults with fault resistances that can be located accurately using one synchronized sample from the other end.

Table 39. Calculated length using the proposed method for zero fault resistance.

Fault type	Calculated Length (km)	% error
LLLG	100.18	0.12
LG	100.7	0.47
LL	99.64	0.24
LLG	100.52	0.34

Table 40. Calculated length using proposed method using one synchronized sample from the other end.

Fault-Type	Fault Resistance (Ω)	Calculated Length (km)	% Error
LLLG	1	99.95	0.03
	10	99.94	0.03
	20	99.93	0.047
LG	1	99.93	0.047
	10	99.92	0.053
	20	99.91	0.06
LL	1	99.87	0.087
	5	99.86	0.093
	10	99.92	0.05
		99.94	0.035

LLG	1	99.91	0.06
	10	99.89	0.07
	20	99.88	0.08

The same transmission line was modified to have a lower impedance angle, and the sending end source was replaced with an IBR. This was to ensure the inverter power factor is significantly different than the impedance angle of the positive sequence line impedance. The IBR is a 100 MVA, 15 kV grid following inverter with controls set to provide full rated power during steady state operation at unity power factor and rated voltage.

This IBR is developed by applying the logic used in the Siemens-Gamesa inverter [48] for a grid-following inverter that applies Q priority during faults based on a Fault Ride Through (FRT) Curve shown in Figure 127. The FRT Curve blocks negative sequence currents and limits the current to 1.1 pu of the inverter rating. It essentially provides the reactive power dictated by the curve, and curtails the real power to adhere to the total current limit.

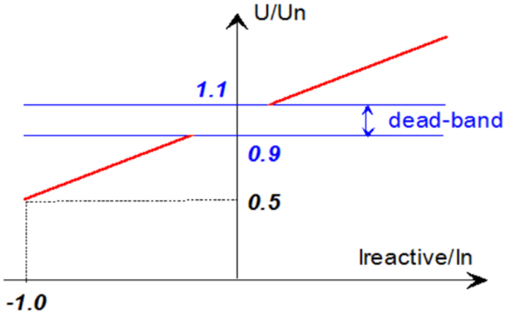

Figure 127. Siemens Logic implementation for grid following inverter.

Table 41. Calculated length using the proposed method in presence of IBR for zero fault resistance.

Fault type	Calculated Length (km)	% error
LLLG	59.75	0.16
LG	60.63	0.42
LL	60.28	0.19
LLG	59.4	0.4

For a LG fault at 60 km from the inverter bus, results with the proposed method are given in Table 41, showing the method is immune to known weaknesses of traditional distance relays that do not perform well without negative sequence currents for polarization. Faults with fault resistances could also be located accurately using one synchronized sample from the other end.

5.2.3. Performance for Faults on Distribution Feeders

The proposed method is tested in the IEEE 123-node test feeder that operates at a nominal voltage of 4.16 kV. The system has unbalanced overhead and underground lines, unbalanced loading with constant current, impedance, power loads, four voltage regulators, shunt capacitor banks, and multiple switches. Seven zones are formed. As shown in Figure 128, each zone can function as an island with 100% IBRs. In zones where loads exceed generation during islanding, load shedding is employed.

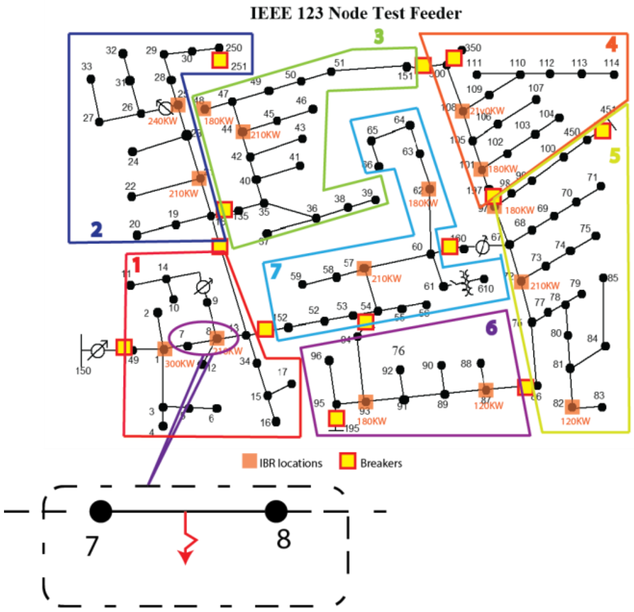

Figure 128. IEEE 123-node test feeder with added IBRs.

The load data and IBR placement with their generation capacity are summarized in Table 42 and Table 43 respectively. In islanded mode, one IBR is operated in grid forming mode and others in grid following mode. To test the proposed method, the 200 ft long unbalanced line between node 7 and 8 in the test feeder has been used.

In grid connected mode, faults were simulated at 100 feet from node 7. Table 44 shows the results using the proposed method in the distribution network with zero fault resistance. Faults with fault resistances could also be located accurately using one synchronized sample from the other end (node 8). For the same line segment, with the feeder now in islanded mode of operation (100% IBR), the method was used to calculate the distance to fault. Table 45 shows the results using the proposed method in the distribution network with zero fault resistance. Faults with fault resistances could also be located accurately using one synchronized sample from the other end (node 8).

Table 42. Load Data of the 123-node Test Feeder

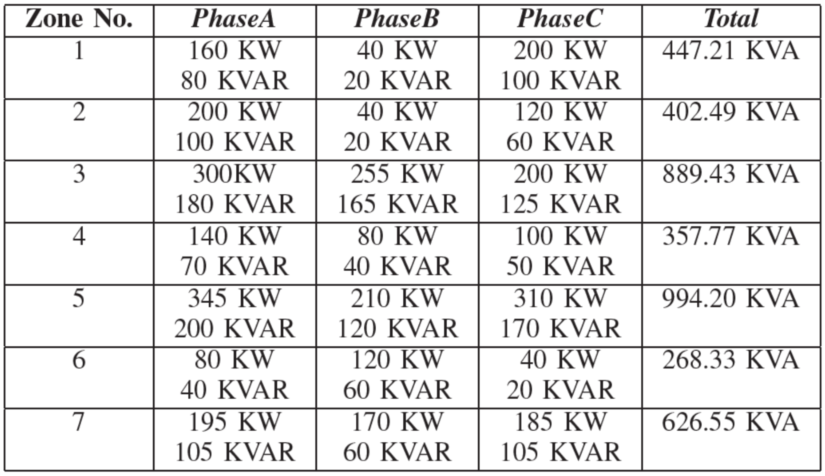

Zone No.	*PhaseA*	*PhaseB*	*PhaseC*	*Total*
1	160 KW 80 KVAR	40 KW 20 KVAR	200 KW 100 KVAR	447.21 KVA
2	200 KW 100 KVAR	40 KW 20 KVAR	120 KW 60 KVAR	402.49 KVA
3	300KW 180 KVAR	255 KW 165 KVAR	200 KW 125 KVAR	889.43 KVA
4	140 KW 70 KVAR	80 KW 40 KVAR	100 KW 50 KVAR	357.77 KVA
5	345 KW 200 KVAR	210 KW 120 KVAR	310 KW 170 KVAR	994.20 KVA
6	80 KW 40 KVAR	120 KW 60 KVAR	40 KW 20 KVAR	268.33 KVA
7	195 KW 105 KVAR	170 KW 60 KVAR	185 KW 105 KVAR	626.55 KVA

Table 43. IBR Placement and Generation Capacity

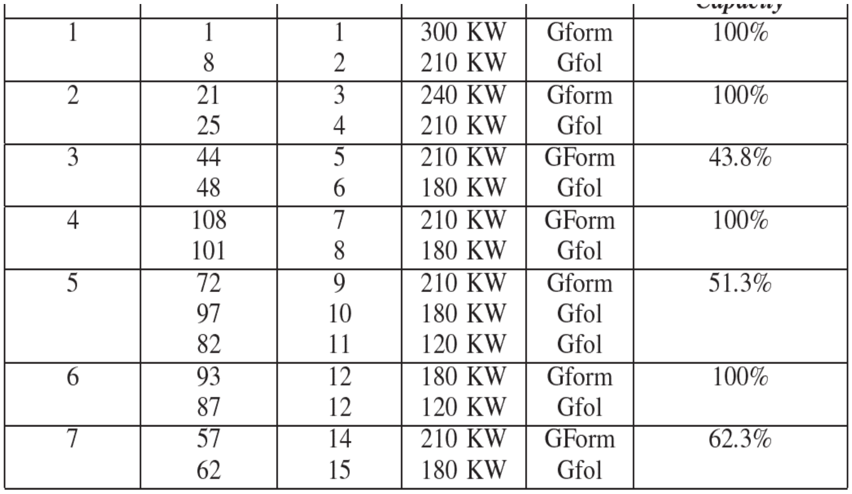

					Capacity
1	1 8	1 2	300 KW 210 KW	Gform Gfol	100%
2	21 25	3 4	240 KW 210 KW	Gform Gfol	100%
3	44 48	5 6	210 KW 180 KW	GForm Gfol	43.8%
4	108 101	7 8	210 KW 180 KW	GForm Gfol	100%
5	72 97 82	9 10 11	210 KW 180 KW 120 KW	Gform Gfol Gfol	51.3%
6	93 87	12 12	180 KW 120 KW	Gform Gfol	100%
7	57 62	14 15	210 KW 180 KW	GForm Gfol	62.3%

Table 44. Calculated length for zero fault resistance in grid connected mode.

Fault type	**Calculated Length (feet)**	**% error**
LLLG	101.05	0.525
LG	100.41	0.2

Table 45. Calculated length for zero fault resistance in islanded mode.

Fault type	**Calculated Length (feet)**	**% error**
LLLG	100.8	0.4
LG	100.4	0.2

5.2.4. Comparing the Performance with a Commercial Time Domain Relay

There is only one time domain relay commercially available: SEL 401L that uses TWs produced by faults. We hooked it up to our RTDS as hardware-in-the-loop. This means the RTDS will convert the voltage and current waveforms from our test setup to analog waveforms (as they occur in real power systems) and send the analog waveforms to the TW relay. TW relay will sample these at 1 MHz. We extract these samples, feed them to our algorithm, and assess the performance of our algorithm. Figure 129 shows this setup.

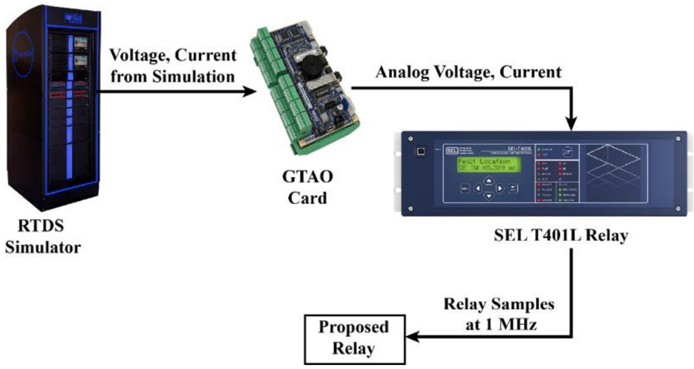

Figure 129. HIL Test-setup

The system simulated in RTDS is shown in Figure 130:

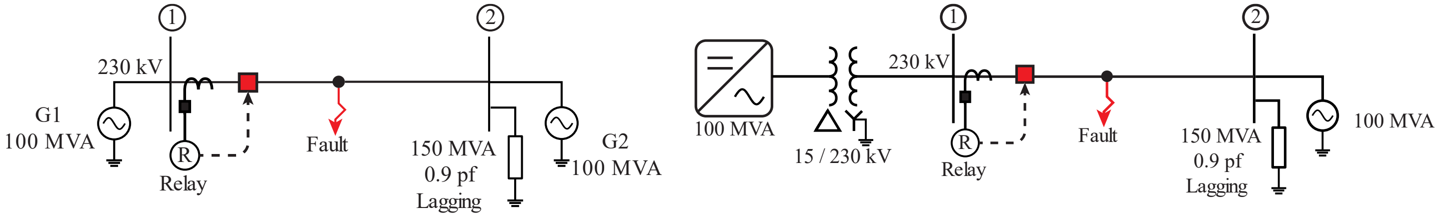

(a) (b)

Figure 130. Simulation system with (a) synchronous generator feeding the fault (b) IBR feeding the fault

Table 46. Comparison between the TW relay and the proposed method for AG fault.

Source Feeding the Fault	Fault instant	Fault distance (km)	Measured distance (km) by TW Relay	Measured distance (km) by proposed relay	%Error-proposed relay
SG	Voltage peak	60	60.628 km	61.96 km	1.3%
SG	Voltage zero	60	Fails	58.63 km	0.91%
IBR	Voltage peak	60	60.41 km	62.2 km	1.46%
IBR	Voltage zero	60	Fails	58.27 km	1.15%

Faults fed by both a synchronous generator (SG) and an IBR for two extreme cases were simulated and used for the tests: (a) when the fault occurs at the peak of the voltage waveform, causing larger voltage transients, and (b) when the fault occurs at voltage zero, resulting in maximum DC offset in the fault current, and negligible voltage transients. Table 46 shows the performance of the proposed relay as well as the TW relay. Predictably, the TW relay fails when faults occur at voltage zero, as no traveling waves are generated.

5.2.5. *Conversion to Directional Relay*

The same formulation was converted to a directional relay that can work at low sampling rates, as time derivatives are only needed for precise fault distance calculation. Equation (B7) can be rewritten as:

$$y = \frac{\mathrm{vs_a}}{\mathrm{Aa}} = \frac{\mathrm{vf_a}}{\mathrm{Aa}} + 1 \qquad \text{(B9)}$$

It can be shown [44] that the sign of dy/dt will be positive for forward fault and negative for reverse faults, even at sampling rates as low as 24 spc. Validation was performed using HIL simulation using SEL 421 relay, that has 32Q element for direction identification.

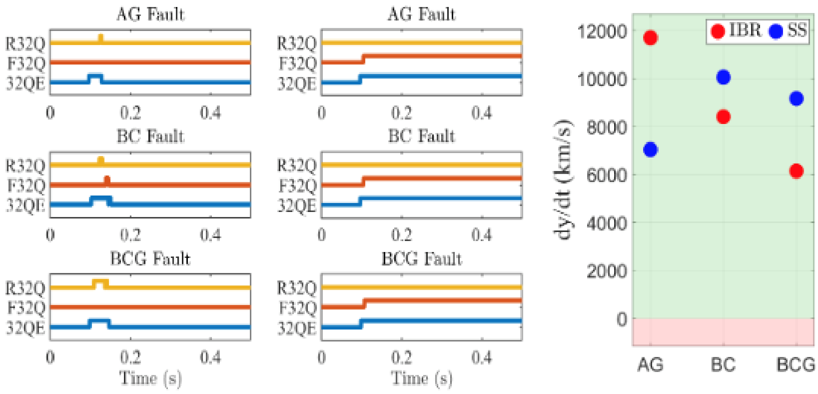

(a) (b) (c)

Figure 131. Direction asserted by (a) 321 directional element when fed by an IBR (b) 32Q1 directional element when fed by an SS and (c) proposed relay using the samples from 32Q1.

Figure 131 shows that throughout the fault period (fault starts at t = 0.1 s), except for a brief initial period, the 32Q elements remain disabled when the fault is fed by an IBR. The 32QE (32Q Enable) signal confirms this behavior. Even during the brief period when the 32Q1 is enabled, it misidentifies forward faults as reverse (R32Q is triggered for AG and BCG faults) or fails to discriminate the fault direction (both R32Q and F32Q are triggered for the BC fault). For faults fed by a synchronous source, it behaves expected. The proposed relay gives positive dy/dt for all faults and hence, correctly identifies the direction.

5.3. Single-Ended Fault Location and Protection of a DC Feeder in a DC Microgrid:

5.3.1. *Theory of Fault Location in a DC Feeder*

Figure 132(a) shows a two-bus DC system with a DC feeder connected between Bus 1 and Bus 2. Two voltage sources with steady state values V1 and V2 are feeding the line from the two buses. At a distance x from Bus 1, a fault with a fault resistance Rf is assumed. Current I0 is flowing from Bus 1 to Bus 2 before the fault. Due to short lines in DC microgrids, line capacitance is ignored in Figure 132, and the line is approximated with an inductance and a resistance only. Other circuit parameters used in the development of theory are as follows:

- R_1, L_1 = resistance and inductance, respectively, of line-section from Bus 1 to fault.
- R_2, L_2 = resistance and inductance, respectively, of line-section from Bus 2 to fault.
- R, L = total resistance and inductance of line.
- r, l = resistance and inductance per unit length of the line.
- $\tau_L = \frac{L_1}{R_1} = \frac{L_2}{R_2}$ = time constant of the line.
- i_1 = Current from Bus 1 to fault.
- i_2 = Current from Bus 2 to fault.

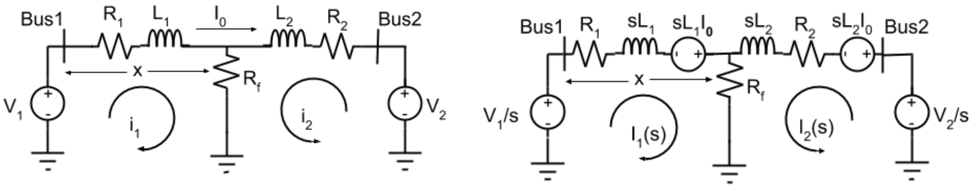

(a) (b)

Figure 132. Two-bus DC circuit with ideal DC sources (a) time-domain representation (b) s domain representation.

Figure 132(b) shows the s domain equivalent of the circuit of Figure 132(a). I1(s) and I2(s) denote the s domain equivalent of currents i1 and i2, respectively. From the theoretical formulation of the previous quarter, current $i_1(t)$ and $i_2(t)$ can be expressed as follows:

$$i_1(t) = K_1 + K_3 * e^{-(\lambda_L+\lambda_f)t} \quad \text{(B10)}$$

$$i_2(t) = K_1' + K_3' * e^{-(\lambda_L+\lambda_f)t} \quad \text{(B11)}$$

Where $\lambda_L = \frac{1}{\tau_L} = \frac{R}{L}$; $\lambda_f = \frac{R_f}{L_p} = \frac{R_f}{L_1||L_2}$ and K_1, K_3, K_1', K_3' are constants.

Through further derivations, it was shown [45] that the fault location x from Bus 1 can be expressed as follows:

$$x = \frac{\begin{vmatrix} v_1(t_1) & i_1(t_1) - I_0 \\ v_1(t_2) & i_1(t_2) - I_0 \end{vmatrix}}{\begin{vmatrix} l * \frac{di_1(t)}{dt}|_{t=t_1} + r * i_1(t_1) & i_1(t_1) - I_0 \\ l * \frac{di_1(t)}{dt}|_{t=t_2} + r * i_1(t_2) & i_1(t_2) - I_0 \end{vmatrix}} \quad \text{(B12)}$$

It can be seen from (B12) that, the fault location method:

- Gives closed-form solution using only local measurements, and;
- Is immune to fault resistance, and;

- Produces results using 3 samples after the fault (as minimum two samples are needed to calculate di/dt), which corresponds to 3 μs for a sampling frequency of 1 MHz.

5.3.2. *Simulation Results with Ideal DC Sources:*

The circuit depicted in Figure 132(a) is simulated in PSCAD with a sampling frequency of 1 MHz, meaning the sampled values are 1 μs apart. Rated system voltage is chosen to be 400 V, as it has been used in a number of papers for DC microgrids. A 100 m long Yorkshire conductor is chosen for the feeder. Circuit parameters are: $r = 1.37\frac{m\Omega}{m}, l = 0.25\frac{\mu H}{m}, V_1 = 400\,V, V_2 = 395\,V, R_f = 0.01\,\Omega,\ I_0 = 36.63\,A$.

Two faults are simulated at $x^{(1)} = 80\,m$ and $x^{(2)} = 40\,m$ distance from Bus 1. The fault inception time was set at $t_0 = 0.1$ s for both the cases. Simulated currents ($iBus1_{sim}$) and calculated currents ($iBus1_{calc}$) using (1) from Bus 1 to fault for both fault distances are plotted in Figure 133. For both cases, calculated and simulated currents are superimposed on each other which validates the theoretical derivation.

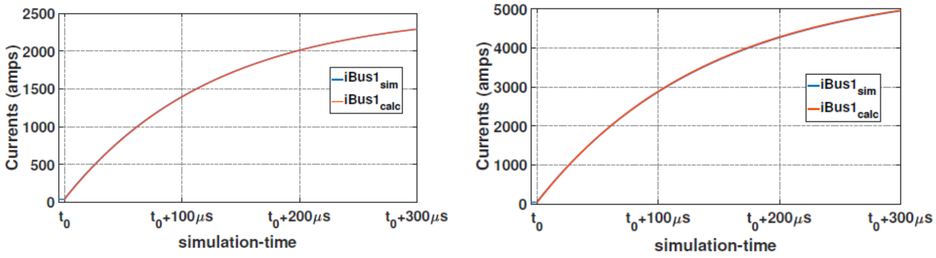

(a) (b)

Figure 133. Simulated and calculated currents from Bus 1 to fault for faults at (a) 80 m distance, (b) 40 m distance from Bus 1.

To validate the method for fault location, measurements of three consecutive samples at three instances, e.g., at 1st, 2nd & 3rd μs after the fault initiation were made, and the fault distance was calculated using (3) for each set of samples. In each case, the current derivative at a specific time-instant (say, t_2) was calculated using measurement at that time instant and the previous measurement, i.e., $\frac{di_1(t_2)}{dt} = (i_1(t_2) - i_1(t_1))/(t_2 - t_1)$. Table 47 shows measured and calculated values, for faults created at 80 m and 40 m from Bus 1. The calculated distance in each case is very close to the actual distance.

Table 47. Calculated distance from Bus 1 to fault.

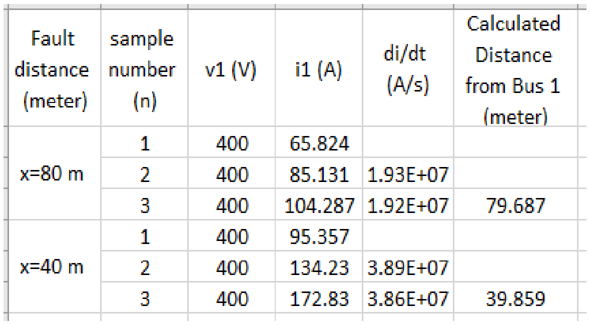

Fault distance (meter)	sample number (n)	v1 (V)	i1 (A)	di/dt (A/s)	Calculated Distance from Bus 1 (meter)
x=80 m	1	400	65.824		
	2	400	85.131	1.93E+07	
	3	400	104.287	1.92E+07	79.687
x=40 m	1	400	95.357		
	2	400	134.23	3.89E+07	
	3	400	172.83	3.86E+07	39.859

So, it can be concluded that fault distance can be calculated, even in presence of fault resistance, using local measurements only, in 3 μs , using the closed-form deterministic solution using (3). This is claimed to be a seminal contribution of this work.

5.3.3. Extension to Feeders with Converter-Based Sources

A converter is used to interface renewable generation to a grid. This converter has a capacitor connected at the DC side, known as the DC link capacitor. When a fault occurs on a DC feeder, currents from the capacitor initially dominate the response. As capacitors resist rapid change in voltage, for a short period of time after fault the capacitor will act like a constant voltage DC source. Thus, measurements from this initial period can be used to determine the fault location modeled by (3).

Figure 134(a) shows a two-bus DC microgrid with dc-dc boost converters connected to the buses instead of ideal voltage sources. Parameters of this test system are listed in Figure 134(b). A T(earth)N(neutral) grounding scheme is chosen for the system, where the grid is unipolar and the neutral is solidly grounded.

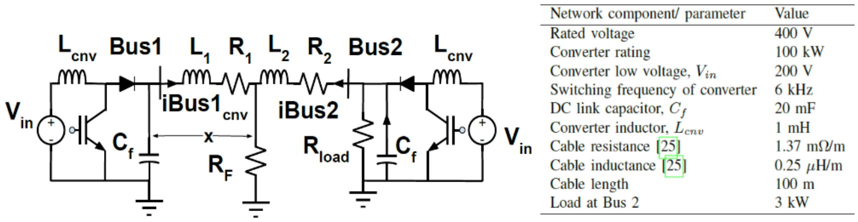

Network component/ parameter	Value
Rated voltage	400 V
Converter rating	100 kW
Converter low voltage, V_{in}	200 V
Switching frequency of converter	6 kHz
DC link capacitor, C_f	20 mF
Converter inductor, L_{cnv}	1 mH
Cable resistance [25]	1.37 mΩ/m
Cable inductance [25]	0.25 μH/m
Cable length	100 m
Load at Bus 2	3 kW

(a) (b)

Figure 134. (a) Two bus DC microgrid fed with converters. (b) Parameters for the system.

The dc-dc boost converter parameters are chosen using typical values for a 100 kW converter and verified through a number of resources. It is assumed that the converter has an ideal DC voltage source at its low voltage (LV) side, representing a PV panel or a battery. The duty cycle is kept fixed, since the initial period after fault is governed by the natural response of an RLC circuit, and the converter control would not activate during that time.

A fault was simulated in the DC feeder of Figure 134 at 0.1 s with a fault resistance of $R_f = 0.01\ \Omega$ at a distance x=80 m from Bus 1. The simulation was run for 0.2 s. Figure 135 shows the currents through different components under this fault condition – current through diode $iBus1_{cnv-d}$, current through capacitor $iBus1_{cnv-c}$, and total current from Bus 1 to fault $iBus1_{cnv}$. The same circuit then was simulated replacing the converters on the two buses with ideal DC sources. The voltages of the DC sources were set at the prefault voltages of Bus 1 and Bus 2 of the DC microgrid with converters. The current from Bus 1 to fault from the circuit with the ideal DC source was plotted in Figure 135 in green $(iBus1_{vs})$. It is to be noticed that for almost 150 μs after the fault initiation, total currents from Bus 1 to fault in both cases are practically equal. Thus, fault location using (B12), which was initially developed for feeders with ideal DC sources, can be extended to feeders with converters as well.

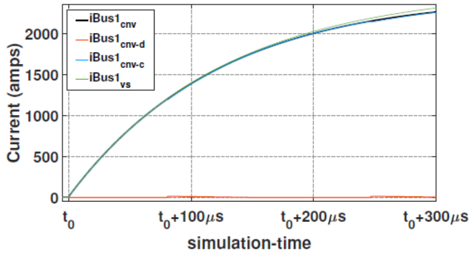

Figure 135. Comparison of faults current sourced by an ideal source and a converter.

To evaluate the performance of the algorithm developed for locating fault, data was generated from the fault simulation with converters at a sampling frequency of 1 MHz. Figure 136 shows the calculated distance of fault from Bus 1 $(dist_{Bus1})$ and Bus 2 $(dist_{Bus2})$ from 5 μs before fault inception to 6 μs after fault inception. Clearly, before fault inception the distance from Bus 1 is much larger than the line length, and within 3 samples after the fault inception ($t_0 = 0.1s$), calculated distances become almost equal to the actual distances of the fault point on the line. Thus, both, detection and location of fault is correctly and accurately performed.

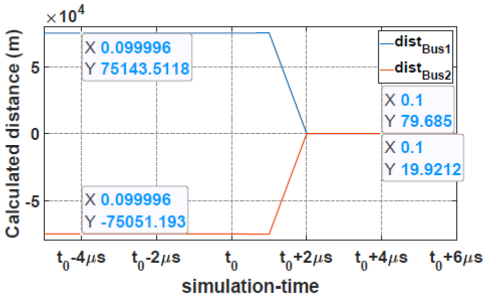

Figure 136. Calculated distances to fault point from Bus 1 and Bus 2.

The accumulated data spanned from 40 μs before the fault inception to 100 μs after. From the 3rd sample after the fault inception time to the end of accumulated data, the calculated distances from Bus 1 varied from 79.69 m to 80.12 m. So, the proposed method provides accurate fault location over an extended range of data points after fault. This is used for main protection of a feeder in a DC microgrid.

5.3.4. Undervoltage Based Backup protection for 4-bus DC Ring Main System

Consider the 4-bus ring system in Figure 137. Every bus is equipped with its own dc-dc converter and resistive loads. All the lines are 100 m long.

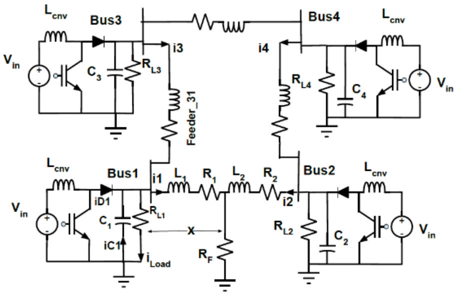

Figure 137. Four bus DC ring system.

When a fault occurs in a DC microgrid, the buses which are electrically nearer to the fault will lose voltage first because of higher capacitive discharge. Therefore, these buses will lose voltage faster than the buses farther away. To show this scenario, a fault was simulated on Feeder_12 of Figure 137, with Rf=0.1 ohm at x1=90 m and x2=10 m distance from Bus 1 and Bus 2, respectively. Voltages of all four buses are plotted in Figure 138. It can be seen that voltages of Bus 1 and Bus 2 are dropping at a faster rate and reach a threshold (say, 360-volt) significantly earlier than Bus 3 and Bus 4.

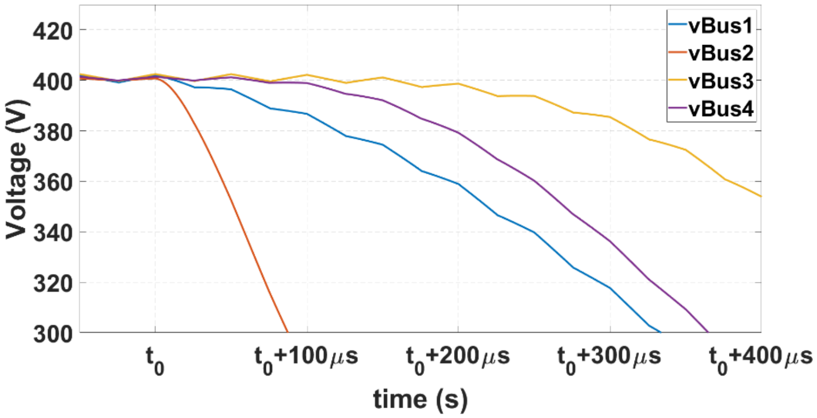

Figure 138. Voltages of different buses due to a fault between Bus 1 and Bus 2.

This can be used effectively for backup. For example, for the case of relay at Bus 3 backing up the relay at Bus 1, the backup relay at Bus 3 can keep calculating the voltage at Bus 1. An undervoltage threshold value (UV_T) of 90% of the nominal voltage (i.e., 360 V) can be set. If the calculated voltage at Bus 1 goes below this threshold, the backup interprets that the main relay has failed to clear the fault and trips the breaker to isolate feeder 31. This approach was verified by changing the converter-capacitance at Bus 1 by up to 20%, and the backup at Bus 3 worked as designed.

Thus, each relay has two modes. It keeps calculating the fault-distance based on equation (B12) and keeps calculating the voltage of the adjacent bus. If the distance calculated drops to a value less than the feeder length, main protection operates (3 samples needed for this) and opens the corresponding breaker and gives out the fault-location result. If this condition is not satisfied and the calculated voltage of the adjacent feeder falls below a threshold, it also opens the same breaker, but this time it would be backing up the fault in the adjacent feeder.

5.3.5. Simulating and Testing Main and Backup Protection on RTDS

The system under consideration is the 4 bus, dc-ac hybrid microgrid shown in Figure 137. The rated voltage for the DC network side is ±400V. Bus 1 has a bipolar voltage-controlled dc-dc boost converter which sets up the voltage for the DC microgrid. Buses 2, 3 and 4 have home units, which are called Nanogrid (NG) boxes. Schematic of the NG boxes is shown in Figure 139. It can be seen that NG boxes are connected to the DC microgrid through a current-controlled dc-dc converter. The low voltage side connects to home battery storage units, rooftop PV optimizers, and a dc-ac inverter to supply the AC loads inside the home.

The main challenge in simulating the circuit for demonstrating the protection scheme is that it must be simulated in 1 µs time step, as it was assumed that the sampling rate would be 1 MHz. To support such high-resolution simulation, RTDS has a special feature called 'Substep environment'. Substep environment allows the user to enter elements in a 'Substep Box' and set a parameter called 'SubstepDivisor' through which the user can fix how many times the substep environment will run in one simulation step for the rest of the system, called main simulation step. So, with the main simulation step being 50 µs, if the user selects 'SubstepDivisor=50', RTDS will simulate the substep box 50 times in one main step, which eventually makes the substep time step equal 1 µs.

To implement the main and backup protection, multiple feeders and more than two buses need to be simulated. However, RTDS produced a 'time-step overflow' error when multiple feeders were simulated under a single substep box.

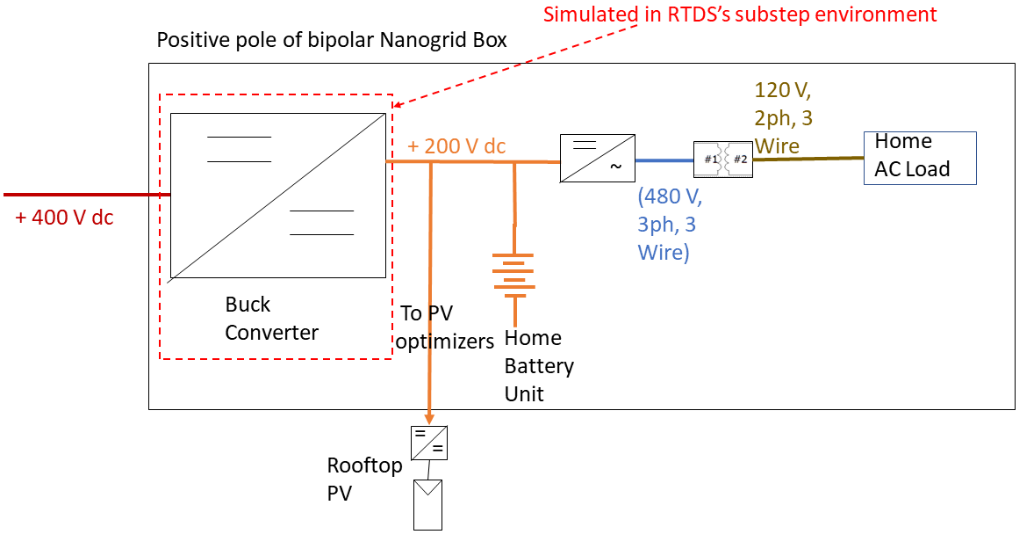

Figure 139. Schematic of Nano Grid box

This issue was resolved by dividing the system into multiple substep boxes and placing every substep box in a different core. Clemson's RT-PACE lab is licensed to use 6-cores in the RTDS. So, for demonstrating the backup while considering the calculation burden, a reduced power system shown in Figure 140 was implemented in the RTDS using 3 cores. The cores were connected to each other through 'substep transmission line interface'. Every transmission line will have two terminals – the sending end (TL1-S) and receiving end (TL1-R) as shown in Figure 140. Core assignments in RTDS for demonstrating backup protection.. 'Substep transmission line' interface permits a system to be broken into separate cores and thus divide the calculation into separate cores so that the computation can be paralleled and the system can run in real-time.

The other 3 cores were used for controls and relaying as shown in Figure 140. The converter on Bus 1 is a voltage-controlled converter, and other converters are current controlled converters. These controls populated two more substep boxes, i.e., two more cores. The last core was used to implement the backup protection function. For implementing these controls and protection functions, voltage and current measurements were needed to be exchanged among the cores. There's a high-resolution transfer block in RTDS substep environment which makes the exchange of the high resolution measurements across different substep boxes possible.

It is to be mentioned that the line between Bus 1 and Bus 2 couldn't be implemented as the inclusion of any more calculation burden generated time-step overflow error. Also, only the dc-dc converter of the NG box was implemented to reduce the calculation burden. This is acceptable for the purpose of the simulation. The backup scheme will be illustrated as follows: A fault on the line between Bus 3 and Bus 4 is created and main protection is disabled. The backup relay R_{L13} should operate.

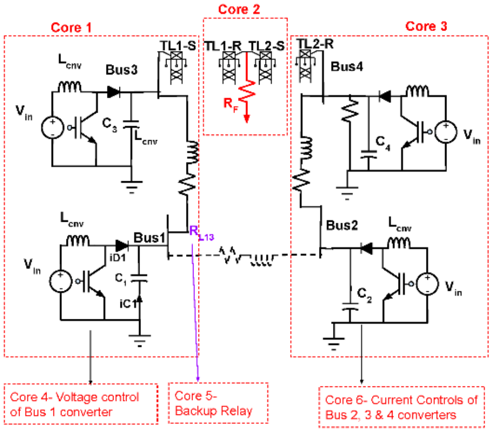

Figure 140. Core assignments in RTDS for demonstrating backup protection.

Backup protection logic:

When there's a fault in the line between Bus 3 and Bus 4, Relay RL13 works as a backup relay, following this logic:

1. R_{L13}, keeps calculating the voltage at Bus 3 (vBus3) and compares with an under-voltage threshold setting $UV_T = 0.8\,pu$.
2. R_{L13} interprets (and thus detects) the main bus is experiencing a fault if vBus3< UV_T.
3. R_{L13} waits for a certain time delay (TD_backup) before generating trip so that the main relay in Bus 3 can get enough time to operate.
4. TD_backup ≥ fault detection by main relay (6 µs) + SSCB operation time (50 µs) = 60 µs (considered in this study).
5. If main relay operates, vBus3 starts to rise and the backup protection gets blocked in R_{L13}.

5.3.6. *Results*

A fault was simulated in the DC feeder at a distance x=80 from Bus 1 on feeders 1-3. It was seen that the software relay R_{L13} at Bus 1 detected and located a fault and sent a trip command within 7 µs of fault inception inside RTDS.

Figure 141 shows the response of the software backup protection relay RL13 inside the RTDS due to a fault on the line between Bus 3 and Bus 4. The fault was incepted at t_0. Figure 141(b) shows the calculated voltage of Bus 3 (V_{Bus3}) and the undervoltage tripping threshold UV_T. It can be seen that approximately at $t_0 + 90\mu s$, the Pickup signal in Figure 141(c) went high after the V_{Bus3} went below UV_T. But the trip signal is generated after the delay TD_backup (60 μs), i.e., approximately around $t_0 + 150\ \mu s$.

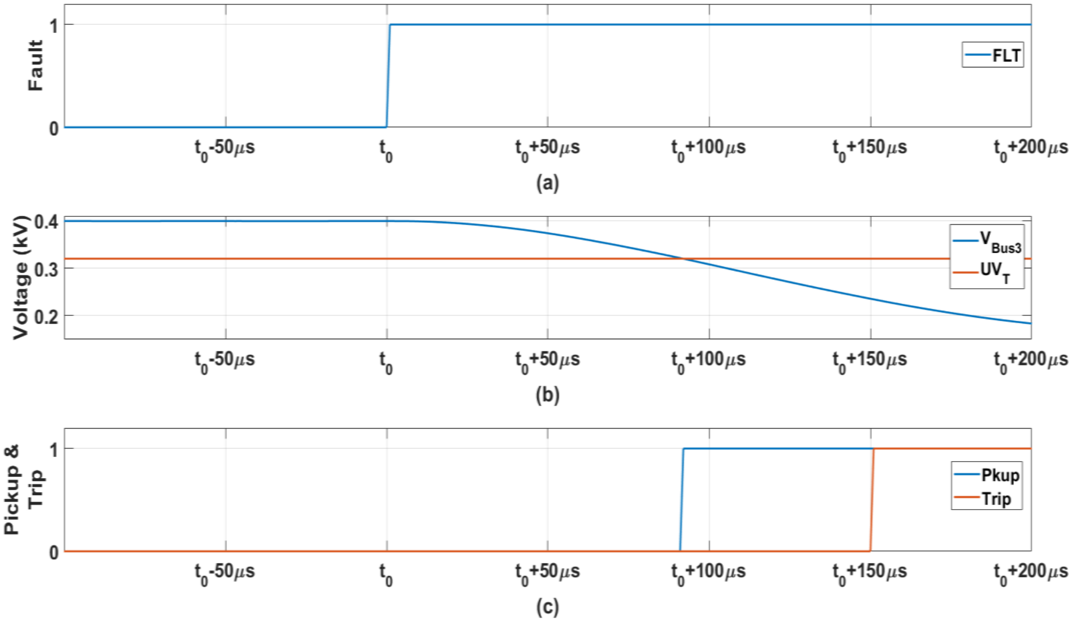

Figure 141. Backup protection demonstration in RTDS

Thus, at this point, both main and backup protection are confirmed to work in real time with software based relays.

5.3.7. Testing the Main Protection in Hardware in the Loop

The microcontroller used was TI's TMS320F3279D. It has four ADC modules which can be used for simultaneous sampling. To simultaneously sample voltage and current, two separate modules were used. The DSP converts the analog values into a 12-bit binary number. For 12-bit resolution there will be 4096 (=2^12) levels. Figure 142 shows the digital voltage and current values sampled by the DSP board at 1 MHz rate. In Figure 142, the current rise and the voltage drop started at the same sample, confirming simultaneous sampling.

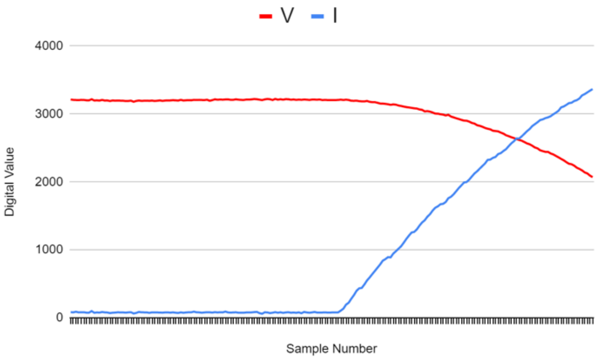

Figure 142. Sampled Voltage and Current by the DSP board.

5.3.8. Calculating Fault Location using the Sampled Values

To verify the performance of the method on the samples data, a fault is simulated at a distance x=80 m. Figure 143 and Figure 144 show a window of voltage and current data containing pre-fault and fault samples. As can be seen, the sampled values contain high frequency noise. To remove the noise, the signals are passed through a low pass filter. It is understood that filtering will introduce delays, but the focus is on making the fault location theory work first. A second order Butterworth low pass filter is used with a cutoff frequency of 20K Hz.

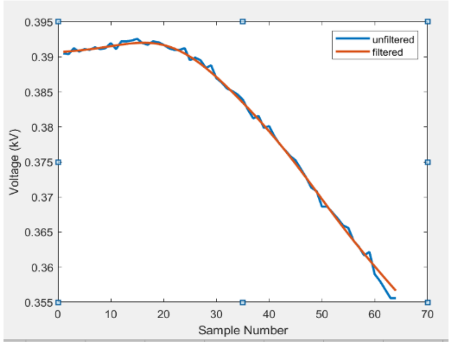

Figure 143. Sampled (unfiltered) and filtered voltage.

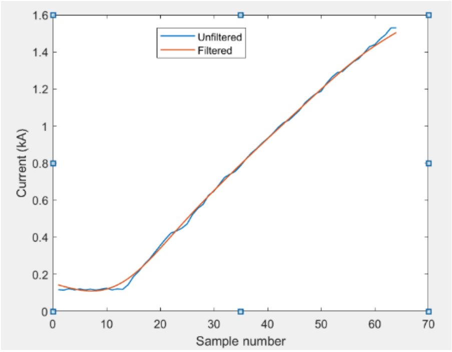

Figure 144. Sampled (unfiltered) and filtered current.

As seen from Figure 144, though filtering is removing the noise, it is changing the trajectory of the current waveform in the vicinity of fault inception (around sample number 10-13). Figure 145 shows the distance calculated by the software relay inside RTDS and the distance calculated using the sampled values from the DSP board. The software relay is behaving as expected, i.e., producing a number which is much larger than the line length before the fault, and producing the correct fault location within three time-samples after fault inception. But, because of the reshaping caused by the filtering, the fault location calculated using the filtered wave gradually approaches the true fault location of 80 m. Also, the calculated fault location oscillates around the true fault location as depicted in Figure 145. Faults were simulated at different distances along the line and similar trends were seen. The relay samples the voltages and currents, applies filter, and performs the fault location calculation within 1 microsecond time – a noteworthy achievement, as such commercial product is not available. The relay is shipped to Sandia National Laboratories for field testing.

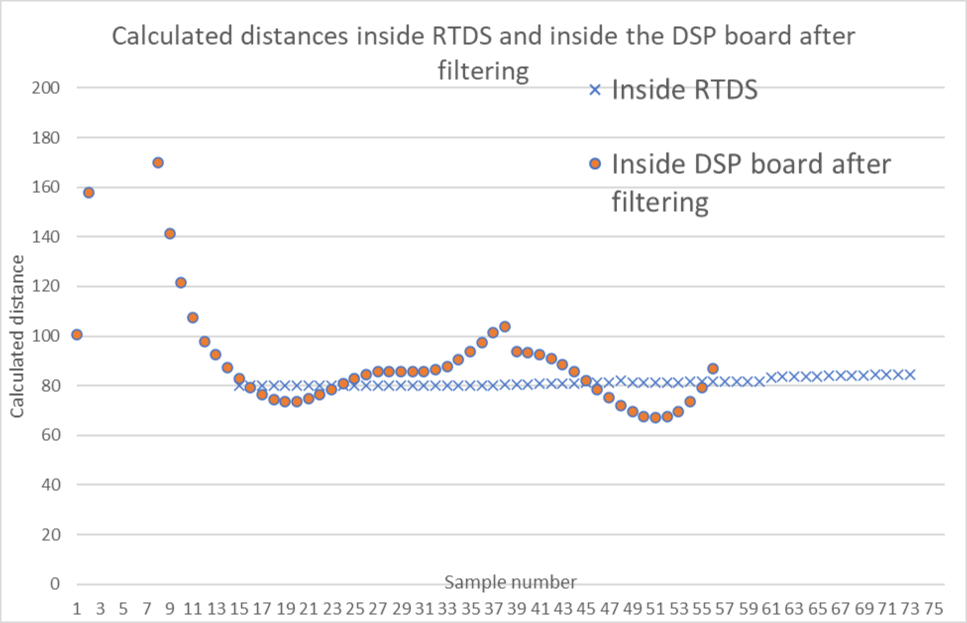

Figure 145. Comparison of calculated fault locations from simulated values (inside the RTDS by software relay) and from sampled values (by the DSP board).

6. DEMONSTRATION

6.1. Overview of the Microgrid

The Kirtland Airforce Base (KAFB) DC Microgrid has been developed and deployed to support residential power service applications since 2019. The microgrid serves ten end-user nodes, including housing and laundry facilities, and doubles as a development testbed for DC microgrid applications at Sandia National Laboratories' DETL. Figure 146 contains a map of the entire KAFB microgrid, spanning approximately 1.5 kilometers in distribution bus length. Some research conducted thus far on the microgrid includes fault detection and exploring alternative microgrid bus topologies to increase resiliency and reliability to the microgrid. The microgrid is made up of a series of interconnected nanogrid boxes, each serving individual housing loads. Each nanogrid features the following: a battery energy storage component, an interface converter for rooftop PV solar, a grid-forming inverter for residential AC loads, and a transfer switch which interfaces to a local utility AC grid. In the event of the DC microgrid being disabled, the transfer switch provides interrupted service to the housing loads from the utility grid. During typical operation, the microgrid is self-sufficient to the end-user, generating enough power through its PV resources to support AC loads and maintain energy storage charge.

The nanogrid units are connected to the hierarchical microgrid network using a 750 V ground-center distribution bus to allow for a ±375 V bipolar distribution bus. This bipolar bus configuration contains a high-impedance grounding scheme, in which current flows through the positive and negative poles rather than through the distribution bus ground. Lower overall bus operating voltages with respect to ground are also achieved, which reduce the risks associated with ground fault scenarios. Each nanogrid relies on a bidirectional interface converter to allow for power flow between its internal DC voltage node and the microgrid's distribution bus. Depending on the nanogrid source generation and load demand, power is transferred between nanogrids through the distribution bus as part of the overall microgrid operation. The bidirectional interface converter for each of the nanogrids limits the current provided and sinked by the nanogrid box, limiting high current peaks found in low-impedance fault conditions from the internal energy storage component. Figure 147 outlines the overall architecture of the nanogrid boxes serving each end-user.

Figure 146. KAFB DC microgrid serving housing, utility, and DETL sites.

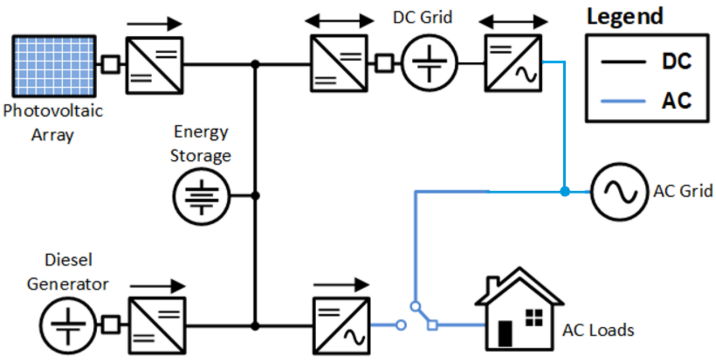

Figure 147. BlockBox nanogrid architecture showing integration of DERs into residential application.

Another key component of the DC microgrid architecture is the Central Energy Park (CEP), acting as the microgrid's hierarchical bus controller. The CEP sets the microgrid distribution voltage and interfaces to the local utility grid through a DC/AC grid-following inverter that allows for bidirectional power flow. Power can be imported/exported between the microgrid and utility based on the generation and demand within the system, notably during the loss of PV power, surplus in generated PV power, and black start conditions. Each nanogrid box is networked to the CEP, located at the KAFB's laundry facility, to allow for coordinated power control in the system. The CEP generates its own power through a local battery energy source, PV solar array field, and backup natural gas generators.

The CEP also serves an important function of protecting the microgrid in the event of faults and transients found on the microgrid bus. First, a high-impedance grounding scheme allows the ground of the system to float between parallel RC networks placed between the bipolar rails. This circuit provides a high-frequency return path while maintaining high-impedance for DC, ensuring that bus current flows between the positive and negative rails and not through the system ground. This is shown in Figure 148(a). Furthermore, a protection device located at the CEP continuously monitors the current from the CEP's node on the microgrid to determine if a fault has occurred. Detecting a fault on the microgrid distribution bus, the protection device can be enabled to immediately disconnect the sourced 750 V and clamp the line to a low impedance, removing any potential voltage or current from being a safety risk to the end user and equipment. When a fault event occurs and the protection device is enabled, each of the nanogrid boxes continue to operate in an islanded configuration. Furthermore, the microgrid bus being disabled removes the fault from affecting the AC utility grid connected through the grid-feeding inverter tie at the CEP. Islanding both the nanogrid boxes and the utility grid allows for the fault to be detected and removed without interrupting service to the end user or affecting utility service outside of the microgrid. Upon the removal of a fault, the microgrid bus can be enabled by coordinating control from the CEP. This is detailed in Figure 148(b).

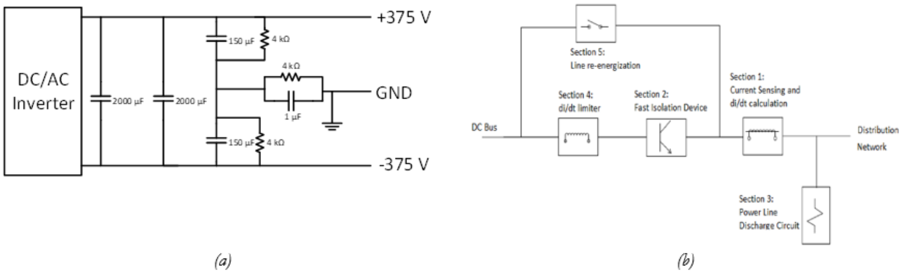

Figure 148. (a) High-impedance grounding scheme found at CEP and (b) protection device used to detect and disable faults.

The KAFB DC microgrid allows for a variety of bus topologies. Two feeds exist between the CEP and the distribution bus connecting each of the ten nanogrid boxes. Through a network of disconnect switches, either radial feeds or a loop feed can be configured for the distribution network. The loop feed advances the distribution capability and redundancy of the system, allowing power to optimally flow through the system based on nanogrid location. Figure 149 and Figure 150 identify two possible bus topologies for the microgrid: 1) a radial feed between the CEP (titled Community Box), and 2) a loop feed that connects directly between the CEP and base housing.

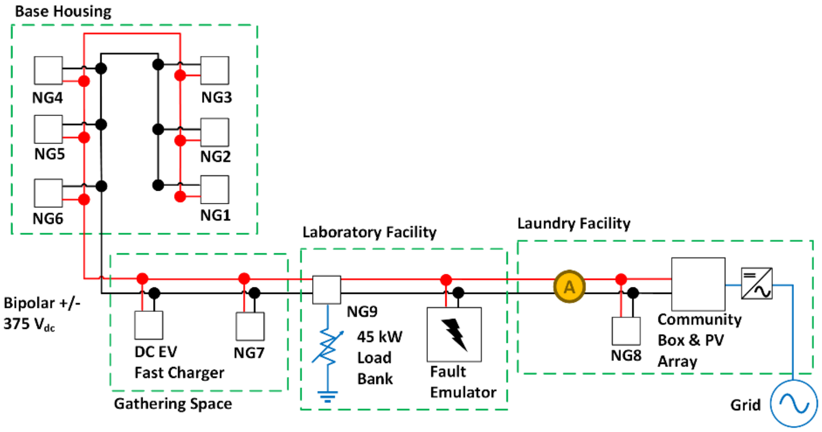

Figure 149. KAFB microgrid architecture in a radial feed bus configuration.

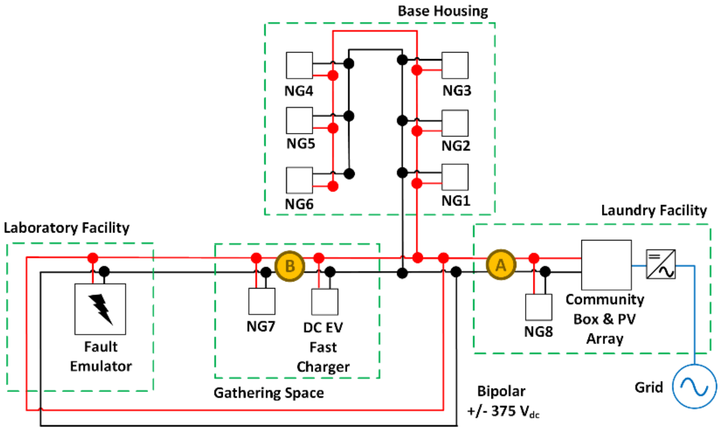

Figure 150. KAFB microgrid architecture in a loop feed bus configuration.

6.2. Sensor Installation

Monitoring for faults at various locations is achieved by using oscilloscopes connecting to voltage probes and current transducers installed onto the microgrid distribution bus. Tektronix P5200A differential voltage probes and Danisense DS50UB-10V (50 A version) or DS600UB-10V (600 A version) current transducers were chosen for their high bandwidth, high measurement scale range, and accuracy for fault capture. The sensors and transducers are connected to a TBS2104B oscilloscope to capture transient waveforms during fault inception using a 20 MHz sampling rate over a 1 second sampling window. While voltage probes are connected directly at the point of measurement, the current transducers can be positioned on the distribution bus to monitor currents flowing to either the fault, the CEP, or into an individual nanogrid box. This allows for a better understanding of how fault currents are distributed through the system.

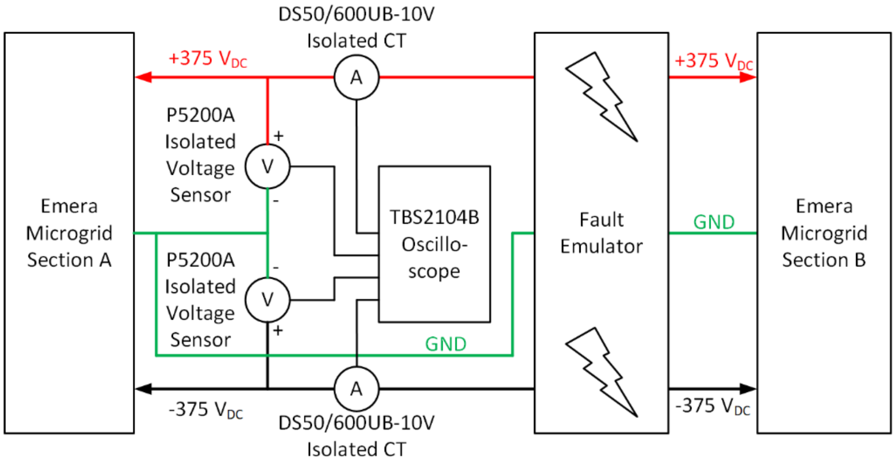

Figure 151. Experimental fault test setup with measurement equipment connected to sections of the microgrid.

6.2.1. Global Positioning System pulse generator

Global Position System (GPS) timing pulse generators were procured and assembled into a field-safe enclosure that can be incorporated into the test setup. The GPS timing pulse generator bundle is shown in Figure 152 and consists of a U-Blox SAM-M8Q GNSS receiver module interfacing with a SparkFun RedBoard programmed to provide boot configuration upon startup. The GNSS receiver module can detect GPS signal and provide a 1 pulse per second (PPS) (1Hz) synchronization pulse demodulated from the received GPS data. These synchronization pulses contain extremely low jitter (<50ns) and provide a means of synchronized time alignment between oscilloscope measurement locations. With a third scope location, a third GPS timing pulse generator was assembled and deployed into the setup.

Disclaimer: the GPS timing pulse generator has been removed from the oscilloscope channel inputs due to the need for additional current and voltage measurements. If further testing requires highly accurate time alignment, the test capability does exist to provide an alignment tool (at the expense of one oscilloscope channel.).

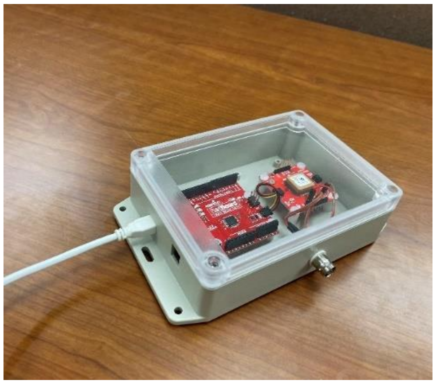

Figure 152. GPS Pulse Generator assembled into polycarbonate enclosure for 3rd scope location.

6.3. Fault Generator and Fault Testing

Emulated faults can be introduced onto the KAFB DC microgrid using a hardware device connected to the main distribution bus. Such fault emulator hardware is shown in Figure 153, and consists of a series/parallel bank of power resistors with a total impedance value configurable between 1 Ω and 1000 Ω. A manually switched electromechanical contactor initiates and clears the fault introduced onto the bus for a duration of time long enough to capture the transient effects of the fault. Further configurable, either line voltage to ground or line voltage to line voltage scenarios can be set up, introducing many positive, negative, and ground-based impedance faults onto the system.

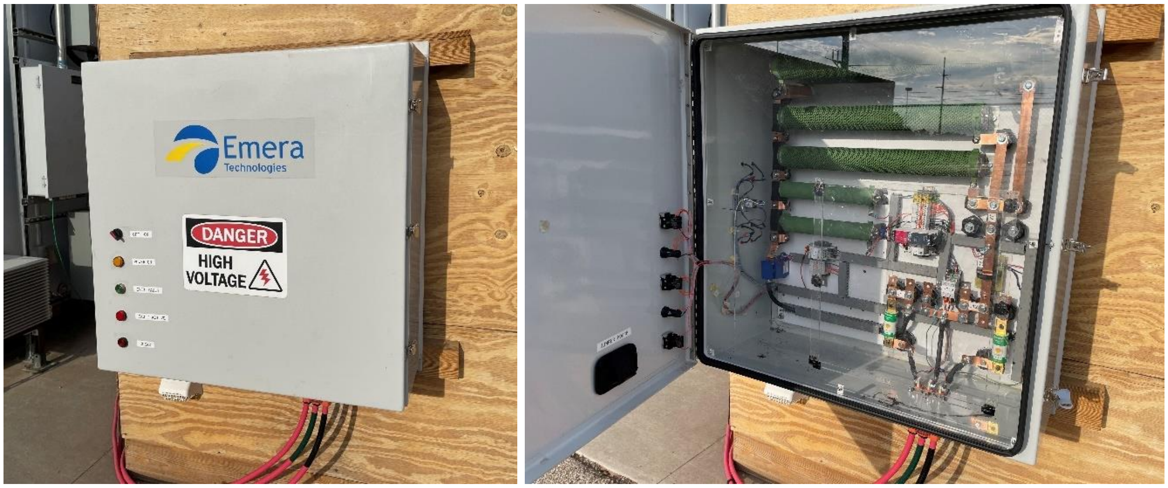

Figure 153. Fault emulator hardware installed onto microgrid distribution bus at the DETL.

As mentioned, there are many sets of test parameters that can be considered on the microgrid, generating a large combination of potential scenarios that can be considered for this study:

- Fault impedances of 1 Ω, 4.7 Ω, 500 Ω, 1000 Ω.
- Fault connection between +375 V to ground, -375 V to ground, +375 V to -375 V.
- Fault emulator located at DETL, near KAFB housing, or CEP.
- Measurement equipment located at the DETL, near KAFB, or CEP.
- Bus topology set for radial feed or loop feed configurations.

6.4. Baseline Measurements

Results captured for a 4.7 Ω bus fault between the +375 V and -375 V distribution lines are shown in Figure 154. In this scenario, the fault emulator was placed at the KAFB Gathering Space and measurements were taken at three different places on the microgrid: at the fault, at the DETL's nanogrid box, and at the CEP's community box. A voltage waveform transition was used for each measurement location to trigger the oscilloscope capture (positive line voltage to ground measurements shown in Figure 154). A few key observations can be made from this data. For one, the transient current is found to be significant at the point of the fault emulator with a peak transient current into the fault of 150 A, which is due to the low fault impedance (4.7 Ω) in relation to the line-to-line bus voltage of 750 V. When the fault is applied, the current contributions from each of the nodes on the microgrid are immediately sunk into the fault emulator's power resistors. The bus voltage does see an instantaneous undershoot transient at 0 seconds, recovering momentarily before the protection device detects the overcurrent event and discharges the distribution bus. Oscillations are seen during the protection device's disabling of the distribution bus, the effect of discharging the bus capacitance of the system, and the line inductance between each nanogrid and the CEP. Additionally, during the activation of the protection device, the positive line voltage inverts its polarity to ground, an effect of fault-current limiting inductances and the internal IGBT device used to shunt the line energy to ground. During this discharge, a reduction in the overall peak current into the fault is observed in relation to the reduction in the bus voltage. While the instantaneous current on the bus is significant, the protection device detects and discharges the fault within 1 millisecond, rapidly correcting a potentially dangerous fault condition. After the fault is detected and cleared, the distribution bus is held at 0 V until the fault can be removed, and the bus can be re-enabled.

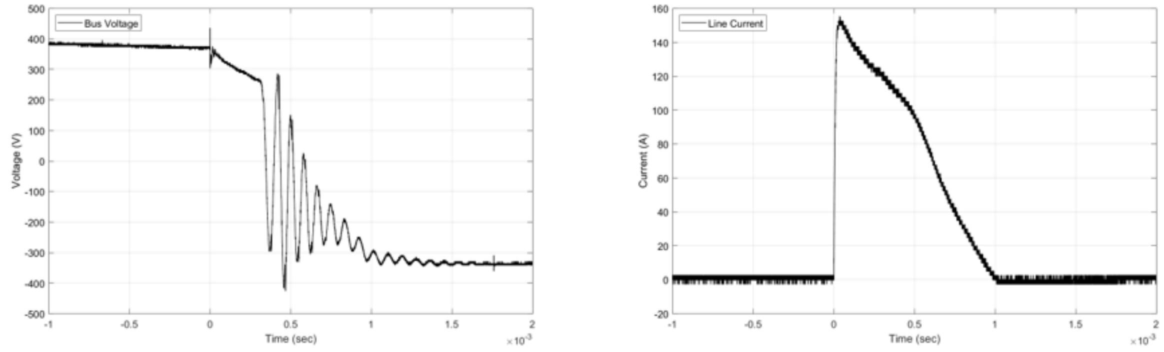

Figure 154. Experimental fault test results for a 4.7 Ω line-to-line fault captured at the fault location (Gathering Space).

Measuring the fault event from the vantage point of the laboratory facility (DETL) nanogrid box looking towards the fault location shows a different fault signature. Figure 155 details a more subdued oscillation on the voltage bus during fault, and different oscillations between the voltage and current during the fault event. Fault currents were still significant but are contained within 2 milliseconds by enabling the protection device.

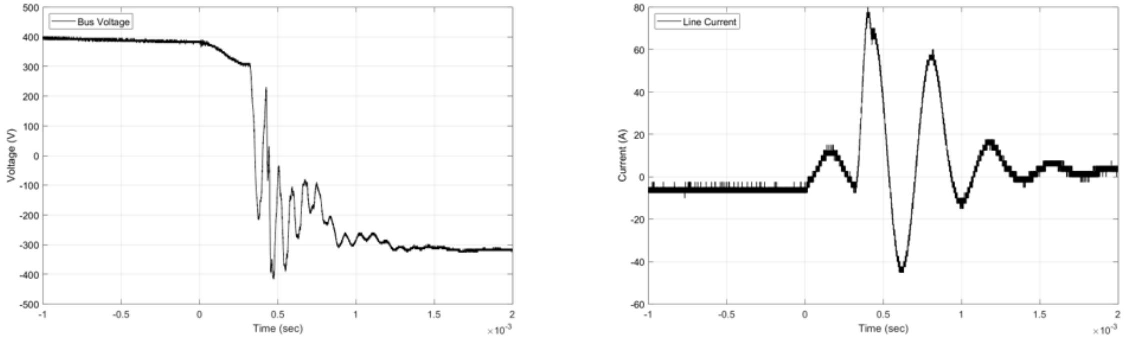

Figure 155. Experimental fault test results for a 4.7 Ω line-to-line fault captured at the DETL's nanogrid box (NG9).

Last observed is the fault behavior seen at the CEP location shown in Figure 156, containing the protection device used to detect and disable faults on the microgrid distribution bus. The current fed out of the CEP shows an increase to 60A before the protection device is enabled and bus current is immediately discharged back into the protection device at a peak level of up to -150 A. The bus voltage shows a fast discharge once the protection device is enabled and less ringing due to the proximity of the measured location to the protection device. The current fed back into the CEP is dissipated in the protection device rather than being fed into its local energy storage or utility grid interconnect.

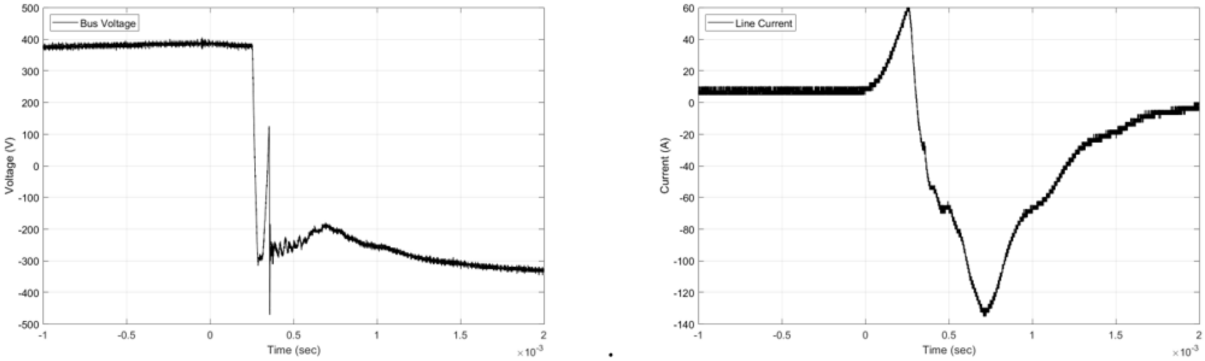

Figure 156. Experimental fault test results for a 4.7 Ω line-to-line fault captured at the CEP (Community Box).

An additional data point captured from this test is the propagation delay found in the voltage waveforms captured during the fault. Shown below in Figure 157 are two voltage waveforms time synchronized using a GPS 1 PPS clock to align the data in post-processing. A 5 μs delay is seen when comparing the bus voltage waveform between the fault location and DETL, suggesting a delay in time between the fault occurring at the fault location and elsewhere on the distribution bus.

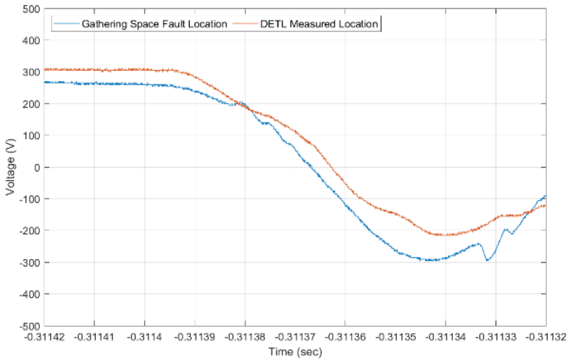

Figure 157. Comparing time-synchronized voltage waveforms (Gathering Space, DETL) during fault event.

A test setup was put together to analyze the DC-side fault current contribution of the grid-tie inverter component within the Emera Microgrid; see Figure 158 for the setup. With the protection device in circuit, and between the fault location and the internal microgrid bus of the microgrid Central unit, faults were executed to capture the fault current contributions from the grid-tie inverter under various loading and islanding states. It was identified that the fault current contribution from the grid-tie inverter does not appear to vary depending on import/export or islanding criteria. Rather, the only contribution seems to be from a fixed quantity, the DC-bus capacitance of the inverter. Figure 159 and Figure 160 compare the monitored currents for the grid-tie inverter in an islanded (isolated from AC grid) and a non-islanded but 0 power flow condition. This test has shown that the additional test point of the islanded microgrid doesn't provide any new information to the fault data.

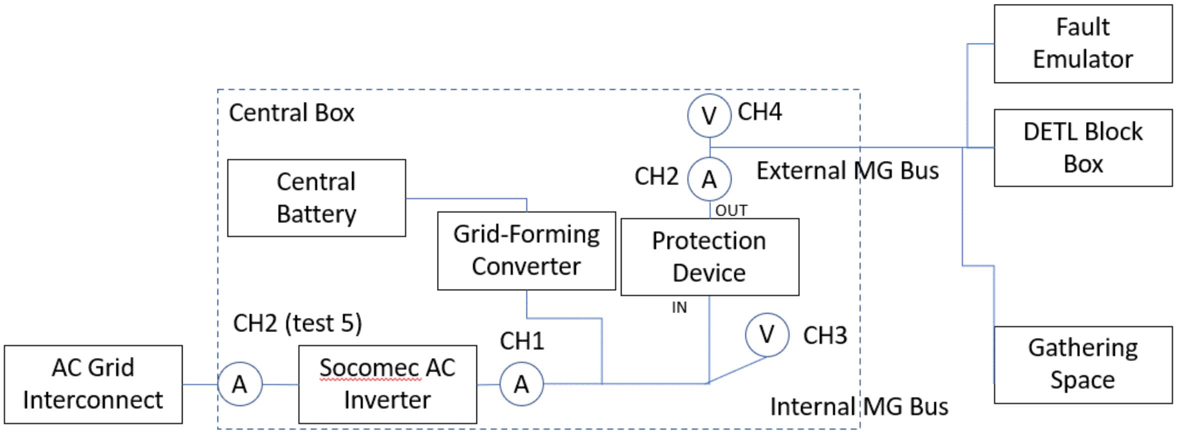

Figure 158. Grid-Tie Inverter Fault Setup

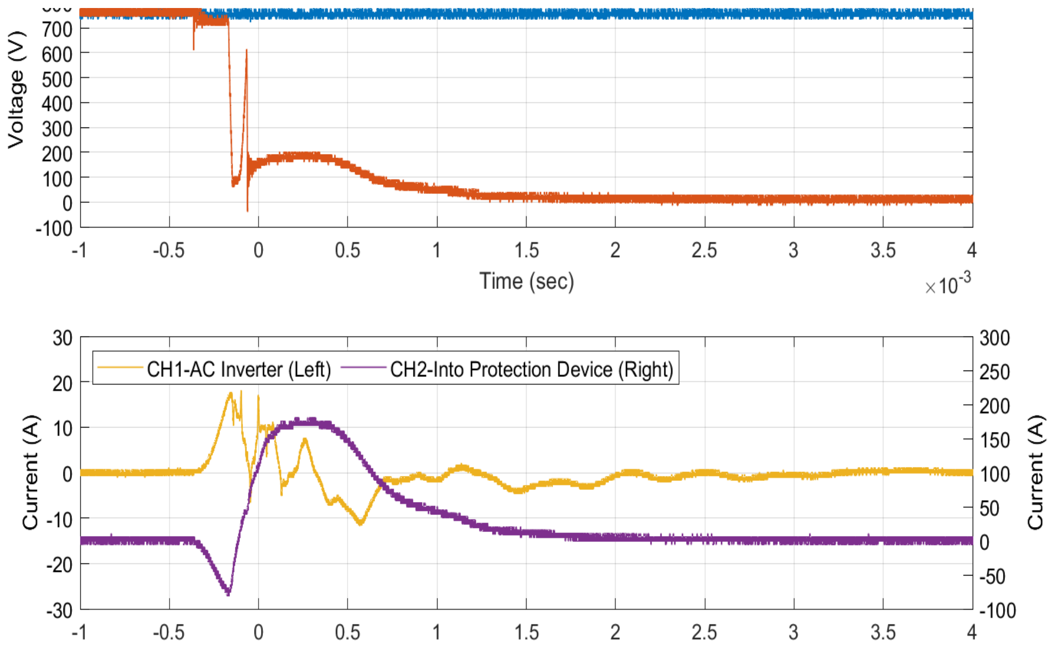

Figure 159. Grid-Tie Inverter Fault Data Socomec Islanded (Fault Contribution in Yellow).

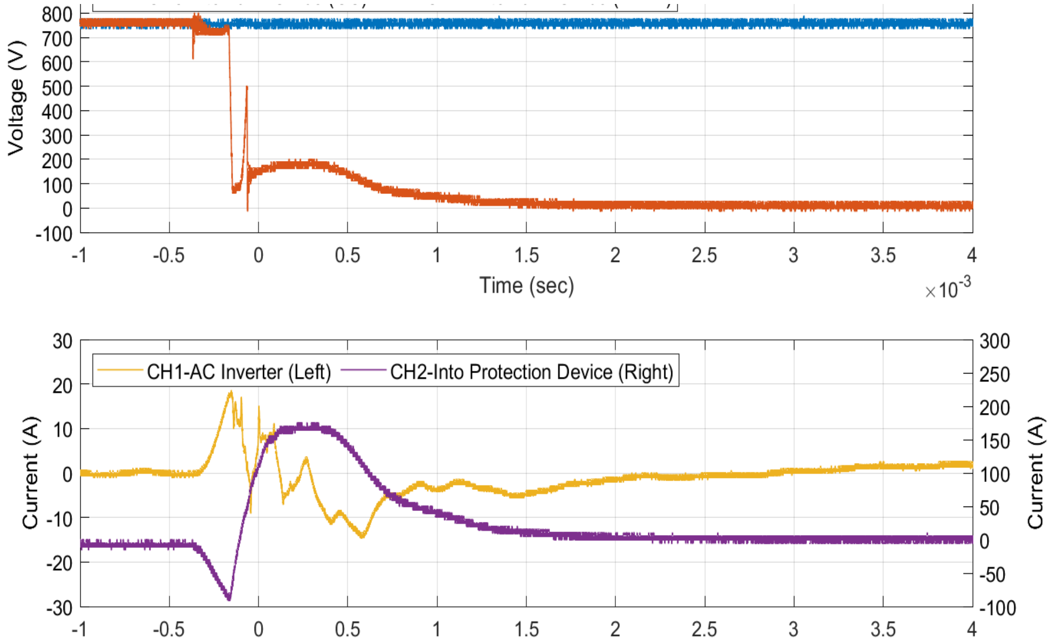

Figure 160. Grid-Tie Inverter Fault Data Socomec Operating at Idle (0 kW) Power State.

The protection device's input and output voltage and current characteristics were also monitored over several fault tests to capture the operating behavior at a 1.1 Ohm pole-to-pole fault impedance as well as to compare the absorbed energy by the discharge branch under a fault-isolation response. See Figure 161 for the sensor layout. Figure 162 captures the protection device's response to a 500-Ohm pole-to-pole fault. The output current of the protection device and the calculated energy dissipated in the line-discharge branch of the protection device are primarily due to the distributed line capacitance of the nanogrid interface converters.

Figure 161. Protection Device Characterization Sensor Locations.

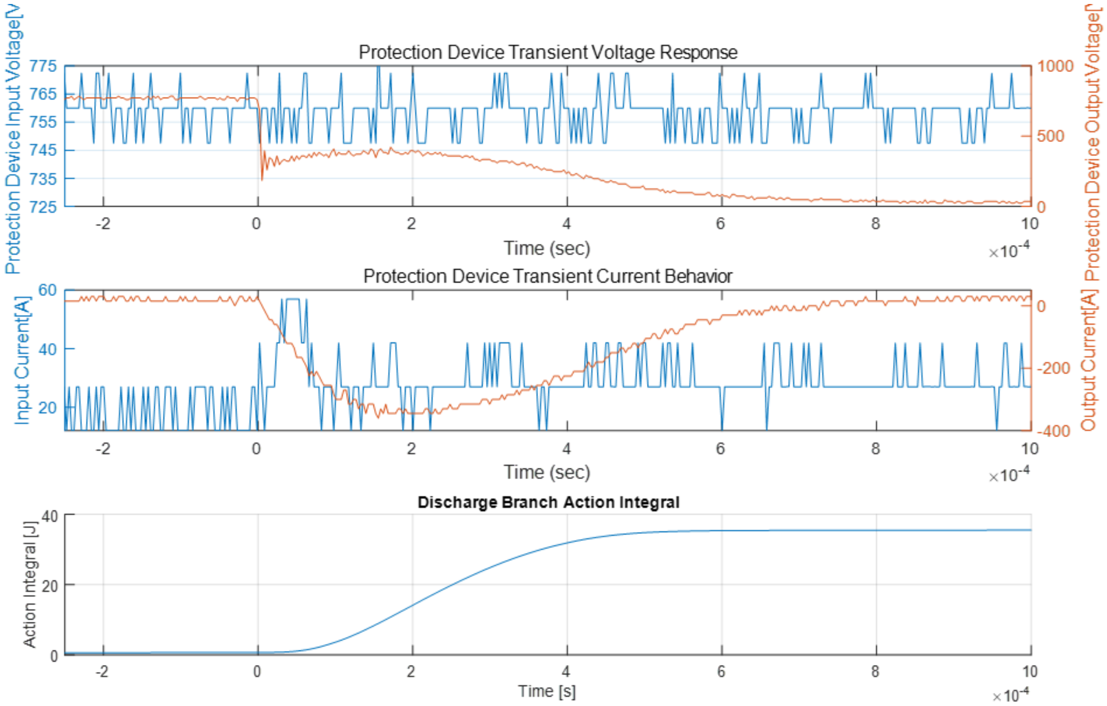

Figure 162. Protection Device Response to 500 Ohm Pole-Pole Fault (Ring Bus Topology).

In Figure 163, the fault impedance was reduced to 4.7 Ohms, but the nanogrid units were isolated from the distribution bus, you can see that the output current is opposite in polarity, this is due to the majority of line energy being removed from the line and the free-wheeling path through the discharge branch's anti-parallel diode, resistor, and the fault impedance being the primary dissipater of the energy built up in the fault current limiting inductors of the protection device. The energy present in the inductors is heavily influenced by the initial current state, the protection device's response time, and the fault impedance. The fault impedance is inversely proportional to the discharge branch dissipation energy. The oscillating current seen at the input of the protection device is due to the impedance between the protection device's 120uF input capacitance, the response-time of the grid-forming converter, and the bulk capacitance of the bus under the transient fault-isolation response of the protection device.

The fault impedance is further reduced to 1.1 Ohms in Figure 164. The fault current is approximately 3-times more than the 4.7 Ohm fault condition, which is in line with the differences in the impedance of the discharge branch's free-wheeling path in the two tests. The tests executed here show that there is still a significant margin in the protection device's operation. However, additional nanogrid interfaces and initial operating current conditions need to be evaluated to fully characterize the limits of the protection device.

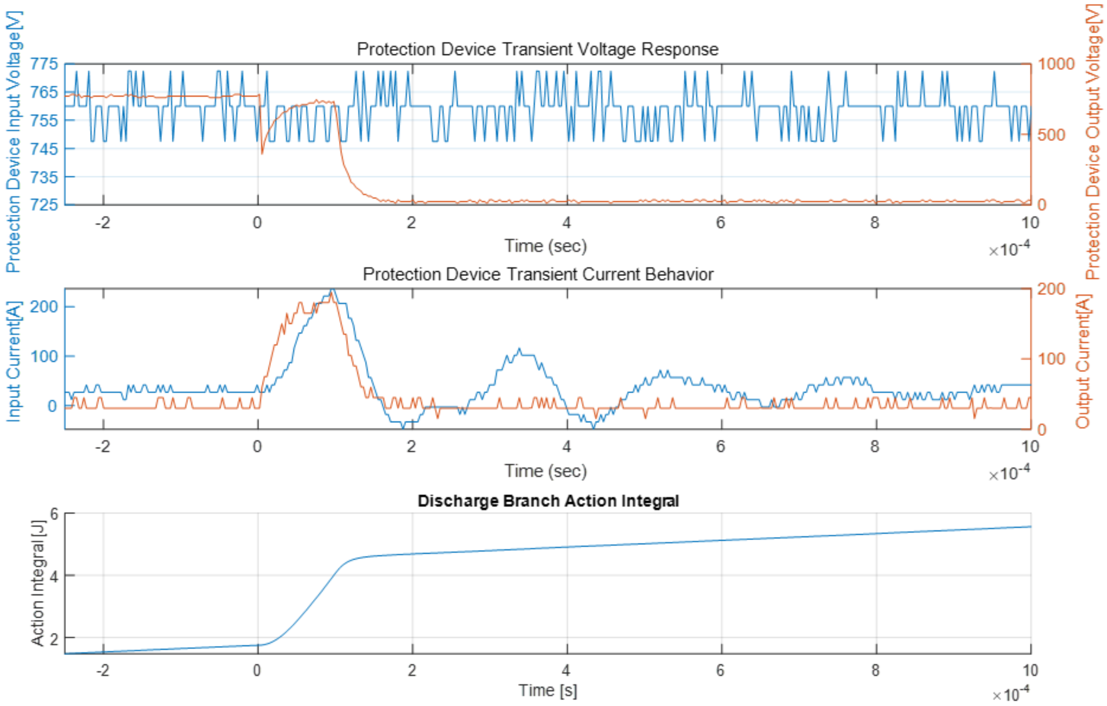

Figure 163. Protection Device Response to a 4.7 Ohm Pole to Pole Fault (Isolated Bus).

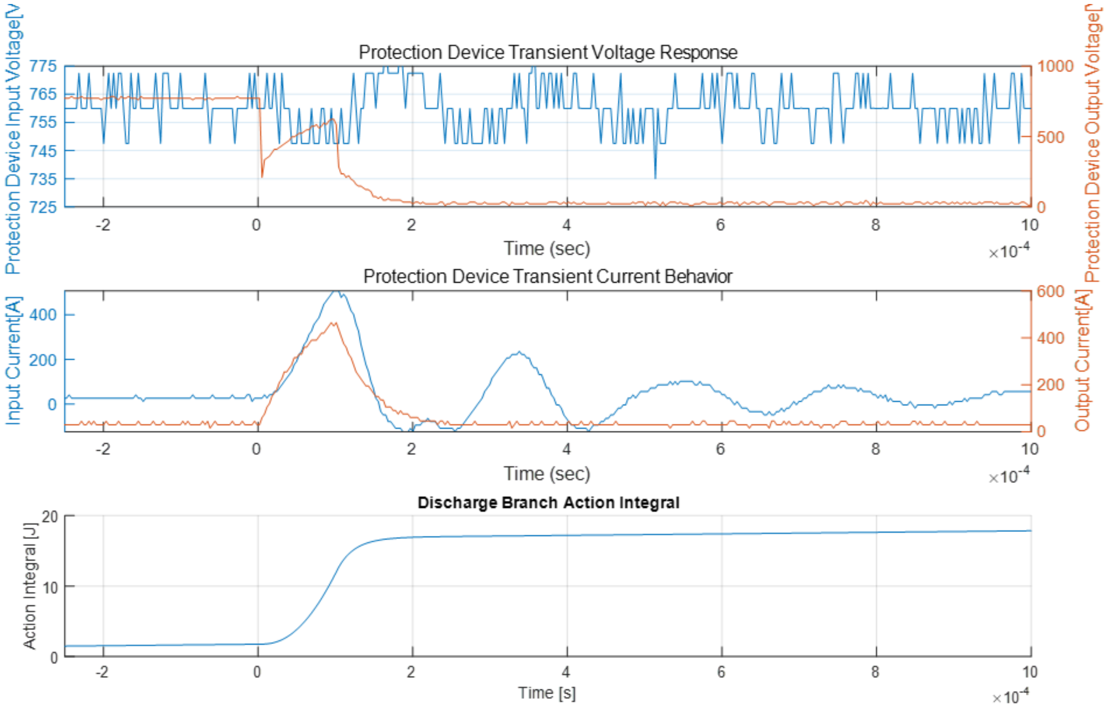

Figure 164 Protection Device Response to 1.1 Ohm Pole-Pole Fault (Isolated Bus).

6.5. Emera Model Development and Validation

For verifying the protection algorithms developed for DC microgrids, a high fidelity PSCAD model was required to replicate the response of Emera DC microgrid under both steady state and fault scenarios. This model was vastly used for developing the algorithms discussed in Sections 4.2 and 4. The PSCAD model is a replica of the Emera microgrid and has frequency-dependent cable models to capture TWs at different frequency ranges.

The main components of the DC microgrid are a voltage-controlled boost converter, nanogrid boxes and a grid following inverter that connects the DC microgrid with the AC distribution grid. Figure 165 shows the schematic of the DC microgrid with the main components. Brief description about the modeling efforts of the DC microgrid components is given subsequent sections.

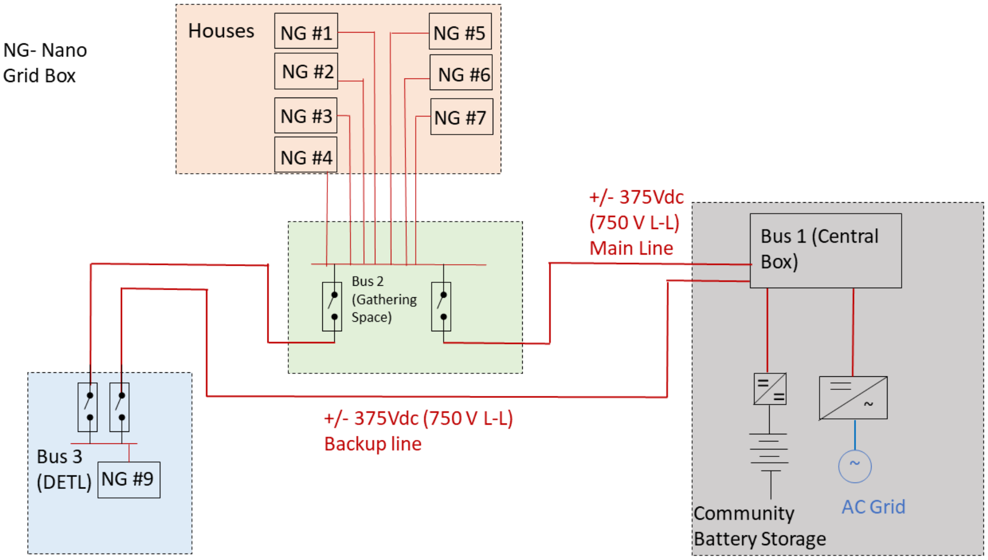

Figure 165. Schematic of EMERA DC microgrid.

6.5.1. *Description of the Energy Storage System (ESS) Boost Converter Model*

The DC microgrid has the voltage-controlled boost converter at the central box bus. The boost converter has a battery energy storage on the low-voltage side which is known as community battery energy storage. The boost converter is bidirectional and hence, can be used for both charging and discharging the community battery. The control of the boost converter is such that, irrespective of the direction and amount of power drawn from the DC microgrid bus, the boost converter keeps the voltage of the DC microgrid constant at ±375 V (750 V pole-to-pole). Figure 166 shows the model of the boost converter. The values of different components, i.e., inductors and capacitors inside the boost converter are gathered primarily from field data if available. Else, their value is calculated using standard equations.

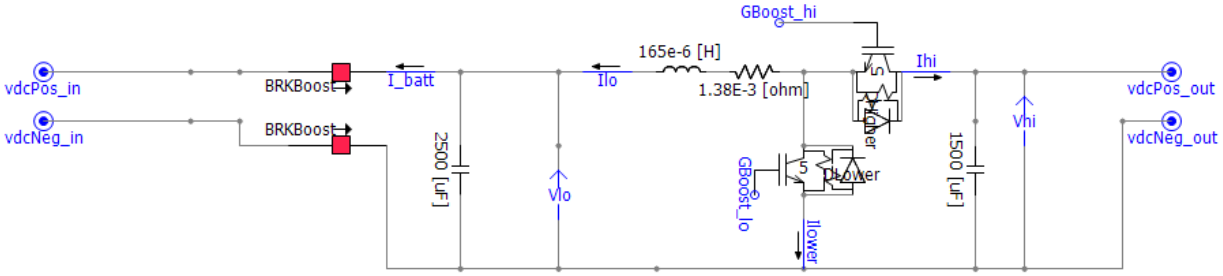

Figure 166. Model of the voltage-controlled boost converter

6.5.2. Description of the Nanogrid Models

Each nanogrid box is connected to the ±375 V DC microgrid bus through a DC-DC buck converters. The LV side rated voltage of the buck converter is 375 V and is connected to a battery unit known as home battery unit. The buck converter operates on the LV side's current control mode. A rooftop PV system is connected to the 375 V bus and is equipped with a maximum power point tracking (MPPT) scheme to capture the maximum power out of the PV panels. To accommodate an accurate simulation of PV systems, we have used the PV panel models in PSCAD. An inverter is modeled to replicate the existing inverters in the nanogrids for interconnecting the AC load inside the house. The inverter works in grid forming mode so that any unbalanced load inside the home can be delivered. The nanogrid box PSCAD model is shown in Figure 167.

As understood, any immediate change in power on the 375 V bus will be compensated by the home battery unit and the voltage will be kept at the rated value. Then, depending on the PV generation, state of charge (SOC) of the home battery, and AC load, the current setpoint of the buck converter can be determined and the current will be controlled accordingly.

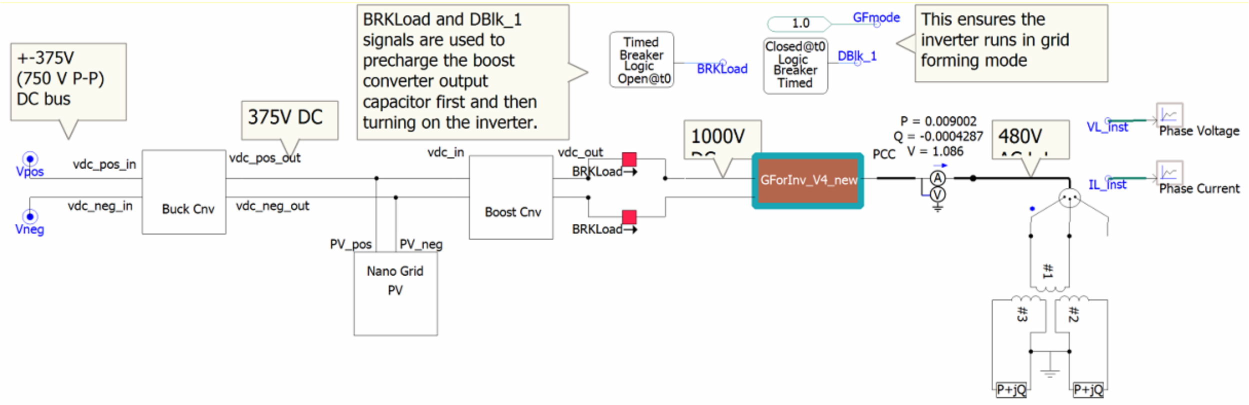
+-375V
(750 V P-P)
DC bus

375V DC

BRKLoad and DBlk_1 signals are used to precharge the boost converter output capacitor first and then turning on the inverter.

This ensures the inverter runs in grid forming mode

1000V DC

480V AC

Figure 167. Nanogrid box model including the DC-DC converters, PV module, BESS, and an inverter.

6.5.3. Description of the Grid following inverter

As stated before, an inverter connects the DC microgrid with the AC distribution grid through a transformer. The DC side of the inverter is connected to the ±375 V DC bus at the Central Box bus. The inverter is a grid following one and runs on a (P,Q) setpoint mode. This (P,Q) setpoint can be calculated by a global energy management system (EMS) depending on the current setpoints on the LV side of the buck converters inside the NG-box and SOC of the community battery energy storage.

6.5.4. Description of the Grounding System

The modeled grounding scheme in the field is shown in Figure 168. This grounding scheme is located on the central box bus and the ±375 V DC bus is grounded only at this point. As can be seen, the DC microgrid has high resistive midpoint grounding scheme. This kind of grounding scheme restricts any high current in case of a ground fault at any point on the bus.

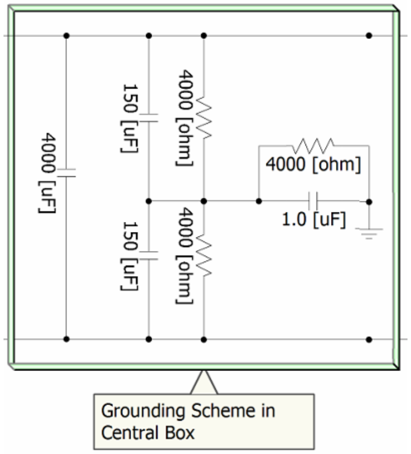

Figure 168. The grounding system model of Emera microgrid in PSCAD.

6.5.5. Fault Response Comparison

In order to verify the fault response from the PSCAD model against the fault response from the actual microgrid, a set of model tuning stages were applied to generate the most accurate results in PSCAD. This included the tuning of the grounding system parameters, the inductance of the fault limiter, the parameters of the frequency dependent cable models (See Figure 169), and utilizing combined resistor, inductor, and capacitor modules to account for the disconnect and short cables that were not the part of the longer cables modelled as frequency dependent models (See Figure 170). The cable parameters like the core inductor and insulator thickness were selected based on the cable manufacturer sheets. The distance between two cables and the cables' aerial height in the microgrid varies at different locations, so these two parameters were tuned to derive the best match in response to faults. A comparison between the real measurements from Emera microgrid and simulated fault current in PSCAD is provided in Figure 119. Figure 119(a) shows the results for a positive pole to ground fault at Gathering Space with 1 Ω resistance when measurements are performed at DETL. Figure 119(b) shows the results for a pole to pole fault at DETL with 4.7 Ω resistance with measurements at the Central Box.

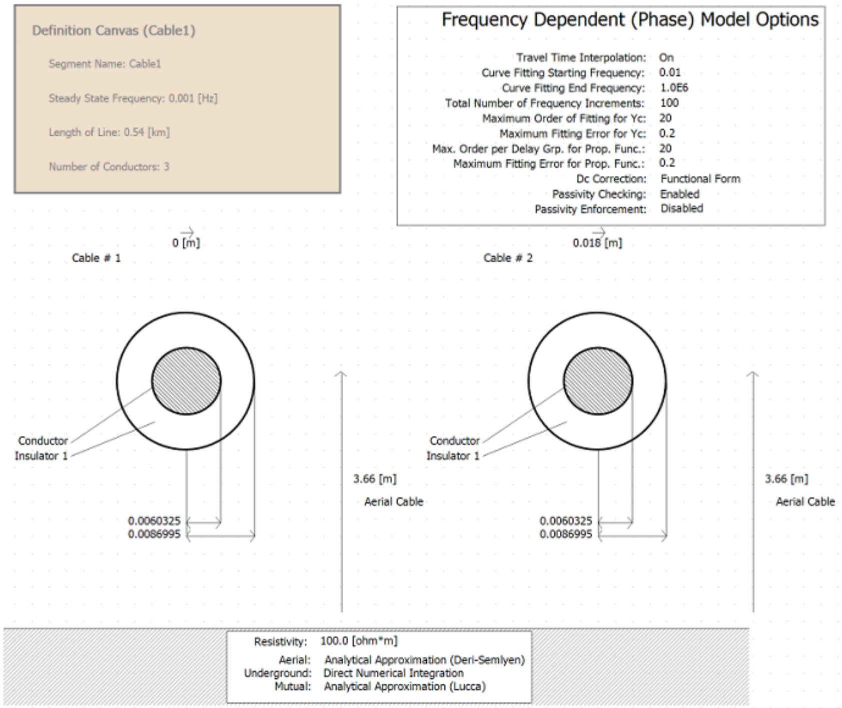

Definition Canvas (Cable1)

Segment Name: Cable1

Steady State Frequency: 0.001 [Hz]

Length of Line: 0.54 [km]

Number of Conductors: 3

Frequency Dependent (Phase) Model Options

Travel Time Interpolation: On
Curve Fitting Starting Frequency: 0.01
Curve Fitting End Frequency: 1.0E6
Total Number of Frequency Increments: 100
Maximum Order of Fitting for Yc: 20
Maximum Fitting Error for Yc: 0.2
Max. Order per Delay Grp. for Prop. Func.: 20
Maximum Fitting Error for Prop. Func.: 0.2
Dc Correction: Functional Form
Passivity Checking: Enabled
Passivity Enforcement: Disabled

Resistivity: 100.0 [ohm*m]
Aerial: Analytical Approximation (Deri-Semlyen)
Underground: Direct Numerical Integration
Mutual: Analytical Approximation (Lucca)

Figure 169. The frequency dependent model used in PSCAD for modeling the microgrid's cables.

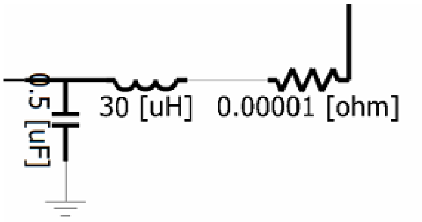

Figure 170. The combined RLC modules utilized for model tunning under fault condition.

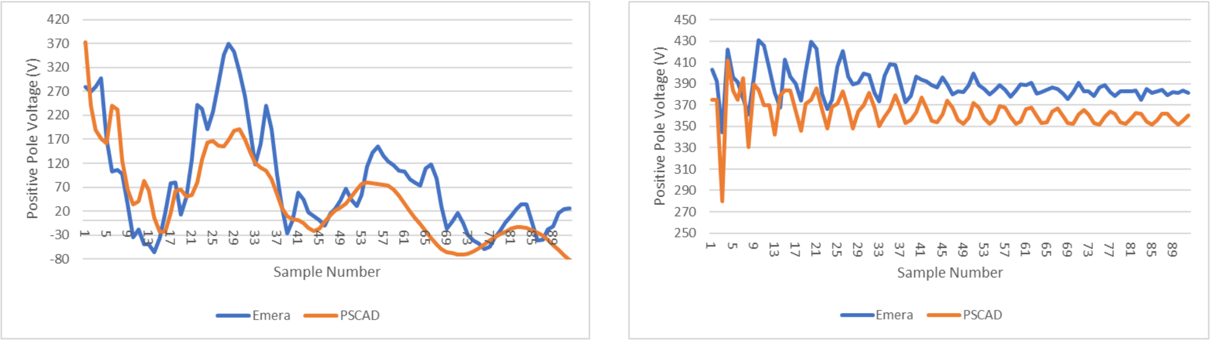

(a) (b)

Figure 171. PSCAD model validation: (a) Positive pole voltage for a positive pole to ground fault at Gathering Space with 1 Ω resistance (measurement at DETL); (b) Positive pole voltage for a pole to pole fault at DETL with 4.7 Ω resistance (measurement at Central Box).

6.6. Microgrid Model for Real-Time Testing [49, 50]

The PSCAD model of the microgrid in the previous section provided high-frequency simulations of traveling waves in the system. For real-time hardware-in-the-loop testing, a MATLAB/Simulink simulation model of the Emera Technologies nanogrids was developed. The state-space average nanogrid model provides power management of the DC microgrid, and is validated based on measurements from the actual microgrid.

The nanogrid is designed to coordinate power between generation and residential load. The internal DC bus voltage of the nanogrid is ~375 V_{DC}. The 9 kWh BESS is connected directly to the internal bus and sets its voltage. Power can also be supplied from a 7.3 kW, 80 V_{DC}, PV array and from a 6 kW, 48 V_{DC} diesel generator. A three-phase, grid-forming (GFM) inverter supplies power to the AC loads of the nanogrid. A transfer switch directs power to the loads from either the nanogrid or an external AC grid. The nanogrid architecture is composed of:

- *DC/DC Boost Converter:* A DC/DC boost converter provides power from the DC diesel generator by stepping the 48 V_{DC} input up to the nanogrid bus voltage.
- *DC/DC Buck-Boost Bidirectional Converter:* A DC/DC bidirectional converter transfers nanogrid power to and from the +/-375 V_{DC} microgrid interconnect.
- *DC/DC Single Ended Primary Inductor Converter:* A Single Ended Primary Inductor Converter (SEPIC) executes the MPPT to extract the maximum power from the PV array.
- *DC/AC Grid-Forming Inverter:* A DC/AC three-phase GFM inverter converts DC power from the nanogrid to serve AC loads.

A block diagram of the nanogrid architecture is illustrated in Figure 172. The state-space equations for the DC converters are V_{link}.

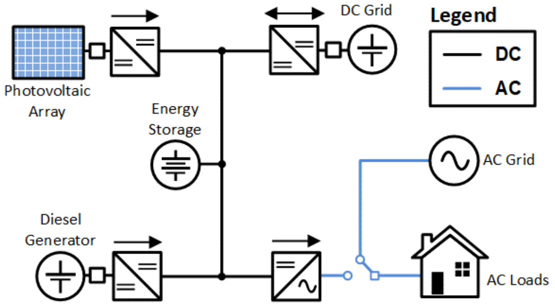

Figure 172. Block diagram of the Nanogrid.

Simulation results characterize the DC nanogrid model's performance under typical operating conditions. As conditions vary, the DC microgrid can provide power through the GFM inverter to the AC loads with a combination of load sharing by the energy sources of the nanogrid and their respective power converter models. In Figure 173, the power flow varies from the DC microgrid into the nanogrid model with a constant load and near constant PV power generation of 6 kW. The power from the DC microgrid is regulated through the bidirectional power converter connecting the microgrid to the internal nanogrid bus. Depending on the voltage level of the microgrid, power flows bidirectionally to support the microgrid and nanogrid power demands. The results between 0 s and 40 s show a low microgrid bus voltage that results in power being sourced to the microgrid from the nanogrid's energy storage. As the microgrid voltage bus increases, as shown from 40 s to 80 s, the direction of microgrid power goes positive, signifying a period where power is sourced to the nanogrid to support the load and provide charge power to the energy storage.

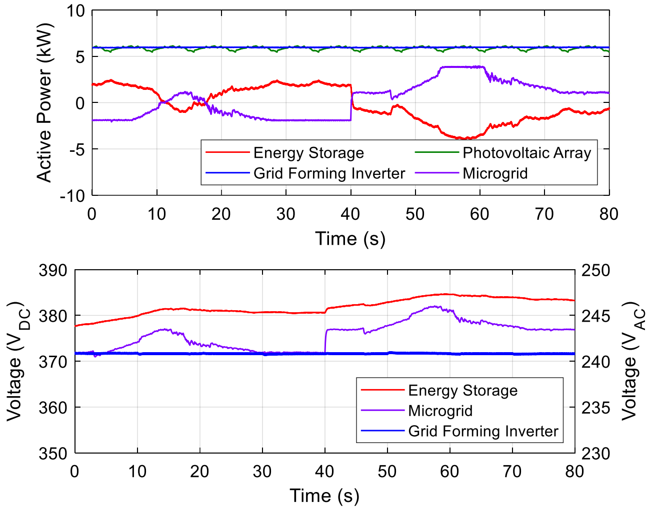

Figure 173. Simulation results obtained for the varying DC microgrid generation/consumption (a) Power (b) Voltage.

Real data from the operational Emera microgrid was then collected and used to validate the dynamic response to changes in generation and load in comparison to the actual dynamics of the DC microgrid and nanogrid. To truly put the simulation to the test, the load and solar irradiance profiles were fed into the model, which would then show the interaction of the nanogrid and microgrid. Figure 174 and Figure 175 show the comparison of the simulated (dashed traces) and experimental (solid traces) power flow and voltage, respectively. The data used in these figures was compressed from its raw 19 hour time period down to a little over a minute for simulation run time purposes.

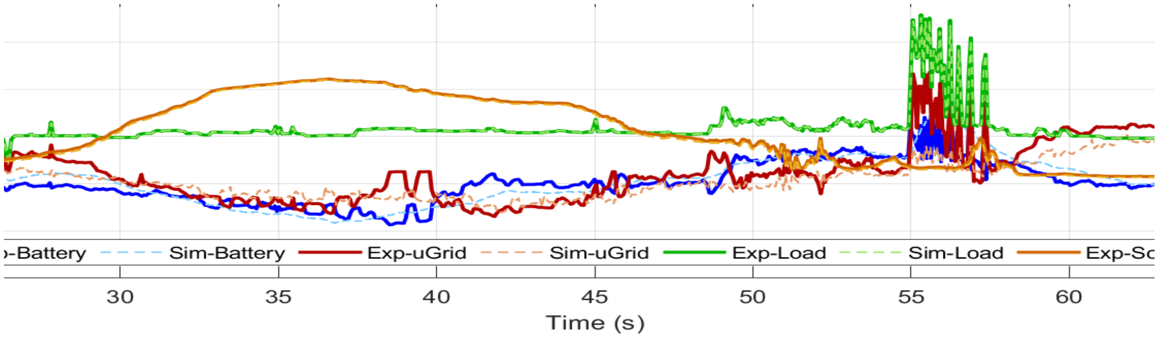

Figure 174. Comparison Between Simulation Model and Field Data collected for a Nanogrid.

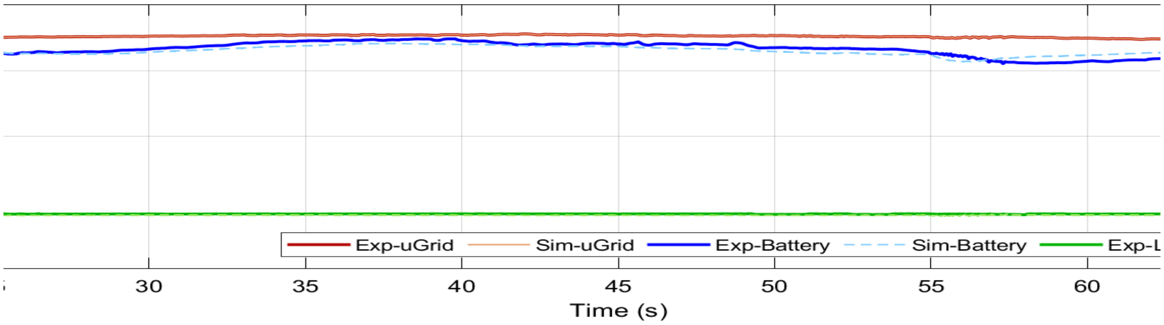

Figure 175. Comparison Between Simulation Model and Field Data collected for a Nanogrid.

A simulation model for the Emera Technologies nanogrid captures a DC microgrid's capability across realistic case scenarios and test conditions. The MATLAB/Simulink model consists of state-space average models defined for the various DC power converters of the system (boost, SEPIC, bidirectional, GFM inverter) and Simscape Power Systems components to represent electrical sources and loads. The sources and loads can be varied based on expected test case scenarios to evaluate the dynamic and steady state performance of the simulation model. The simulation results show that the nanogrid model functions as a DC microgrid that coordinates multiple energy sources to provide reliable load power over the varying environmental conditions.

6.7. Development of High-Frequency Fault Location Hardware

The fault detection embedded system is mounted onto a custom-made signal conditioning board. Three fault emulator hardware assemblies are completed and prepared for fault testing in the field. The fault emulator hardware consists of a custom analog sensor interface PCB that provides signal conditioning between external voltage and current sensor equipment and a real-time DSP controller from Texas Instruments, the TMS320F28379D control CARD. One of the tested prototypes is shown in Figure 176. The circuit boards are each assembled into a polycarbonate enclosure and provide external connectors for connecting sensors, input supply power, and USB communications. Each of the three hardware assemblies have been tested on the bench using a separate playback DSP board that provides a sampled fault waveform (via a digital to analog converter), which is injected into the fault detecting circuit prototype box.

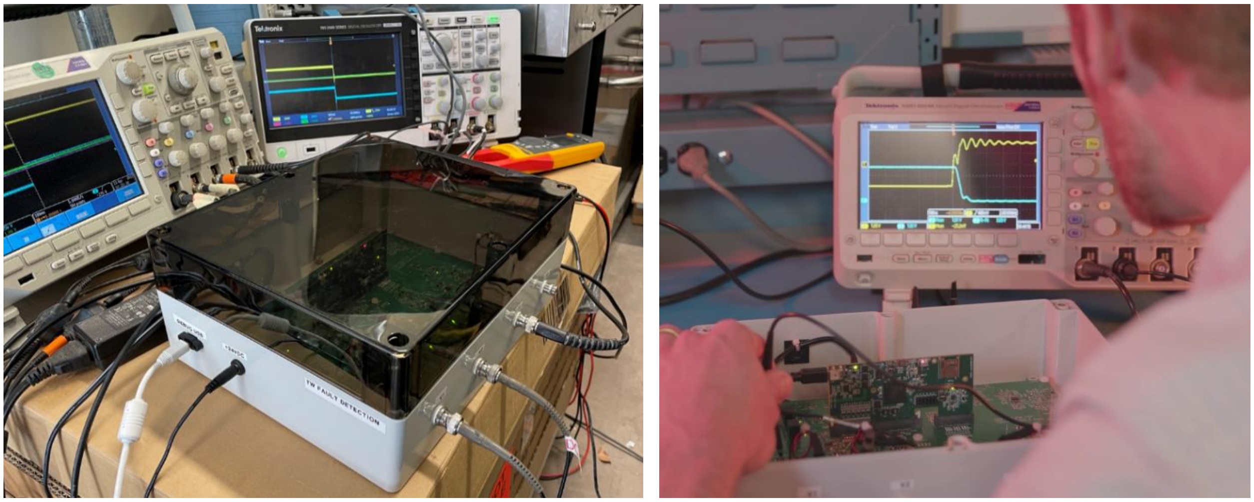

Figure 176. TW detection prototype box.

Analog signal processing circuitry (prior to the ADC inputs) provides signal gain/attenuation and filtering. A differential inverting amplifier stage is designed using a THS4531A that allows the sensor full-scale range to be attenuated to the acceptable input range of the ADC inputs. Furthermore, the differential op-amp provides a 1.5 V common mode bias for the sensor signal to allow sensor inputs to swing by positive and negative in value. Voltage attenuation for the input amplifier is designed to allow a maximum sensed signal range to be scaled down to the 0-3 V analog range of the ADC, corresponding to the 0-4096 unsigned integer range for the ADC's 12-bit sampling registers. Scaling is achieved by the conversion ratio of the transducers along with the attenuation of the differential amplifier stage prior to ADC input (set through the inverting amplifier's feedback resistors). Equations (1) and (2) capture the entire analog-to-digital signal conversion for voltage and current, ADCV and ADCI, respectively.

$$ADCV = \left(Sensor\ (V) * \frac{V}{500\ V} * \frac{0.75\ V}{V} + 1.5\ V\right) * \frac{4096}{3\ V} \tag{1}$$

$$ADCI = \left(Sensor\ (A) * \frac{V}{50\ A} * \frac{0.15\ V}{V} + 1.5\ V\right) * \frac{4096}{3\ V} \tag{2}$$

Some light filtering in the form of 10 pF and 100 pF capacitors is provided in the analog differential amplifier stages to filter any high-frequency noise coupled into the measurement during operation in a noisy field environmental. A lowpass cutoff of 10 MHz is designed to allow the 1 MHz TW signal content to pass, while blocking any much higher Electro-Magnetic Interference (EMI)/ Radio-Frequency (RF) noise found on the sensed waveforms. Figure 177 details the input circuit used to condition voltage and current sensor outputs into the ADC through the differential amplifier input stage.

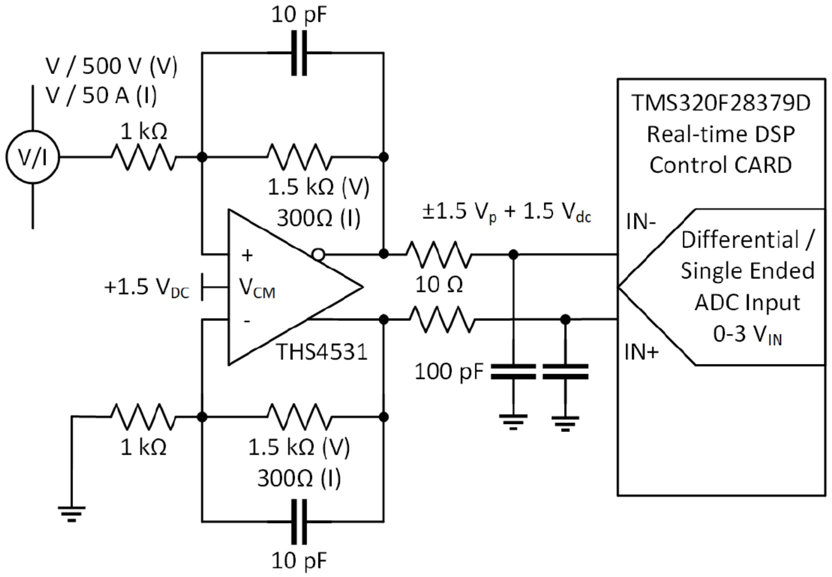

Figure 177. Analog interface circuitry used to condition sensed voltage/current outputs to correct ADC input range.

The data sampling and storage process mandates efficient use of the DSP's resources, such as memory and CPU cycle management. The simultaneous high-sampling rate (1 µs) of three signals and the sample-by-sample digital filtering on one of them requires the use of two CPU units of the DSP: the main CPU and the CLA unit, which operates in parallel with the main CPU and shares the same clock at a running frequency of 200 MHz. With a sampling rate of 1 µs, the DSP has only 200 clock cycles to sample, store, and process each sampled value. As illustrated in Figure 178, the CLA initiates the sampling process by simultaneously activating three independent analog-to-digital (A/D) converter modules. Once the samples are taken, one of them is filtered and compared to a threshold for fault detection. The foregoing process takes 70 clock cycles, leaving only 130 clock cycles before the next sampling stage occurs. Such 130 cycles are insufficient to store the three samples and the filter output (4 samples in total) in circular buffers, which is a process that takes around 150 cycles. For this reason, the four samples are moved to the main CPU through a specific memory location shared by both processing units. Once in the main CPU, each sample is stored in a circular buffer with a maximum size of 128 elements. Since both processing units run in parallel, the tasks performed by the main CPU can extend 70 cycles after the subsequent set of samples has been taken, as depicted by the red rectangle in Figure 178. This allows the main CPU to use 200 cycles to complete its corresponding tasks without overruns.

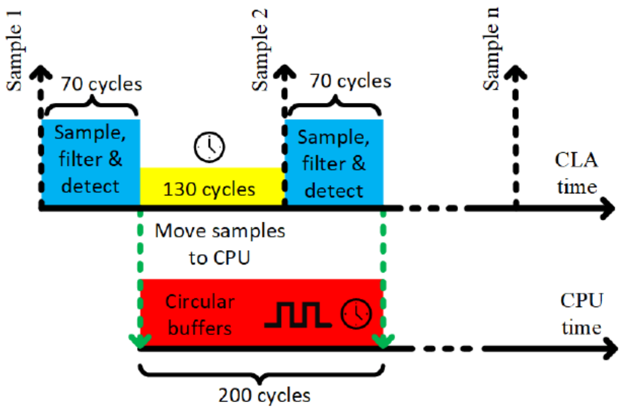

Figure 178. CPUs and clock management of the DSP.

The fault-detection process relies on capturing the high-frequency features that TWs launch at fault inception. Given the stringent time restrictions described in the previous section, a simple and reliable way to detect high-frequency transients is by using a second-order, high-pass digital filter derived by discretizing a continuous time transfer function with high-pass characteristics and a cutoff frequency of 100 kHz. The filter's difference equation results in an infinite impulse response (IIR) characteristic, described by:

$$y[k] = x[k] - 1.855x[k-1] + 0.8547x[k-2] + 1.158y[k-1] \ + 0.4112y[k-2] \qquad (3)$$

The flow diagram in Figure 179 illustrates the software implementation for sampling, fault detection, and data storage processes. The blocks in blue are implemented in the CLA, whereas the blocks in green are implemented in the main CPU. The CLA starts the process by sampling three signals and filtering one of them using the previously introduced filter equation. Then, the current filter output is compared to a user-given threshold for fault detection. The four samples are stored in their corresponding circular buffers if no fault is detected. The subsequent 128 post-fault data samples are stored in a fault array if a fault is detected. Once this array is complete, the pre-fault circular buffers are unwrapped and merged with the post-fault arrays. This way, at the end of a fault detection process, each recorded signal will have an array of 256 samples, half related to pre-fault dynamics, and the other half to post-fault dynamics.

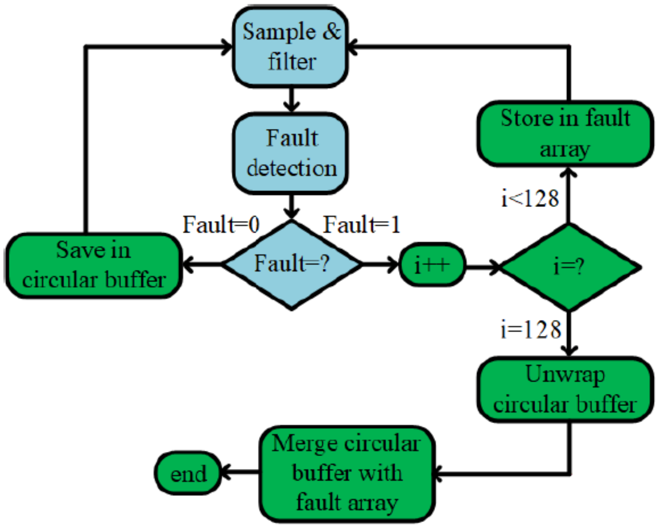

Figure 179. Sampling, fault detection, and data storage process.

6.8. Field Testing with Relay

6.8.1. Installation and Implementation in the Field

Further testing incorporated the hardware setups from Section 6.7 into the Emera MG at three different locations during fault testing. The DSP box is connected to the microgrid using the same probe setup described in Section 6.2. The three fault detection hardware assemblies will run concurrently during a fault event and be used to properly identify and locate the fault event by exercising the fault emulator and capturing traveling wave events. Figure 180 shows the location and connection of the DSP box into the microgrid.

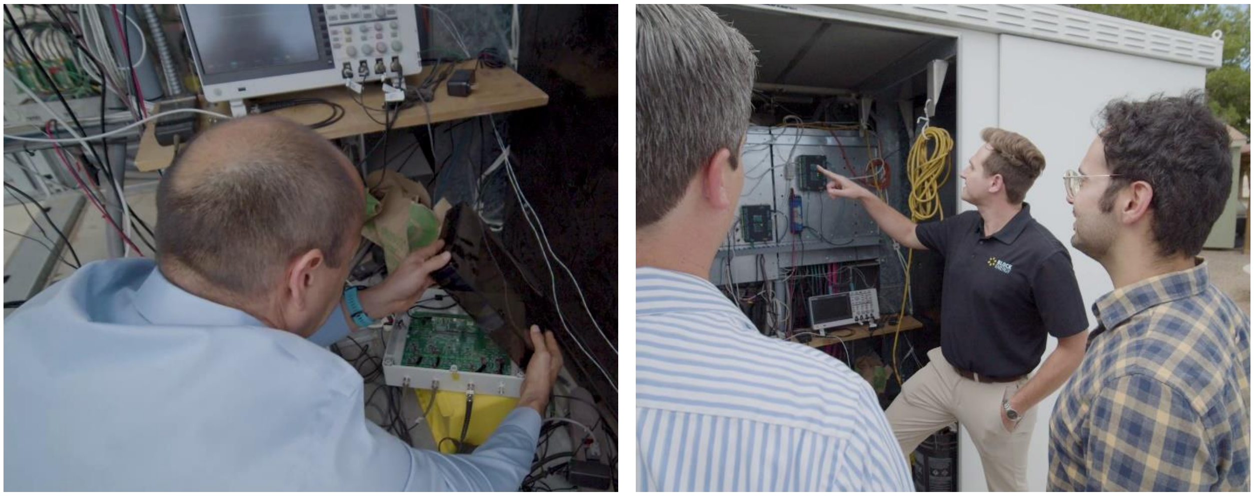

Figure 180. Installation and connection of the DSP box into the microgrid.

The DSP relay is controlled from a laptop that is placed in the measuring location. The code is loaded and executed from a local Code Composer installation. The execution of the code can be monitored from other locations by remoting into the aforementioned laptop. A rudimentary Python interface has been created using Python to read variables that are sent over to the laptop using SCI. The main control center is located at the Gathering Space. In addition, an oscilloscope is placed in parallel to get additional measurements. Figure 181 shows the information flow in the described setup.

Figure 181. Data flow in the presented testing methodology, assuming that the DSP box is located at the Central Box.

Figure 182 shows the communication and visualization from both the DSP and the oscilloscope. The DSP sends waveforms and predicts fault location through SCI communication back to the control room for real-time monitoring.

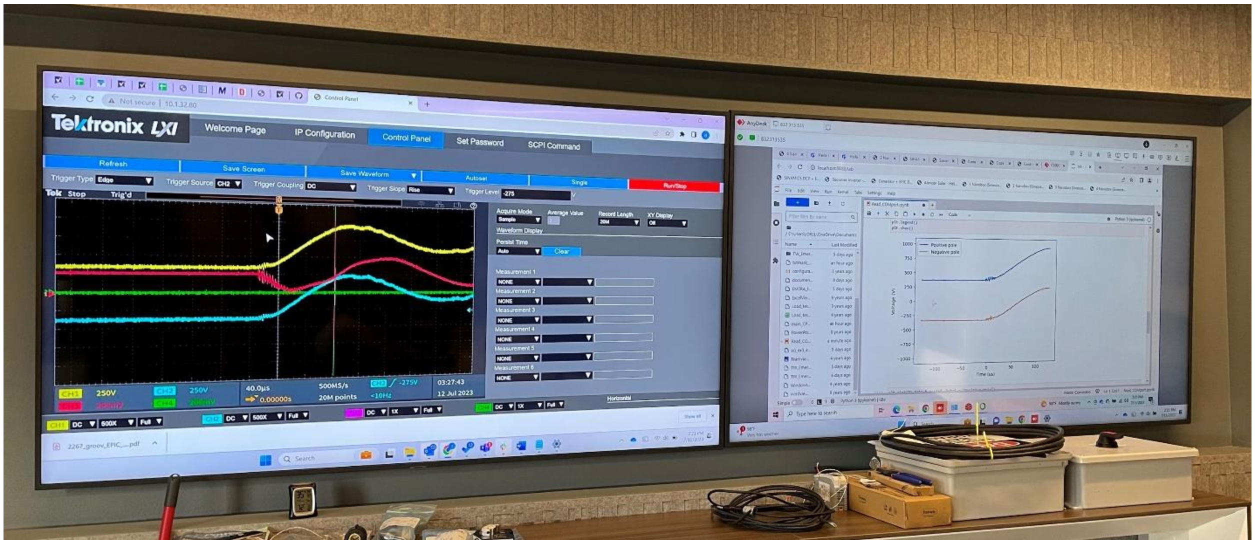

Figure 182. Control room monitoring setup showing fault detection and location results.

6.8.2. *Fault Detection and Recording*

The proposed TW fault detection algorithm has been tested under several fault types, resistance values, and locations using the fault generator described in Section 6.3. These parameters are summarized on Table 48. Three types of faults are considered: PPG, NPG, and PP The estimated detection delay time is calculated as the time difference between the first anomalous filter output value and the first value above the detection threshold. For anomaly detection, the Z-score test with eight standard deviations is employed. The standard deviation and mean are calculated from pre-fault normal operation values. In the tested fault scenarios, the detection delay ranges between 1 and 13 µs, depending on the case.

Table 48. Tested Fault Parameters and Recorded Detection Delays.

Fault location	Fault parameters	Measurement location	Detection delay (μs)
Laboratory Facility	P-G, 4.7Ω	Gathering Space	5
Laboratory Facility	P-G, 1Ω	Gathering Space	6
Laboratory Facility	N-G, 4.7Ω	Gathering Space	8
Laboratory Facility	N-G, 4.7Ω	Gathering Space	2
Laboratory Facility	P-G, 4.7Ω	Laundry Facility	13
Laboratory Facility	N-G, 1Ω	Laundry Facility	1

In Figure 183 to Figure 185, the voltage and current measurements, as well as the computed filter output, are shown for a P-G fault, 4.7 Ω, located at the Laboratory Facility and measured from the Gathering Space. The match between the DSP and the oscilloscope for voltage measurements is very accurate. There is just a slight offset on the negative pole voltage measurements. The filter output significantly correlates with the high-frequency transients observed in the positive pole voltage signal. Regarding the TW arrival time, the filter output magnitude increases abruptly. A few microseconds later, the magnitude is larger than the pre-defined detection threshold (whose value is set to 170), indicating the TW arrival. The discrepancy in the currents is due to some mVs offset in the oscilloscope input.

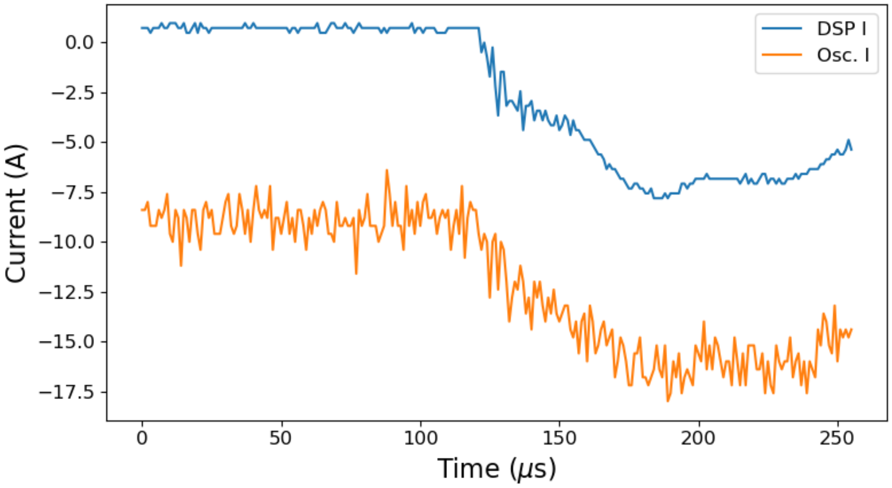

Figure 183. Positive and negative pole voltage measurements.

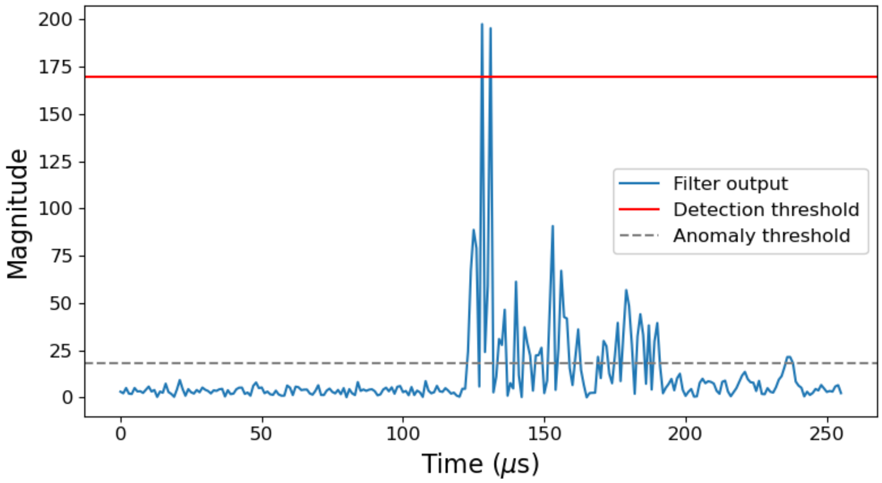

Figure 184. Absolute value of filter output.

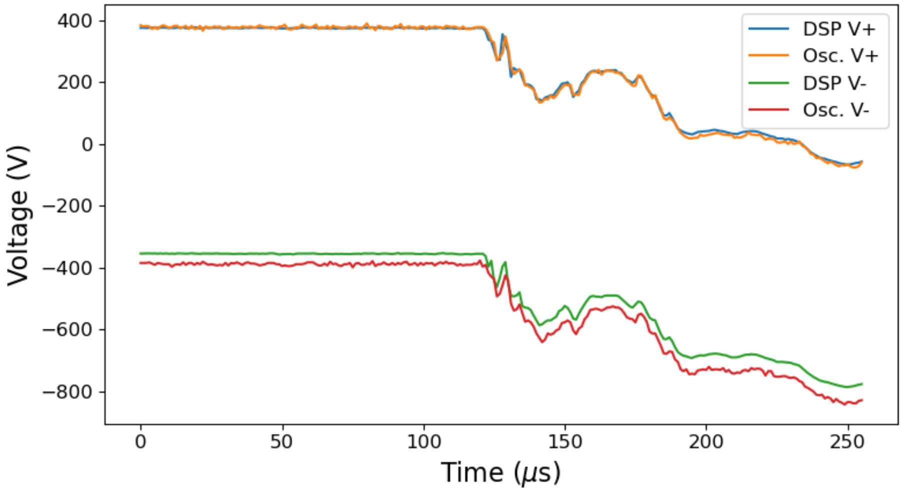

Figure 185. Positive pole current measurements.

6.8.3. Fast Fault Type and Location Class Algorithm Results

We conducted field testing on the Emera microgrid when TWPD is at CENT and DETL. For the case of TWPD at DETL, the measurements were performed at the cable going from DETL to GATH, and pole-to-ground faults were applied at GATH. The DSP output accurately predicted the fault type as 2, indicating a pole-to-ground fault at GATH from Table 38 in Section 4.2.3. The predicted outcome from DSP is shown in Figure 186.

For the TWPD at CENT location, the team created a monitoring panel at the gathering space of microgrid so visitors can observe the fault measurements in real time, as well as the location of the fault on a circuit diagram when a fault occurs. A fault emulator was used to apply positive and negative pole-to-ground fault with 1 Ω resistance at DETL. Herein, the captured TWPD's response on the monitoring screen is shown in Figure 187. As seen, the monitoring screen correctly shows the location of the fault.

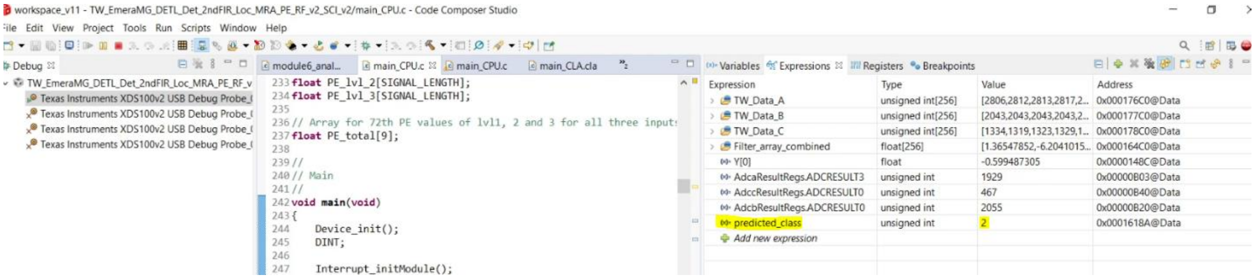

```
float PE_lvl_2[SIGNAL_LENGTH];
float PE_lvl_3[SIGNAL_LENGTH];

// Array for 72th PE values of lvl1, 2 and 3 for all three input:
float PE_total[9];

//
// Main
//
void main(void)
{
    Device_init();
    DINT;

    Interrupt_initModule();
```

Expression	Type	Value	Address
TW_Data_A	unsigned int[256]	[2806,2812,2813,2817,2...	0x000176C0@Data
TW_Data_B	unsigned int[256]	[2043,2043,2043,2043,2...	0x000177C0@Data
TW_Data_C	unsigned int[256]	[1334,1319,1323,1329,1...	0x000178C0@Data
Filter_array_combined	float[256]	[1.36547852,-6.2041015...	0x000164C0@Data
Y[0]	float	-0.599487305	0x0000148C@Data
AdcaResultRegs.ADCRESULT3	unsigned int	1929	0x00000B03@Data
AdccResultRegs.ADCRESULT0	unsigned int	467	0x00000B40@Data
AdcbResultRegs.ADCRESULT0	unsigned int	2055	0x00000B20@Data
predicted_class	unsigned int	2	0x0001618A@Data
Add new expression			

Figure 186. Fault prediction using DSP where TWPD is at DETL when a pole-to-ground fault occurs at GATH.

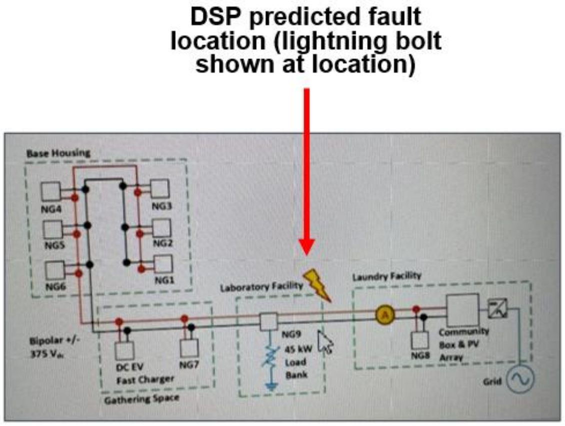

Figure 187. The TWPD's monitoring screen when TWPD is at CENT and a pole-to-ground fault occurs at DETL.

6.8.4. *Fast Fault Distance Location Algorithm Results*

The fast fault location technique described in Section 1 has been tested for the ring configuration previously shown in Figure 150. The detection method is set up to protect the line in purple in Figure 188. The DSP can be located either at the Central Box or at the Gathering Space.

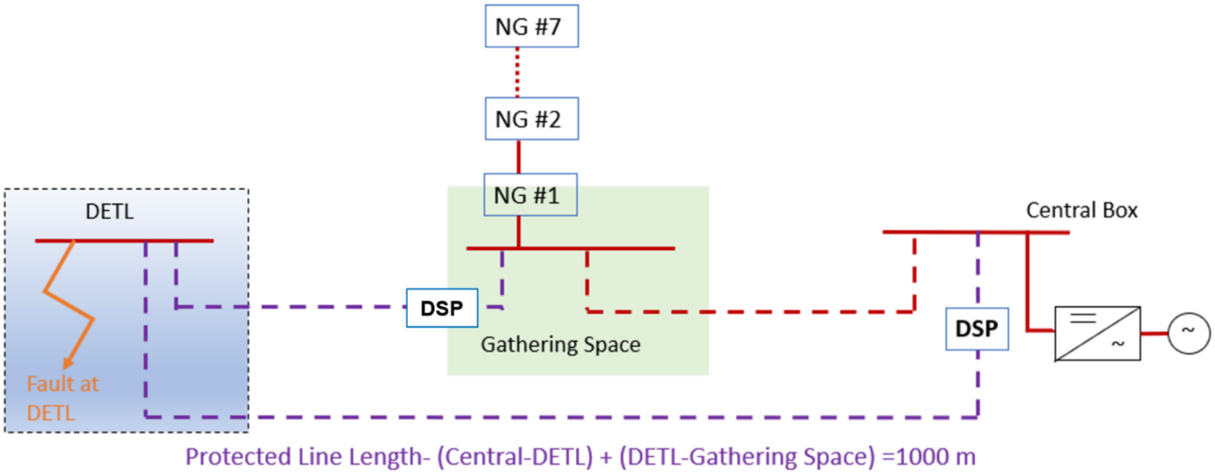

Figure 188. Fault location setup for KAFB Emera Microgrid.

Figure 189 shows the results of the fault location circular buffer for the DSP located at the Central Box. The detection of this positive to ground 1 ohm fault is correct, meaning the primary protection does detect the fault (note the measured distance comes within the 400 m value), and will operate. However, as described in Section 5.3.8, due to the reshaping of the waveform by the filter, the location is off. The distance between the Central Box and DETL is about 400 m, but the estimation is about 1066 m after 90 microseconds. Longer wait time may give a closer estimate. The selection of filter to bring the estimate closer is identified as future scope of work.

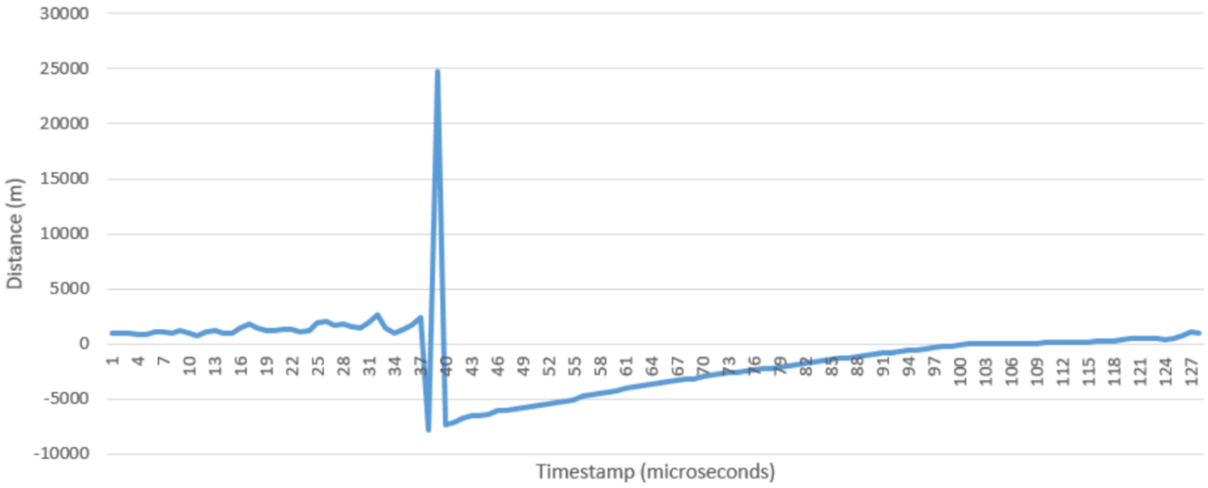

Figure 189. Circular buffer of the estimated fault distance.

7. CONCLUSIONS

This report summarized the work for the Department of Energy (DOE) Solar Energy Technologies Office (SETO) funded project 36533 "Adaptive Protection and Control for High Penetration PV and Grid Resilience". New methods for optimal adaptive protection, artificial intelligence or machine learning based protection, and time domain traveling wave protection are developed and demonstrated in hardware-in-the-loop and a field demonstration. The proposed algorithms facilitate the coordinated protection of highly DER penetrated distribution systems. As opposed to the logic-based adaptive protection technologies, the proposed model-based APP is not contingency-specific, i.e., it can adapt in real-time given the latest power system conditions. Moreover, the proposed modular protection platform and introduced LAMP units significantly help with the enhancement of power system resilience as they ensure the reliable operation of protection system under the communication network outage. Our DC microgrid protection methods were demonstrated in the field to provide time domain fast tripping protection. This project innovated power system protection to enable the grid of the future with high penetrations of inverter-based resources and the ability to detect and remove faults for power system resilience quickly and accurately.

7.1. Accomplishments and Final Deliverables

This project resulted in 19 journal publications, 45 conference papers, 41 non-paper presentations, 8 graduate students supported, 4 patent applications, 3 best paper awards, 2 best poster awards, and an R&D100 award.

The adaptive protection platform was demonstrated using real-time hardware-in-the-loop platform with the communication between all relays and devices. The final code is publicly available at https://github.com/sandialabs/Protection-settings-optimizer.

The traveling wave protection and time domain fault location algorithms were implemented in custom DSP hardware boxes and extensively tested and demonstrated in a microgrid on Kirtland Air Force Base.

7.2. Project Publications

7.2.1. Journal Papers

1. S. Augustine, M. J. Reno, S. M. Brahma, and O. Lavrova, "Fault Detection and Current Control for a Standalone DC Microgrid Using Current Derivative and Adaptive Droop", Journal of Emerging and Selected Topics in Power Electronics, 2020. [51]
2. R. C. Matthews, T. R. Patel, A. Summers, M. J. Reno, and S. Hossain-McKenzie, "Per-Phase and 3-Phase Optimal Coordination of Directional Overcurrent Relays Using Genetic Algorithm", Energies, 2021.[6]
3. F. Wilches-Bernal. A. Bidram, M. J. Reno, J. Hernandez-Alvidrez, P. Barba, B. Reimer, R. Montoya, C. Carr, and O. Lavrova, "A Survey of Traveling Wave Protection Schemes in Electric Power Systems", IEEE Access, 2021.[52]
4. A. S. Wunderlich, D. Bauer, E. Santi, R. A. Dougal, A. Benigni, R. Bennett, L. E. Zubieta, "Protection Scheme for Fast Detection and Interruption of High-Impedance Faults on Rate-Limited DC Distribution Networks", IEEE Journal of Emerging and Selected Topics in Power Electronics, 2021.[53]

5. F. Wilches-Bernal, M. J. Reno, J. Hernandez-Alvidrez, “A Dynamic Mode Decomposition Scheme to Analyze Power Quality Events”, IEEE Access, 2021. [28]
6. M. J. Reno, S. Brahma, A. Bidram, and M. E. Ropp, “Influence of Inverter-Based Resources on Microgrid Protection: Part 1: Microgrids in Radial Distribution Systems”, IEEE Power and Energy Magazine, 2021.[54]
7. R. Montoya, B. Poudel, A. Bidram, and M. J. Reno, “DC microgrid fault detection using multiresolution analysis of traveling waves”, International Journal of Electrical Power & Energy Systems, 2022.[39]
8. P. Adhikari, S. Brahma, P. H. Gadde, “Source-Agnostic Time-Domain Distance Relay”, IEEE Transactions on Power Delivery, 2022.[43]
9. M. B. Gani and S. Brahma, “A Closed-Form Mathematical Model and Method for Fast Fault Location on a Low Voltage DC Feeder Using Single-Ended Measurements”, IEEE Open Access Journal of Power and Energy, 2022.[45]
10. B. Poudel, A. Bidram, M. Reno, and A. Summers, “Zonal machine learning-based protection for distribution systems”, IEEE Access, 2022.[19]
11. M. Jimenez-Aparicio, M.J. Reno, F. Wilches-Bernal, “Traveling Wave Energy Analysis of Faults on Power Distribution Systems”, Energies, 2022.[55]
12. M. Jimenez-Aparicio, J. Hernandez-Alvidrez, A. Y. Montoya, and M. J. Reno, “Embedded, Real-Time, and Distributed Traveling Wave Fault Location Method Using Graph Convolutional Neural Networks”, Energies, 2023.[35]
13. S. Paruthiyil, A. Bidram, and M. Reno, “A Physics-informed Learning Technique for Fault Location of DC Microgrids Using Traveling Waves”, IET Generation, Transmission, and Distribution, 2023.[41]
14. C. O. Gonzalez-Candelario, R. Darbali-Zamora, E. E. Aponte-Bezares, J. D. Flicker, J. C. Neely, L. J. Rashkin, J. F. Patarroyo-Montenegro, F. Andrade-Rengifo, “Evaluation of an Autonomous Control Scheme for Interconnected DC Microgrids Using a Power Hardware-in-the-Loop Platform”, IEEE Access, 2023.[50]
15. A. R. Kurup, A. Summers, A. Bidram, M. J. Reno, and M. Martinez-Ramon, “Ensemble models for circuit topology estimation, fault detection, and classification in distribution systems”, Sustainable energy, grids and networks, 2023.[20]
16. M. Jimenez-Aparicio, F. Wilches-Bernal, M. J. Reno, “Local, Single-Ended, Traveling-Wave Fault Location on Distribution Systems Using Frequency and Time-Domain Data”, IEEE Access, 2023.[36]
17. M. Jimenez-Aparicio, T. Patel, M. J. Reno, J. Hernandez-Alvidrez, "Protection Analysis of a Traveling-Wave, Machine-Learning Protection Scheme for Distributions Systems With Variable Penetration of Solar PV" IEEE Access, 2023. [56]
18. S. Pati, M. Biswal, S. J. Ranade, O. Lavrova, and M. J. Reno, “Evaluating the use of Shapelets in Traveling Wave based Fault Detection and Classification in Distribution Systems”, IEEE Transactions on Industry Applications, 2024. [57]
19. L. Blakely, M. J. Reno, J. Azzolini, C. B. Jones, D. Nordy, “Applying Sensor-based Phase Identification with AMI Voltage in Distribution Systems”, IEEE Access, 2024. [58]

7.2.2. Conference Proceeding Publications

1. D. Sikeridis, A. Bidram, M. Devetsikiotis, M. J. Reno, “A Blockchain-Based Mechanism for Secure Data Exchange in Smart Grid Protection Systems”, IEEE Consumer Communications & Networking Conference (CCNC), 2020. [59]
2. B. Reimer, T. Khalili, A Bidram, M. J. Reno, R. C. Matthews, “Optimal Protection Relay Placement in Microgrids”, IEEE Kansas Power and Energy Conference (KPEC), 2020. [60]
3. T. Patel, S. Brahma, J. Hernandez-Alvidrez, and M. J. Reno, “Adaptive Protection Scheme for a Real-World Microgrid with 100% Inverter-Based Resources”, IEEE Kansas Power and Energy Conference (KPEC), 2020.[61]
4. N. S. Gurule, J. Hernandez-Alvidrez, R. Darbali-Zamora, M. J. Reno, J. D. Flicker, “Experimental Evaluation of Grid-Forming Inverters Under Unbalanced and Fault Conditions”, IEEE Industrial Electronics Conference (IECON), 2020.[62]
5. B. Poudel, D. Ruiz Garcia, A. Bidram, M. J. Reno, and A. Summers, “Circuit topology estimation in an adaptive protection system”, North American Power Symposium (NAPS), 2021.[63]
6. T. Patel, P. Gadde, S. Brahma, J. Hernandez-Alvidrez, and M. J. Reno, “Real-time Microgrid Test Bed for Protection and Resiliency Studies”, IEEE North American Power Symposium (NAPS), 2021.[64]
7. C. B. Jones, A. Summers, M. J. Reno, “Machine Learning Embedded in Distribution Network Relays to Classify and Locate Faults”, IEEE Innovative Smart Grid Technologies (ISGT), 2021.[65]
8. M. Jiménez Aparicio, S. Grijalva, and M. J. Reno, “Fast Fault Location Method for a Distribution System with High Penetration of PV”, Hawaii International Conference on System Sciences (HICSS), 2021.[23]
9. C. Francis, R. D. Trevizan, M. J. Reno, and V. Rao, “Topology Identification of Power Distribution Systems Using Time Series of Voltage Measurements”, IEEE Power and Energy Conference at Illinois (PECI), 2021.[66]
10. A. K. Summers, R. C. Matthews, T. Patel, and M. J. Reno, “Power System Protection Parameter Sensitivity Analysis with Integrated Inverter Based Resources”, IEEE Photovoltaic Specialists Conference (PVSC), 2021.[2]
11. N. S. Gurule, J. A. Azzolini, R. Darbali-Zamora, and M. J. Reno, “Impact of Grid Support Functionality on PV Inverter Response to Faults”, IEEE Photovoltaic Specialists Conference (PVSC), 2021.[67]
12. A. R. Kurup, M. Martinez-Ramon, A. Summers, A. Bidram and M. Reno, “Deep learning based circuit topology estimation and fault classification in distribution systems”, IEEE ISGT Europe, 2021.[68]
13. M. Jimenez-Aparicio, M. J. Reno, P. Barba, and A. Bidram, “Multi-Resolution Analysis Algorithm for Fast Fault Classification and Location in Distribution Systems”, IEEE International Conference on Smart Energy Grid Engineering (SEGE), 2021.[31]
14. L. Zubieta, Y. Zhang, and D. Bauer, “Protection Scheme for a Residential DC Microgrid”, IEEE International Conference on DC Microgrids (ICDCM), 2021.[69]
15. S. Paruthiyil, R. Montoya, A. Bidram, and M. J. Reno, “A Numerical Method for Fault Location in DC Systems Using Traveling Waves”, IEEE North American Power Symposium (NAPS), 2021.[70]

16. P. Adhikari, S. Brahma, P. H. Gadde, “Addressing the Performance of Distance Relays in Presence of Inverter Based Resources”, IEEE North American Power Symposium (NAPS), 2021.[71]
17. F. Wilches-Bernal, M. Jiménez-Aparicio, and M. J. Reno, “A Machine Learning-based Method using the Dynamic Mode Decomposition for Fault Location and Classification”, IEEE Innovative Smart Grid Technologies (ISGT), 2022.[33]
18. F. Wilches-Bernal, M. Jiménez-Aparicio, and M. J. Reno, “Algorithm for Fast Fault Location and Classification Based on Mathematical Morphology and Machine Learning”, IEEE Innovative Smart Grid Technologies (ISGT), 2022.[32]
19. D. R. Garcia, B. Poudel, A. Bidram, M. J. Reno, “Substation-level Circuit Topology Estimation Using Machine Learning”, IEEE Innovative Smart Grid Technologies (ISGT), 2022.[72]
20. A. Summers, T. Patel, R. Matthews, and M. J. Reno, “Prediction of Relay Settings in an Adaptive Protection System”, IEEE Innovative Smart Grid Technologies (ISGT), 2022.[18]
21. S. T. Ojetola, M. J. Reno, J. Flicker, D. Bauer, and D. Stoltzfuz, “Testing Machine Learned Fault Detection and Classification on a DC Microgrid”, IEEE Innovative Smart Grid Technologies (ISGT), 2022.[21]
22. S. Paul, S. Grijalva, M. Jiménez-Aparicio, and M. J. Reno, “Knowledge-based Fault Diagnosis for a Distribution System with High PV Penetration”, IEEE Innovative Smart Grid Technologies (ISGT), 2022.[30]
23. J. Jimenez-Aparicio, M. J. Reno, and F. Wilches-Bernal, “Asynchronous Traveling Wave-based Distribution System Protection with Graph Neural Networks”, IEEE Kansas Power & Energy Conference (KPEC), 2022.[34]
24. N. S. Gurule, J. Hernandez-Alvidrez, M. J. Reno, and J. Flicker, “Multiple Inverter Microgrid Experimental Fault Testing”, IEEE Photovoltaic Specialists Conference (PVSC), 2022.[73]
25. J. A. Azzolini, N. S. Gurule, R. Darbali-Zamora, and M. J. Reno, “Analyzing Hosting Capacity Protection Constraints Under Time-Varying PV Inverter Fault Response”, IEEE Photovoltaic Specialists Conference (PVSC), 2022.[74]
26. J. Hernández-Alvídrez, M. Jiménez-Aparicio, and M. J. Reno, “Impact of Modeling Assumptions on Traveling Wave Protective Relays in Hardware in the Loop”, IEEE PES General Meeting, 2022.[26]
27. M. Jimenez-Aparicio, M. J. Reno, F. Wilches-Bernal, “Shapley Additive Explanations for Traveling Wave-based Protection on Distribution Systems”, IEEE North American Power Symposium (NAPS), 2022.[24]
28. F. Miyagishima, O. Lavrova, M. J. Reno, J. Hernandez-Alvidrez, S. Augustine, S. Ranade, “Numerical Analysis of Traveling Waves in Power Systems with Grid Forming Inverters”, IEEE North American Power Symposium (NAPS), 2022.[75]
29. R. C. Matthews, T. R. Patel, A. K. Summers, and M. J. Reno, “Optimal Coordination of Distance and Overcurrent Relays with Sparse Placement”, IEEE North American Power Symposium (NAPS), 2022.[76]
30. R. C. Matthews, T. R. Patel, A. Summers, and M. J. Reno, “A Graph Theory Approach for Placing Overcurrent Relays and Reclosers for Economical Protection of Meshed Transmission Networks”, IEEE North American Power Symposium (NAPS), 2022.[77]

31. A. Montoya, M. Jimenez-Aparicio, J. Hernandez-Alvidrez, and M. J. Reno, “A Fast Microprocessor-Based Traveling Wave Fault Detection System for Electrical Power Networks”, IEEE Innovative Smart Grid Technologies (ISGT), 2023.[38]
32. M. Jimenez-Aparicio, J. Hernandez-Alvidrez, and M. J. Reno, “Fast Traveling Wave Detection and Identification Method for Power Distribution Systems Using the Discrete Wavelet Transform”, IEEE Innovative Smart Grid Technologies (ISGT), 2023.[29]
33. R. Darbali-Zamora, A. R. R. Dow, F. Palacios II, J. D. Flicker, D. Bauer, “Development of a State-Space Average Nanogrid Model for DC Microgrid Power Management Applications”, IEEE Innovative Smart Grid Technologies (ISGT), 2023.[49]
34. S. T. Ojetola and M. J. Reno, “Time Series Classification for Detecting Fault Location in a DC Microgrid”, IEEE PES Grid Edge Technologies Conference & Exposition, 2023.[22]
35. S. Paruthiyil, A. Bidram, M. Jimenez Aparicio, J. Hernandez, and M. J. Reno, “Hardware Implementation of a Traveling Wave Protection Device for DC Microgrids”, IEEE Kansas Power & Energy Conference (KPEC), 2023.[42]
36. R. Darbali-Zamora, J. Johnson, M. J. Reno, “Parametric Analysis of Photovoltaic Inverters Under Balanced and Unbalanced Voltage Phase Angle Jump Conditions”, IEEE Photovoltaic Specialists Conference (PVSC), 2023.[78]
37. B. Poudel, A. Bidram, and M. J. Reno, “Local Adaptive Modular Protection for Transmission Systems”, IEEE PES General Meeting, 2023.[79]
38. J. Hernandez-Alvidrez, M. Jimenez-Aparicio, and M. J. Reno, “Limitations of Double-Ended Traveling-Wave Protection Schemes in Distribution Systems”, IEEE PES General Meeting, 2023.[80]
39. M. Jimenez-Aparicio, J. Hernandez-Alvidrez, A. Y. Montoya, and M. J. Reno, “Micro Random Forest: A Local, High-Speed Implementation of a Machine-Learning Fault Location Method for Distribution Power Systems”, IEEE PES General Meeting, 2023.[37]
40. A. R. R. Dow, M. J. Reno, M. Jimenez-Aparicio, D. Bauer, D. Ruiz, and B. Ward, “Testing and Characterization of Fault Scenarios of a Hierarchical DC Microgrid for Residential Applications”, CIGRE US National Committee (USNC) Grid of the Future (GOTF) Symposium, 2023.[81]
41. J. Hernandez-Alvidrez, A. R. R. Dow, M. Jimenez-Aparicio, M. J. Reno, D. Bauer, and D. Ruiz, “Field Validation of a Local, Traveling-Wave, Fault Detection Method for DC Microgrids”, IEEE Innovation Smart Grid Technologies Latin America (ISGT LA), 2023. [82]
42. A. Bidram, M. J. Reno, T. Patel, D. J. Kelly, Y. Alkraimeen, “Modeling of Inverter-Based Resources for Protection Studies Considering Momentary Cessation”, IEEE Innovation Smart Grid Technologies Latin America (ISGT LA), 2023. [7]
43. C. J. Kelly, T. Patel, R. C. Matthews, A. Summers, M. J. Reno, and Y. Dong, “Incorporating Conductor Damage Constraint for Adaptive Protection Optimization in Distribution Networks”, IEEE Innovation Smart Grid Technologies Latin America (ISGT LA), 2023.[9]
44. J. Yusuf, M. E. Ropp, and M. J. Reno, “Protection Approaches for Self-Healing Microgrids Using Only Local Measurements”, IEEE Innovative Smart Grid Technologies (ISGT), 2024. [83]
45. D. Zintsmaster, M. B. Gani, S. Brahma, M. J. Reno, M. Jimenez Aparicio, and J. Hernandez-Alvidrez, “Hardware Implementation and Validation of a dc Protection Scheme Based on Local Measurements”, IEEE Texas Power and Energy Conference (TPEC), 2024. [84]

7.3. Patents

- Munim Bin Gani, Sukumar Brahma, "Topology Agnostic Detection and Location of Fault in DC Microgrid Using Local Measurements", 17/899,173
- Felipe Wilches Bernal, Matthew J. Reno, Javier Hernandez Alvidrez, "A Dynamic Mode Decomposition Scheme to Detecting Power Quality Events", 17/864,990
- Ali Bidram, Binod Poudel, Matthew J. Reno, Adam Summers, "Zonal Machine Learning-based Protection for Distribution Systems", 18/225,087
- Miguel Jimenez Aparicio, Trupal Patel, Javier Hernandez Alvidrez, Matthew J. Reno, Armando Montoya, "Systems and Methods for Fast Fault Detection and Protection Using Discrete Wavelet Transform", 63/534,222

7.4. Path Forward

For adaptive protection, there is still work to be done for incorporating more detailed models of microgrids and grid-forming inverters. Most commercial short circuit software, such as PSS®CAPE used in this project, is limited in its ability to study off-grid system or systems with high penetrations of inverter-based resources. This work was also focused on the distribution level. Future work funded by APRA-E is investigating how some of these methods can be applied at the transmission level.

For the distribution and microgrid time domain relays, additional pilot projects and demonstration are needed. The custom DSP box has been selected by the DOE Office of Technology Transitions (OTT) for the Energy I-Corps program to seek potential commercialization opportunities. DOE Cybersecurity, Energy Security, and Emergency Response (CESER) has also funded follow-on work to see how the relay could be applied for wildfire ignition prevention.

8. REFERENCES

[1] Siemens. (2021). *Stay reliable with highly-detailed protection simulation and analysis*. Available: https://new.siemens.com/global/en/products/energy/energy-automation-and-smart-grid/grid-resiliency-software/psscape.html

[2] A. K. Summers, R. C. Matthews, T. Patel, and M. J. Reno, "Power System Protection Parameter Sensitivity Analysis with Integrated Inverter Based Resources," in *2021 IEEE 48th Photovoltaic Specialists Conference (PVSC)*, 2021, pp. 2339-2344.

[3] D. Goldberg, "Genetic Algorithms in Search, Optimization and Machine Learning,. Addition-Westly," *Reading MA,* 1989.

[4] A. F. Gad. (2021). *Pygad: An intuitive genetic algorithm python library*.

[5] A. Hagberg, P. Swart, and D. S Chult, "Exploring network structure, dynamics, and function using NetworkX," Los Alamos National Lab.(LANL), Los Alamos, NM (United States)2008.

[6] R. C. Matthews, T. R. Patel, A. K. Summers, M. J. Reno, and S. Hossain-McKenzie, "Per-Phase and 3-Phase Optimal Coordination of Directional Overcurrent Relays Using Genetic Algorithm," *Energies,* vol. 14, no. 6, p. 1699, 2021.

[7] M. J. R. A. Bidram, T. Patel, D. J. Kelly, Y. Alkraimeen, "Modeling of Inverter-Based Resources for Protection Studies Considering Momentary Cessation," presented at the IEEE Innovation Smart Grid Technologies Latin America (ISGT LA), 2023.

[8] "IEEE Standard for Interconnection and Interoperability of Distributed Energy Resources with Associated Electric Power Systems Interfaces--Amendment 1: To Provide More Flexibility for Adoption of Abnormal Operating Performance Category III," *IEEE Std 1547a-2020 (Amendment to IEEE Std 1547-2018),* pp. 1-16, 2020.

[9] T. P. D. J. Kelly, R. C. Matthews, A. Summers, M. J. Reno, and Y. Dong, "Incorporating Conductor Damage Constraint for Adaptive Protection Optimization in Distribution Networks," presented at the IEEE Innovation Smart Grid Technologies Latin America (ISGT LA), 2023.

[10] Z. Zhihong, Z. Yue, C. Lei, and H. Z. Wang Bin, "Research on the protection range of distance protection zone I for short transfmission line," in *China International Conference on Electricity Distribution*, Tianjin, 2018.

[11] A. A. Subbu, "Improved method for multiterminal line protection based on reverse distance backup zones," in *IET International Conference on Developments in Power System Protection (DPSP 2010)*, Manchester, 2010.

[12] K. W. Leung, "Computer-aided setting calculation for distance zone 2 and zone 3 protection," in *International Conference on Advances in Power System Control, Operation and Management*, Hong Kong, 1991.

[13] D. Uthitsunthorn and T. Kulworawanichpong, "Distance protection of a renewable energy plant in electric power distribution systems," in *International Conference on Power System Technology*, Zhejiang, 2010.

[14] R. C. Matthews, T. R. Patel, A. K. Summers, and M. J. Reno, "Optimal Coordination of Distance and Overcurrent Relays with Sparse Placement," in *2022 North American Power Symposium (NAPS)*, Salt Lake City, 2022: IEEE.

[15] (2023). *Sandia Protection Settings Optimizer*. Available: https://github.com/sandialabs/Protection-settings-optimizer

[16] S. Šandi, B. Krstajić, and T. Popović, "pypmu—open source python package for synchrophasor data transfer," in *2016 24th Telecommunications Forum (TELFOR)*, 2016, pp. 1-4: IEEE.

[17] S. Šandi, T. Popović, and B. Krstajić, "Python implementation of ieee c37. 118 communication protocol," *ETF Journal of Electrical Engineering,* vol. 21, no. 1, pp. 108-117, 2015.

[18] A. Summers, T. Patel, R. Matthews, and M. J. Reno, "Prediction of Relay Settings in an Adaptive Protection System," in *2022 IEEE Power & Energy Society Innovative Smart Grid Technologies Conference (ISGT)*, 2022, pp. 1-5: IEEE.

[19] B. P. Poudel, A. Bidram, M. J. Reno, and A. Summers, "Zonal Machine Learning-Based Protection for Distribution Systems," *IEEE Access,* vol. 10, pp. 66634-66645, 2022.

[20] A. R. Kurup, A. Summers, A. Bidram, M. J. Reno, and M. Martínez-Ramón, "Ensemble models for circuit topology estimation, fault detection and classification in distribution systems," *Sustainable Energy, Grids and Networks,* vol. 34, p. 101017, 2023.

[21] S. T. Ojetola, M. J. Reno, J. Flicker, D. Bauer, and D. Stoltzfuz, "Testing machine learned fault detection and classification on a dc microgrid," in *2022 IEEE Power & Energy Society Innovative Smart Grid Technologies Conference (ISGT)*, 2022, pp. 1-5: IEEE.

[22] S. T. Ojetola and M. J. Reno, "Time Series Classification for Detecting Fault Location in a DC Microgrid," in *2023 IEEE PES Grid Edge Technologies Conference & Exposition (Grid Edge)*, 2023, pp. 1-5: IEEE.

[23] M. Jimenez Aparicio, S. Grijalva, and M. Reno, "Fast Fault Location Method for a Distribution System with High Penetration of PV," in *Proceedings of the 54th Hawaii International Conference on System Sciences*, 2021, p. 3205.

[24] M. Jimenez-Aparicio, M. J. Reno, and F. Wilches-Bernal, "Shapley Additive Explanations for Traveling Wave-based Protection on Distribution Systems," in *IEEE North American Power Symposium (NAPS)*, 2022.

[25] M. Jiménez-Aparicio, M. J. Reno, and J. W. Pierre, "The High-Resolution Wavelet Transform: A Generalization of the Discrete Wavelet Transforms," in *2022 IEEE 13th Annual Ubiquitous Computing, Electronics & Mobile Communication Conference (UEMCON)*, 2022, pp. 0395-0401: IEEE.

[26] J. Hernández-Alvídrez, M. Jiménez-Aparicio, and M. J. Reno, "Impact of Modeling Assumptions on Traveling Wave Protective Relays in Hardware in the Loop," in *IEEE PES General Meeting*, 2022.

[27] J. Hernández-Alvídrez, M. Jiménez-Aparicio, and M. J. Reno, "Testing Double-Ended Traveling-Wave Protection Schemes in Distribution Systems," in *2023 IEEE Power & Energy Society General Meeting (PESGM)*, 2023, pp. 1-5: IEEE.

[28] F. Wilches-Bernal, M. J. Reno, and J. Hernandez-Alvidrez, "A Dynamic Mode Decomposition Scheme to Analyze Power Quality Events," *IEEE Access,* vol. 9, pp. 70775-70788, 2021.

[29] M. Jimenez-Aparicio, M. J. Reno, and J. Hernandez-Alvidrez, "Fast Traveling Wave Detection and Identification Method for Power Distribution Systems Using the Discrete Wavelet Transform," in *2023 IEEE Power & Energy Society Innovative Smart Grid Technologies Conference (ISGT)*, 2023, pp. 1-5: IEEE.

[30] S. Paul, S. Grijalva, M. J. Aparicio, and M. J. Reno, "Knowledge-Based Fault Diagnosis for a Distribution System with High PV Penetration," in *2022 IEEE Power & Energy Society Innovative Smart Grid Technologies Conference (ISGT)*, 2022, pp. 1-5: IEEE.

[31] M. Jiménez-Aparicio, M. J. Reno, P. Barba, and A. Bidram, "Multi-resolution analysis algorithm for fast fault classification and location in distribution systems," in *2021 IEEE 9th International Conference on Smart Energy Grid Engineering (SEGE)*, 2021, pp. 134-140: IEEE.

[32] F. Wilches-Bernal, M. Jiménez-Aparicio, and M. J. Reno, "An Algorithm for Fast Fault Location and Classification Based on Mathematical Morphology and Machine Learning," in

2022 IEEE Power & Energy Society Innovative Smart Grid Technologies Conference (ISGT), 2022, pp. 1-5: IEEE.

[33] F. Wilches-Bernal, M. Jiménez-Aparicio, and M. J. Reno, "A Machine Learning-based Method using the Dynamic Mode Decomposition for Fault Location and Classification," in *Proceedings of the Thirteenth Conference on Innovative Smart Grid Technologies (ISGT), New Orleans, LA, USA*, 2022, pp. 24-28.

[34] M. Jiménez-Aparicio, M. J. Reno, and F. Wilches-Bernal, "Asynchronous Traveling Wave-based Distribution System Protection with Graph Neural Networks," in *2022 IEEE Kansas Power and Energy Conference (KPEC)*, 2022, pp. 1-6: IEEE.

[35] M. Jiménez-Aparicio, J. Hernández-Alvidrez, A. Y. Montoya, and M. J. Reno, "Embedded, Real-Time, and Distributed Traveling Wave Fault Location Method Using Graph Convolutional Neural Networks," *Energies,* vol. 15, no. 20, p. 7785, 2022.

[36] M. Jimenez-Aparicio, F. Wilches-Bernal, and M. J. Reno, "Local, Single-Ended, Traveling-Wave Fault Location on Distribution Systems Using Frequency and Time-Domain Data," *IEEE Access,* 2023.

[37] M. Jimenez-Aparicio, J. Hernandez-Alvidrez, A. Y. Montoya, and M. J. Reno, "Micro Random Forest: A Local, High-Speed Implementation of a Machine-Learning Fault Location Method for Distribution Power Systems," in *2023 IEEE Power & Energy Society General Meeting (PESGM)*, 2023, pp. 1-5: IEEE.

[38] A. Y. Montoya, M. Jimenez-Aparicio, J. Hernandez-Alvidrez, and M. J. Reno, "A Fast Microprocessor-Based Traveling Wave Fault Detection System for Electrical Power Networks," in *2023 IEEE Power & Energy Society Innovative Smart Grid Technologies Conference (ISGT)*, 2023, pp. 1-5: IEEE.

[39] R. Montoya, B. P. Poudel, A. Bidram, and M. J. Reno, "DC microgrid fault detection using multiresolution analysis of traveling waves," *International Journal of Electrical Power & Energy Systems,* vol. 135, p. 107590, 2022.

[40] M. Reno, M. Jimenez Aparicio, F. Wilches-Bernal, J. Hernandez Alvidrez, A. Montoya, P. Barba, J. Flicker, A. Dow, A. Bidram, and S. K. Paruthiyil, "Signal-Based Fast Tripping Protection Schemes for Electric Power Distribution System Resilience," Sandia National Laboratories, SAND2022-13167, 2022.

[41] S. K. Paruthiyil, A. Bidram, and M. J. Reno, "A physics-informed learning technique for fault location of DC microgrids using traveling waves," *IET Generation, Transmission & Distribution,* vol. 16, no. 23, pp. 4791-4805, 2022.

[42] S. K. Paruthiyil, A. Bidram, M. J. Aparicio, J. Hernandez-Alvidrez, and M. J. Reno, "Hardware Implementation of a Traveling Wave Protection Device for DC Microgrids," in *2023 IEEE Kansas Power and Energy Conference (KPEC)*, 2023, pp. 1-5: IEEE.

[43] P. Adhikari, S. Brahma, and P. H. Gadde, "Source-agnostic time-domain distance relay," *IEEE Transactions on Power Delivery,* vol. 37, no. 5, pp. 3620-3629, 2021.

[44] S. B. P. Adhikari, "Source-Agnostic Time-Domain Directional Relay," *IEEE Transactions on Power Delivery,* 2024.

[45] M. B. Gani and S. Brahma, "A closed-form mathematical model and method for fast fault location on a Low voltage dc feeder using single-ended measurements," *IEEE Open Access Journal of Power and Energy,* vol. 9, pp. 523-536, 2022.

[46] S. B. M. B. Gani, "A Coordinated Main and Backup Protection Scheme for LV dc Microgrids Using Local Measurements," *IEEE Transactions on Power Delivery,* 2024.

[47] M. B. Gani, "A coordinated main and backup protection scheme for LV dc microgrids using single-ended measurements," Clemson University, 2023.

[48] A. Rajapakse, R. Majumder, S. G. R. Energy, and R. Nelson, "Modification of Commercial Fault Calculation Programs for Wind Turbine Generators," *IEEE Power Energy Society (June 2020),* p. 81, 2020.

[49] R. Darbali-Zamora, A. R. Dow, F. Palacios, J. D. Flicker, and D. Bauer, "Development of a State-Space Average Nanogrid Model for DC Microgrid Power Management Applications," in *2023 IEEE Power & Energy Society Innovative Smart Grid Technologies Conference (ISGT)*, 2023, pp. 1-5: IEEE.

[50] C. O. Gonzalez-Candelario, R. Darbali-Zamora, E. E. Aponte-Bezares, J. D. Flicker, J. C. Neely, L. J. Rashkin, J. F. Patarroyo-Montenegro, and F. A. Rengifo, "Evaluation of an Autonomous Control Scheme for Interconnected DC Microgrids Using a Power Hardware-in-the-Loop Platform," *IEEE Access,* 2023.

[51] S. Augustine, M. J. Reno, S. M. Brahma, and O. Lavrova, "Fault current control and protection in a standalone DC microgrid using adaptive droop and current derivative," *IEEE Journal of Emerging and Selected Topics in Power Electronics,* vol. 9, no. 3, pp. 2529-2539, 2020.

[52] F. Wilches-Bernal, A. Bidram, M. J. Reno, J. Hernandez-Alvidrez, P. Barba, B. Reimer, R. Montoya, C. Carr, and O. Lavrova, "A survey of traveling wave protection schemes in electric power systems," *IEEE Access,* vol. 9, pp. 72949-72969, 2021.

[53] A. S. Wunderlich, D. Bauer, E. Santi, R. A. Dougal, A. Benigni, R. Bennett, and L. E. Zubieta, "Protection scheme for fast detection and interruption of high-impedance faults on rate-limited DC distribution networks," *IEEE journal of emerging and selected topics in power electronics,* vol. 9, no. 3, pp. 2540-2549, 2020.

[54] M. J. Reno, S. Brahma, A. Bidram, and M. E. Ropp, "Influence of inverter-based resources on microgrid protection: Part 1: Microgrids in radial distribution systems," *IEEE Power and Energy Magazine,* vol. 19, no. 3, pp. 36-46, 2021.

[55] M. Jiménez-Aparicio, M. J. Reno, and F. Wilches-Bernal, "Traveling Wave Energy Analysis of Faults on Power Distribution Systems," *Energies,* vol. 15, no. 8, p. 2741, 2022.

[56] M. Jimenez-Aparicio, T. R. Patel, M. J. Reno, and J. Hernandez-Alvidrez, "Protection Analysis of a Traveling-Wave, Machine-Learning Protection Scheme for Distributions Systems With Variable Penetration of Solar PV," *IEEE Access,* vol. 11, pp. 127255-127270, 2023.

[57] S. Pati, M. Biswal, S. J. Ranade, O. Lavrova, and M. J. Reno, "Evaluating the Use of Shapelets in Traveling Wave Based Fault Detection and Classification in Distribution Systems," *IEEE Transactions on Industry Applications,* vol. 60, no. 2, pp. 2507-2516, 2024.

[58] L. Blakely, M. J. Reno, J. A. Azzolini, C. B. Jones, and D. Nordy, "Applying Sensor-Based Phase Identification With AMI Voltage in Distribution Systems," *IEEE Access,* vol. 12, pp. 1235-1249, 2024.

[59] D. Sikeridis, A. Bidram, M. Devetsikiotis, and M. J. Reno, "A blockchain-based mechanism for secure data exchange in smart grid protection systems," in *2020 IEEE 17th Annual Consumer Communications & Networking Conference (CCNC)*, 2020, pp. 1-6: IEEE.

[60] B. Reimer, T. Khalili, A. Bidram, M. J. Reno, and R. C. Matthews, "Optimal protection relay placement in microgrids," in *2020 IEEE Kansas Power and Energy Conference (KPEC)*, 2020, pp. 1-6: IEEE.

[61] T. Patel, S. Brahma, J. Hernandez-Alvidrez, and M. J. Reno, "Adaptive protection scheme for a real-world microgrid with 100% inverter-based resources," in *2020 IEEE Kansas Power and Energy Conference (KPEC)*, 2020, pp. 1-6: IEEE.

[62] N. S. Gurule, J. Hernandez-Alvidrez, R. Darbali-Zamora, M. J. Reno, and J. D. Flicker, "Experimental evaluation of grid-forming inverters under unbalanced and fault conditions,"

in *IECON 2020 The 46th Annual Conference of the IEEE Industrial Electronics Society*, 2020, pp. 4057-4062: IEEE.

[63] B. Poudel, D. R. Garcia, A. Bidram, M. J. Reno, and A. Summers, "Circuit topology estimation in an adaptive protection system," in *2020 52nd North American Power Symposium (NAPS)*, 2021, pp. 1-6: IEEE.

[64] T. Patel, P. Gadde, S. Brahma, J. Hernandez-Alvidrez, and M. J. Reno, "Real-time microgrid test bed for protection and resiliency studies," in *2020 52nd North American Power Symposium (NAPS)*, 2021, pp. 1-6: IEEE.

[65] C. B. Jones, A. Summers, and M. J. Reno, "Machine learning embedded in distribution network relays to classify and locate faults," in *2021 IEEE Power & Energy Society Innovative Smart Grid Technologies Conference (ISGT)*, 2021, pp. 1-5: IEEE.

[66] C. Francis, V. Rao, R. D. Trevizan, and M. J. Reno, "Topology identification of power distribution systems using time series of voltage measurements," in *2021 IEEE Power and Energy Conference at Illinois (PECI)*, 2021, pp. 1-7: IEEE.

[67] N. S. Gurule, J. A. Azzolini, R. Darbali-Zamora, and M. J. Reno, "Impact of Grid Support Functionality on PV Inverter Response to Faults," in *2021 IEEE 48th Photovoltaic Specialists Conference (PVSC)*, 2021, pp. 1440-1447: IEEE.

[68] A. R. Kurup, M. Martínez–Ramón, A. Summers, A. Bidram, and M. J. Reno, "Deep learning based circuit topology estimation and fault classification in distribution systems," in *2021 IEEE PES Innovative Smart Grid Technologies Europe (ISGT Europe)*, 2021, pp. 01-05: IEEE.

[69] L. Zubieta, Y. Zhang, and D. Bauer, "Protection scheme for a residential DC microgrid," in *2021 IEEE Fourth International Conference on DC Microgrids (ICDCM)*, 2021, pp. 1-7: IEEE.

[70] S. K. Paruthiyil, R. Montoya, A. Bidram, and M. J. Reno, "A Numerical Method for Fault Location in DC Systems Using Traveling Waves," in *2021 North American Power Symposium (NAPS)*, 2021, pp. 1-6: IEEE.

[71] P. Adhikari, S. Brahma, and P. H. Gadde, "Addressing the Performance of Distance Relays in Presence of Inverter Based Resources," in *2021 North American Power Symposium (NAPS)*, 2021, pp. 1-6: IEEE.

[72] D. R. Garcia, B. Poudel, A. Bidram, and M. J. Reno, "Substation-level circuit topology estimation using machine learning," in *2022 IEEE Power & Energy Society Innovative Smart Grid Technologies Conference (ISGT)*, 2022, pp. 1-6: IEEE.

[73] N. S. Gurule, J. H. Alvidrez, M. J. Reno, and J. Flicker, "Multiple Inverter Microgrid Experimental Fault Testing," in *IEEE Photovoltaic Specialists Conference (PVSC)*, 2022.

[74] J. A. Azzolini, N. S. Gurule, R. Darbali-Zamora, and M. J. Reno, "Analyzing Hosting Capacity Protection Constraints Under Time-Varying PV Inverter Fault Response," in *2022 IEEE 49th Photovoltaics Specialists Conference (PVSC)*, 2022, pp. 0431-0438: IEEE.

[75] F. Miyagishima, O. Lavrova, M. J. Reno, J. Hernandez-Alvidrez, S. Augustine, and S. Ranade, "Numerical Analysis of Traveling Waves in Power Systems with Grid Forming Inverters," presented at the IEEE North American Power Symposium (NAPS), 2022.

[76] R. C. Matthews, T. R. Patel, A. K. Summers, and M. J. Reno, "Optimal Coordination of Distance and Overcurrent Relays with Sparse Placement," in *2022 North American Power Symposium (NAPS)*, 2022, pp. 1-6: IEEE.

[77] R. C. Matthews, T. R. Patel, A. K. Summers, and M. J. Reno, "A Graph Theory Approach for Placing Overcurrent Relays and Reclosers for Economical Protection of Meshed Transmission Networks," in *2022 North American Power Symposium (NAPS)*, 2022, pp. 1-6: IEEE.

[78] R. Darbali-Zamora, J. Johnson, and M. J. Reno, "Parametric Analysis of Photovoltaic Inverters Under Balanced and Unbalanced Voltage Phase Angle Jump Conditions," presented at the IEEE Photovoltaic Specialists Conference (PVSC), 2023.

[79] B. P. Poudel, A. Bidram, and M. J. Reno, "Local Adaptive Modular Protection for Transmission Systems," in *2023 IEEE Power & Energy Society General Meeting (PESGM)*, 2023, pp. 1-5: IEEE.

[80] J. Hernández-Alvídrez, M. Jiménez-Aparicio, and M. J. Reno, "Limitations of Double-Ended Traveling-Wave Protection Schemes in Distribution Systems," presented at the IEEE PES General Meeting, 2023.

[81] A. R. R. Dow, M. J. Reno, M. Jimenez-Aparicio, D. Bauer, D. Ruiz, and B. Ward, "Testing and Characterization of Fault Scenarios of a Hierarchical DC Microgrid for Residential Applications," presented at the CIGRE US National Committee (USNC) Grid of the Future (GOTF) Symposium, 2023.

[82] J. Hernandez-Alvidrez, A. R. R. Dow, M. Jimenez-Aparicio, M. J. Reno, D. Bauer, and D. Ruiz, "Field Validation of a Local, Traveling-Wave, Fault Detection Method for DC Microgrids," presented at the IEEE Innovation Smart Grid Technologies Latin America (ISGT LA), 2023.

[83] J. Yusuf, M. E. Ropp, and M. J. Reno, "Protection Approaches for Self-Healing Microgrids Using Only Local Measurements," in *2024 IEEE Power & Energy Society Innovative Smart Grid Technologies Conference (ISGT)*, 2024, pp. 1-5.

[84] D. Zintsmaster, M. B. Gani, S. Brahma, M. J. Reno, M. Jimenez-Aparicio, and J. Hernandez-Alvidrez, "Hardware Implementation and HIL Validation of a Local Measurement Based dc Protection Scheme," presented at the IEEE Texas Power and Energy Conference (TPEC), 2024.

[85] V. Cook, *Analysis of Distance Protection*. Hoboken: John Wiley & Sons, Incorporated, 1985.

[86] D. D. Fentie, "Understanding the dynamic mho distance characteristic," in *69th Annual Conference for Protective Relay Engineers (CPRE)*, College Station, 2016: IEEE.

[87] Q. Verzosa, "Understanding the Various Methods of Residual Compensation, Setting the Resistive Reach of Polygon Characteristics," in *32nd Annual Western Protective Relay Conference*, Spokane, 2005: IEEE.

APPENDIX A.

Inverse-Time Overcurrent Relays

Let M_{ij} be the multiples of pickup for relay ij. That is, M_{ij} represents magnitude of the phasor domain fault current $\tilde{I}_{ij}^{f}$ relative to the designated pickup current magnitude I_{ij}^{pickup} so that:

$$M_{ij} = \frac{|\,\tilde{I}_{ij}^{f}|}{I_{ij}^{pickup}}. \tag{12}$$

The operating time for an inverse-time overcurrent relay ij is:

$$T_{ij} = \begin{cases} TDS\left(\frac{k_{ij}}{M_{ij}^{\alpha_{ij}} - P_{ij}} + c_{ij}\right) + B_{ij}, & if\ M_{ij}^{\alpha_{ij}} > P_{ij} \\ \infty, & otherwise \end{cases}. \tag{13}$$

k_{ij}, α_{ij}, c_{ij}, and B_{ij} are parameters specific to the relay characteristics selected. TDS_{ij} is the time dial setting for the relay. The parameters for common types of inverse-time overcurrent relays utilized in the US are summarized in Table 49.

Table 49. Parameters for SEL-751 relay with characteristic described by (13).

Γ	Relay Type	Description	*k*	*c*	*α*	*P*	*B*
1	U1	Moderately Inverse	0.0104	0.0226	0.02	1	0
2	U2	Inverse	5.95	0.018	2	1	0
3	U3	Very Inverse	3.88	0.0963	2	1	0
4	U4	Extremely Inverse	5.67	0.0352	2	1	0
5	U5	Short-Time Inverse	0.00342	0.0062	2	1	0

If $M_{ij}^{\alpha_{ij}} \leq P_{ij}$ for either a primary relay or its backup, the coordination constraint associated with the pair is omitted from the MINLP formulation. This is to avoid division by zero and negative operating times. Such degenerate cases may cause spurious results or convergence failure.

Definite-Time Overcurrent Relays

Definite-time overcurrent relays are similar to the inverse-time overcurrent relays as it pertains to operating characteristics. Both operate based on relation to some set pickup current value. However, as its name suggests, the definite-time overcurrent relay operates after a fixed time delay once the pickup current threshold has been exceeded. As such, the operating time for the definite-time overcurrent relay is:

$$T_{ij} = \begin{cases} t_{ij}, & if\ M_{ij} > 1 \\ \infty, & otherwise \end{cases}, \tag{14}$$

where t_{ij} is the set operating times for definite-time overcurrent relay ij. M_{ij} is defined as in (12). The definite-time overcurrent relay trip is triggered with a fixed delay t_{ij} as soon as the pickup current is exceeded.

Distance Relays

For the distance relay, the operating time is a function of both current and voltage. Therefore, it is the most expensive relay of the three due to the required purchase of both a current and voltage transformer for measurement. The distance relay uses current and voltage measurements to estimate a load impedance.

The impedance is estimated using:

$$\tilde{Z}_{est} = \frac{\tilde{V}^{meas}}{\tilde{I}^{meas}}. \tag{15}$$

where $\tilde{V}^{meas}$ and $\tilde{I}^{meas}$ are the measured bus voltage and line current respectively.

As discussed in [85], distance protection elements cannot be set to deliver high speed protection to 100% of the line. Some of the causes of this limitation are:

1. measurement errors induced by voltage and current transformers;
2. errors in approximated line parameters;
3. relay calibration and transient errors.

If the relay were set to cover 100% of the distance to the next protective device, it would be impossible to ensure that relay operation does not occur for a fault slightly outside the intended trip region. Instead, as discussed in [14], a reduced line coverage approach in generally utilized.

The time-distance characteristic for a standard three-zone protection scheme is depicted in Figure 190. The standard setup for the relay is to strip instantaneously for a fault which occurs in the first 80-85% of the line length. 85% is utilized in the figure. This is referred to as Zone 1. The vertical axis of the figure denoted time as t. The horizontal axis L is length down the line. Zone 2 covers 100% of Line 1 and 50% of Line 2. Zone 2 covers 100% of Line 1 and 50% of Line 2. A Zone 2 trip occurs after a 0.4 s delay. Zone 3 covers all of Line 1, all of Line 2, and 25% of Line 3. A Zone 3 trip occurs after a delay of 0.8 s.

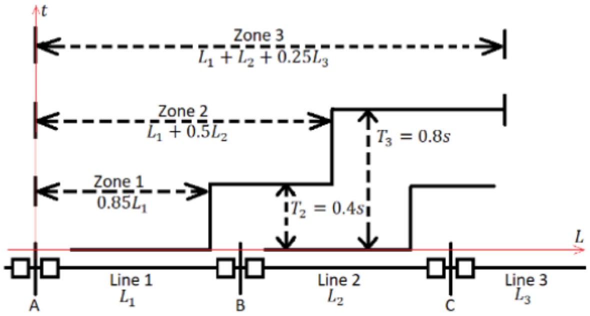

Figure 190. Time-distance characteristic for standard three-zone distance protection scheme. The vertical axis is trip time and the horizontal axis is length down the line.

Mho Characteristics

According to [85], the mho characteristic is utilized in many countries for distance protection schemes. It is suitable for measurements and does not require a separated directional element since it is inherently directional.

Consider again the three zones of protection for the line shown in Figure 190. The mho characteristics for the line are as follows. The impedances of Line 1, Line 2, and Line 3 are $\tilde{Z}_1$, $\tilde{Z}_2$, and $\tilde{Z}_3$ respectively. Zone 1 covers 85% of Line 1. Therefore, the diameter of the mho circle is directed from (0,0) to 85% of this line impedance. That is, for Zone 1, the mho circle is centered at $\left(0.85\frac{R_1}{2}, 0.85\frac{X_1}{2}\right)$ with a diameter of $|0.85\tilde{Z}_1|$. We define this as:

$$dZ = Z_r = Z, \tag{16}$$

where Z_r is the reach impedance of the zone, and Z is the measured impedance. As discussed in [86], the trip conditions can be stated as follows, where angles are limited to $(-180\,\circ, 180°]$.

Operate (inside mho):

$$\arg\left(\frac{dZ}{Z}\right) \in (-90°, 90°) \tag{17}$$

Restrain (outside mho):

$$\arg\left(\frac{dZ}{Z}\right) \in (-180°, 90°) \cup (90°, 180°] \tag{18}$$

Intermediate (on the mho circle):

$$\arg\left(\frac{dZ}{Z}\right) = \pm 90°. \tag{19}$$

For a more detailed description of reasoning behind this logic, the reader is referred to [86].

Sample mho circles are shown in Figure 191. The observed fault impedance is 0.2+j0.2-per unit. This impedance is outsize the Zone 1 mho circle and inside the Zone 2 and Zone 3 mho circles. Therefore, Zone 1 will restrain, Zone 2 will trip after a delay, and Zone 3 will trip after an additional delay if Zone 2 trip malfunctions.

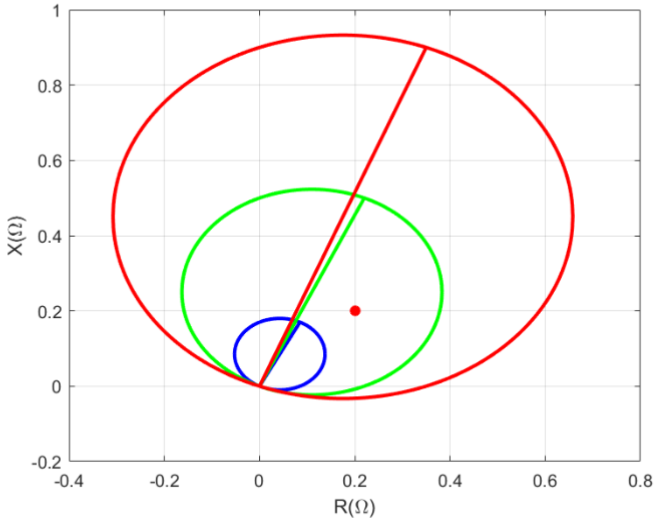

Figure 191. Sample mho circles. The line impedances are $\tilde{Z}_1 = 0.1 + j0.2$, $\tilde{Z}_2 = 0.2 + j0.25$, and $\tilde{Z}_3 = 0.1 + j0.3$. The diameters of the circles are plotted to represent the reach of each zone.

Current Compensation Factor

According to [87], correct operation of ground distance relay s is highly dependent upon correct application of residual or zero-sequence current compensation factor. As discussed in [87], the zero-sequence compensation factor is calculated as:

$$k_0 = \frac{Z_0}{Z_1} - 1, \tag{20}$$

where Z_0 and Z_1 are the zero- and positive-sequence impedances observed by the relay respectively. The adjusted value for the measured impedance observed by the relay is:

$$Z_{relay,x} = \frac{\tilde{V}_x}{\tilde{I}_x + k_0 I_0} - 1, \tag{21}$$

where $\tilde{I}_x$ is the measured phasor current of phase x, $\tilde{V}_x$ is the measured phasor voltage of phase x, and I_0 is the zero-sequence current. Compensation for the example shown in Figure 24 is shown in Figure 192. It can be seen that the estimated impedance value (marked in red) moves closer to the Zone 1 trip boundary.

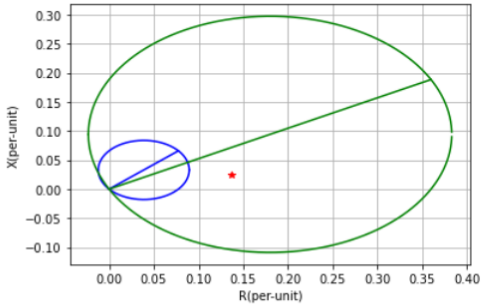

Figure 192. Sample mho circles using algorithm summarized in Figure 23 utilizing zero-sequency compensation factor k_0. The reach of each zone is the same as that shown in Figure 24. However, the observed fault impedance marked in red shifts inward when taking the zero-sequence current into account.

DISTRIBUTION

Email—Internal

Name	Org.	Sandia Email Address
Summer Ferreira	8812	srferre@sandia.gov
Matthew Reno	8813	mjreno@sandia.gov
Technical Library	1911	sanddocs@sandia.gov

Email—External

Name	Company Email Address	Company Name
John Seuss	john.seuss@ee.doe.gov	DOE SETO